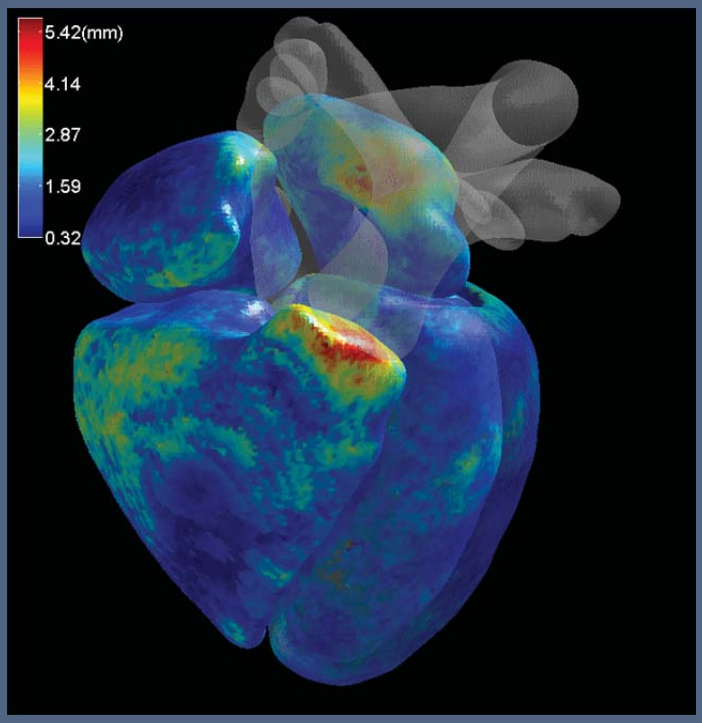

Automatic Whole Heart Segmentation Based on Image Registration

ZHUANG, Xiahai PhD Thesis 2010 UCL

(reprint in 2014)

Automatic Whole Heart Segmentation Based on Image Registration

ZHUANG, Xiahai

A dissertation submitted in partial fulfillment

of the requirements for the degree of

Doctor of Philosophy

of the

University College London

Centre for Medical Image Computing

Department of Medical Physics and Bioengineering

University College London

2010

I, Xiahai Zhuang, confirm that the work presented in this thesis is my own. Where information has been derived from other sources, I confirm that this has been indicated in the thesis.

Abstract

Whole heart segmentation can provide important morphological information of the heart, potentially enabling the development of new clinical applications and the planning and guidance of cardiac interventional procedures. This information can be extracted from medical images, such as these of magnetic resonance imaging (MRI), which is becoming a routine modality for the determination of cardiac morphology. Since manual delineation is labour intensive and subject to observer variation, it is highly desirable to develop an automatic method. However, automating the process is complicated by the large shape variation of the heart and limited quality of the data. The aim of this work is to develop an automatic and robust segmentation framework from cardiac MRI while overcoming these difficulties.

The main challenge of this segmentation is initialisation of the substructures and inclusion of shape constraints. We propose the locally affine registration method (LARM) and the free-form deformations with adaptive control point status to tackle the challenge. They are applied to the atlas propagation based segmentation framework, where the multi-stage scheme is used to hierarchically increase the degree of freedom. In this segmentation framework, it is also needed to compute the inverse transformation for the LARM registration. Therefore, we propose a generic method, using Dynamic Resampling And distance Weighted interpolation (DRAW), for inverting dense displacements. The segmentation framework is validated on a clinical dataset which includes nine pathologies.

To further improve the nonrigid registration against local intensity distortions in the images, we propose a generalised spatial information encoding scheme and the spatial information encoded mutual information (SIEMI) registration. SIEMI registration is applied to the segmentation framework to improve the accuracy. Furthermore, to demonstrate the general applicability of SIEMI registration, we apply it to the registration of cardiac MRI, brain MRI, and the contrast enhanced MRI of the liver. SIEMI registration is shown to perform well and achieve significantly better accuracy compared to the registration using normalised mutual information.

Acknowledgements

First of all, I feel so lucky to be a member of my big family where people love, care, and support each other without any conditions. In particular, I am so grateful to my mom, a hard-working and warm-hearted Chinese rural female who always sacrifices a lot for the family. Without the figure she set up for me, I may not be strong enough to finish this PhD.

I would like to thank my supervisors, Sebastien Ourselin, David Hawkes, and Derek Hill. Without their supervision and financial support from their research grants, I would not have the chance to start this PhD programme, let alone to finish it. I also would like to thank David Atkinson for examining my first- and second-year reports and giving me useful comments, thank Daniel Rueckert and Dean Barratt for examining and commenting my PhD thesis, and thank Simon Arridge and Graeme Penney for their helps to my research.

I have had a great time in CMIC where we had a fantastic research team. The colleagues have been friendly and willing to help each other, and I benefited a lot from the seminars, journal club, and discussion with these people. In particular, I would like to thank Christiana Christodoulou, Freddy Odille, and Yipeng Hu for reading my thesis and papers, Oscar Camara-Rey, Julia Schnabel, Bill Crum, Mingxing Hu, Andrew Melbourne, Ged Ridgway, Kelvin Leung, and Gang Gao for their helpful discussions. I have been very lucky to collaborate with the image science research group in King's College London, who provided the clinical data for the experiments in my thesis, particular thanks to Redha Boubertakh, Sergio Uribe, Kawal Rhode, YingLiang Ma, Cheng Yao, Reza Razavi, and Tobias Schaeffter.

Finally, I would like to acknowledge these drinks, coffee/ tea breaks and chats, trips and parties, and all the people involved, bringing laugh and warmth to my PhD study and making it easier and more colourful. The time will be always remembered.

Contents

1 Introduction **16**

1.1 Background and motivation 16
1.2 Objective and challenge 17
1.3 Contribution 21
1.4 Thesis structure 22

2 Clinical Background and Medical Imaging **24**

2.1 Cardiovascular disease 24
2.1.1 Coronary heart disease 24
2.1.2 Tetralogy of Fallot 25
2.2 Cardiac functional index 26
2.2.1 Global functional indices 26
2.2.2 Regional functional indices 27
2.3 Introduction to non-ionising radiation imaging 29
2.3.1 Cardiac MRI 29
2.3.2 Echocardiography 32

3 Literature Review and Theory **35**

3.1 Literature review on segmentation 35
3.1.1 Introduction 35
3.1.2 Texture classification using EM algorithm 36
3.1.3 Boundary-searching with deformable models 38
3.1.4 Atlas propagation using image registration 42
3.1.5 Conclusion and research direction 44
3.2 Image registration and theory 46
3.2.1 Introduction 46
3.2.2 Transformation models 49
3.2.3 Similarity measures 51
3.2.4 Conclusion 55

4 Local Structure Preservation Using Locally Affine Registration **56**

4.1 Locally affine transformation and registration 56
4.1.1 Related work 56
4.1.2 Region-based registration 58

4.1.3 Problem statement . . . 58
4.2 LARM: Locally Affine Registration Method . . . 59
4.2.1 Diffeomorphic transformation . . . 59
4.2.2 Global intensity class linkage . . . 60
4.3 DRAW: Dynamic Resampling And distance Weighted interpolation . . . 62
4.4 Phantom data experiments . . . 64
4.4.1 Experiment-1: DRAW for inverting transformations . . . 64
4.4.2 Experiment-2: LARM vs region-based registration . . . 66
4.5 Cardiac MR data experiments . . . 67
4.5.1 MR data used in this thesis . . . 68
4.5.2 Experiment-3: Ventricle segmentation using Rreg . . . 69
4.5.3 Experiment-4: Initialisation in whole heart segmentation . . . 72
4.5.4 Experiment-5: Whole heart segmentation using LARM . . . 74
4.6 Conclusion . . . 75

5 Constrained Driving Forces in Nonrigid Registration 76
5.1 FFD registration and problem statement . . . 76
5.2 FFDs with adaptive control point status . . . 78
5.2.1 Directional optimisation . . . 79
5.3 Experiments and results . . . 80
5.3.1 Experiment-1: Registration using phantom data . . . 80
5.3.2 Experiment-2: Application to whole heart segmentation . . . 82
5.4 Conclusion . . . 84

6 Whole Heart Segmentation 85
6.1 Introduction . . . 85
6.2 Segmentation framework . . . 86
6.3 Atlas construction . . . 87
6.4 Experiments and results . . . 88
6.4.1 Experimental set-up . . . 88
6.4.2 Sensitivity to different atlases . . . 91
6.4.3 Performance using alternative techniques . . . 92
6.4.4 Performance of the proposed framework . . . 94
6.5 Conclusion . . . 99

7 Preliminary Results of Exploratory Extension Work 100
7.1 Whole heart segmentation from multi-slice cardiac MRI . . . 100
7.1.1 Data and experimental setup . . . 100
7.1.2 Results and discussion . . . 101
7.2 Whole heart segmentation from compounded 3D echocardiography . . . 102
7.2.1 Motivation . . . 102
7.2.2 Method . . . 103
7.2.3 Experiment . . . 105

7.3 Whole heart segmentation using multi-atlas strategy . . . 108
7.3.1 Method . . . 108
7.3.2 Data and experimental setup . . . 109
7.3.3 Results and discussion . . . 109

8 Spatial Information Encoded Mutual Information 112
8.1 Interpretation of the problem . . . 112
8.1.1 Definition of terms and notations . . . 112
8.1.2 Insight into the problem . . . 114
8.2 Related work . . . 116
8.3 SIEMI: Spatial Information Encoded Mutual Information . . . 118
8.3.1 Encoding spatial information . . . 118
8.3.2 Similarity measure . . . 120
8.3.3 Driving forces and optimisation . . . 121
8.3.4 Choice of $\mathcal{W}_s(x)$ and unifying exiting work . . . 122
8.4 Experiments: SIEMI and different spatial encoding schemes . . . 123
8.4.1 Experiment-1: Local ascent VS global steepest ascent optimisation . . . 123
8.4.2 Experiment-2: Weighting function using cubic B-spline . . . 125
8.4.3 Experiment-3: Spatial information encoding using mixture model . . . 125
8.4.4 Experiment-4: LARM and SIEMI registration . . . 126
8.5 Experiments: Applications . . . 128
8.5.1 Experiment-5: Application to cardiac MRI and whole heart segmentation 128
8.5.2 Experiment-6: Application to dynamic contrast enhanced MRI . . . 130
8.6 Conclusion . . . 132

9 Conclusion and Future Work 134
9.1 Conclusion . . . 134
9.2 Limitation and future work . . . 136

List of Figures

1.1 Heart anatomy from the anterior view (left) and interior view (right). Images from Thibodeau and Patton (2004). 17

1.2 (a) The three views (sagittal, axial, and coronal views) of an MR image from a healthy volunteer; (b) the corresponding three views of a successful segmentation, defined by the green contour, superimposing on (a); (c) the three views of an MR image from a patient with right ventricle hypertrophy; (d) the corresponding three views of an erroneous segmentation, defined by the red contour, superimposing on (c). MR data from Guy's and St Thomas' Hospital, London. 18

1.3 Erroneous segmentation induced from indistinct boundaries, the red arrows point out the regions of errors: (a) Intersected surfaces between the left atrium and right atrium; (b) false delineation of the tricuspid valve and the correction delineation in blue; (c) epicardium leaking. Notice that the image contrast could be very different from different MR data due to the variation of the subject and scanning conditions. MR data from Guy's and St Thomas' Hospital, London. . 19

2.1 Illustration of coronary heart disease (left), image from National Institutes of Health [online] (2008), and Tetralogy of Fallot (right), image from National Institutes of Health [online] (2009). 24

2.2 Bullseye diagram of the 17 segments of the left ventricular myocardium (Cerqueira et al., 2002). 28

2.3 MRI scanner (a), image from Philips Healthcare [online] (2009a); coil with 32 receive channels for chest scanning (b), image from Philips Healthcare [online] (2009b); Echocardiography system (c), image from Philips Healthcare [online] (2009c). 29

2.4 MRI acquisition and K-space construction. 30

2.5 Ultrasound waves are generated, which are absorbed, scattered back and transmitted during propagation (a); echo pulses are received, which are reflected from boundaries between tissue types with different acoustic impedances and back to reach the receiving transducer (b); image is reconstructed based on time delay (position encoding) and amplitudes of echo pulses (intensity) (c). 32

2.6 A cardiac ultrasound image from the long-axis view (left) and short-axis view (right). Red arrows point to shadowing artefacts. Ultrasound image from Guy's and St Thomas' Hospital, London. 33

3.1 Table of the typical segmentation works on cardiac MRI, selected from the literature. The *Result* column presents the mean surface-to-surface or point-to-surface segmentation error (mean) or root mean square (RMS) of the error. The best result of Koikkalainen et al. (2008), where they compared several augmentation methods to improve the segmentation accuracy, is presented in this table. 37
3.2 Initialisation using a global affine transformation induces an overlap of local substructures at great vessels, atria and ventricles (left); the refinement based on this generates erroneous registration results (right). MR data from Guy's and St Thomas' Hospital, London. 45
3.3 Myocardium segmentation problems: including papillary muscle into myocardium (middle) and segmentation leaking in epicardium (right). MR data from Guy's and St Thomas' Hospital, London. 46
3.4 Illustration of image registration 47
3.5 Framework of image registration 47
3.6 Illustration of Powell optimisation (left) and gradient descent optimisation (right). 49

4.1 A diagram demonstrating region-based registration, where $\{G_i\}$ are local affine transformations and $\{V_i\}$ are the corresponding local regions, T is the resultant global transformation field, procedures REG, Overlap Correction, and Interpolation are defined in the text,. 58
4.2 A diagram demonstrating the overlap correction procedure of two local regions, V_1 and V_2, after the application of two local affine transformations. 59
4.3 Pseudo-code for implementing the new locally affine registration method, LARM. 61
4.4 DRAW using inverse distance interpolation from forwardly transformed scatter points (a); resampling more points within a pixel when the transformation field causes expansion (b); resampling more points in other directions when the transformation field causes anisotropic contraction (c) in one direction. 62
4.5 Phantom data used to generate dense displacement. (a) shows a rigid box in a fixed field; (b) shows the deformation field when the rigid box rotates 85 degrees; (c) shows the deformation field when the rigid box scales down to half size in one direction and rotates 10 degrees; (d) shows the deformation field when the rigid box scales up to twice the original size in one direction and rotates 10 degrees. 64
4.6 The scales of the inverse-consistency error with applied rotation (a) and scaling (b). 65
4.7 Floating image (a), subimages (within red line) of the left bar $\mathcal{M}_L$ (b) and the right bar $\mathcal{M}_R$ (c); reference image (d) as registration task one, reference image (e) as registration task two, reference image (f) as registration task three. 66
4.8 Overlapping of the reference and floating images of the three registration tasks: (a) before registration; (b) after registration using LARM; (c) after using the region-based registration (Rreg). 67

4.9 Deformation meshes of the registration results of LARM: (a) of task one; (b) of task two; (c) of task three. Upper row is the forward transformations and lower row is the inverse transformations using DRAW. 68

4.10 Atlas image and the ventricle segmentation labels superimposed on the MR image. 69

4.11 The mean surface distance distribution and standard deviation of the surface distance from healthy volunteer data and patient data (a); and the average volume difference and volume overlap of them (b). This figure shows the difference between the segmentation results by using Affine+Fluid and Rreg+Fluid. . . . 71

4.12 Atlas image and the segmentation labels of anatomical substructures superimposing onto it. 72

4.13 The registration accuracy of the three initialisation methods. 73

5.1 (a): the reference MR image; (b): the FFD mesh on the reference space with unnecessary active control points (white dots); (c): the floating image. (d): an example showing the epicardium leaking in a segmentation using standard FFD registration for the segmentation refinement. 77

5.2 Registration of an ellipse, the reference image to a circle, the floating image using adaptive control point status FFDs. The white dots in (a) are special control points explained in the text. (b) shows the FFD meshes, the contour of the ellipse, and the contour of the inverse-transformed floating image. The black dots are activated control points and the arrows demonstrate the registration driving forces. (c) gives the floating image inversely transformed into the reference space at different registration steps. (d) demonstrates the deformed FFD meshes at different registration steps whose concatenation gives the resultant transformation. 78

5.3 Images used in the experiment: (a): three views of the reference image; (b): the floating image; the images are with simulated noise and ghosting artefacts. (c)-(e): a single view of the three mask images (red) superimposing on the floating image, (c) 20 mm width, (d) 30 mm width, and (e) 40 mm width. 80

5.4 Three views, sagittal, transverse, coronal views of segmented contour superimposing on the MR images. These are four random examples of using the LARM_ACPS registration scheme (left) and the LARM_FFDs scheme (right). 83

6.1 The framework of automatic whole heart segmentation based on atlas propagation. 86

6.2 Left: an atlas intensity (MR) image using a reference space of the mean shape of 10 volunteer data. Right: corresponding segmentation, atlas label image of the atlas intensity image. Images are shown in sagittal, transverse, and coronal views. The numbers in the atlas label image indicate the names of local regions: left ventricle (1), right ventricle (2), left atrium (3), right atrium (4), myocardium (5), pulmonary artery (6), and aorta (7). 88

6.3 The individual plots and the Box-and-Whisker diagrams of the *Whole Heart* segmentation errors using the RMS surface-to-surface error measure, ϵ_{rms}. Left: the errors of the 19 pathological cases using the proposed segmentation approach combined with the three different atlases. Right: the errors of the 37 cases using the three different segmentation frameworks. Note that the red crosses are these considered as outliers in the box plots. 91
6.4 The worst cases by the three segmentation methods. Subject-1 is the worst case of the *Affine_FFDs*, subject-116 is the worst case of *LARM_FFDs*, and subject-9 is the worst case of *LARM_ACPS*. Images are displayed with delineated contour superimposed on the MR images, in sagittal, transverse, and coronal views. Subject-1 and subject-9 are pathological cases while subject-116 is a healthy case. 93
6.5 Three segmentation cases. Images are displayed with delineated contour superimposing on the MR images, in four-chamber (top) and short-axis (bottom) views. Subject-119 is a healthy case while subject-10 and subject-43 are pathological cases. The *Whole Heart* segmentation errors of them in ϵ_{rms} measure are 2.39 mm, 3.17 mm, and 2.86 mm respectively. GD: gold standard segmentation; PS: propagated segmentation. 94
6.6 The individual plots and the Box-and-Whisker diagrams of the RMS surface distance measure, ϵ_{rms}, segmentation errors using the proposed segmentation method. This figure gives the errors of each substructures as well as the *Whole Heart* from the 37 cases. 95
6.7 Two views showing the error map of surface-to-surface distance for the whole heart segmentation by the proposed method. (Please refer to the web version of this article for interpretation of the color map. A movie showing the color map from other angles can also be found at http://www.cs.ucl.ac.uk/staff/X.Zhuang/.) 96
6.8 Bland-Altman plots of the segmented volumes using the proposed method and the gold standard segmentation volumes, for the blood cavities of the left ventricle, the left atrium, the right ventricle, and the right atrium, the volume of the left ventricle myocardium, and the whole heart volume including all these substrucutres. Middle line is the bias (mean), upper and lower lines are the 2 standard deviations. 97
6.9 Bland-Altman plot (top) and linear regression plot (bottom) of all segmented volumes using the proposed method and the gold standard segmentation volumes. 98

7.1 The short-axis and long-axis slices of the short-axis multi-slice (left) and long-axis multi-slice (right) segmentation examples. 100
7.2 The individual plots and the Box-and-Whisker diagrams of the segmentation errors using the RMS surface distance measure, ϵ_{rms}. This figure gives the errors of each substructures as well as the *Whole Heart* from the 37 simulated multi-slice cases. 101

7.3 Example images and outputs from algorithms used during segmentation process, (a) view from apical scan; (b) view from parasternal view; (c) compounded image from 12 scans; (d) corresponding segmentation labels of (c). 103

7.4 Manual correction to construct the gold standard of a compounded 3D echo. Top-left: short-axis view; top-right: two-chamber view; bottom-left: four-chamber view; bottom-right: orthogonal planes. 106

7.5 Illustration of the segmentation propagation results of four cases. The first row is short-axis view, the second row is the four-chamber view and the third row is the two-chamber view. 107

7.6 The segmentation accuracy, assessed by Dice coefficient, of each substructure and the mean of the five structures. The results of three segmentation framework are presented: the segmentation propagation by using single *Mean atlas*, using multi-atlas ranked by the prior information of *NMI similarity*, and multi-atlas ranked the posterior information of Dice segmentation errors, referred to as *Post information*. 110

7.7 The over segmentation (left) and empty segmentation (right) of the left ventricle after fusion. 111

8.1 (a) T1-weighted brain image without an intensity non-uniformity field; (b) T1 image with an intensity non-uniformity field; (c) the non-uniformity field map; (d) the deformation field of registering (a) to (b) using normalised mutual information measure; (e) the deformation field of registering the two images using the proposed registration method. The error bar is the indicator for (d) and (e). A larger erroneous deformation is presented in (d) compared to (e). The error of (d) also follows the pattern of the bias field map in (e), while the registration error in (e) is evidently reduced. Brain MR data downloaded from BrainWeb. . 114

8.2 (a) A Shepp-Logan phantom (Jain, 1989, page 438); (b) The same phantom with an extra intensity class, indicated by the arrow, to simulate a tumour or an intensity non-uniformity block; (c) the resultant image of registering floating image (b) to reference image (a), using normalised mutual information: the region was contracted as pointed out by the arrow; (d) the displacement field of the registration described in (c), where red arrows indicate the displacement vector direction. The displacement field of using the proposed registration method is very close to identity and the resultant image is almost identical to (b) by human eyes. Therefore, they are not displayed in the figure. 114

8.3 The spatial variable s, associated local region Ω_s, transformation parameter θ_s, weighting function $\mathcal{W}_s(x)$, and associated joint histogram table $\mathcal{H}_s$ and entropy measure $\mathcal{S}_s$. The spatial information encoded similarity measure is the vector representation of $\{\mathcal{S}_s\}$. 118

8.4 The mean warping index every10 iteration steps. The first 100 steps are the 20 mm spacing FFD registration while the last 40 steps are the 10 mm spacing FFD registration. 124

8.5 The Box-and-Whisker diagrams of the SIEMI registration results using the cubic B-spline in Eq. (8.21) and the Gaussian with $l = 2$ in Eq. (8.23) for spatial information encoding. 125
8.6 The cardiac MR images for registration. Left: The MR image superimposed on by the contour of four pre-defined local regions. Right: The MR image with a 100% bias field and deformed by an initial transformation with warping index of 7.54 mm. 127
8.7 Example of an MR image (a) and its manually delineated surfaces (b). Images shown in sagittal, axial, and coronal views. 128
8.8 The individual plots and the Box-and-Whisker diagrams of the segmentation errors using the RMS surface distance measure, ϵ_{rms}. This figure gives the errors of each substructures as well as the *Whole Heart* from the 37 subjects. . . 130
8.9 One example of the simulated dynamic contrast enhanced MR data in 15 time points. The first row shows the time point 1 to 5 (from left to right), and the second and third rows show from time point 6 to 10 and time point 11 to 15, respectively. Images courtesy of Andrew Melbourne. 131
8.10 Registration accuracy of the liver by the two methods in the four simulated cases. 132

List of Tables

4.1 The parameters of the 3D whole heart MRI sequence. 69

4.2 Segmentation accuracy of Rreg+Fluid using surface distance measures. This table also gives the percentages of error scales: 0-2 mm, 2-5 mm, and > 5 mm. 70

4.3 Segmentation accuracy after each registration step and the p-values of the paired t-test between the errors of the two registration schemes: Affine+Fluid and LARM+FLuid. 74

5.1 The registration errors (RMS surface distance) and computation time of the four registration schemes. mm: millimeter, min: minute. 82

5.2 The segmentation error, RMS surface distance, and the percentage $(\%)$ of the error ranges: $<$2 mm, 2-5 mm, and $>$5 mm. 82

6.1 Surface-to-surface segmentation errors in millimeters, ϵ_{rms} of the three methods and errors ϵ_{mean}, ϵ_{std}, and percentage with different ranges: < 2 mm, $2-5$ mm, and > 5 mm, of the 37 cases by the proposed approach. 94

6.2 Segmentation errors by the proposed method using volume measures: Dice coefficient, volume overlap, percentage of volume difference (Diff), p-value and 0.95 confidence interval (CI) of the difference of the segmentation errors, unit mL, and Pearson correlation R. 96

7.1 Surface-to-surface segmentation errors, ϵ_{rms}, ϵ_{mean}, ϵ_{std}, and the volume measures, Dice coefficient, volume overlap, percentage of volume difference (Diff), and Pearson correlation of the 37 cases,. *Whole Heart* in volume measures means *All Substructures*. 101

7.2 The segmentation accuracy presented in volume difference. Row *Before* means the segmentation before the nonrigid registration (but after a global affine registration), row *After* means after the nonrigid registration. 107

8.1 The registration accuracy, given by the warping index, of the four registration schemes. The table also gives the ratios of computation time of the other three methods compared to that of SIEMI, and the p-values of the two tailed, paired t-test between the other three groups and SIEMI. 124

8.2 The warping index (0.01 mm) of the FFD registration results using different cost functions on the T1-T1 with 0%, 20%, 40% bias fields. Row T1-T1 gives the mean accuracy of the three different bias levels. 126

8.3 The warping index (mm) of the locally affine registration results using different cost functions on cardiac MR images with 0%, 50%, 100% bias fields. 127
8.4 The errors of NMI and SIEMI registration are assessed using the root mean square (RMS) surface distance between the surfaces of the two images. The table also gives the p-value and 95% confidence interval (CI) of the two tailed, paired t-test between the two groups of registration results. 129
8.5 Surface-to-surface segmentation errors, ϵ_{rms} (mm), of the whole heart segmentation framework using NMI and SIEMI in the refinement registration and their two tailed, paired t-test P-value of each substructure as well as the Whole Heart. 129

Chapter 1

Introduction

This chapter gives an introduction to this thesis. Section 1.1 describes the clinical background and motivation of this work; Section 1.2 presents the research objective and challenges; Section 1.3 defines the research scope and gives the main points of contribution; and Section 1.4 outlines the structure of this thesis.

1.1 Background and motivation

According to the World Health Organisation (WHO)[1], an estimated 17.5 million people died from cardiac vascular diseases (CVDs) in 2005, accounting for 30% of global deaths (Fact Sheet No. 317, World Health Organization, 2007). CVDs will remain the leading cause of death in the coming decade, and almost 20 million people are expected to die from them by 2015. Early diagnosis and effective treatment play a key role in patient recovery. Therefore, there is great emphasis in the development of novel advances in medical imaging and image computing to be introduced to clinical practice and medical research.

In the past few decades, the provision of morphological and pathological information from medical imaging has made revolutionary impacts in healthcare. Among the diverse imaging modalities, magnetic resonance imaging (MRI) is increasing in popularity owing to its recent technical improvement that enables fast three-dimensional (3D) imaging (Earls et al., 2002; Westbrook et al., 2004). With the ability to provide good contrast between soft tissues and a wide field of view (FOV), cardiac MRI provides clear anatomical information of the heart. The accurate extraction and precise interpretation of this information enable the development of new clinical applications such as functional analysis (Frangi et al., 2001) and patient-specific simulation (Sermesant et al., 2006), contributing to the improvement of cardiology.

Image segmentation, extracting volume and shape of anatomical regions, is one of the key computing procedures that have been employed in cardiological applications. Segmentation provides quantitative information (van der Geest et al., 1997) and enables the computation of many cardiac functional indices (Frangi et al., 2001). Manual delineation is demanding of both technical and clinical knowledge, and it is also subject to intra- and inter-observer errors. It is therefore desirable to produce unbiased and reproducible segmentation using automatic image computing technology. This fully automated processing is particularly essential in clinical studies where a large number of images need segmenting.

During the last decade, a lot of research has been focused on the segmentation of the

[1] World Health Organisation website: www.who.int

ventricles or myocardium (Suri, 2000; Pham et al., 2000; Frangi et al., 2001; Rueckert et al., 2002; Lorenzo-Valdes et al., 2002; Mitchell et al., 2002; Kaus et al., 2004; Noble and Boukerroui, 2006; Pilgram et al., 2006; Lynch et al., 2008). By contrast, only a few recent works have involved the whole heart, including the ventricles, myocardium, atria, and great vessels (Lotjonen et al., 2004; Ecabert et al., 2008). The rich literature in ventricle segmentation may be attributed to the fact that quantitative analysis of the ventricle and myocardium provides crucial information for diagnosing coronary heart diseases (Setser et al., 2000; Ordas and Frangi, 2005), while the poor literature in the segmentation of the whole heart is probably due to the technical difficulties of acquiring MR data covering the whole heart and achieving this automated segmentation.

However, fully automatic *whole heart segmentation* has great potential for cardiac applications:

- It provides segmentation for local regions of the heart, which enables the quantitative functional analysis on these anatomical regions such as measuring ejection fraction of the atria or ventricles.
- The geometrical information of the whole heart provides a wider field of view in the planning and guidance of cardiac interventional procedures such as radio frequency ablation.
- It is anticipated that the functional analysis using whole heart segmentation may detect subtle functional abnormalities or changes of the heart. This is important for patients who otherwise have normal systole in ventricles but suspected abnormal function in other regions.

In the next section, we will first state our research objective and then discuss the main challenges to achieve this objective.

1.2 Objective and challenge

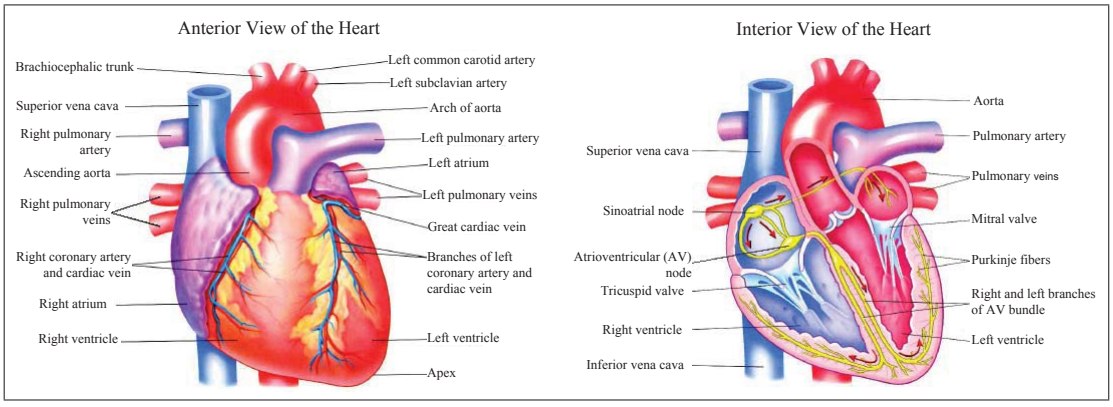

Figure 1.1: Heart anatomy from the anterior view (left) and interior view (right). Images from Thibodeau and Patton (2004).

Figure 1.1 shows the heart anatomy from the anterior and interior views. The main structure of the heart consists of the *four chambers* and great vessels. The four chambers include the left ventricle, right ventricle, left atrium, and right atrium.

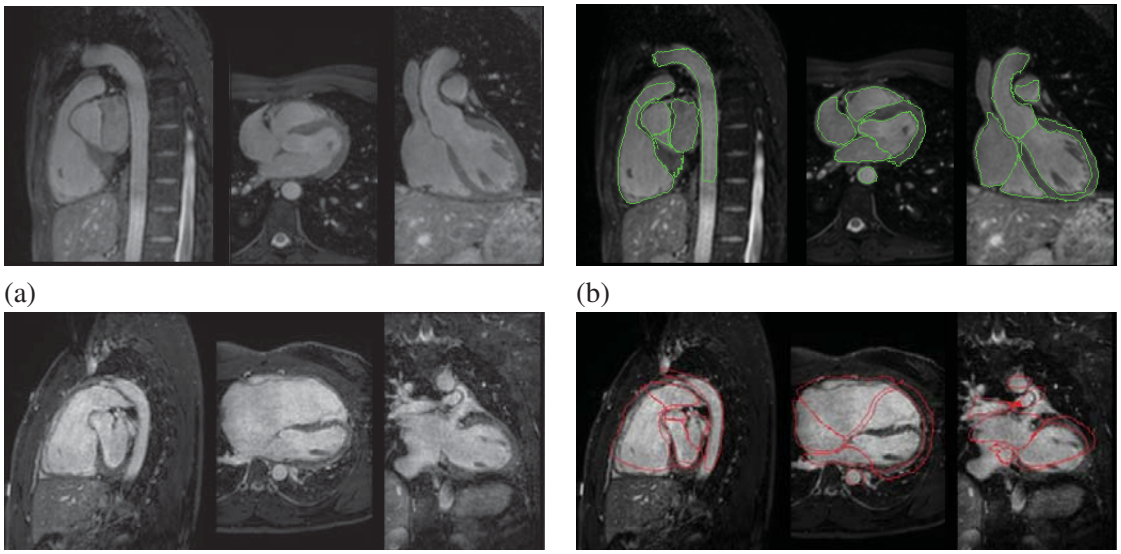

(a) (b)

(c) (d)

Figure 1.2: (a) The three views (sagittal, axial, and coronal views) of an MR image from a healthy volunteer; (b) the corresponding three views of a successful segmentation, defined by the green contour, superimposing on (a); (c) the three views of an MR image from a patient with right ventricle hypertrophy; (d) the corresponding three views of an erroneous segmentation, defined by the red contour, superimposing on (c). MR data from Guy's and St Thomas' Hospital, London.

The research objective is to develop technology for the segmentation of these *substructures*, whose automated processing is difficult. This section will address these challenges and discuss the potential solutions. We first give the three facts which create difficulties in obtaining automatic segmentation. We then interpret them as three technical issues. Finally, we outline two main fields of technology.

Three facts

There are three main facts contributing to the technical difficulties of fully automated whole heart segmentation.

(1) The *heart shape* can vary significantly across different subjects, or from the same subject at different cardiac conditions.

For example, Figure 1.2 (a) shows an MR image from a healthy volunteer and (c) is from a patient with right ventricle *hypertrophy*, an abnormal, severely dilated right ventricle. The segmentation of (a) using the prior knowledge from a training set of healthy volunteer data achieved a success, as the result shows in (b); while the segmentation of (c) failed due to the hypertrophy, as the result shows in (d).

This shape variation presents a big challenge when using statistical shape priors to estimate *unseen* cases, where "unseen" refers to the images that need segmentation. This is because it is practically difficult, if it is not impossible, to capture all possible heart shapes from different pathologies using a prior model trained from a limited training dataset.

(2) The boundaries between some anatomical substructures are *indistinct*. For example, Figure 1.3 shows three cases and their erroneous segmentation results.

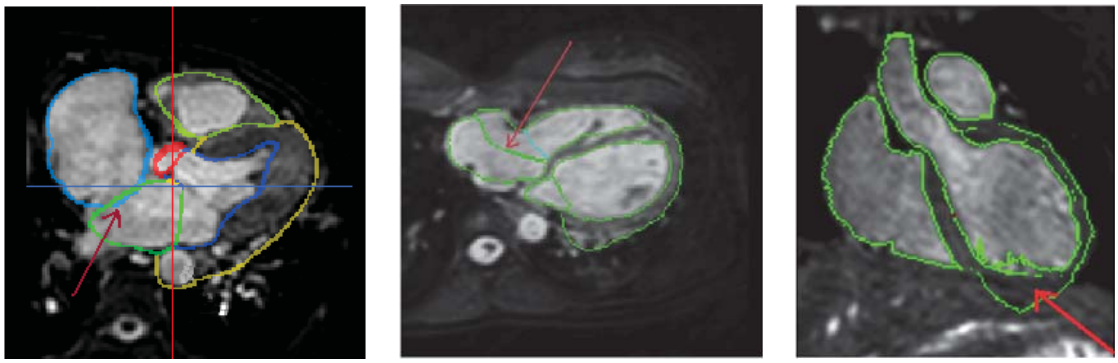

(a) (b) (c)

Figure 1.3: Erroneous segmentation induced from indistinct boundaries, the red arrows point out the regions of errors: (a) Intersected surfaces between the left atrium and right atrium; (b) false delineation of the tricuspid valve and the correction delineation in blue; (c) epicardium leaking. Notice that the image contrast could be very different from different MR data due to the variation of the subject and scanning conditions. MR data from Guy's and St Thomas' Hospital, London.

Figure 1.3 (a) shows an example of the indistinct boundary between the left and right atria due to the thin atrial walls and the close distance between them. This may induce an incorrect delineation of the boundary between the atria, or even produce intersected surfaces.

Figure 1.3 (b) shows an incorrect delineation of the boundary between the right ventricle and the right atrium. This is a commonly seen error in automatic segmentation when the substructures are not well initialised, because the valves between chambers or great vessels are usually not clearly imaged in these MRI sequences.

Figure 1.3 (c) shows a case of *epicardium leaking*, also known as *myocardium leaking*, due to the indistinct boundary between the myocardium and its adjacent tissues. Epicardium leaking means the epicardium is incorrectly delineated to its adjacent tissues, such as the liver in this case.

The indistinctness makes the automatic segmentation difficult for the *lower level* techniques that do not have a prior *model* for segmentation guidance (Suri, 2000). In the model-based approaches, the prior knowledge can be built into the model before the segmentation and the model can be used to supervise the segmentation during the process. Therefore, it is advantageous to use these approaches to tackle the indistinctness in the cardiac images.

(3) Clinical data may contain noise, motion artefacts, and intensity inhomogeneity. This presents the main challenge for a segmentation tool which relies solely on the intensity information in the unseen images to define the tissue boundary.

Three technical issues

The majority of reported works, to the best of our knowledge, employ a prior model and propagate the segmentation information in the model to unseen images in cardiac MR segmentation. To achieve a robust and realistic segmentation, there are three technical issues:

(I) *Initialisation*

The propagation assumes that the correspondence of boundary points should be optimal after the deformable adaptation. However, this adaptation does not guarantee a true anatomical correspondence if the surfaces of the model and the unseen image have not been closely initialised.

(II) *Sufficient information*

Clinical data usually have noise, artefacts, and intensity inhomogeneity, which are collectively referred to as *intensity inconsistencies*. The driving forces used to deform the surfaces of the model should be robust against these intensity inconsistencies. Many studies employ boundary-searching techniques to drive the deformable adaptation of the model and define the boundary profiles using the intensity information within a small region. However, this limited information loses the global intensity information of the unseen image, and thus the local adaptation may be vulnerable to the intensity inconsistencies.

(III) *Diffeomorphism*

It is desirable that the propagation from the model to the unseen image is a one-to-one mapping, namely a diffeomorphic segmentation. Without the diffeomorphism, the topology of the heart may no longer be preserved, and this may lead to errors such as two or more surfaces intersecting each other, as the example shows in Figure 1.3 (a).

Two research directions

One of the most popular frameworks to achieve the propagation is to use a deformable shape model with boundary-searching techniques (Kaus et al., 2004; van Assen et al., 2006; Lynch et al., 2008; Andreopoulos and Tsotsos, 2008; Koikkalainen et al., 2008). Most of the reported works have important contribution to overcome the segmentation issues we discussed in the previous section. However, it is still difficult to provide a framework which can deal with all the challenges based on the existing methods.

An alternative framework is to propagate a pre-constructed atlas image to unseen images using image registration techniques. This atlas has the segmentation information of all the substructures of interest. Compared to the other methods, this framework has the following two advantages:

- Intensity-based registration makes full use of the global intensity information from the registration images, such as mutual information (MI) (Viola and Wells, III, 1997; Maes et al., 1997) or normalised mutual information (NMI), which have been shown to be robust against noise and different intensity distributions (Studholme et al., 1999; Rueckert et al., 1999). These registration algorithms can include more complex information than the boundary searching techniques for the segmentation propagation process.

  Furthermore, spatial information can be considered as an extra channel (Studholme et al., 2006; Loeckx et al., 2007, 2010). The MI registration encoding spatial information is expected to further improve the registration performance against the intensity inconsistencies mentioned earlier. It should be noted that the intensity inconsistencies present

a common problem in the registration of medical images. Hence, the outcome of this research can also benefit many other applications.

- Diffeomorphic nonrigid registration has been well developed in the image computing literature (Crum et al., 2005; Rueckert et al., 2006; Vercauteren et al., 2007; Ashburner, 2007). Using the diffeomorphic registration, we can then achieve a diffeomorphic propagation from the atlas to the unseen image.

The reported studies in the literature have only partially resolved the three technical issues (Mitchell et al., 2002; Lorenzo-Valdes et al., 2002; Lotjonen et al., 2004). In the next section, we will define the research scope of this thesis and outline the main contributions.

1.3 Contribution

This work focuses on investigating image registration techniques and their application in automated whole heart segmentation. We mainly used the cardiac MR data for experiments, which were acquired using state-of-the-art hardware and acquisition protocols (please refer to Section 4.5.1 for detail). The key contributions of this thesis are as follows:

- For the initialisation issue, we propose a new locally affine registration method (LARM) which globally deforms the image but locally preserves the shapes of substructures of the heart. With the initialisation from LARM, we then further propose a new nonrigid registration approach which adaptively sets the control point status of a free-form deformation grid, referred to as ACPS FFD registration. Both LARM and ACPS FFD registration are designed to be diffeomorphic.

- For the sufficient information issue, first of all we guarantee that the registration algorithms used in the whole heart segmentation framework, including LARM and ACPS FFD registration, should keep *the global intensity information*.

  We then investigate the problem of the entropy-based nonrigid registration and propose to encode the spatial information in the registration. A unified framework of spatial information encoding is then proposed and a nonrigid registration method, the spatial information encoded mutual information, is developed.

- We propose a registration-based segmentation propagation framework for cardiac MRI and validate the method using a test set which represents a large diversity and variation of morphologies and involves a variety of pathologies. At the same time, a generic method, which is required in the segmentation framework, is proposed to invert dense displacements to produce the inverse transformation of a registration result.

- Finally, we show some exploratory applications with preliminary results, to demonstrate the applicability and extensibility of the algorithms developed during the doctoral research. These applications include the whole heart segmentation of multi-slice cardiac MRI and 3D echocardiography, the whole heart segmentation incorporating multi-atlas strategy, and the accurate nonrigid registration of brain MRI and dynamic contrast enhanced MRI of the liver.

1.4 Thesis structure

Chapter 2 provides the background knowledge. We first introduce the background of cardiac diseases of which the clinical data will be used in the experiments of this thesis. We then review the cardiac functional indices which are crucial in quantitative clinical applications and can be computed from the results of registration and segmentation. Finally, we give a brief introduction to the imaging technology of cardiac MRI and ultrasound.

Chapter 3 provides the literature review of image segmentation and the theory of image registration. The review of segmentation is focused on model-based approaches. We explain the rationale for the choice of using registration-based propagation methods to achieve whole heart segmentation. We then give an introduction to image registration theory and in particular focus on the transformation models and similarity measures. The problems of applying existing techniques to the segmentation framework are discussed and proposals for improvement are given.

Chapter 4 introduce the locally affine transformation model, the region-based registration, and a new registration algorithm: the locally affine registration method (LARM). A generic method for inverting dense displacement, Dynamic Resampling And distance Weighted (DRAW) interpolation, is presented in this chapter. Experiments for evaluating LARM and DRAW using both phantom and *in vivo* data are done to demonstrate their performance. The work of the region-based registration and its application to cardiac MR segmentation experiments has been presented at SPIE 2008 (Zhuang et al., 2008a) and MIUA 2008 (Zhuang et al., 2008b). The work of LARM and DRAW, including the phantom data experiments and the application to the whole heart segmentation of MR data, has been presented at MICCAI 2008 (Zhuang et al., 2008c).

Chapter 5 presents a nonrigid registration method which constrains the computation of driving forces to maintain the heart shape during the process, based on the adaptive control point status free-form deformations (ACPS FFDs). This registration significantly improves the run-time, and more importantly, improves the robustness of cardiac MR registration, especially in the myocardium region. Unlike the usage of penalty terms, this constraint is implicitly done within the optimisation procedure and no parametrisation is required to weigh the different terms within a cost function. The work in this chapter has been presented at FIMH 2009 (Zhuang et al., 2009b).

Chapter 6 presents a whole heart segmentation framework, based on atlas propagation and image registration, using the three new techniques: LARM, DRAW, and ACPS FFDs. We propose to use a series of transformation models to maintain the competition of preserving the shape of local substructures and increasing the flexibility of the transformation models. A simple atlas without statistical shape information is used and the construction is described. The validation includes the assessment of the importance of using different atlases, the improvement of the proposed registration algorithms compared to the alternative techniques, and the performance of the proposed segmentation framework in a test dataset containing a wide diversity of pathologies. The work in this chapter has been published in IEEE Transactions on Medical Imaging (Zhuang et al., 2010c).

Chapter 7 explores three new applications of extending the whole heart segmentation

framework presented in Chapter 6. Firstly, we illustrate the application of the segmentation framework to the multi-slice cardiac MRI. Then, we extend the framework to the whole heart segmentation of 3D echocardiography. We propose to use the compounded 3D echocardiography to extend the field of view and develop a new similarity measure combining three channels of information for the registration of the compounded ultrasound images. Finally, we demonstrate the application of combining the segmentation framework with the multi-atlas strategy for whole heart segmentation. The work on the echocardiography segmentation has been accepted as an oral presentation to ISBI 2010 (Zhuang et al., 2010d) and the extension of the multiple classifier strategy work has been accepted for publication at MICCAI 2010 (Zhuang et al., 2010b).

Chapter 8 presents a unified framework to incorporate spatial information into the entropy-based registration and proposes a new nonrigid registration, spatial information encoded mutual information (SIEMI). Firstly, we provide an insightful interpretation of the problems in nonrigid mutual information (MI) registration. Then, we describe the theory of encoding spatial information and the framework of SIEMI registration. To efficiently search the optimum of SIEMI, we propose to use the local ascent optimisation scheme instead of optimising a scalar measure derived from the vector measure. Finally, we show that the proposed framework can unify some existing methods.

We employ a set of experiments to validate the proposed method, including the comparisons of SIEMI registration using alternative techniques and the application of SIEMI in cardiac MR registration and the whole heart segmentation framework. We also show exploratory application such as the registration of brain MRI and dynamic contrast enhanced MRI of the liver.

The work of the spatial information encoding theory has been presented at IPMI 2009 (Zhuang et al., 2009a). The work of SIEMI registration has been accepted as an oral presentation at WBIR 2010 (Zhuang et al., 2010a). The extension work has been submitted to IEEE Transactions on Medical Imaging (Zhuang et al., 2011).

Chapter 9 concludes this thesis and discusses the limitations and potential future work.

Chapter 2

Clinical Background and Medical Imaging

Section 2.1 presents the clinical background of cardiovascular disease. Section 2.2 surveys the cardiac functional indices, which can be automatically computed using registration and segmentation results of the clinical data. Section 2.3 introduces cardiac MRI and Echocardiography (echo) imaging technology and their applications.

2.1 Cardiovascular disease

Cardiovascular disease (CVD) is one of the main killer diseases (Fact Sheet No. 317, World Health Organization, 2007). In this section, two types of heart diseases are introduced: coronary heart disease (CHD) and Tetralogy of Fallot (ToF). The data used in our experiments were mainly from these two pathologies.

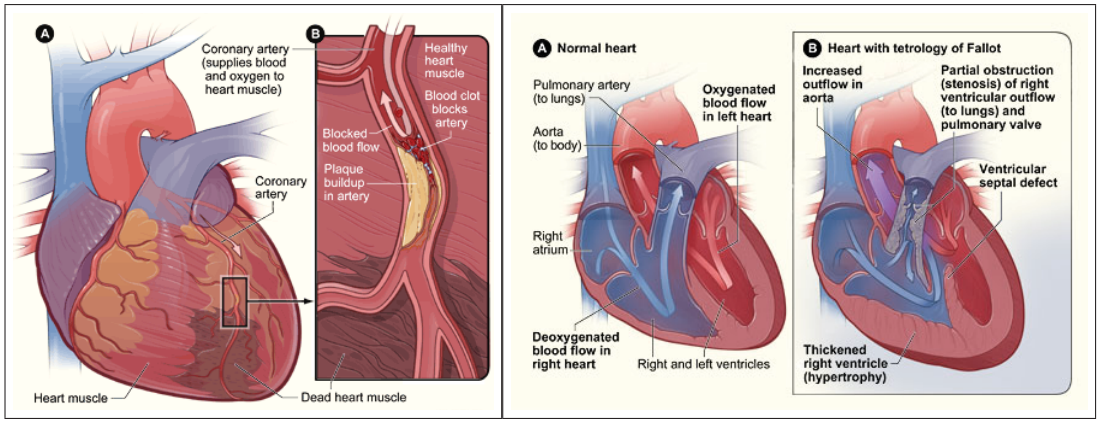

Figure 2.1: Illustration of coronary heart disease (left), image from National Institutes of Health [online] (2008), and Tetralogy of Fallot (right), image from National Institutes of Health [online] (2009).

2.1.1 Coronary heart disease

CHD, also known as coronary artery disease or ischemic heart disease, is the most common form of heart diseases. This section will introduce the pathophysiology of CHD and then two common treatments available in the clinical practice.

2.1.1.1 Pathophysiology

CHD is a result of progressive build-ups of fatty deposits within the walls of coronary arteries. These deposits are atheromatous plaques, including fatty acids, cholesterol, calcium mineral and fibrous connective tissues. Such deposition may have been occurring for decades prior to

the demonstration of symptoms. During the time, the accumulated atheromatous plaques causes narrowing of the lumen, leading to the limited or blocked supply of oxygen-rich blood to the *myocardium*, the heart muscle. Such deficiency of oxygen-rich blood supply causes blood-starvation to the cells of the myocardium and induces myocardium *ischaemia*. Figure 2.1 (left) demonstrates the development of CHD.

Ischemic myocardium is viable and its damage is reversible if diagnosed and treated early. However, it is common that the ischaemia could have been developing for decades and finally lead to permanent damage, referred to as *infarction* in clinics, before it gets effective treatments. Unlike ischaemia which benefits more from cardiac revascularisation, infarct myocardium will turn into scar tissues whose damage is irreversible. Such scarring is the main cause of heart failures. It is therefore critical to identify ischemic myocardium in patients and assess their severity such as transmural extend in order to apply preventative measures to reduce the risk of infarction.

2.1.1.2 Treatment

Treatment management of a patient differs according to a number of factors. Pharmacological treatment is a simple and conservative strategy, but most of the cases patients will benefit more from *revascularisation*, including angioplasty and coronary artery bypass grafting (CABG).

Angioplasty is a non-surgical procedure which involves inserting a *catheter*, a plastic tube with a deflated balloon on its tip, into the artery and moving the tip to the location of narrowing with the guidance of a tracking system. Once the catheter is positioned at the clogged artery, the balloon will be inflated to expand, dislodging and removing the plaques aside and widening the lumen. If required, the balloon can also be packed with a tightly collapsed *stent*, a mesh-like tube. Once the balloon inflates, the stent will expand to firmly cling to the inside wall of the artery. It will stay permanently in the lumen to support the widened artery. Several weeks later, the lining of the artery will grow to cover the stent.

There are cases that the widened artery *restenoses*, narrows again, after some time. Therefore, some angioplasty operations use drug-eluting stents to improve the performance. This stent can elute a drug to smooth the plaques and prevents them from accumulation.

Coronary artery bypass grafting (CABG) is an open-chest surgery. The aim of this procedure is to bypass the clogged artery to supply *red blood*, oxygen-rich blood, to the ischemic myocardium. Normally, an artery from other parts of the patient's body, such as arms or legs, will be taken to connect the myocardium and the aorta to bypass the obstructed artery. Single, double, triple, quadruple, or even quintuple arteries might be bypassed during a CABG surgery, but the number of arteries undergoing bypass does not indicate the severity of the disease.

2.1.2 Tetralogy of Fallot

ToF is the most common type of congenital heart disease which becomes evident during infancy. A baby with ToF often shows blue skin due to the supply of poorly oxygenated blood to the body. ToF could involve up to four heart malformations at one time: pulmonary artery stenosis, overriding aorta, ventricular septal defect, and right ventricular hypertrophy. Figure 2.1 (right) shows the difference between healthy hearts and those affected by ToF.

ToF causes less blood to flow to the lungs, resulting in a heavy pumping burden of the right ventricle. The defects mix blue blood with red and cause low oxygen-carrying blood

to supply to the circulation of the blood system, contributing to the symptom of *blue baby*. A correction of the heart malformation is commonly taken for patients with ToF at their early ages. However, a regular follow-up check is highly recommended regarding to the complications such as pulmonary regurgitation and pulmonary valve restenosis, etc. Cardiac MRI has been recommended (Oosterhof et al., 2006) for follow-up studies of patients with corrected ToF because of its high performance in clinical practice, including the following four aspects:

- Firstly, cardiac MRI has high contrast for soft tissue, providing good anatomical information for studying the malformation of the heart.
- Secondly, cardiac MRI provides velocity mapping and quantitative value of pulmonary flow. This provides information for the computation of pulmonary regurgitation volumes and identification of patients who need pulmonary valve replacement.
- Furthermore, cardiac MRI performs well in quantitative calculation of volumes such as to obtain ejection fraction of the right ventricle for patients with pulmonary or tricuspid valve regurgitation.
- Finally, some special sequences such as delayed enhancement cardiac MRI can identify the scar tissue.

2.2 Cardiac functional index

In this section, we review the cardiac functional indices widely used in clinical applications. These indices provide crucial information for interpreting functional conditions of the heart in a quantitative and objective manner.

These indices are classified into two categories: global indices and regional indices. Global indices, though mostly only concerning ventricles, provide pathological information of a heart from its global behaviour or features. Those indicators can be referred for assessing myocardial contractility, abnormality of the ventricles such as hypertrophy. They include ventricular volume and mass, cardiac output (CO), stroke volume (SV), ejection fraction (EF), and global wall motion (GWM). Regional indices provide the functional indicators related to more specific local regions, being able to identify regional abnormality. They include regional wall motion, wall thickness and thickening, strain, and myocardial perfusion reserve index.

2.2.1 Global functional indices

Ventricle Volume, including left and right ventricles at different phases, is generally calculated to derive other functional indices such as ventricular mass (VM), CO, SV and EF, as well as its own usage for assessing hypertrophy. Left ventricle hypertrophy is indicative of increased risk of mortality, while right ventricle hypertrophy is a signal of severity of Tetralogy of Fallot. The value is derived by computing the volume between the *epicardium* (epicardial surface) and *endocardium* (endocardial surface). *Septum*, septal myocardium, is normally assumed to be a part of the left ventricle.

Ventricular Mass (VM) is obtained by multiplying ventricular volume with the density of the muscle tissue, typically using 1.05 g/cm^3 (Frangi et al., 2001). It is another important

indicator for assessing ventricular hypertrophy and is often normalised by the weight of body or total body surface to enable inter-subjection comparisons.

Stroke Volume (SV) and *Cardiac Output* (CO) are both directly related to the pumping ability of myocardium and its contractile function. SV is the volume difference between the *end-diastolic* (EDV) and *end-systolic* (ESV) phases. CO is defined as the output volume per minute of oxygen-carrying blood from the left ventricle to supply the body system, which is computed by multiplying SV and the heart beat rate. Both of these two measures are indicative of how well the heart is pumping blood. Alternatively, like VM, SV and CO can be normalised with the weight or surface of the subject to enable inter-subject comparisons.

Ejection Fraction (EF) is defined as the ratio between the SV and end-diastolic volume:

$$\text{EF} = \frac{\text{SV}}{\text{EDV}} \times 100\% = \frac{\text{EDV-ESV}}{\text{EDV}} \times 100\% \,. \tag{2.1}$$

EF is one of the most widely used measures for assessing heart contractility. Those with reduced EF typically have worse prognosis and significant reduction of EF means poorer contractility and may attribute to myocardium ischaemia.

Global Wall Motion (GWM) is used for studying myocardial motions during cardiac cycles, evaluating the contractility of myocardium and assessing the performance of the heart function in diagnosis or prognosis. GWM is also an indicator for studying the remodelling of the heart after revascularisation. In many applications, GWM is computed by integrating the regional wall motions of all segments.

2.2.2 Regional functional indices

A widely recognised regional analysis technique for left ventricle myocardium is using the 17-segment division model, shown in Figure 2.2. Cerqueira et al. (2002) suggested this is the best model for the regional assessment of wall motion and wall thickness.

Regional wall motion (RWM), similar to GWM, is defined as the myocardial movement of each segment. The functional abnormality of myocardium affects its contraction movement when the heart works to circulate the blood system. Hence, studying its motion provides an indication on how healthy a specific segment is. In clinical practice, visual assessment is normally used to score the RWM index as a semi-quantitative evaluation. This is done by experienced cardiologists in order to classify the segments into four different healthiness levels: normal/ hyperkinetic, hypokinetic, akinetic, and dyskinetic (Cigarroa et al., 1993; Jaume et al., 2004). To achieve automatic assessment, it is possible to define the average radial distance from the myocardial region to the central axis as the RWM using image computing technology (Ordas and Frangi, 2005):

$$\text{WM} = \frac{\delta_{ES} - \delta_{ED}}{\delta_{ED}} \times 100\% \,, \tag{2.2}$$

where, δ_{ES} and δ_{ED} are the radial distances from the region points on the endocardial surface to the centre axis of the blood cavity at end-systolic (ES) and end-diastolic (ED) phases respectively. When the motion is defined for other phases of the whole cardiac cycle, then δ_{ES} is defined as the radial distance at the certain phase. This enables RWM-time-curve analysis by computing the RWM value for each segment and plotting the value against the cardiac phase time for dys-synchrony analysis. Comparing the motion with statistical models built from

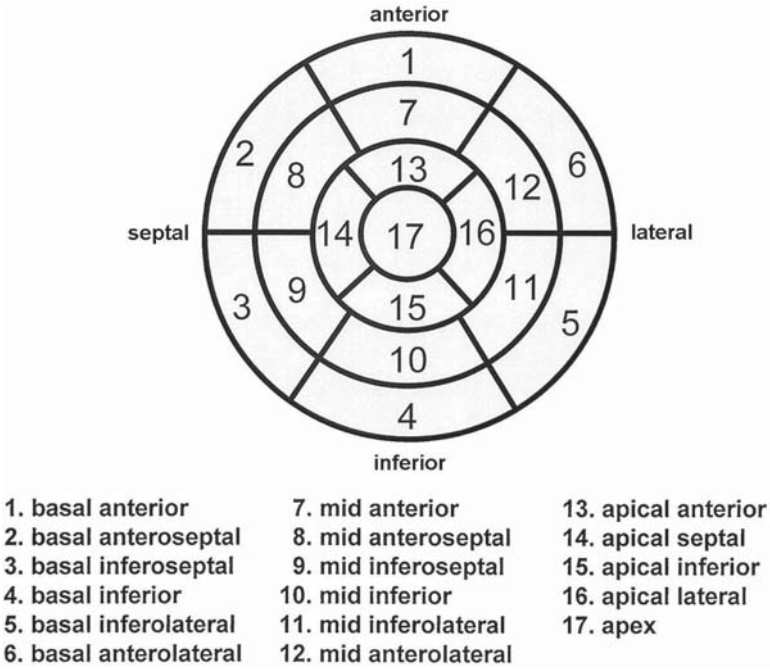

Figure 2.2: Bullseye diagram of the 17 segments of the left ventricular myocardium (Cerqueira et al., 2002).

training datasets can assess the similarity and difference between them. For example, Chandrashekara et al. (2003); Perperidis et al. (2005); Suinesiaputra et al. (2004, 2005) employed principle component analysis (PCA) or independent component analysis (ICA) to extract the modes of variation from their training data and applied the model to identify the abnormality of myocardium motions of new subjects.

Wall thickness (WT) or *wall thickening* (WN) is a measure related to the thickness of myocardium at different phases. It is an alternative technique to RWM, though some studies argued that WT/ WN should be more sensitive in detecting dysfunctional contractility of myocardium (Lieberman et al., 1981; Azhari et al., 1990). In manual assessment, four score levels are typically defined for WT/ WN: normal, mildly reduced, moderately reduced, and severely reduced (Cigarroa et al., 1993; Jaume et al., 2004), providing a semi-quantitative result. To achieve fully quantitative and automatic analysis, WN can be defined as:

$$\mathrm{WN} = \frac{\eta_{ES} - \eta_{ED}}{\eta_{ED}} \times 100\% \tag{2.3}$$

where, η is the thickness of myocardium at a local region, defined as the distance between the endocardial and epicardial surfaces. Similar to RWM analysis, η_{ES} can be the thickness at any cardiac phase when it comes to the whole cardiac cycle. Sheehan et al. (1986) proposed to use a *central line* idea to compute WT/ WN. It should be noted that this is also applicable to RWM as well. This idea has become popular and many studies have contributed to its application (Bolson and Sheehan, 1993; Bolson et al., 1995; van der Geest et al., 1997; Ordas and Frangi, 2005).

Strain Analysis is the fractional change of the length from a rest state to a stressed state,

reported to be superior to wall thickening analysis in discriminating infarct myocardium from ischemic ones (Gotte et al., 2001). In cardiac analysis, the rest state typically refers to the end-diastole and the stressed state is any one of the systolic phases. Two strain analysis methods have been described: Lagrangian strain and Rational strain.

Myocardial Perfusion Reserve Index (MPRi) is used in perfusion MRI. It focuses on the signal intensity changes of the myocardium and assesses the abnormality of a region by computing the curve of signal intensity uptake. Normal tissue has a higher slope of uptake and therefore a high value of MPRi, while myocardial regions with MPRi less than 1.5 are regarded as being correlated to ischaemia (Cullen et al., 1999; Earls et al., 2002). The challenge for MPRi analysis is the relatively low contrast and spatial resolution of perfusion MRI.

Function analysis can be largely automated given the success of segmentation and registration of MR images. Currently, they are mostly done manually or semi-automatically with manual correction (for segmentation) and visually observed (for registration) in clinical practice. However, many research studies have started to investigate the automated processing to generate quantitative analytical results using computer, imaging, and image computing technology.

2.3 Introduction to non-ionising radiation imaging

(a) (b) (c)

Figure 2.3: MRI scanner (a), image from Philips Healthcare [online] (2009a); coil with 32 receive channels for chest scanning (b), image from Philips Healthcare [online] (2009b); Echocardiography system (c), image from Philips Healthcare [online] (2009c).

MRI and ultrasound (US) are two important imaging techniques which have no ionising radiation. In this section, we will introduce the physical basis and application of techniques in cardiovascular studies.

2.3.1 Cardiac MRI

MRI is an imaging modality which provides good contrast between soft tissue and a wide field of view. It has been widely used in cardiovascular as well as neurological, musculoskeletal, and oncological studies. In this section, we will give a brief introduction to MRI and applications of cardiac MRI.

2.3.1.1 Basic Physics

The human body has a large proportion of water which consists of hydrogen atoms. The spin of hydrogen nuclei, protons (^{1}H), creates magnetic moments due to the electric charge of pro-

tons. When these spinning magnetic moments, or simply called spins, are placed in a strong external magnetic field B_0, they will try to align to this field and generate a net magnetic field M parallel to B_0. The nuclei precess around the direction of B_0 at Larmor frequency ω_0, which is proportional to the strength of B_0: $\omega_0 = \gamma B_0$, where γ is a constant value for hydrogen.

The net magnetic moment M is tilted when applying a radio-frequency (RF) pulse that is perpendicular to the main magnetic field B_0. The frequency of the RF should be the same as that of the spins (Larmor frequency ω_0) to cause the resonance. When this RF is removed, the spins start realigning to B_0, causing M to return parallel to B_0 again. This realignment is referred to as relaxation. During the relaxation, the spins release energy, emitting RF signal. The conductive coil receives this signal and sends to a computer for image reconstruction.

2.3.1.2 Tissue contrast

The intensity of MRI is related to the strength of the response signal, which depends on the combination of three factors: T1 and T2 relaxation, and proton density. Proton density determines the maximal strength of the free induction decay (FID) signal. Higher density means stronger response signal.

The contrast of MRI is also related to T1 and T2 relaxation. The magnetic moment of a spin has two components, the longitudinal and transverse magnetisation. They align to a steady state in the main magnetic field B_0 and are *tipped* when the RF is applied. During the relaxation, the recovery of longitudinal magnetisation of a spin, called longitudinal or T1 relaxation, occurs exponentially to a constant time T1. The recovery of transverse magnetisation, called T2 relaxation, is related to another constant time T2. Different types of tissues normally have different T1 and T2 values. Since the response signal is measured at a time interval after the relaxation, the strength of the signal differs from different tissues due to their different signal decay caused by T1 and T2 relaxation.

2.3.1.3 Spatial encoding and k-space

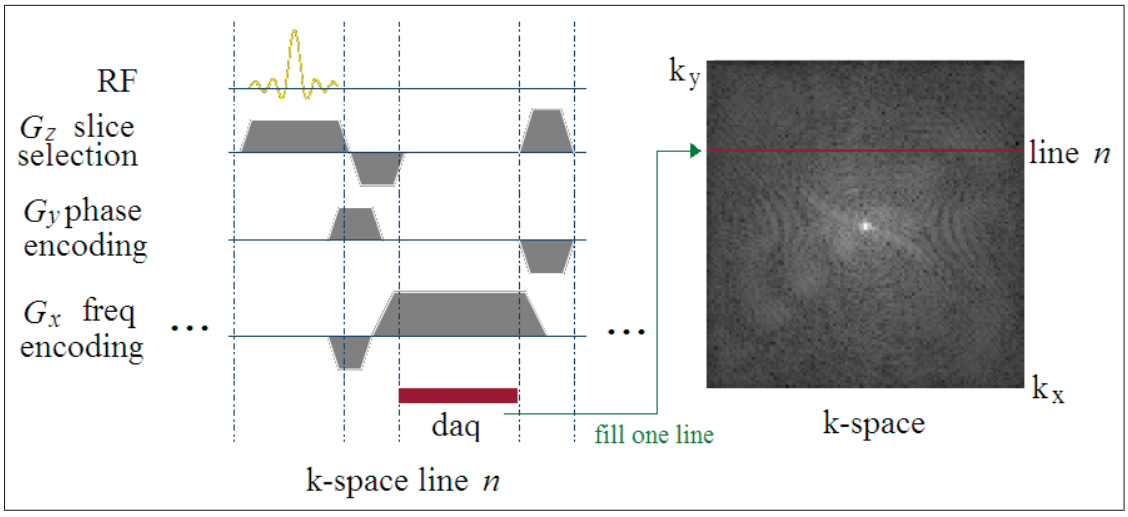

Figure 2.4: MRI acquisition and K-space construction.

Magnetic field gradients are used to differentiate the spatial position of protons. A gradient, G_e, is applied to the main magnetic field, B_0, such that $\tilde{B}_0 = B_0 + G_e$ This gradient will cause

the Larmor frequency of spins to vary according to the magnetic field strength $\tilde{\mathrm{B}}_0$. The spatial position of spins is then encoded by gradient G_e based on their different Larmor frequencies.

The recording and reconstruction of the MR signal is normally explained with k-space. The data in k-space is in the frequency domain from which an inverse Fourier transform gives the image in the spatial intensity domain. To construct the k-space, the first step is to select a slice (2D) or slab (3D) along the z-direction of the scan orientation, where the field gradient G_z is applied. By choosing a special band width of the RF which determines a range of Larmor frequencies, the slice to be excited can then be decided based on G_z. The frequency and phase encoding is then used to differentiate the spatial coordinate within the slice. As Figure 2.4 shows, after the RF excitation, a magnetic gradient G_y is applied. This causes the magnetisation to be dephased and the dephasing varies according to their coordinates in the y-direction. After G_y is removed, another gradient G_x along the x-direction is applied. This gradient causes the resonance frequency to vary in the x-direction. As a result, the response signal varies in frequency in x-direction due to G_x, and differs in phase in y-direction due to G_y applied previous to G_x. The data acquisition with frequency encoding from G_x corresponds to one line in k-space, while the amplitude of the gradient G_y of phase encoding decides which line in k-space to fill, as demonstrated in Figure 2.4.

2.3.1.4 Application

Cardiac MRI is the generalisation of the application of MRI to heart related studies. The good contrast and wide field of view provide a clear anatomy of the heart, which is useful for both morphological and pathological studies. Figure 2.3 (a) and (b) show a state-of-the-art MRI system (a) and coil used in our collaborated clinical partners.

Anatomical structure is informative in evaluating some heart diseases such as congenital heart diseases (anatomical malformation). Two cardiac MRI techniques are preferred in imaging morphological information.

One is the *black-blood* technique (Edelman et al., 1991; Simonetti et al., 1996) which suppresses signal from flowing blood by removing either the pre-saturate RF or inverse pulse or both of them. Hence, it provides very good contrast between the myocardium and blood cavities, enabling good delineation of the endocardium (Berr et al., 2005).

The other technique images inflowing blood with brighter signals, and is referred to as *bright-blood* technique. One important technique of this type is the steady state free precession (SSFP). Several advantages can be obtained by using this technique such as better signal to noise ratio and contrast to noise ratio, and consistent signal intensity over cardiac cycles (Pereles et al., 2001; Barkhausen et al., 2001). Furthermore, with the acquisition time shortened about the order of three folds, SSFP enables higher resolution than the traditional sequences. The 3D isotropic balanced-SSFP (Uribe et al., 2007) eases the scan preparation such that planning the conventional short-axis or four-chamber view is not required. This is because these views can be achieved in post-processing by transforming the 3D isotropic volumes acquired from any other views, without introducing heavy interpolation artefacts such as *staircase*. One of the drawbacks of this technique is its poor contrast in the depiction of epicardium, which presents one of the main challenges for image registration and segmentation of epicardium.

With the clear geometrical information from MR images, most of the functional indices

reviewed in section 2.2 can be easily computed, given the segmentation and registration process has been achieved (Frangi et al., 2001).

2.3.2 Echocardiography

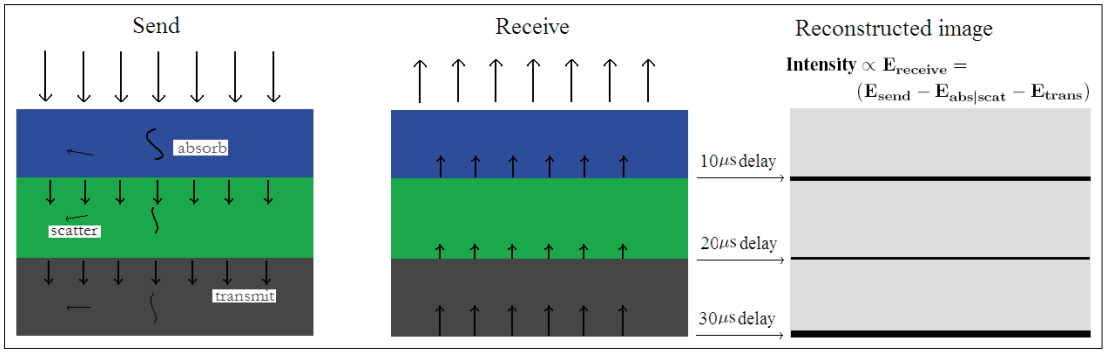

Figure 2.5: Ultrasound waves are generated, which are absorbed, scattered back and transmitted during propagation (a); echo pulses are received, which are reflected from boundaries between tissue types with different acoustic impedances and back to reach the receiving transducer (b); image is reconstructed based on time delay (position encoding) and amplitudes of echo pulses (intensity) (c).

Ultrasound imaging, also known as ultrasonography, relies on the use of a piezoelectric transducer to transmit and receive high frequency (typically 2-20MHz) sound waves. Most modern ultrasound devices employ so-called pulse-echo imaging (illustrated schematically in Figure 2.5) to interrogate soft-tissue. In this method, a two- or three-dimensional image is reconstructed from the relative timings of transmitted and received ultrasound pulses, which encode depth information (assuming a constant speed of sound in tissue), and the amplitude of the received pulses (or echoes). The procedure is summarised by the following steps (please refer to Figure 2.5):

- A short electrical pulse applied to the transducer causes the transducer surface to vibrate at its characteristic frequency. Since the transducer is in physical contact with the skin surface, with water-based gel provide a continuous medium through which ultrasound energy can be transmitted (commonly known as acoustic coupling), ultrasound waves propagate into and through the tissue. As the waves propagate through the tissue, they lose energy, a phenomenon known as attenuation. Absorption via heating is the main cause of energy loss, but scattering and refraction also play a part. In soft tissue, scattering occurs due to small-scale variations in material properties, and hence the speed of sound, on a scale comparable to the wavelength of the propagating ultrasound waves.

- Using a simplified model of ultrasound physics, the predominant echoes are generated at boundaries between different tissue types which correspond to a change in acoustic impedances. Using a simplified physical model where these boundaries are smooth, the echoes are reflected according to Snell's law which states that the angle of incidence and reflection with respect to the perpendicular to the boundary are equal. However, in reality, tissue interfaces typically contain microscopic imperfections on the same scale as

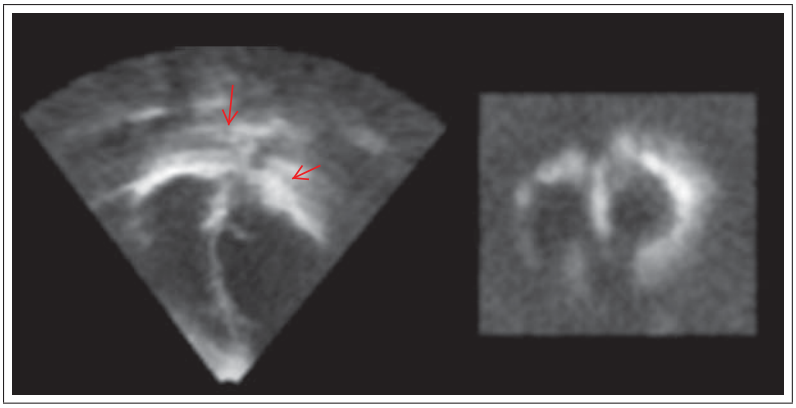

Figure 2.6: A cardiac ultrasound image from the long-axis view (left) and short-axis view (right). Red arrows point to shadowing artefacts. Ultrasound image from Guy's and St Thomas' Hospital, London.

the wavelength of the ultrasound. In this case, scattering occurs and is the primary source of echoes in real ultrasound imaging.

- Once the echo pulses arrive at the transducer surface, they generate an electrical pulse, which is amplified and detected by the probe electronics. It is these signals that are used to reconstruct the gray-level images: after amplitude modulation, the relative timing of the received echo and the transmitted pulse are converted into a depth measurement, perpendicular to the transducer surface, using the relation that (assuming a constant speed of sound through tissue) the time between the transmitted pulse and corresponding echo is proportional to twice the depth of the structure producing the echo. Since modern clinical ultrasound transducers are usually made up of an array of transducer elements, multiple scan-lines can be generated by repeating this process for different positions along the transducer surface. This is achieved by activating small contiguous groups of transducer elements in array in sequence to generate a series of pulses along a focused beam. These scan-lines then form the columns of a so-called B-mode image. The pixel intensity is proportional to the amplitude of the received pulse after log compression. As noted above, ultrasound pulses are attenuated as they propagate. This means that received pulses have much smaller amplitudes than the initial transmitted pulses generated from the transducer, but also that echoes from deep structures have a smaller amplitude than echoes from more superficial structures. To compensate for this effect, a process of amplitude adjustment, called time-gain compensation (TGC), is used in which the received signal is amplified according to the depth (equivalent to the receive time) of the received pulses. TGC is normally adjusted on the scanner by the operator.

- Finally, the scan-lines are mapped to a regular grid and filtered to produce the displayed image. Clinical B-mode images are typically updated at a rate 5-100Hz, allowing real-time scanning.

Echocardiography, commonly referred to as simply *echo* by cardiologists, is ultrasonography of the heart. Figure 2.3 (c) shows an echo system used by our collaborating clinical partner and Figure 2.6 shows an example of a clinical echocardiographic scan. Besides the advantages

of being a safe, non-invasive, inexpensive, and portable imaging modality, echocardiography also has the advantage of enabling real-time imaging, which is extremely important for a dynamic organ such as the heart and provides useful functional information for studying valve-related diseases, such as *regurgitation*, a condition where the blood flows back through the partially closed valves. The dynamic information from echo is also useful for evaluating wall motion which provides a clinical indication for the occurrence and severity of coronary heart diseases, as discussed in Chapter 2.1 and 2.2.

Echocardiography also enables the structure and size of cardiac anatomy to be assessed, providing information for detecting morphological abnormalities of the heart. However, the images must be interpreted in the presence of artefacts, such as speckle and acoustic shadowing (see Figure 2.6). Image noise and artefacts present a substantial challenge for automatic image processing algorithms. Furthermore, unlike most alternative cardiac imaging modalities, such as MR and CT, echocardiography has a limited field of view (FOV) determined by the length of the transducer array and the maximum depth ultrasound penetration (typically, 5-20cm for cardiac imaging). As a result, echocardiography normally cannot image the whole heart using a single scan, as shown by the image in Figure 2.6. Subsequently, the value of 3D echocardiography in terms of a wide FOV is gaining increasing clinical interest. Matrix array transducers provide a means of acquiring 3D ultrasound image data rapidly from a volume at frame rates of up to several volumes per second. However, cardiac gating and volumetric compounding are necessary to maximise the FOV and image quality in practice (Grau and Noble, 2005; Grau et al., 2007; Yao et al., 2009; Rajpoot et al., 2009b).

Chapter 3

Literature Review and Theory

3.1 Literature review on segmentation

This section reviews the segmentation literature. Section 3.1.1 gives an introduction to segmentation. Section 3.1.2 to 3.1.4 surveys the literature related to three categories of model-guided segmentation. Section 3.1.5 provides the research direction and the rationale for this direction.

3.1.1 Introduction

In medical image processing, segmentation is a process to partition one or a series of images into different regions or to delineate boundaries of these regions. The segmented regions normally have important information for clinical usages. The goal of segmentation is to extract and separate the desired information, and the result is a set of new images providing each piece of the information.

In this review, we will first introduce the theory of threshold, edge detection, and region growing methods. These methods are data-driven and usually considered as low-level segmentation algorithms (Suri, 2000). This is because the segmentation solely relies on the information available from the image. Then, we will classify the high-level methods, the model-guided approaches, into three categories and review the existing works in detail in the following sections.

Threshold: One can use thresholding of intensity values to extract a region of interest. A successful thresholding requires that the intensity distribution of the region of interest should not be overlapping with that of other regions in the image histogram. This requirement is evidently too strong for the segmentation of cardiac MR images. For example, a failure may occur in the segmentation of myocardium, because the intensity of the myocardium could be similar to that of the liver as shown in Figure 1.3 (c). Another example is the separation of the blood pool into different anatomical regions, such as the right atrium and ventricle segmentation shown in Figure 1.3 (b). The intensity range of the atrial blood cavities could overlap with that of the ventricular blood cavities. Therefore, prior anatomical knowledge would be needed in order to defining the boundary between these regions.

Edge detection: Edge detection takes the intensity values of neighbouring points into consideration when deciding the boundaries between regions. A review and comparison between a number of algorithms can be found in (Heath et al., 1997). Points with high magnitude of intensity gradient are usually considered as having a high probability of being edge points. Canny (1987) assumed that points with local maximal gradient, zero second directional derivatives, should be edge candidates. This assumption makes the detection easier and more robust

to noise using a technique, known as *hysteresis*, to protect true edge with low gradient value. Hysteresis also contributes to producing more continuous contours, to avoid *dash-like* edges. Edge detection techniques can be also used as a boundary profile in boundary-searching-based segmentation (Rouchdy et al., 2007).

Region growing: Region growing incorporates the knowledge that pixels in the same region are connected and have a similar intensity value. This is also assumed in the procedure of growing the region. Starting from a selected seed point, the algorithm expands the volume by assimilating neighbour pixels that match a predefined similarity criterion using intensity mean, intensity variance, shape smoothness, and a combination of them. The key step of this method is to define the similarity criterion which usually needs parametrisation to avoid the leaking problem. Furthermore, the seed point is normally manually selected, and this also could lead to different results from different observations.

Model-guided: The lower level techniques listed above are mainly driven by the data themselves without a pre-constructed model for shape guidance. This however makes segmentation too flexible and can result in random and unrealistic shapes due to the noise, artefacts, and indistinct boundaries presented in the image. Model-based methods utilise the prior information coming from the models for guidance. These techniques have been widely used in automatic or semi-automatic cardiac image segmentation. For terminology simplicity, any one of the deformable models, probabilistic atlases, and intensity atlases is referred to as a *model*. Based on different usages of the model, we classify the techniques into three groups:

- texture classification using Expectation-Maximisation (EM) algorithm,
- boundary-searching with deformable shape models,
- atlas propagation using image registration.

In the following three sections, we will review the typical works reported in the literature. Figure 3.1 provides the table summarising these works.

3.1.2 Texture classification using EM algorithm

EM segmentation refers to the texture classification methods which employ EM optimisation to estimate the parameters of a texture label model. In this model, each pixel is assigned with a classification label. By modelling the intensity distribution of each tissue, the probability of the labelling can be estimated given the parameters of the model associated with this tissue being available. For example, it is common to assume that the intensity of a tissue has a Gaussian distribution, which is defined by the intensity mean and standard deviation. EM is used to maximise the likelihood of labelling parameters given the current estimation. In this segmentation, contextual information is incorporated by means of Markov Random Field (MRF) to improve the performance and robustness to noise. An average-intensity atlas, known as an atlas of *a priori* probability maps, is also used for the initial estimation of the parameters.

EM classification methods have been successfully applied in statistical classification for brain MR images (Leemput et al., 1999; Zhang et al., 2001) where the images are of better quality (higher signal-to-noise ratio). The intensity classes of gray matter, white matter, and cerebrospinal fluid are also quite separable in MR images. Lorenzo-Valdes et al. (2003, 2004)

	Method	Segmentation area and data	Results (mm)	Comments
Lorenzo-Valdes et al. (2003,2004)	Region classification using EM algorithm	Ventricles and myocardium segmentation from multi-slice cine MR	2.21-2.99 (mean)	Cons: no solution is provided for extension to separation between atria and ventricles or the separation of the papillary muscle from myocardium
Lynch et al. (2008)	Region classification using EM algorithm with priors of incompressibility	Same as above	1.2475±1.3369 (mean) 1.8670 (RMS)	Pros: the incorporation of myocardium incompressibility prior knowledge improves segmentation performance in 4D cases Cons: same as above
Hautvast et al. (2006)	Active contour model and propagate manual delineation to other phases	Same as above	1.12-2.64 (RMS)	Pros: no need of training and the applicability to all pathologies. Cons: the limited automation due to the user-interaction to define an initial contour such as that of the end-diastolic phase
Pluempitiwiriyawej et al. (2005)	Active contour model and propagate the boundary of a conic equation model to unseen data	Ventricle and myocardium segmentation from high resolution rat MR	N/A	Pros: a simple implementation. Cons: only preliminary validation on rat data which had a fixed field-of-view unclosing the heart region
Kaus et al. (2003, 2004)	Active contour model with the training information from the statistical shape model and segmentation propagation	Myocardium segmentation from multi- slice cine MR	2.28-2.62 (mean)	Pros: the two types of prior information, the spatially varying features and the surface connectivity, improve the robustness. Cons: limited accuracy and the dependence on the training data set to construct the satistical shape model
van Assen et al. (2006)	Same as above	Left ventricle from arbitrary oriented MR	1.14-3.19 (mean)	Pros: good robustness claimed. Cons: need manual interaction for initialisation and limited accuracy due to the limited flexibility of statistical shape model
Ecabert et al. (2008)	Same as above	Whole heart segmentation on CT	0.82±1.00 (mean)	Pros: good accuracy reporpted. Cons: the validation is not independent and the applicability was only tested on data from similar pathology
Koikkalainen et al. (2008)	Same as above	Whole heart segmentation	2.06±0.55 (mean) (best)	It is a work on comparisons of several methods to artificially augment the variability of the statistical shape model used in the segmentation.
Peters et al. (2007, 2009)	Same as above	Whole heart segmentation	0.76±0.30 (mean)	Pros: good accuracy reported. Cons:limited applicability to similar pathology only and the dependent validation which may lead to bias conclusion of the actually performance of the approach
Rouchdy et al. (2007)	A deformable elastic model for segmentation proagation	Ventricles and myocardium from cine MR	N/A	Cons: only test segmentation on four mice data
Lorenzo-Valdes et al. (2002)	Registration-based propagation, from the end diastolic phase to other phases	Ventricles and myocardium from multi-slice cine MR	N/A	Cons: limited accuracy and limited automation impact (manual segmentation on one phase before propagation)
Mitchell et al. (2002)	Registration-based propagation using active appearance model for registration	Left ventricle from multi-slice MR	2.63-2.75 (mean)	Pros: good robustness and wide applicability Cons: limited accuracy due to the constraint from the poor deformation flexibility of the model
Lapp et al. (2004)	Registration-based propagation using statistical deformation model to constrain the flexibility of the deformation	Ventricles and myocardium from multi-slice cine MR	4.0±1.6 (mean)	Cons: limited accuracy in the leave-one-out experiment
Lotjonen et al. (2004)	Registration-based propagation using acitve appearance model with extended flexibility	Whole heart segmentation from cardiac MRI of different orientations	2.53±0.70 (mean)	Pros: extended flexibility of the model improves the accuracy of the segmentation methods of this kind Cons: the validation was done on data from healthy volunteers and hence the robustness of the method is questionable

Figure 3.1: Table of the typical segmentation works on cardiac MRI, selected from the literature. The *Result* column presents the mean surface-to-surface or point-to-surface segmentation error (mean) or root mean square (RMS) of the error. The best result of Koikkalainen et al. (2008), where they compared several augmentation methods to improve the segmentation accuracy, is presented in this table.

applied it to the segmentation of ventricles from cine cardiac MR data. Lynch et al. (2008) further incorporated the myocardium incompressibility as priors into the 4D segmentation. These cardiac data were multi-slice short-axis orientated images, covering the heart from the apex up to the basal planes. The myocardium and ventricular blood cavities could be well separated based on their intensity. The visual segmentation results in their papers showed that the papillary muscle, a small structure with a similar intensity distribution to the myocardium, was only partly included into the ventricle cavity. Some cases showed the majority of the papillary muscle was included into the myocardium. Also, the boundaries of the classified regions were not as smooth as the surface delineation provided by the other two categories of methods that will be reviewed in the next two sections. Finally, the classification mainly relies on the different intensity distributions to separate adjacent regions. This raises the question whether the classification is extensible to the whole heart segmentation of cardiac MRI where the intensity distributions of the four chambers and the great vessels can be almost identical. To the best of knowledge, no work has been reported on this attempt.

3.1.3 Boundary-searching with deformable models

Active contour or snake method (Kass et al., 1988) is a framework which minimises an energy associated with the current contour. This energy is a linear combination of internal and external energy terms. The external energy is supposed to be minimal when the active contour reaches the ground-truth boundary position. The internal energy is supposed to be minimal when the shape of the active contour has the desired or predefined properties. Active contour is one of the most popular frameworks in model-based segmentation to deal with objects with complex shapes such as brain or heart, where a model of the object is used for shape guidance when defining the internal energy terms. The shape most close to the model is the shape most desired.

Boundary-searching based segmentation achieves automation by deforming the surface of a pre-constructed model towards the detected boundaries in unseen images, while at the same time constraining the model within a reasonable shape from the *a priori* knowledge of the model. The searching is done by optimising an energy function combining both the external and internal energy terms, similar to the idea of the active contour model (Kass et al., 1988). The terms defined within the external energy vary between each research group, but the main idea is similar and related to the distance between the boundary points of the model and the searched boundary candidates. The internal energy is more variable, though its definition is usually related to the shape of the prior model.

The prior model is crucial in this category of segmentation approaches. A number of different representations of this shape model have been used, including manually delineated contours, mathematical models, point distribution models, deformable mesh models, and volumetric models with or without bio-mechanical properties. The works are presented chronologically for each model representation in the following survey.

Hautvast et al. (2006) addressed the three common challenges presented in automatic segmentation, providing a useful motivation and discussion for other segmentation frameworks:

(1) the trade-off between decreasing user interaction and providing good initialisation,

(2) the *myocardium leaking* problem such as to the papillary muscle and liver,

(3) the difficulty of weighting and parametrising different terms in the cost function.

They reduced the user-interaction to solely defining an initial contour delineation, such as from end-diastolic (ED) phase, which could be propagated to other phases for automation. The model is the initial manual delineation, providing guidance for automatic segmentation such as delineating the boundary between the papillary muscle and the myocardium. The internal energy is related to the local contour curvature, and the external energy is based on the intensity difference between the reference and unseen images on the perpendicular direction of the contour.

They did a validation on sixty-nine cine cardiac MR cases from both the short-axis (SA) and long-axis (LA) orientation. The quantitative validation were only calculated on end-systolic (ES) phases due to the massive manual work of building a gold standard for all phases, and they argued that the propagation to other phases should be no worse than the segmentation on the ES phases. Their segmentation results are presented below, where LV and RV are acronyms of left ventricle and right ventricle respectively:

Contour	ϵ_{mean}(mm)	ϵ_{rms}(mm)	ϵ_{max}(mm)
SA LV Endocardium	2.23 ± 1.10	2.64 ± 1.30	5.00 ± 2.72
SA LV Epicardium	1.84 ± 1.04	2.27 ± 1.35	4.70 ± 3.63
SA RV Endocardium	2.02 ± 1.21	2.63 ± 1.77	7.87 ± 8.11
LA LV Endocardium	1.82 ± 0.61	2.31 ± 0.87	5.76 ± 2.62
LA LV Epicardium	0.92 ± 0.42	1.12 ± 0.61	2.38 ± 2.41

The main advantage of this work is that it does not need a shape training stage; hence it is applicable to any pathological cases. However, using the manual delineation on the first phase to initialise the propagation limits the automation as manual delineation of the first phase is required for each subject.

Pluempitiwiriyawej et al. (2005) used a conic equation to model the ventricle cavity as an ellipsoid. The internal energy was defined to the contour smoothing term, $J(C) = \int_C ds$, and the external energy was the combination of the matching function based on regional intensity and the distance to the detected edges. The profile for defining the optimal edge points was based on magnitude of image intensity gradient. This model is simple in construction and elegantly formulated in maths for deriving the internal energy. However, more complex modelling may be needed in order to model the structure of the whole heart.

Medial representation (M-Reps) (Siddiqi and Pizer, 2008) is a more sophisticated tool to model objects with irregular shapes. Pizer et al. (2003) demonstrated its applicability in image segmentation for several different applications, but that for cardiac images had not been included. Pilgram et al. (2006) built a heart model based on M-Reps, which shows the possibility of applying M-Rep to this task, but the application to whole heart segmentation, to the best of our knowledge, has not been reported.

The point distribution model (PDM) is usually reported together with a statistical shape model (SSM). The SSM is also known as the active shape model (ASM). SSM is constructed from a training set by means of the principle component analysis (PCA), given that all the training cases have been mapped to a common space (Cootes et al., 1995). SSM can also be constructed using other model representations such as the deformable mesh model, volumetric model, which is also referred to as a statistical deformation model (Rueckert et al., 2003).

SSM assumes the variation of the shape in a group is multi-dimensional Gaussian distributed. If the shape of an unseen image falls within this distribution, the segmentation can be

easily achieved by adapting the weights of the dominating modes from the PCA (Mitchell et al., 2002). The advantage of using this segmentation framework is that the shape of segmented images is easily guaranteed to be realistic. However, a disadvantage is that the accuracy of the segmentation may be reduced due to the limited flexibility of the SSM. A more popular way of using SSM can be summarised as follows (Weese et al., 2001):

- The SSM is firstly used as a global initialisation by adapting the weights of the PCA modes.

- The flexibility of the shape is then extended by using a local adaptation. In this adaptation, driving forces are computed from a combination of external and internal energy terms as an active contour model. The internal energy term, maintaining a realistic shape of the model, is related to the distance between the current shape to a closest shape within the variability of the SSM.

Kaus et al. (2003, 2004) proposed a framework to segment the myocardium from multi-slice cine MR images, and they validated the segmentation on the ED and ES phases. The profile of detecting boundary points were based on *learned* ranges of intensity values and intensity gradient. The searching direction was the normal vector of each triangle center of their mesh model. The external energy was computed based on the distance between the centre of the triangles and their detected corresponding boundary points. The internal energy penalised both the distance between the current shape and originally initialised surface shape and the deviation between endo- and epi-cardial surfaces. Compared to other works, this study included two types of prior information, the spatially varying features and the surface connectivity, to improve the segmentation robustness. However, these constraints may also limit the flexibility of the deformable model to achieve high accuracy when the model is not closely initialised to the unseen image at the beginning. The accuracy reported in this study, the mean surface distance, is given below. The result of the endocardial surface does not seem to evidently report a statistically significant improvement from the initialisation, considering the standard deviation is 0.93 mm and the difference of mean is only 0.19 mm.

Error(mm)	Mean ED[ES]	Standard Deviation	Maximum
Endocardial surface			
Initialisation	2.47[3.05]	1.87[2.11]	20.92[22.83]
Result	2.28[2.76]	0.93[1.02]	13.83[15.43]
Epicardial surface			
Initialisation	3.73[4.02]	1.93[2.35]	21.88[22.97]
Result	2.62[2.92]	0.75[1.38]	12.35[17.67]

van Assen et al. (2006) reported a ventricle segmentation framework for arbitrarily oriented MR images. They claimed that segmentation method was not limited to the MRI sequence and widely applicable. First of all, the initialisation of the model to the unseen image was semi-automatic, which improves the segmentation robustness, but leads to reduced automation. Furthermore, this study did not report very good segmentation accuracy as a semi-automatic tool, such as 2.23 ± 0.46 mm mean point-to-surface error for the epicardium segmentation of short-axis MRI. The limited accuracy was due to the constrained flexibility of the SSM, similar to the work of Kaus et al. (2003, 2004).

Ecabert et al. (2008) extended the work of Kaus et al. (2004) and applied it to whole heart segmentation of CT data. Three technical contributions were presented in this work:

- They addressed the importance and difficulty of localisation, to globally initialise the deformable model to the heart location in the CT image, and proposed to use the generalised Hough transform for this task.

- They introduced the parametric adaptation process which included the piecewise-affine adaptation. This adaptation significantly increased the flexibility of the model to achieve a much better initialisation. At the same time, it also had the affinity constraints on the local regions, and hence was able to maintain the shape of the substructures. This adaptation did not employ extra internal energy to constrain the shape of the model. They showed that the mean error mainly improved by the first couple of modes of the PCA model in Fig. 9 of the paper. The SSM adaptation using all the modes from PCA only achieved 1.7 mm mean accuracy. By contrast, the parametric adaptation further improved it to 1.3 mm.

- They refined the segmentation by optimising both the transformation parameters and the coordinates of vertices of the mesh model within the competition of the external and internal energy. They validated their study using the leave-one-out strategy, and the CT segmentation for whole heart achieved 0.82 ± 1.00 mm mean surface distance error.

Koikkalainen et al. (2008) investigated different methods of artificially enlarging the training set for SSM to extend its flexibility. The two best enlargement techniques were the nonrigid movement and the technique that combines PCA and a finite element model (FEM). These two methods achieved a mean surface-to-surface error of 2.06 ± 0.55 and 2.06 ± 0.58 mm respectively in the whole heart segmentation which includes four chamber endocardium and left ventricle epicardium.

Peters et al. (2007, 2009) applied the segmentation framework of Ecabert et al. (2008) to volumetric cardiac 3D MR images. The validation study on a dataset with limited variety of heart abnormality reported mean surface distance error of 0.76 ± 0.30 mm, which is the best result reported to our knowledge. However, the validation was not independent, as the meshes of gold standard segmentation came from the same mesh model of their segmentation tool with manual correction. Furthermore, the test data they used had the same or similar pathology, while a number of other studies were validated using a variety of pathologies. Therefore, an objective inter-work comparison would be difficult.

The validation in (Ecabert et al., 2008; Peters et al., 2007, 2009) used the data from the similar pathology where the heart shape might not vary so significantly. In this case, the PCA model should be expected to be able to capture the variation of the heart shape from the test data set and thus provide a good initialisation. Therefore, the boundary-searching process was able to find the optimal boundary within a small searching area. However, the heart shape of test data in clinics, coming from a variety of pathologies, should vary more significantly as the test set used in the thesis shows in Chapter 6. The variation of the heart shape presents the main challenge for the segmentation to achieve a robust automation and hence manual interaction is used in practical studies (van Assen et al., 2006, 2008).

Furthermore, the SSM does not naturally guarantee a one-to-one mapping, i.e. a diffeomorphic segmentation, from the model to the unseen image. This may contribute to a common phenomenon that two or more segmented surfaces intersect each other in the result, as the example shown in Figure 1.3 (a). Diffeomorphism has the advantage of topology preservation and is desirable in some applications. Instead, a deformable model which includes physical properties, such as a biomechanical FEM, can be used to tackle this. The advantage of this model is that the constraints are implicitly applied from the physical properties of the model itself, instead of using weighted energy terms. The main concern however is the computation time for solving FEM equations and the construction of such a model with correct material property settings.

Rouchdy et al. (2007) generated a deformable elastic template with a nonlinear material property and applied it to rodent cardiac MRI segmentation. In this work, the mesh model was first localised to the unseen data using an affine registration. The boundary-searching technique, using detected Canny edges (Canny, 1987), was then employed as the driving force to locally deform the mesh to refine the segmentation of local details. The deformation was regularised by the nonlinear elastic property of the physical model, and hence a more realistic deformation field was produced during the adaptation. It should be noted that this elastic model was not a cardiac biomechanical model.

Summary of problems

The majority of the segmentation works reported good results as we reviewed above. They also have the advantage of being computational fast. However, there are three technical challenges of achieving whole heart segmentation, and no work, to our knowledge, has shown the ability to tackle all of them.

First of all, boundary-searching is normally done within a small area such as along the normal direction to the model surface in a limited distance, assuming the corresponding edge point could be found. To ensure the correctness of the assumption, the model needs to be closely initialised to the true position in the unseen image. This is however a challenging task in the fully automatic segmentation (Pham et al., 2000) and is difficult to achieve considering the large shape variability from pathological cases.

Furthermore, the boundary profile, which determines the boundary point candidates, is mainly based on the information from a small local area of the unseen image such as the intensity value, and the intensity gradient. This profile is however sensitive to intensity inconsistency such as noise and artefacts, and intensity distribution variations.

Finally, most of these techniques do not naturally guarantee a diffeomorphic segmentation, which induces two or more segmented surfaces intersecting each other in the result.

3.1.4 Atlas propagation using image registration

Since the boundary-searching based segmentation propagation methods have the difficulties to deal with all the three challenges mentioned above, an alternative technique is proposed for the segmentation propagation: the registration-based method. A registration-based segmentation propagation framework works by registering a pre-constructed atlas, having every region of interest segmented, to unseen images for segmentation propagation. There are three advantages of this framework:

- By using the information based similarity measures such as the mutual information (MI) or normalised mutual information (NMI), the segmentation propagation becomes less sensitive to noise, artefacts, and different intensity distributions. This is because in the registration process, the alignment of each local region is based on a large amount of information from the whole images.

- The segmentation propagation can retrieve these boundaries with low contrast or that are not clearly discernible in the unseen images, through the global warping of the atlas.

- To preserve the topology of the heart, the resultant transformation of the registration should be diffeomorphic, which is nowadays well studied and achievable (Crum et al., 2005; Rueckert et al., 2006; Vercauteren et al., 2007; Ashburner, 2007).

This segmentation idea has been implemented in brain MR image where the shape from inter-subjects has less variability. For example, Dawant et al. (1999); Hartmann et al. (1999) employed the atlas from one single subject as the template for propagation. Rohlfing and Maurer (2005) showed that multi-atlas combined with decision fusion techniques could improve the segmentation performance, but the atlas still used one single image.

The main difficulty of applying the registration-based framework to whole heart segmentation is to estimate the appropriate spatial mapping, namely the resultant transformation from the registration process. Usually, the standard registration scheme uses a global affine registration to *localise* the heart, and then apply a nonrigid registration with a transformation containing a large number of degrees of freedom, such as free-form deformations (FFDs) (Rueckert et al., 2002), to *refine* the local details. However, one common issue of the segmentation-propagation and boundary-based techniques is their relative sensitivity to initialisation, making the algorithms less robust to large shape variability, commonly seen when dealing with pathologies.

Lorenzo-Valdes et al. (2002) proposed to construct a subject-specific atlas for each subject from ED phase and propagate this atlas to other phase images from the same subject. They implemented this idea to MRI ventricle segmentation and the registration scheme was the same as the work of Rueckert et al. (2002). The ED phase provided a good initialisation for local substructures as well as the global structure to its neighbour phases after a global affine registration. By using a serial propagation strategy for other phases (normally over ten phases), they achieved a robust segmentation framework. The limitation of this work is that the subject-specific atlas was only applied to images from the same subject. Hence, the automation impact is limited, similar to the work of Hautvast et al. (2006).

Mitchell et al. (2002) constructed an active appearance model (AAM) (Cootes et al., 1999) and used both the statistical intensity and shape information for the registration. They matched the AAM to an unseen image by optimising modes of both the textual and shape PCA models. The used the root mean square (RMS) of intensity difference as the similarity measure. A good robustness and wide applicability was shown in the paper. In an ideal segmentation, the AAM should be identical to the unseen image in terms of both the textual and shape after the registration. However, this is practically difficult in clinics, because the shape variability of pathological data is large while the flexibility of the PCA model is limited to its training set. Therefore, the accuracy reported in the paper was not as good as other studies considering the

interest of segmentation was the left ventricle: 2.75 ± 0.86 mm for the endocardial contours and 2.63 ± 0.76 mm for the epicardium using surface-to-surface distance measure.

Lapp et al. (2004) reported a similar work for ventricle segmentation of 3D/4D images. Unlike the work of Mitchell et al. (2002), they built the AAM using a statistical deformation model (SDM) (Rueckert et al., 2003). On one hand, they assumed that the registration between different MR images can be successfully achieved in order to build the SDM. On the other hand, they employed another registration using AAM to unseen images for segmentation propagation. Therefore, this method may have either limited segmentation robustness or limited accuracy in its performance. The results reported in the study were 2.2 ± 1.1 mm for the leave-none-out scheme and 4.0 ± 1.6 mm for the leave-one-out test using the mean absolute distance measure as the segmentation error measure.

Lotjonen et al. (2004) extended the AAM framework to the whole heart, including the myocardium and the blood cavities of the four chambers, and applied it to cardiac MR images from different orientations. To extend the deformation flexibility of the AAM, they included the information of the coordinate of boundaries of all training data and built the information into a probabilistic atlas to penalise the deformation according to the probability of the appeared landmarks. The cost function then becomes:

$$Cost = E_{NMI} + \lambda E_{model}$$

where E_{MI} is the NMI similarity measure, $E_{model} = \frac{1}{N}\sum_i \log[p(\mathrm{x}_i)]$, $p(\mathrm{x}_i)$ is the probability of landmark x_i mapped to the probabilistic atlas. The template image for registration is the mean shape and mean texture from the AAM. They argued this mean template should be better than an image from one single case. The mean texture should be able to improve the signal-to-noise ratio of the template, but it is questionable whether the mean shape is necessarily closer to the unseen image when it comes to different pathologies in clinics.

They showed that this extension of flexibility using a probabilistic atlas achieved better accuracy than only using the statistical shape information constructed either by PCA or independent component analysis (ICA) or without any statistical information. The accuracy in mean surface-to-surface distance to manual segmentation, in millimetre is given below:

Left Ventricle	Right Ventricle	Left Atrium	Right Atrium	Epicardium	ALL
2.01 ± 0.31	2.37 ± 0.50	2.56 ± 0.88	2.93 ± 1.30	2.77 ± 0.49	2.53 ± 0.70

However, the test data used in the work were acquired from healthy subjects whose heart shapes were supposed to be less variable compared to that from different pathologies. The robustness of the method is hence still questionable in clinical applications.

3.1.5 Conclusion and research direction

In conclusion to the whole heart segmentation, model-guided approaches are preferred due to the complexity of this task. The works in the literature mainly focus on propagating segmentation, through either an atlas or a deformable model, to unseen images. The propagation is mainly done by using the boundary-searching or image registration techniques.

Boundary-searching, commonly used with a deformable model, is the most common technique published in the past ten years. It has the advantage of a fast computation owing to the local adaptation only considering the information of a small area. The state-of-the-art imple-

mentation can segment one volume within one minute using a state-of-the-art personal computer (Peters et al., 2007). However, the limited information for local adaptation also accounts for the reduced robustness of the boundary-searching process against noise and artefacts, given that a fully automated tool is pursued.

Registration-based propagation provides an alternative solution for the propagation. The well developed registration techniques can provide those features desired in whole heart segmentation, such as good robustness against low quality images, good flexibility of the deformation model to achieve high accuracy, and diffeomorphism. With a successful registration between the atlas and the unseen image, the segmentation of the unseen image becomes available. Therefore, the research direction of this doctoral work is to develop robust techniques to achieve this registration.

The main challenge is to model the spatial transformation between the cardiac images from different subjects. On one hand, the registration needs a flexible modelling method to achieve high accuracy for the segmentation. On the other hand, the registration needs a shape constraint on the flexibility to achieve a realistic deformation field, and thus a realistic segmentation. To obtain a compromise between them, we propose to use an adaptive trade-off in such a way that the registration starts with strong shape constraints and little flexibility. During the registration, we increase the flexibility of the model while lessening the constraint. This is done by using a series of transformation models whose degree of freedom increases slowly along with the registration process. Correspondingly, the constraints of maintaining the global shape will gradually relax. According to the registration models, we divided this process into two steps: initialisation registration and refinement registration.

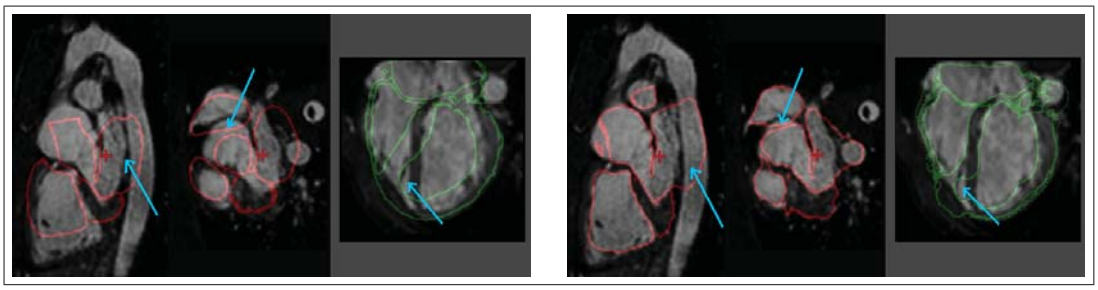

Figure 3.2: Initialisation using a global affine transformation induces an overlap of local substructures at great vessels, atria and ventricles (left); the refinement based on this generates erroneous registration results (right). MR data from Guy's and St Thomas' Hospital, London.

Initialisation includes global localisation of the heart and local correspondence of substructures such as the four chambers and great vessels. An affine transformation is usually used for the localisation. For example Rueckert et al. (2002); Lorenzo-Valdes et al. (2002) used a single global affine registration, and Montagnat and Delingette (2005) applied the affine deformation constraint to their deformable model for the initialisation. The affine registration or constraint maintains the heart shape. However, it is difficult to provide a good local initialisation for substructures. This is demonstrated in Figure 3.2 (left). As a result, an erroneous segmentation was produced after using a fluid registration for refinement, shown in Figure 3.2 (right).

Refinement registration is done by nonrigid registration with large degrees of freedom. It

is needed in order to achieve an accurate segmentation, since the initialisation step only gives a close correspondence between the structures of the images. For the whole heart segmentation, there are two concerns:

- Our collaborated clinicians prefer to exclude the papillary muscle from the myocardium and include it into the blood cavities. This was claimed to be more convenient for their clinical studies. However, the intensity value of the papillary muscle and the myocardium are similar in cardiac MR images. Image registration tends to include the papillary muscle into myocardium as shown in Figure 3.3 (middle) if no proper prior knowledge is used.
- The boundary between the myocardium and its adjacent tissues is not always distinct in our *in vivo* MR data. The delineation of the epicardium could hence leak to the adjacent liver tissue, as shown in Figure 3.3 (right).

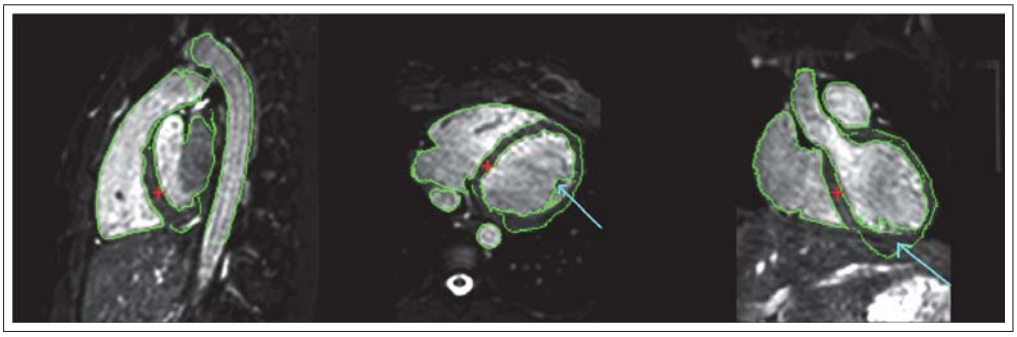

Figure 3.3: Myocardium segmentation problems: including papillary muscle into myocardium (middle) and segmentation leaking in epicardium (right). MR data from Guy's and St Thomas' Hospital, London.

3.2 Image registration and theory

This section presents the theory of image registration. Section 3.2.1 introduces the basic knowledge of image registration. Section 3.2.2 focuses on the transformation models. Section 3.2.3 introduces the popular similarity measures. Finally, section 3.2.4 concludes this section and outlines current problems.

3.2.1 Introduction

Medical image registration is one of the major topics in the medical image computing field (Hajnal et al., 2001). Image registration can be considered as a process to compute one or one series of spatial transformations which map one or one series of medical images to other one with accurate spatial correspondence. This correspondence means the mapped points from the two groups of images are from the same anatomical position. The result of an image registration process can be the transformations, or the transformed resultant images, or both the transformations and resultant images. The transformations provide spatial mappings between the two groups of images, and the resultant images are in the same coordinate system as that of the reference images. The process of image registration provides the capability to fuse or compare the information of two groups of images in the same coordinate system. The registration images

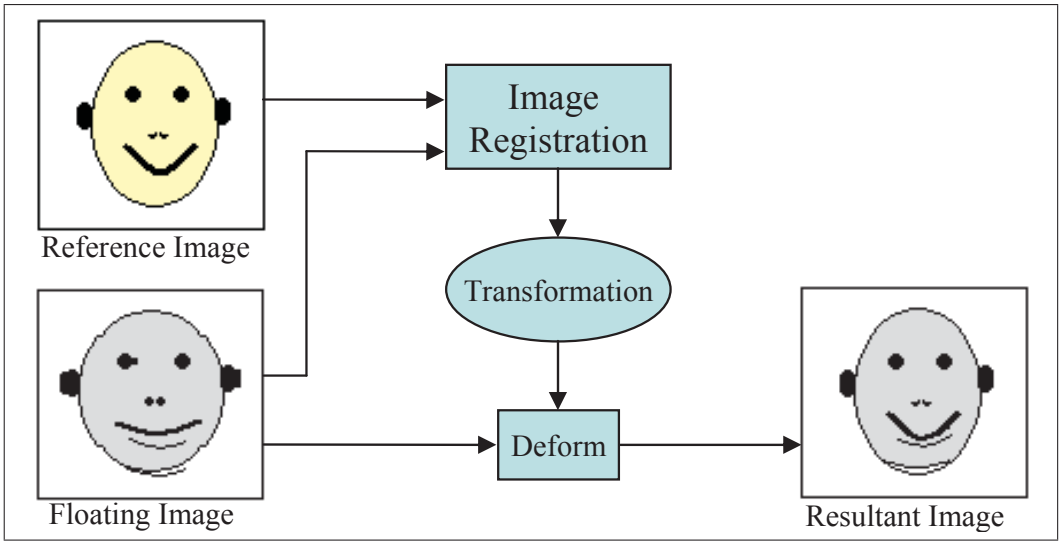

Figure 3.4: Illustration of image registration

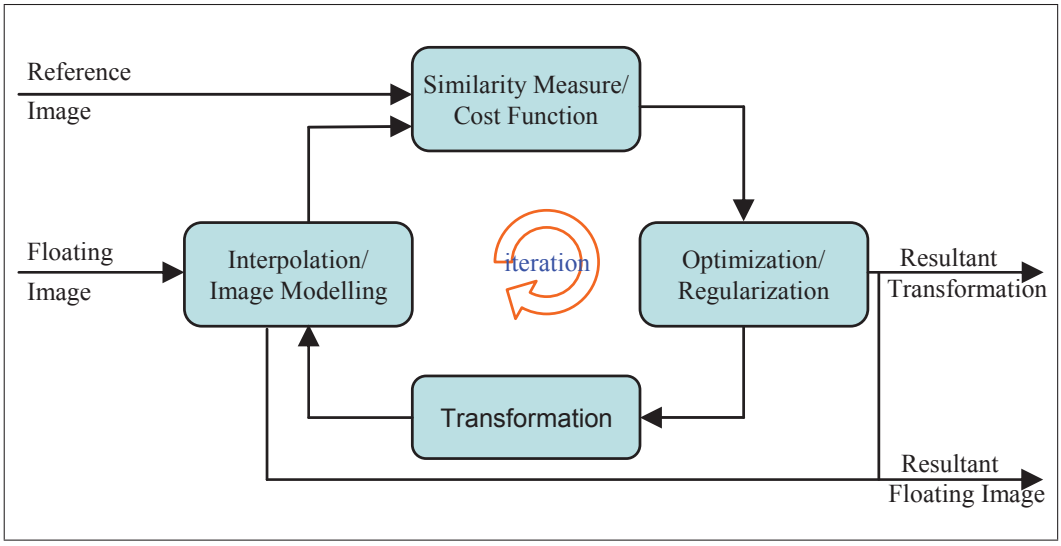

Figure 3.5: Framework of image registration

can be acquired from different time points, different modalities, and from different subjects or populations. Figure 3.4 gives a demonstration of registering two images.

In this work only the registration of two images is studied. An image registration process includes the following technical components: two intensity images for registration including the reference image and the floating image, an interpolation method to model spatially continuous intensity images from the discrete grid images, spatial transformation models, a similarity measure as the cost function, which may also include penalty or regularisation terms, an optimisation method which may also have regularisation step to smooth the deformation field, and the registration result. Figure 3.5 highlights all these components in a flowchart.

Image: The medical images studied in this work are represented in pixels, or referred to as *voxels* in three dimensions, on a regular discrete grid. They can be two-dimensional (2D), three-dimensional (3D), or four-dimensional (4D) which may also be referred to as 3D plus time dimension (3D+t). The image pair, referred to as the reference image and the floating image,

can be in the same dimension such as 2D to 2D and 3D to 3D, or in different dimensions such as 2D to 3D registration. This work only considers images of the same number of dimensions.

Interpolation: Since the images only have intensity values defined on the regular discrete grid points, interpolation is required when there is a need to obtain intensity values between grid points, such as resampling the images during image registration, or outputting the transformed resultant image. There are three interpolation methods widely used in image registration, namely nearest-neighbour interpolation, linear interpolation, and B-spline interpolation. Nearest-neighbour interpolation is the most computationally fast and least accurate method, while B-spline interpolation is the most accurate and least computationally fast algorithm. There are other higher order interpolation methods that are able to provide better accuracy, such as sinc interpolation. However, these are less likely to be used in the resampling of the floating image during the registration process due to its expensive computation. A trade-off between the run-time and accuracy is needed. Linear interpolation is fast and also provides good accuracy, while in the registration where high order of differentiability is desired, B-spline interpolation may be preferred (Thévenaz and Unser, 2000).

In mutual information based registration, partial volume interpolation (Maes et al., 1997) was proposed to construct the joint histogram table. The computation time for this interpolation is similar to that of the linear interpolation. Pluim et al. (2000) compared the interpolation artefacts of these two methods and found that partial volume interpolation creates additional dispersion in the joint histogram while linear interpolation usually decreases the dispersion. Also the effects of interpolation artefacts to mutual information become more pronounced, especially using partial volume interpolation, when only a small number of sample points are used for the construction of joint histogram.

With the consideration of smoothing the joint histogram table and thus the resultant probability density functions (PDFs), it is proposed to use a Parzen window function such as the Gaussian kernel function (Viola and Wells, III, 1997) or the cubic B-spline kernel function. Thévenaz and Unser (2000); Loeckx et al. (2006) used the latter because it has the advantageous property of having a local support which is potentially more computationally efficient.

Optimisation: Optimisation is the process of searching for an optimal solution for a defined problem or function following a certain strategy. In retrospective image registration, optimising the cost function is commonly done in an iteration scheme. Two methods are introduced here: Powell's conjugate gradient ascent/descent method and gradient ascent/descent method.

Powell's conjugate gradient ascent/descent method (Powell, 1964), also simply referred to as Powell optimisation, works as follow: In each iteration of the optimisation, it first searches for optima from the current position P_{00} sequentially along n directions and at the same time updates the current position by the new optimal position during each search. The n directions are normally chosen to be the coordinate axis directions defined by the n transformation parameters. Then, after finishing all the provided directions, it will then search for an optimum along the direction of $P_{0n} - P_{00}$ to replace the current position as P_{10}. P_{10} is ideally a good approximation of the true optimum. However, in practice, especially in high dimensional problems, more iterations are required to ensure that it does not step into a local optimum and then

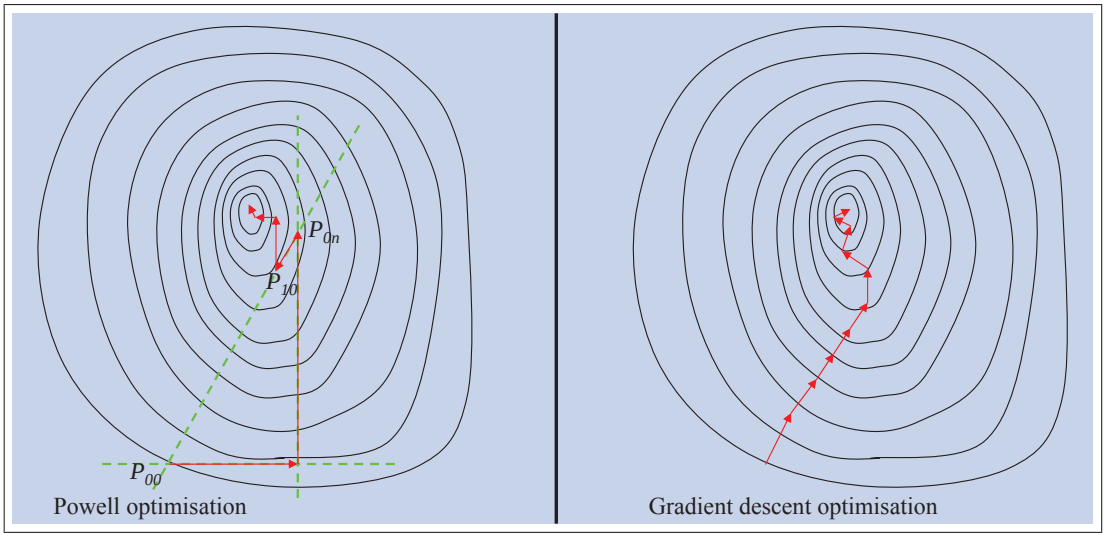

Figure 3.6: Illustration of Powell optimisation (left) and gradient descent optimisation (right).

to guarantee a good accuracy. This procedure is illustrated in figure 3.6 (left). One advantage of Powell optimisation is that it does not require the cost function to be differentiable and no derivative is taken for each iteration.

The gradient ascent/descent method, also known as a method of steepest ascent/descent, searches for the optimum of the cost function along the directions of gradient vectors of the cost function. At each iteration, the scheme needs to compute the first order derivative of the cost function and decide the step length to advance, as figure 3.6 (right) illustrates. Ideally, the optimisation gets closer to the optimum after each iteration and finally converges to the solution. There are two popular implementations of advancing in each iteration step. One is to use a regularisation scheme by adaptively decreasing the length in each advancing step:

$$L(i) = \begin{cases} l, & i = 0 \\ L(i-1)R(i), & i > 0 \end{cases} \quad \text{and} \quad R(i) = \begin{cases} 1, & \nabla\mathcal{C}_i \cdot \nabla\mathcal{C}_{i-1} \geq 0 \\ r, & \nabla\mathcal{C}_i \cdot \nabla\mathcal{C}_{i-1} < 0 \end{cases}$$

where l is a user defined length for the first iteration, $L(i)$ is the advancing length at iteration i, and $R(i)$ is a function of the cost function gradients at current and last iteration steps, $\nabla\mathcal{C}_i$ and $\nabla\mathcal{C}_{i-1}$, to decide whether use the user defined regularisation rate $r \in [0.5, 1)$. The other scheme is to use the line search routine, advancing along the direction of $\nabla\mathcal{C}_i$ until reaching a local optimum (Klein et al., 2007). The scheme needs a technique to search for the optimum along the gradient direction and the searching operation decides the advancing length.

We adopt the gradient ascent/descent optimisation method with the regularisation scheme for all the registration experiments in this thesis.

Transformation and **Similarity measure** are the two topics studied in this thesis. Hence, more detailed introduction and discussion of them will be given in section 3.2.2 and 3.2.3.

3.2.2 Transformation models

In most of the nonrigid registration tasks, it is required to use a series of transformation models to estimate the spatial difference between the two images. According to the linearity of the transformations, they can be classified into three categories: linear transformations, nonlinear

transformations, and locally affine transformations.

Linear transforamtions: Linear transformations maintain the linearity and parallel property of lines after the transformation, hence maintain the global shape of the subject. They include the following three models:

- Rigid transformation, can be defined with 6 degrees of freedom (DOFs) in 3D problems: three translation parameters and three rotation parameters.
- Similarity transformation, can be defined with 9 DOFs in 3D problems: 6 rigid parameters plus 3 scaling ones.
- Affine transformation, can be defined with 15 DOFs in 3D problems: 9 similarity parameters plus 6 skew ones.

Linear transformations have low DOFs and the registration provides limited accuracy when the images have local deformations. The examples are that when the images are acquired from different subjects, or from different time points of a subject and this subject has local deformations due to pathological progress. In these situations, nonlinear registration is desired. However, owing to the global property of linear transformations and being able to initialise the images in the same physical coordinate with large capture ranges, linear registration is normally done prior to the nonlinear registration to improve its performance.

Nonlinear transformations: Nonlinear transformations, also referred to as nonrigid or deformable transformations, have high DOFs. The registration can provide local deformations to align the local difference. Unlikely the linear transformations, it is arguable how realistic the transformations are for medical image registration. Some groups constructed biomechanical models to simulate the proper deformations of certain tissues such as the heart (Sermesant et al., 2003, 2006). The registration using these models is supposed to be more realistic. However, in practice the implementation of such a validated model could be difficult and the computation of the registration may be too time consuming. The majority of the works in the literature tried to employ simplified models to *estimate* the deformation fields between the images. These simple models may not relate to the real property of the imaging tissues. The registration techniques using these transformations include elastic and fluid registration (Christensen et al., 1994; Crum et al., 2003, 2005), demon registration, and the registration using free-form deformations (FFDs).

Among these, the cubic B-spline FFD registration (Rueckert et al., 1999) is one of the most popular methods due to its easy implement and high efficiency in both modelling and computation. The cubic B-spline kernel function is defined as follows:

$$\beta^{(3)}(a) = \begin{cases} \frac{1}{6}(4 - 6a^2 + 3|a|^3), & 0 \le |a| < 1 \\ \frac{1}{6}(2 - |a|)^3, & 1 \le |a| < 2 \\ 0, & 2 \le |a| \end{cases}$$

and a FFD transformation T of $\mathbf{x} = [x, y, z]$ in 3D is:

$$T(\mathbf{x}) = \mathbf{x} + \sum_{i,j,k} \mathbf{c}_{ijk} \beta^{(3)}(\frac{x - \phi^x_{ijk}}{l_x}) \beta^{(3)}(\frac{y - \phi^y_{ijk}}{l_y}) \beta^{(3)}(\frac{z - \phi^z_{ijk}}{l_z}) \,,$$

where $\mathbf{c}_{ijk}$ and $[\phi^x_{ijk}, \phi^y_{ijk}, \phi^z_{ijk}]$ are the displacement vector and coordinate of control point ϕ_{ijk}, respectively, and $[l_x, l_y, l_z]$ is the FFD grid spacing in each dimension.

Locally affine transformations: There is a special type of transformations whose DOFs are between that of the linear and nonlinear transformations, locally affine transformations. A locally affine transformation model consists of a set of rigid or affine transformations, each of which is only defined to be effective in a local region, a subvolume of the image. For elsewhere without a local transformation, an interpolation based on the set of local transformations is calculated. The transformation model can be expressed as follows:

$$T(x) = \begin{cases} G_i(x), & x \in V_i, i = 1 \dots n \\ \textbf{Interpolate } \{G_i(x_i) | i = 1, \dots, n\}, & x \notin \bigcup_{i=1}^{n} V_i \end{cases} ,$$

where $\{G_i\}$ are the local affine transformations assigned to the corresponding local regions $\{V_i\}$. In the implementation of the registration, a concatenation of a series of such locally affine transformations is commonly used to model a large displacement with diffeomorphism:

$$T = T_1 \circ T_2 \cdots T_{N-1} \circ T_N \ .$$

The advantage of using these transformations in image registration is that they have both the global nonlinearity and the local linearity. The global nonlinearity can provide better accuracy compared to a global affine transformation and the local linearity can preserve the local shape of substructures. The registration can be applied after a global affine registration to provide a better initialisation of substructures between the two images for the following nonrigid registration.

3.2.3 Similarity measures

In medical image registration, one of the popular topics is to investigate the intensity-based similarity measures for retrospective registration. These intensity-based registration methods employ the intensity information from the registration images to assess the similarity between the images. Compared to feature points-based registration methods, this registration takes longer to compute due to the large amount of information taken into computation. However, this registration needs less pre-processing on the registration images. For example, the extraction of feature information is not required, thus no manual processing is involved. Practically, it is able to provide fully automatic image processing using computers, and hence it is desirable in the registration-based fully automatic whole heart segmentation framework. This section will provide theory of three popular similarity metrics that can be directly computed from the intensity of the images, viz. mean of squared intensity difference, cross correlation, and mutual information (MI). Another three methods, intensity gradient difference, normal vector, and local phase registration will be also introduced here. These metrics are not directly computed from the intensity values, but instead from some continuously defined features that can be automatically calculated from the intensity of the images. Therefore, they are also fully automatic and is useful in registration of ultrasound images where the intensity values are not as reliable as the imaged features.

Let I_r be an image, referred to as the reference image, I_f another image, referred to as the floating image, T the transformation associated with I_f, $S(I_r, I_f, T)$ the similarity measure of the reference image and the transformed floating image, and x the sample point from the overlapped volume V.

Mean of squared intensity difference:

$$S_{MSID}(I_r, I_f, T) = \frac{1}{|V|}\sum_{x\in V}(I_r(x) - I_f(T(x))^2 \ .$$

S_{MSID} assumes that the intensity values of corresponding points in the registration images are the same and their intensity difference is minimised when the images are perfectly matched. Hence, this metric is not recommended for images with different intensity distributions.

Cross correlation: Cross correlation, also known as correlation coefficient, is a more robust metric against noisy data and applicable to different intensity distributions with an affine relationship, i.e. $I_1 \approx bI_2 + a$. It is computed as the ratio between the covariance of the two sample point sets of the two images and the product of the individual deviations of them: The cross correlation is:

$$S_{CC}(I_r, I_f, T) = \frac{\sum_{x\in V}\left[(I_r(x) - \bar{I}_r)(I_f(T(x)) - \bar{I}_{T,f})\right]}{\sqrt{\sum_{a\in V}(I_r(a) - \bar{I}_r)^2}\sqrt{\sum_{b\in V}(I_f(T(b)) - \bar{I}_{T,f})^2}} \ ,$$

where $\bar{I} = \frac{\sum_{a\in V} I(a)}{|V|}$ is the mean intensity value of all sample points from volume V.

Mutual information (MI): MI-based similarity metrics have been the most widely used and most successfully applied algorithms in medical image registration since its invention by the two groups, viz. Collignon et al. (1995) and Viola and Wells, III (1995). MI is based on information (entropy) theory and only assumes an *intensity class correspondence* instead of intensity correspondence between the registration images (see Chapter 8 for detail). This enables its wide application in both mono-modality and multi-modality registration tasks (Studholme et al., 1999; Rueckert et al., 1999; Pluim et al., 2003).

There are three forms of MI summarised by Pluim et al. (2003):

$$\begin{aligned} MI(I_r, I_f, T) &= \sum_{r,f} p(r,f)\log\frac{p(r,f)}{p(r)p(f)} \\ &= H(I_r) + H(T(I_f)) - H(I_r, T(I_f)) \\ &= H(T(I_f)) - H(T(I_f)|I_r) \ , \end{aligned}$$

where $p(\circ)$ are the marginal and joint probability distribution functions (PDFs), and $H(\circ)$ are the marginal and joint entropies of the reference image I_r and transformed floating image I_f with transformation T. These three forms in this equation correspond to three interpretations for the functionality of MI, as follows:

- The first form is related to the Kullback-Leibler distance between two distributions p and q, defined as $\sum_i p(i)\frac{p(i)}{q(i)}$. Accordingly, the MI measure is interpreted as the Kullback-Leibler distance between the joint intensity probability distribution $p(r, f)$ and the assumed independent marginal distribution $p(r)p(f)$. When this distance is maximised, the joint distribution is at its least similar to the independent distribution, meaning the two images are mostly dependent, and thus most similar.

- The second form is related to the joint entropy of the two images, which can be described

by the dispersion of the joint histogram table. The less dispersion the joint histogram is, the better the two images are assumed to be registered. Under this interpretation, the maximisation of MI is related to the minimisation of the dispersion of the joint histogram table.

- The final form is related to the mutual *uncertainty* of the two images. The conditional entropy $H(T(I_f)|I_r)$ means the uncertainty of the transformed floating image $T(I_f)$ when the reference image I_r is known. While $H(T(I_f)$ is the uncertainty of $T(I_f)$, MI can be express as "the amount of uncertainty about image $T(I_f)$ minus the uncertainty about $T(I_f)$ when I_r is known" (Pluim et al., 2003).

Studholme et al. (1999) argued that the MI registration only computes the value on the overlapped volume of the images. However, the MI metric was not invariant to the size of the overlapped volume. This paper proposed normalised MI, an overlap invariant metric, by computing the ratio between the sum of the two marginal entropies and the joint entropy:

$$NMI(I_r, I_f, T) = \frac{H(I_r) + H(T(I_f))}{H(I_r, T(I_f))} .$$

An improved robustness was also demonstrated in their validation.

Intensity gradient difference: Penney et al. (1998) introduced the intensity gradient-based measures and compared the performance of several similarity metrics when applied to the registration of a CT scan to a fluoroscopy image of a spine phantom. The gradient difference measure in this paper was computed as follows:

$$S_{GD}(I_r, I_f, T) = \sum_{d=1...n} \sum_{x \in V} \frac{A_d}{A_d + \left[\frac{\partial I_r}{\partial x_d}(x) - s\frac{\partial T(I_f)}{\partial x_d}(x)\right]^2} ,$$

where A_d is the variance of the difference of gradient images in d dimension:

$$A_d = \text{Variance}\left[\frac{\partial I_r}{\partial x_d}(x) - s\frac{\partial T(I_f)}{\partial x_d}(x)\right].$$

s in both of the two equations above is a scaling factor to compensate the gradient difference between the two images, and thus is an application or image dependent parameter required to be determined. The gradient difference was reported to work better than other metrics in the work of Penney et al. (1998), where structures of soft tissues and thin lines were presented as differences in the registration images.

Normal vector, normalised vector of intensity gradient: Zhuang et al. (2005); Zhuang and Gu (2006); Zhuang (2006) proposed to normalise the gradient vectors, referred to as normal vectors, of images and computed the similarity using the sum of dot product (squared cosine of the intersected angle θ_x) of the corresponding normal vector pairs:

$$S_{NV}(I_r, I_f, T) = \sum_{x \in V} \cos^e \theta_x = \sum_{x \in V} \left[\frac{\nabla I_r(x) \cdot \nabla T(I_f)(x)}{||\nabla I_r(x)|| \cdot ||\nabla T(I_f)(x)||}\right]^e , \tag{3.1}$$

where $\nabla I(x)$ is the gradient vector of the image at coordinate x.

Both Griffin (2001) and Karacali (2007) theoretically proved that the local MI or the MI defined for an infinitesimal aperture at x could be related to θ in the following way:

$$\lim_{s\downarrow 0} MI(x) = -\ln(|\sin\theta_x|) = -\frac{1}{2}\ln(1-\cos^2\theta_x)\ .$$

Therefore, the similarity metrics based on normal vectors can be considered as summing the local MI over the overlapped volume V. Zhuang and Gu (2006) argued that compared to MI, the registration using eq. 3.1 was however sensitive to noise in the images due to the locality of the measure. By contrast, the MI computation benefits from the procedures of histogram binning and histogram smoothing. Haber and Modersitzki (2006) introduced a regularisation scheme to compute the normal vector, which is differentiable in iso-intensity areas and the resultant measure is more robust to areas with small intensity gradient:

$$\text{Normal Vector}(x) := \frac{\nabla I(x)}{||\nabla I(x)||_\varepsilon} = \frac{\nabla I(x)}{\sqrt{\nabla I(x)^{\mathrm{T}}\nabla I(x)+\varepsilon^2}}.$$

Biesdorf et al. (2009) proposed to introduce a regularisation factor in the logarithm to reduce the sensitivity to the noisy driving forces to improve the robustness:

$$MI_{new}(x) : \{\log_2|\epsilon+\sin\theta|\} \longrightarrow \min\ .$$

Local phase: Let I be a 3D image in the spatial domain, the local phase, providing a quantitative, continuous and contrast invariant description of local features in images, can be derived using the monogenic signal (Mellor and Brady, 2005; Grau et al., 2007):

$$\phi(\mathrm{x}) = \mathrm{atan2}(\sqrt{\sum_{d=1}^{3}(g(\mathrm{x})*h_d(\mathrm{x})*I(\mathrm{x}))^2},\ g(\mathrm{x})*I(\mathrm{x})),$$

where, g is a zero mean band-pass filter such as the log-Gabor filter (Grau et al., 2007), convoluted with I to constitute the even component of the signal; $\{h_d\}$ are the odd anti-symmetric filters in the spatial domain, $i = 1, 2, 3$, whose expression in the frequency domain H_i is:

$$H_d(u_1,u_2,u_3) = \frac{u_i}{\sqrt{u_1^2+u_2^2+u_3^2}}.$$

The local orientation of the signal can be estimated as:

$$o_d(\mathrm{x}) = \frac{g(\mathrm{x})*h_d(\mathrm{x})*I(\mathrm{x})}{\sqrt{\sum_{d=1}^{3}(g(\mathrm{x})*h_d(\mathrm{x})*I(\mathrm{x}))^2)}}.$$

Given the local phase, including phase value ϕ and orientation $\{o_d\}$, a similarity metric can be computed using the mean square difference of the phase value ϕ, the cross correlation of ϕ, the local phase mutual information (Zhang et al., 2007), or the cosine value of the phase difference combined with the dot product of the orientation vectors (Grau et al., 2007).

3.2.4 Conclusion

The problems of applying existing techniques for the inter-subject registration tasks in the whole heart segmentation framework are summarised into two categories, as follows:

- **Transformation estimation:** The traditional registration frameworks use a global affine transformation for initialisation and refine the local details with a high DOF non-rigid registration such as the fluid or FFD registration (Rueckert et al., 2002). The initialisation using a global affine registration is however not good enough for images from different subjects, where the heart shape varies dramatically. Hence, the first problem is posed in the initialisation step. Also, in the nonrigid registration, constraints and regularisation processes are needed to achieve a robust result such as to produce a realistic deformation field between the two registration images. The second problem is posed in the refinement registration where the shape constraints should be incorporated into the transformation modelling and registration process.

- **Mutual information measure:** In the whole heart segmentation framework, the intensity distribution of the intensity image from the heart atlas is commonly different from that of an unseen image. Hence, MI-based similarity measures are used owing to their robustness against different intensity distributions. However, the standard MI or normalised MI measures do not take into consideration the spatial different of each pixel within the field of view. This may make them less appropriate when the intensity classes of tissues in the images do not correspond well. It should be noted that this is a general issue of MI-based registration posed for many applications, instead of solely for cardiac MR registration. Therefore, the research work on this part is more independent and the proposed method is applicable to many other applications.

Chapter 4

Local Structure Preservation Using Locally Affine Registration

This chapter describes the development of registration methods which preserve shapes of local substructures. Section 4.1 introduces the locally affine transformation model and existing registration methods. Section 4.2 elaborates on a new algorithm: the locally affine registration method (LARM) which keeps global intensity class linkage and diffeomorphism. Section 4.3 describes a method of inverting transformations based on Dynamic Resampling And distance Weighted interpolation (DRAW). Section 4.4 provides two phantom experiments to demonstrate the performance of DRAW and LARM. Section 4.5 uses clinical MR data to evaluate the performance of alternative initialisation methods in whole heart image registration and applying LARM to the whole heart segmentation. The MR data used in this work and the rationale of choosing this acquisition protocol are also presented in Section 4.5.1. The conclusion is drawn in section 4.6.

4.1 Locally affine transformation and registration

Registration using locally affine transformations, also called piece-wise affine or poly-affine transformations, is an attractive registration alternative for applications where a single global affine transformation cannot provide enough accuracy, while a nonrigid registration would incorrectly affect the local topology due to large shape variations. The registration using locally affine transformations, namely locally affine registration, assigns a local affine transformation to each substructure such as four chambers and great vessels in heart images to further initialise them. This transformation model globally deforms the image, while locally still preserves the shapes of the pre-defined local regions, the substructures. The registration is normally applied after a global affine registration to provide better initialisation, which is crucial for some nonrigid registration to achieve success.

In the following, we firstly review the related work; then we introduce the region-based registration; and finally we describe the current problems.

4.1.1 Related work

Here are the studies on the locally affine transformation model and the registration.

Little et al. (1997), to the best of our knowledge, was the first study to address this transformation model and discuss its application in medical image registration. In this work, they only incorporated the rigid substructures and positions of landmarks to interpolate a deformation

field based on the inverse distance weighted scheme (Shepard, 1968):

$$T(x) = \begin{cases} G_i(x), & x \in V_i, i = 1 \dots n \\ \sum_{i=1}^{n} w_i(x) G_i(x_i), & x \notin \bigcup_{i=1}^{n} V_i \end{cases} , \tag{4.1}$$

where G_i is a local affine transformation assigned to a local region or a landmark V_i, and $w_i(x)$ is a normalised weighting factor related to the distance $d_i(x)$ between x and V_i.

Pitiot et al. (2003) employed the similar idea to hierarchically partition the registration images into subimages. The corresponding subimages in the image pair were then registered using the block matching algorithm (Ourselin et al., 2001).

Arsigny (2006); Commowick et al. (2006, 2008) extended the registration method by using a *Log-Euclidean polyaffine framework* for the interpolation of a global deformation field from a set of local affine transformations. This interpolation is done by averaging *infinitesimal* displacements associated with each affine component. The resultant transformation is obtained by integrating an ordinary differential equation (ODE).

Zhang et al. (2007) applied the registration framework (Little et al., 1997) to register cardiac US and MR images. The similarity measure was based on local phase of the images, instead of intensity. This work also provided an automatic method to adaptively detect landmarks which were used for the definition of local regions.

A common disadvantage of all the studies above is that the registration of each substructure is done independently of the registration of other structures. This potentially leads to two problems:

- Each local affine transformation is optimised without taking into account the surrounding substructures. This *passive* local process makes the registration less reliable for preserving the global shape of the organ.

- The registration of each local region does not take the global intensity information of the images into the computation of the similarity measure. Without this global information, the registration loses the global intensity class linkage and reduces the robustness against different intensity distributions. The *global intensity class linkage* refers to the intensity class correspondence estimated from the global scale of the two images (see Section 8.1.1 for detail). Zhang et al. (2007) computed local phase based on the whole image, but still computed the similarity measure of a local registration based on a local area.

Narayanan et al. (2005) proposed a different idea of locally affine transformation and registration. In this work, each affine transformation G_i is only defined on a centre, called a seed point x_i. A global deformation field is then interpolated using:

$$T_i(x) = e^{\lambda(r)} A e^{\lambda(r)} S(x - x_i) + \lambda(r') L + x_i \, , \tag{4.2}$$

where, A, S, and L are the rotation, scaling, and translation matrices of the affine transformation G_i, respectively; $\lambda(r) = e^{-\frac{d^2}{2\sigma^2}}$ is a function of distance $r = ||x - x_i||$ and σ determines the locality of G_i: the smaller value of σ the more local effects of this transformation; $r' = ||e^{\lambda(r)} S(x - x_i)||$. This registration has a set of seed points and each seed point has a set of

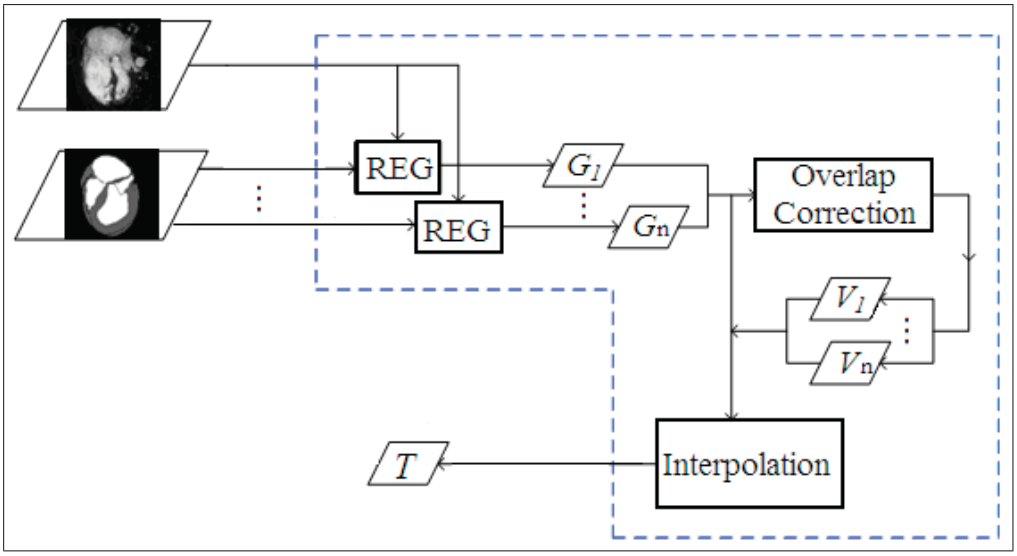

Figure 4.1: A diagram demonstrating region-based registration, where $\{G_i\}$ are local affine transformations and $\{V_i\}$ are the corresponding local regions, T is the resultant global transformation field, procedures REG, Overlap Correction, and Interpolation are defined in the text,.

locally affine transformations which have different values of σ. The resultant transformation is the concatenation of all these locally affine transformations:

$$T = T_1 \circ T_2 \cdots T_{N-1} \circ T_N \ . \tag{4.3}$$

As each T_i globally deforms the whole image, the registration result does not preserve the shape of substructures.

4.1.2 Region-based registration

The region-based registration algorithm, referred to as Rreg, extracts a set of anatomically meaningful local regions from the reference image and registers each of them to the floating image (Zhuang et al., 2008a). For the example of registering a cardiac atlas image to an MR image, the local substructures, including ventricles, atria, aorta, and pulmonary artery, can be *a priori* defined in the atlas. To enable each of the local affine registrations, it only includes the intensity information of a local area, thus loses the global intensity information. Figure 4.1 demonstrates an application of Rreg to the registration of a cardiac atlas and an MR image, where *REG* is an affine registration using the NMI similarity measure (Studholme et al., 1999), *Interpolation* is the procedure of computing a global transformation field using Eq. (4.1), and *Overlap Correction* is a procedure to correct the volumes of pre-defined local regions to avoid overlap after local affine transformations, as demonstrated in Figure 4.2. A detailed explanation of Overlap Correction will be given later in Eq. (4.6).

4.1.3 Problem statement

- Rreg does not use the global intensity information in the local affine registration. This means that it loses the global linkage of intensity classes between subimages, and consequantly impairs the robustness against images with different intensity distributions or from different modalities.

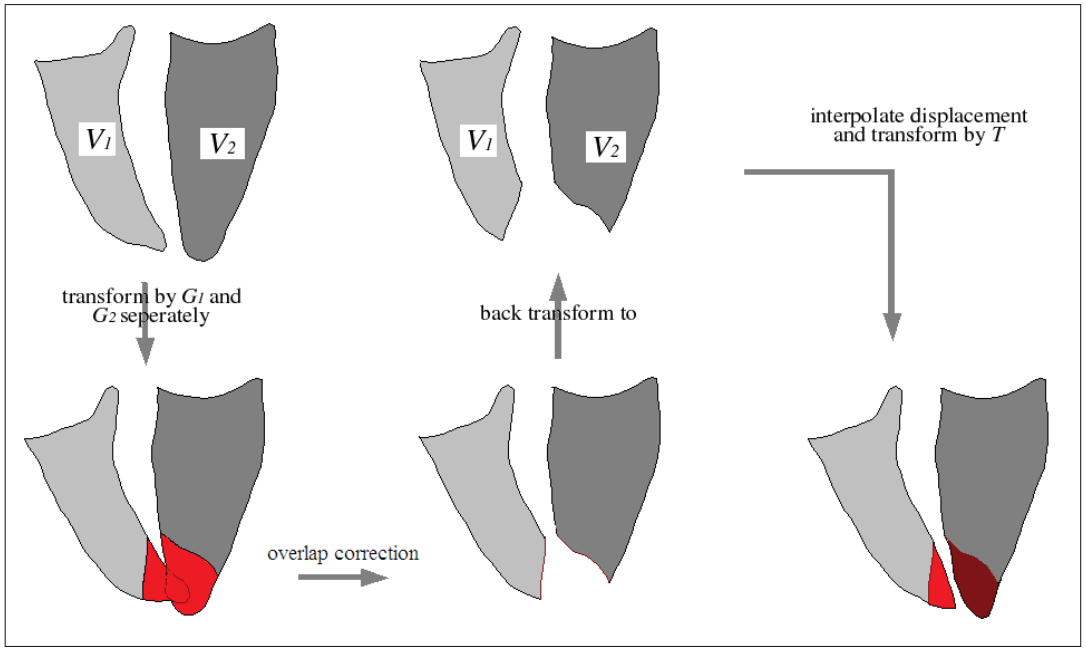

Figure 4.2: A diagram demonstrating the overlap correction procedure of two local regions, V_1 and V_2, after the application of two local affine transformations.

- In Rreg, the interpolation using the inverse distance weighted scheme in Eq. (4.1) does not guarantee a diffeomorphic global transformation field to preserve the topology.

4.2 LARM: Locally Affine Registration Method

In this section, we elaborate on a new locally affine registration method called LARM, which has two advantages:

- LARM adopts an efficient regularisation scheme to achieve a diffeomorphic transformation result.
- LARM optimises each affine transformation competitively within a global cost function to keep the global intensity class linkage.

4.2.1 Diffeomorphic transformation

Let $\{V_i\}$ be the set of pre-defined local regions which have a minimal distance between each other; let $\{G_i\}$ be the set of the assigned local affine transformations. To achieve a global transformation T from $\{G_i\}$, an interpolation method, referred to as *direct fusion*, based on the distance weighted interpolation (Shepard, 1968; Little et al., 1997) is used:

$$T(x) = \begin{cases} G_i(x), & x \in V_i, i = 1 \dots n \\ \sum_{i=1}^{n} w_i(x) G_i(x_i), & x \notin \bigcup_{i=1}^{n} V_i \end{cases}, \tag{4.4}$$

where $w_i(x)$ is a normalised weighting factor related to the distance $d_i(x)$ between point x and region V_i:

$$w_i(x) = \frac{1/(d_i(x))^e}{\sum_{i=1}^{n} 1/(d_i(x))^e}, \tag{4.5}$$

where $d_i(x)$ is computed from the closest distance between x and a point in volume V_i. In this transformation model, a global affine transformation can also be assigned to the boundary of the region of interest and e is set to 2 for computational efficiency.

However, two reasons can cause non-diffeomorphism by this direct fusion.

- Firstly, the local regions can overlap each other after the individual transformations. To guarantee non-overlapping, a correction of the local regions is required during the registration:

$$\begin{aligned} V_i &= G_i^{-1}\big(G_i(V_i) - \oplus_L(R_{ij})\big) \\ &= V_i - G_i^{-1}\big(\oplus_L(R_{ij})\big) \end{aligned} \quad , \tag{4.6}$$

  where, $R_{ij} = \bigcup_{i \neq j}(G_j(V_j))$ is the volume of other local regions that V_i should not overlap after transformations. Operation $\oplus_L$ is a morphological dilation with length L, L=10 mm in our implementation for the cardiac MR application to leave enough space for the interpolation. It should be noted that when $\{G_i\}$ are all identity transformations such as at the beginning of registration, the correction using Eq. (4.6) also guarantees that there is at least L distance between each local region. Figure 4.2 demonstrates the procedure of overlap correction.

- Secondly, when the displacements of the local transformation are large, the interpolation of a global transformation using Eq. (4.4), also referred to as *direct fusion*, may produce folding (Arsigny et al., 2005). A regularisation step monitoring the Jacobian J_T of the deformation field is then needed:

$$J_T = \sum_{i=1}^{n} \frac{\partial w_i}{\partial x} \cdot G_i + \sum_{i=1}^{n} w_i \cdot \frac{\partial G_i}{\partial x} = \nabla \mathbf{W} \cdot \mathbf{G}^{\mathrm{T}} + \nabla \mathbf{G} \cdot \mathbf{W}^{\mathrm{T}} \,, \tag{4.7}$$

  where $\mathbf{W} = \{w_1, \cdots, w_n\}$ and $\mathbf{G} = \{G_1, \cdots, G_n\}$. If the determinant of the Jacobian, $\det(J_T)$, drops below a threshold (e.g. $\det(J_T) < 0.5$), a new image-pair is then generated from the original one using the current deformation field and the locally affine transformation model is reset to the identity transformation for a new optimisation process. Therefore, the resultant transformation of the registration is the concatenation of a series of transformations:

$$T = T_m \circ T_{m-1} \circ \ldots \circ T_1 \,. \tag{4.8}$$

  Since all the $\{T_j \mid j = 1 \ldots m\}$ are diffeomorphic, the composed T preserves this property as well.

4.2.2 Global intensity class linkage

To optimise the local affine transformations, traditional methods register local regions individually and hence optimise the affine transformations independently (Little et al., 1997; Zhuang et al., 2008a; Commowick et al., 2008). This independent optimisation however can decrease the registration robustness due to the loss of global intensity linkage between local regions. Therefore, we propose to search for the optimal affine transformations within a global scheme, where each of them is optimised competitively. To achieve this, a global cost function such

For each optimisation step
  Global transformation, $F(x) = T \circ G$, and $T = T_m \circ T_{m-1} \circ \ldots \circ T_1$
  Optimise global affine transformation G
  Optimise local affine transformation G_i of T_m, compute derivative using Eq. (4.11)
  Regularisation step:
    For each region V_i in $\{V_i\}$
      Overlap correction using Eq. (4.6)
      If V_i needs correction and is corrected, then
        If volume size of V_i is zero, then END registration
        else re-compute the distance transformation of V_i for Eq. (4.5)
    End of each region V_i in $\{V_i\}$
    If MIN$(\det(J_{T_m})) < 0.5$, then
      new a T_{m+1}, $T = T_{m+1} \circ T$, and $m = m + 1$
  End of Regularisation
End of Optimisation

Figure 4.3: Pseudo-code for implementing the new locally affine registration method, LARM.

as MI is used and the driving forces are based on the gradient of the MI with respect to the transformation parameters. The main advantage is that the computation of the cost function and the driving forces are based on the whole image volume, and hence the global intensity class linkage is preserved.

The derivative of MI can be obtained by differentiating the entropies, which can be computed from the derivative of the probability distribution function (PDF). Let (l, k) be a joint histogram bin from the target image I_t and source image I_s, ω be the kernel density estimation function, the derivative of joint PDF $p(l, k) = \sum_x \omega(I_t(x)) \cdot \omega(I_s(T(x)))$ with respect to a transformation parameter θ_i of G_i is:

$$\begin{aligned} \partial p(l,k)/\partial\theta_i &= \textstyle\sum_x \omega(I_t(x)) \cdot (\partial\omega(I_s(T(x)))/\partial\theta_i) \\ &= \textstyle\sum_x \omega(I_t)\nabla\omega(\nabla I_s(y)|_{y=T(x)} \cdot \partial G_i(x)/\partial\theta_i) w_i(x) \quad . \\ &= \textstyle\sum_x W(x) \end{aligned} \tag{4.9}$$

Given a point x which has a small value for $d_j(x)$, such that $d_j(x)/d_i(x) << 1$, then $w_i(x)$ tends to zero, making $W(x)$ tend to zero.

Given a volume Ω_i and the complementary volume $\bar{\Omega}_i$, we then rewrite the joint PDF as $p(l, k) = P_{\Omega_i} + P_{\bar{\Omega}_i}$, where $P_{\Omega_i} = \sum_{x\in\Omega_i} \omega(I_t)\omega(I_s)$ and $P_{\bar{\Omega}_i} = \sum_{x\in\bar{\Omega}_i} \omega(I_t)\omega(I_s)$. Therefore, the driving force related to the derivative of the entropy becomes:

$$\mathcal{F}_H(\theta_i) := \frac{\partial H}{\partial\theta_i} = -\sum_{l,k} (1 + \log p(l,k)) \left(\frac{\partial P_{\Omega_i}}{\partial\theta_i} + \frac{\partial P_{\bar{\Omega}_i}}{\partial\theta_i} \right) = \mathcal{F}_H(\theta_i)|_{\Omega_i} + \mathcal{F}_H(\theta_i)|_{\bar{\Omega}_i} \; . \tag{4.10}$$

where $\mathcal{F}_H(\theta_i)|_{\Omega_i} = -\sum_{l,k}(1+\log p(l,k))\frac{\partial P_{\Omega_i}}{\partial\theta_i}$ and $\mathcal{F}_H(\theta_i)|_{\bar{\Omega}_i} = -\sum_{l,k}(1+\log p(l,k))\frac{\partial P_{\bar{\Omega}_i}}{\partial\theta_i}$. Let U_i be a superset volume of V_i such that when $x \in \bar{U}_i$, one of the follow two conditions can be met. One condition is $w_i(x)$ tends to zero and the other is that x is within the background, not of interest for the heart registration or segmentation process. Let $\Omega_i = U_i$, then $\mathcal{F}_H(\theta_i)|_{\bar{\Omega}_i}$ is summarised from the contribution of either relatively negligible small forces or less relevant

forces coming from the background. Therefore, the driving force related to the derivative is computed as:

$$\mathcal{F}_H(\theta_i) := \mathcal{F}_H(\theta_i)|_{\Omega_i} = -\sum_{l,k} \frac{\partial P_{\Omega_i}}{\partial \theta_i}(1 + \log p(l,k)) \; . \tag{4.11}$$

Since $(1 + \log(p(l,k)))$, which preserves the global intensity linkage, is constant for all transformation parameters, the computation complexity of Eq. (4.11) is only $O(|U_i \cap V|)$, which compares with $O(|V|)$ for Eq. (4.10), where V is the volume of the target image. Eq. (4.11) not only accelerates the run-time, but also blocks driving forces coming from the background such as the liver and abdomen, where the shape and intensity across subjects vary more significantly.

Figure 4.3 outlines the framework of the proposed LARM and describes the pseudo-code of our implementation. A global affine transformation is composed with the concatenated T for the global transformation. The regularisation step includes the overlap correction and monitoring Jacobian for T concatenation.

4.3 DRAW: Dynamic Resampling And distance Weighted interpolation

In this section we introduce a generic method for inverting dense displacement fields using Dynamic Resampling And distance Weighted interpolation (DRAW).

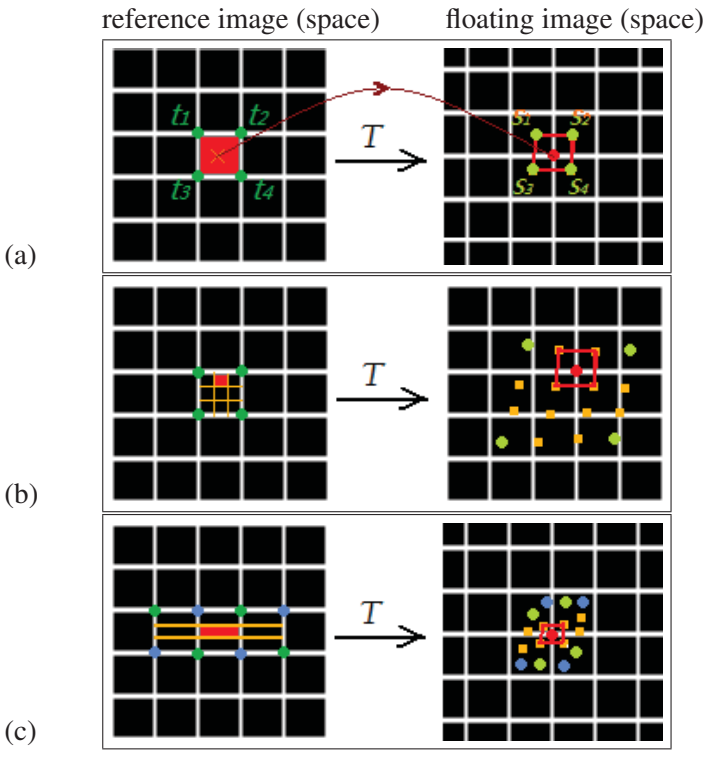

Figure 4.4: DRAW using inverse distance interpolation from forwardly transformed scatter points (a); resampling more points within a pixel when the transformation field causes expansion (b); resampling more points in other directions when the transformation field causes anisotropic contraction (c) in one direction.

Let T be a diffeomorphic transformation, mapping a coordinate t in reference image space to a coordinate s in float image space, i.e. $s = T(t)$. To compute the inverse transformation

T^{-1} of T, we extend the *scatter-point and distance-weighted* scheme (Crum et al., 2007) to directly interpolate $t = T^{-1}(s)$ for s. Given $\{s_i\}$, a set of close scatter points of s as the light green points in Figure 4.4 (a), the interpolated inverse transformation $T_I(s)$ is computed as:

$$T_I(s) = s + \sum_i w(s_i) \cdot (t_i - s_i) \,, \tag{4.12}$$

where $\{s_i\}$ are points transformed by T from the point set $\{t_i\}$ in the reference image space and $w(s_i)$ is the normalised weighting function computed from the distance between s_i and s (refer to Eq. (4.5) for detail). It is assumed that an accurate estimation can be achieved given the following two conditions stand (for simplicity word *pixel* is used for both the 2D and 3D image element):

- Condition 1: One closest point s_i can be found from each octant (3D) or quadrant (2D) of s within one pixel dimension.
- Condition 2: The $\{s_i\}$ should be transformed from the scatter points $\{t_i\}$ which are all within the volume of one pixel size.

As shown in Figure 4.4 (a), the inverse transformation of point s, the red point in the floating image, can be interpolated from its neighbouring green points $\{s_i\}$ which are transformed from the green points $\{t_i\}$ in the target image. In a diffeomorphic transformation field T, the ground truth $T^{-1}(s)$ and the interpolated inverse transformation $T_I(s)$ should both be within the volume enclosed by $\{t_i\}$, i.e. the red area in Figure 4.4 (a). We assume this because the algorithm is designed to invert dense displacement fields, and the deformation within the pixel in the target image may not have detailed definition and can be simply estimated as an affine transformation. Therefore, the interpolation error $|T_I(s) - T^{-1}(s)|$ should not be larger than the diameter of the enclosed volume.

Two situations make it difficult to meet these two conditions:

- Firstly, if T represents deformational expansion at $\{t_i\}$, then the scatter points $\{s_i\}$ can be too distant from s (shown in Figure 4.4 (b)): the pixel-size volume V_t enclosed by the vertex points, the dark green points $\{t_i\}$, are sparsely transformed into a bigger area V_s in the floating image space, where a grid point s lies. In this case, one may not be able to find any of the sparse points required in Condition 1 for the interpolation of $T_I(s)$. To obtain this point set, we propose to resample more points within V_t and transform them to the floating image space, as shown in the Figure 4.4 (b). The number of resampled points, $S_{\hat{e}}$, is estimated as:

  $$S_{\hat{e}} = \max(1, |J : \hat{e}|) \,, \tag{4.13}$$

  where, J is the Jacobian matrix of T and $|J : \hat{e}| = |\hat{e} \times J \times \hat{e}|$. The symbol $|J : \hat{e}|$ represents the volume change in the direction of $\hat{e}$, where $\hat{e}$ is the standard basis of the Euclidean space $\Re^{\mathrm{d}}$.

- Secondly, if T represents anisotropic contraction at $\{t_i\}$, then the scatter points $\{t_i\}$ may not be within one pixel dimension in the reference image space, as shown in Figure 4.4

(c): if $|J : \hat{e}_j|/|J : \hat{e}_k| > 1$, the closest scatter points $\{s_i\}$ of s are mapped from their corresponding points $\{t_i\}$ which are the dark green dots in Figure 4.4 (c). The enclosed volume V_t by point set $\{t_i\}$ is not within one pixel dimension and hence the interpolation using Eq. (4.12) violates Condition 2. To improve this situation, we propose to resample more points in the other orthogonal directions inside V_t to provide a closer scatter point set $\{s_i\}$ and a corresponding point set $\{t_i\}$ from one pixel dimension:

$$S_{\hat{e}_j} = \prod_k \max(1, |J : \hat{e}_j|/|J : \hat{e}_k|) \, , j, k = 1, 2, \ldots, \mathrm{d} \, . \tag{4.14}$$

Combining Eq. (4.13) and 4.14, we get the number of resample points needed from the volume of a pixel:

$$S_{\hat{e}_j} = \max(1, |J : \hat{e}_j|) \cdot \prod_k \max(1, |J : \hat{e}_j|/|J : \hat{e}_k|) \, , j, k = 1, 2, \ldots, \mathrm{d} \, . \tag{4.15}$$

4.4 Phantom data experiments

4.4.1 Experiment-1: DRAW for inverting transformations

Data and experimental setup

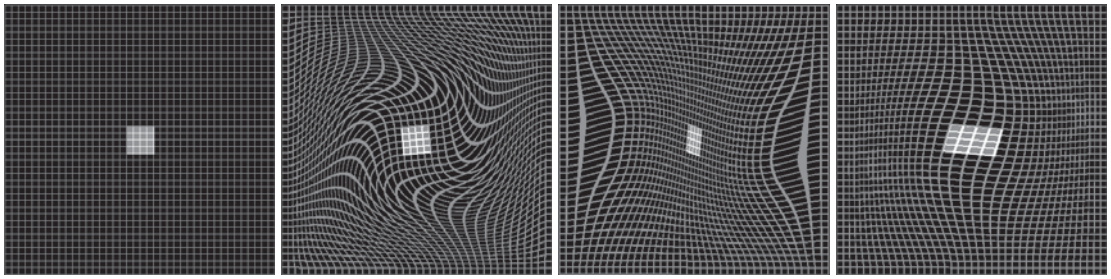

(a) (b) (c) (d)

Figure 4.5: Phantom data used to generate dense displacement. (a) shows a rigid box in a fixed field; (b) shows the deformation field when the rigid box rotates 85 degrees; (c) shows the deformation field when the rigid box scales down to half size in one direction and rotates 10 degrees; (d) shows the deformation field when the rigid box scales up to twice the original size in one direction and rotates 10 degrees.

In this experiment, three groups of transformations are generated and then inverted by DRAW. The first group is a set of more generic dense displacements used to assess the overall performance of DRAW. The last two groups are specifically designed affine transformations, anisotropic scaling-down and scaling-up, which are used to evaluate the performance of DRAW in scaling situations.

The image used to generate the transformations is shown in Figure 4.5 (a) and is of resolution $401 \times 401 \times 3$ and voxel size $0.5 \times 0.5 \times 0.5$ mm. The assumed reference and floating images in the procedure of inverting transformations have the same resolution and voxel size.

The first group of transformations are generated by rotating the central rigid box and fixing the boundaries of the reference image. By using a set of rotations from 5 to 85 degrees, seventeen dense displacements are created using Eq. (4.4) to interpolate them as locally affine

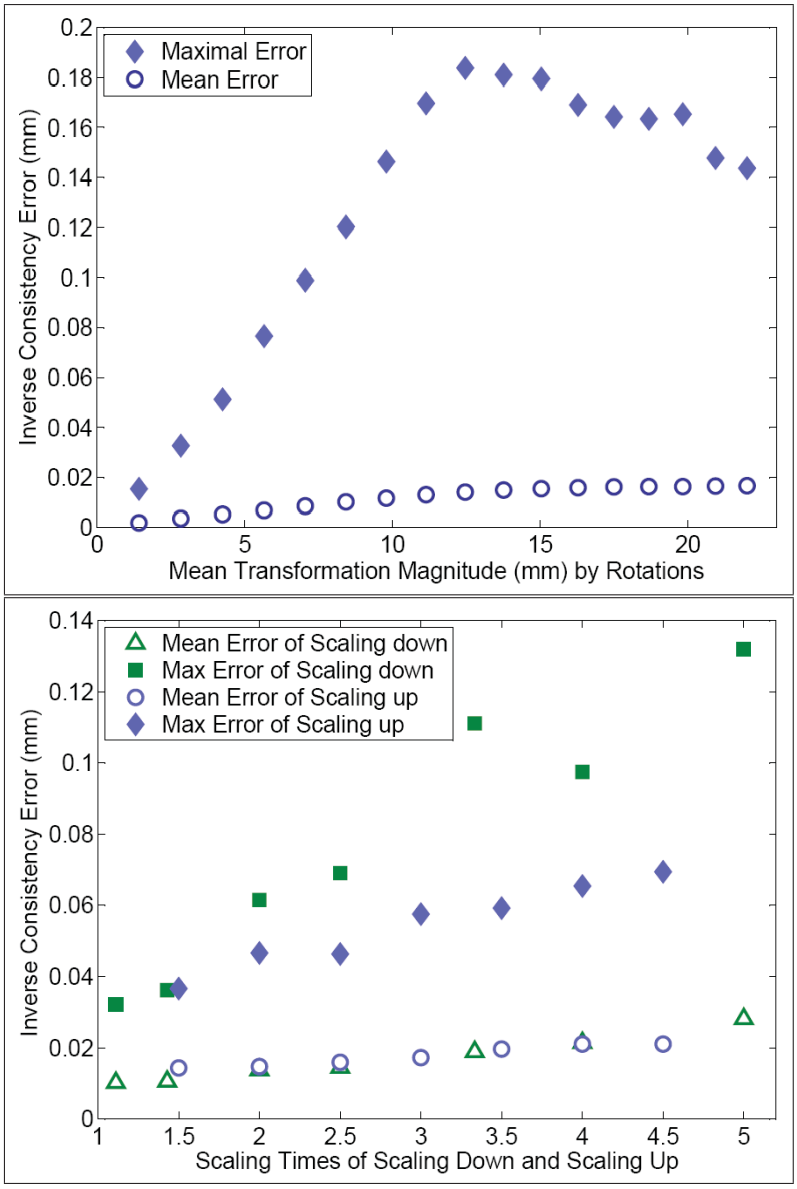

Figure 4.6: The scales of the inverse-consistency error with applied rotation (a) and scaling (b).

transformation fields. Each displacement field includes a rigid rotation in the centre and non-linear expansions and contractions elsewhere. Figure 4.5 (b) shows the displacement of using a rotation of 85 degrees.

The second group is generated by scaling down the rigid box in one direction and rotating it 10 degrees. This group has 7 displacement fields using the scaling values of 0.9, 0.7, 0.5, 0.4, 0.3, 0.25, and 0.2. The mean magnitude ranges from 3 mm to 8 mm. Figure 4.5 (c) shows the displacement of using a scaling value of 0.5.

The third group is generated by scaling up the rigid box in the x-axis direction and also has 7 displacement fields using the scaling values of 1.5, 2.0, 2.5, 3.0, 3.5, 4.0, and 4.5. The mean magnitude ranges from 6 mm to 36 mm. Figure 4.5 (d) shows the displacement of using a scaling value of 2.

Results

The error is computed using the inverse-consistency (IC), $|T(T_I(s)) - s|$, within the floating image space. Both the mean and maximal values are recorded for each case. Figure 4.6 (a) presents the IC errors of inverting the first group of transformations. The errors are plotted against the mean of transformation magnitude of each displacement field. Figure 4.6 (b) gives the IC errors of inverting the second and third groups of transformations. In the latter two groups, only the points within the central rigid box area are taken into account when computing the IC error in order to focus on the error caused by anisotropic scaling. The errors are plotted against the scaling magnitude. It should be noted that the magnitude of a down-scaling value is computed from its inverse for example the magnitude of 0.2 is 5 (1/0.2).

Conclusion

The maximal errors of all three groups are less than the voxel size, which is however not the case for the currently reported methods surveyed in Crum et al. (2007). In addition, the maximal IC errors in the first group reach the largest value at a 45-50 degrees rotation, instead of 85 degree which has the largest magnitude of displacement, and the mean errors tend to converge from the position of 45-50 degrees. This indicates that the IC error does not necessarily increase according to the increased magnitude of displacements. Finally, in the last two groups, the maximal IC errors by up scaling transformations are more stable than by down scaling transformations, even though the transformation magnitudes of down scaling are much smaller.

4.4.2 Experiment-2: LARM vs region-based registration

(a) (b) (c) (d) (e) (f)

Figure 4.7: Floating image (a), subimages (within red line) of the left bar $\mathcal{M}_L$ (b) and the right bar $\mathcal{M}_R$ (c); reference image (d) as registration task one, reference image (e) as registration task two, reference image (f) as registration task three.

Data and experimental setup

The data used in this experiment are shown in Figure 4.7. The floating image and three reference images all have two local regions, referred to as left and right *bars*. The registration tasks are simulated to multi-modality since the intensity distribution of the floating and reference images are different.

The purpose of this experiment is to demonstrate the advantage of keeping global intensity class linkage in multi-modality registration. Both Rreg and LARM are employed to register these three tasks and assess their performance based on the registration results. Two locally affine transformations are assigned to the left and right bars. For Rreg, the subimages $\mathcal{M}_L$ and $\mathcal{M}_R$ are defined as the rectangular areas of the bars with a morphological dilation of 20 mm, as shown in Figure 4.7 (b) and (c). The overlap correction is also used for Rreg in the fusion of the locally affine transformations. For LARM, the area (volume in 2D) $\{U_i\}$ used in Eq. (4.11)

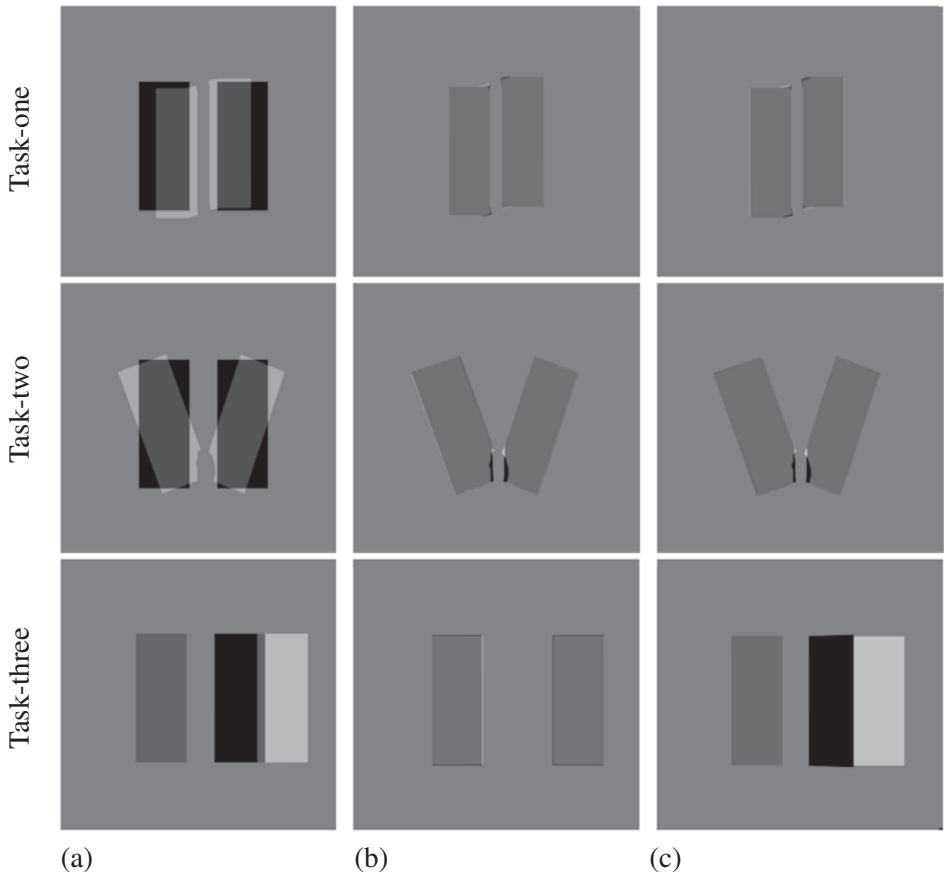

Figure 4.8: Overlapping of the reference and floating images of the three registration tasks: (a) before registration; (b) after registration using LARM; (c) after using the region-based registration (Rreg).

is also defined to the same size as that of $\mathcal{M}_L$ and $\mathcal{M}_R$.

The registrations use NMI similarity measure and gradient ascent optimisation scheme.

Results

Figure 4.8 shows the registration results of the three tasks using LARM (b) and Rreg (c). Both have achieved success in task one and two, but Rreg failed in task three while LARM succeeded attributed to the advantage of maintaining global intensity class linkage. Figure 4.9 gives the inverse transformations of the three diffeomorphic fields from the registration results of LARM.

Conclusion

This experiment has demonstrated the advantage of LARM over Rreg in registering images with different intensity distribution. LARM has achieved a success in task three thanks to the global intensity class linkage, which helped register the right bar when its position is initially far away in the reference and floating images. Furthermore, LARM demonstrated the ability of achieving diffeomorphic registration.

4.5 Cardiac MR data experiments

This section describes the application of LARM and Rreg to cardiac MR data. The registration in these experiments uses NMI similarity measure and gradient ascent optimisation scheme.

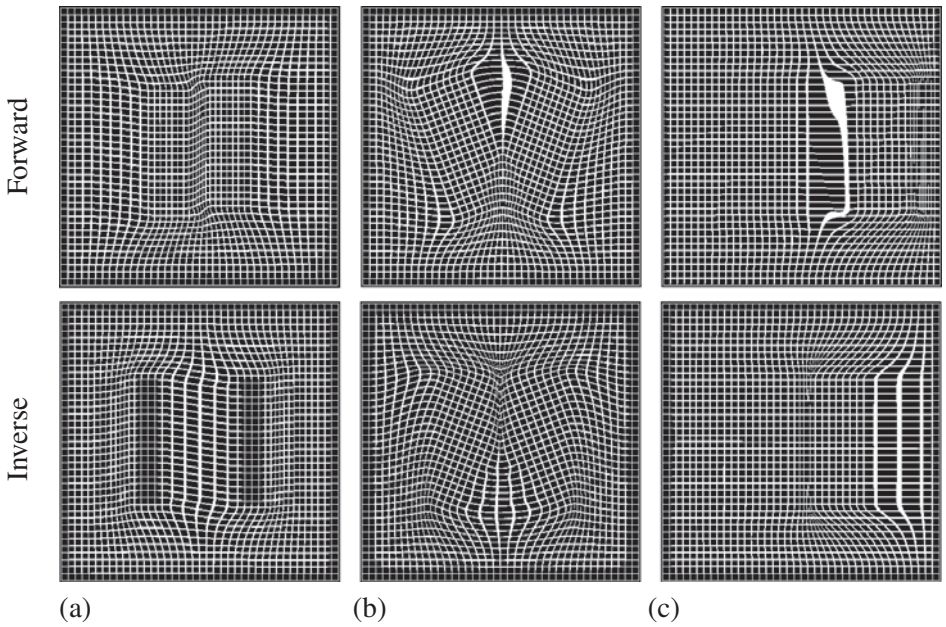

Figure 4.9: Deformation meshes of the registration results of LARM: (a) of task one; (b) of task two; (c) of task three. Upper row is the forward transformations and lower row is the inverse transformations using DRAW.

4.5.1 MR data used in this thesis

This PhD work mainly focuses on volumetric, isotropic cardiac magnetic resonance (MR) images with whole heart coverage using a novel MR imaging (MRI) sequence developed at the Imaging Science Division, King's College London (Uribe et al., 2007). This sequence is the balanced steady state free precession (b-SSFP) for whole heart imaging. The imaging has either one (ED phase) or two (dual phases) trigger delay (s), with a preview T2 preparation and fat saturation pulse. A 3D triggering b-SSFP turbo field echo (TFE) sequence (with arrhythmia rejection) has been modified in order to enable the acquisition of selected cardiac phase(s) at a user defined time. The sequence has been implemented on 1.5T clinical scanners (Philips Medical System, Best, The Netherlands), shown in Figure 2.3 (a), equipped with 32 independent receive channels, shown in Figure 2.3 (b), at Guy's Hospital and St. Thomas' Hospital, London. For both cardiac phases, a fat saturation and T2-prep pulses (14) are used to null fat and to increase the contrast between blood and cardiac muscle. A free breathing scan is realised by enabling one navigator beam before data acquisition and the trigger delays of the end-diastolic phase is selected manually with a preview T2 preparation and FAT saturation pulse. The gating window for the free-breathing scan is controlled to be around 6 mm in volunteers given they have received a breath-with-regular-pattern training. However, this is not guaranteed for the patient data acquisitions and the gating window is normally set to larger value in order to reduce the acquisition time. It should be noted that a wider gating window means less acquisition time but more pronounced artefacts. Table 4.1 gives the parameters of this sequence.

All the cardiac MR data used in this doctoral work were acquired at Guy's Hospital and St. Thomas' Hospital, London.

Rationale of using the sequence The use of this 3D SSFP sequence in cardiac MRI is be-

Table 4.1: The parameters of the 3D whole heart MRI sequence.

Field of view	$\sim 280 \times 240 \times 140$ mm
Acquired resolution	$\sim 2 \times 2 \times 2$ mm
Reconstructed resolution	$\sim 1 \times 1 \times 1$ mm
No. of slices	110 - 180
TR/ TE	~ 3.8 ms/ ~ 1.9 ms
TFE factor	15 - 20
Sense	2 anterior posterior 1-1.5 right left
Flip angle	~ 60 degrees
No. of phases	1 (ED phase) or 2 (dual phases)
Trigger modality	Trigger

coming routine clinical practice and is used increasingly in clinical studies, particularly where it is important to get accurate information about the geometry of the cardiac chambers. The advantage of using this sequence is that the acquired images are isotropic and of high resolution. The interpolation of these images can more accurately interpret the geometry of the heart, which compares advantageously with the data from the standard multi-slice or breath-hold multi-chunk MRI sequences. The multi-slice cine MRI is widely used in routine clinical practice. However, it provides limited coverage of view to the ventricles and is used for assessment of regional and global ventricular function. There are many works that describe the segmentation of these multiple 2D cine SSFP images and their focus remains on the assessment of ventricular function rather than cardiac geometry.

This 3D SSFP sequence has been compared to the state-of-the-art multi-slice sequence by Uribe et al. (2008). Comparable results have been found for the quantification of cardiac volumes and functions. The correlation values were shown to be greater than 0.95 and no significant difference was recognised for stroke, end-systolic, or diastolic volumes in either of the ventricles (Uribe et al., 2008).

4.5.2 Experiment-3: Ventricle segmentation using Rreg

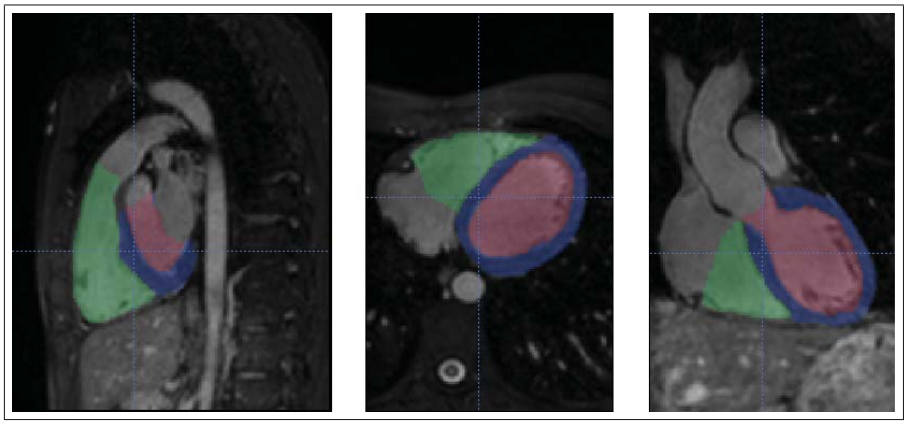

Figure 4.10: Atlas image and the ventricle segmentation labels superimposed on the MR image.

Data and experimental setup

In this experiment, ventricle segmentation is achieved by registering an atlas image to unseen images. Two registration schemes are used and their results are compared:

Table 4.2: Segmentation accuracy of Rreg+Fluid using surface distance measures. This table also gives the percentages of error scales: 0-2 mm, 2-5 mm, and > 5 mm.

	(mm)	0-2	2-5	> 5	Mean	STD
Volunteers	left ventricle endocardium	94%	4%	2%	0.8 ± 0.2	0.9 ± 0.4
	right ventricle endocardium	92%	6%	2%	0.9 ± 0.1	0.9 ± 0.3
	left ventricle epicardium	80%	15%	5%	1.2 ± 0.2	1.2 ± 0.3
Patients	left ventricle endocardium	67%	22%	11%	1.8 ± 0.6	1.7 ± 0.9
	right ventricle endocardium	60%	23%	17%	2.2 ± 1.0	1.7 ± 0.8
	left ventricle epicardium	70%	11%	9%	1.6 ± 0.4	1.4 ± 0.3

- An affine registration for initialisation and a fluid registration for refinement (Affine+Fluid);
- An affine registration for localisation, then Rreg to further initialise the two ventricles, and finally a fluid registration for refinement (Rreg+Fluid).

The fluid registration is based on Crum et al. (2003, 2005) with a force mask applied to exclude the forces generated from the background (Zhuang et al., 2008a).

The atlas image comes from a cardiac MR image which was acquired from a healthy volunteer. The substructures, including the left ventricle blood cavity, right ventricle blood cavity, and the myocardium, have been manually delineated from the MR image. Figure 4.10 shows the corresponding segmentation labels superimposed on the MR image. Another eight MR images from four healthy volunteers and four Tetralogy of Fallot patients are tested as the unseen images. Each of them has a manual segmentation, regarded as gold standard.

The segmentation error is only assessed on the left ventricle endocardium, left ventricle epicardium, and right ventricle endocardium of the heart. Two types of measures are used to assess the accuracy of the segmentation results.

- Surface distance measures: The mean and standard deviation (STD) of the surface distance between the automatic segmentations and gold standard are computed.
- Volume measures: The volume difference, $\frac{|V_{gold}-V_{seg}|}{V_{gold}}$, and the volume overlap (Crum et al., 2006), $\frac{V_{gold}\cap V_{seg}}{V_{gold}\cup V_{seg}}$, between the segmented volumes V_{seg} and gold standard V_{gold} are computed.

Result

Figure 4.11 (a) displays the mean and STD of the surface distance measures. The mean surface distance by Rreg+Fluid is 1.0 ± 1.0 mm on the four volunteer data, and 1.6 ± 1.8 mm on the four patient data; the errors of the patient and volunteer data by Affine+Fluid are 1.3 ± 1.4 mm and 2.0 ± 2.0 mm, respectively. Figure 4.11 (b) plots the mean of volume difference and overlap volume measure: again Rreg+Fluid has a better result than Affine+Fluid. With an initialisation of the substructure, the Rreg+Fluid scheme performed better, though the improvement was not evidently very significant.

Finally, Table 4.2 gives the detailed error distribution of the segmentation result using Rreg+Fluid: the percentage of points whose distance is within 0 to 2 mm, 2 to 5 mm, and more

(a)

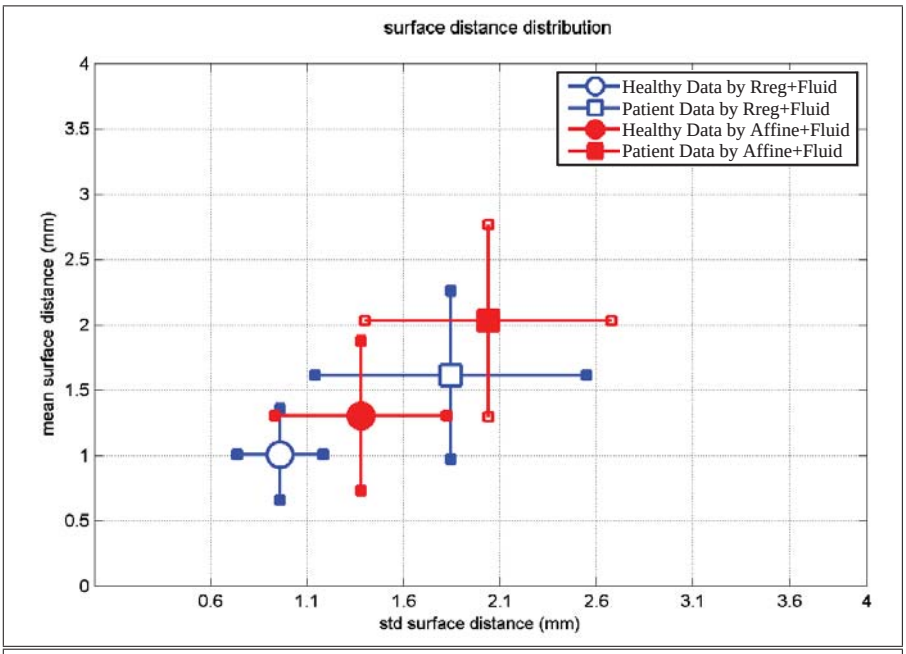

(b)

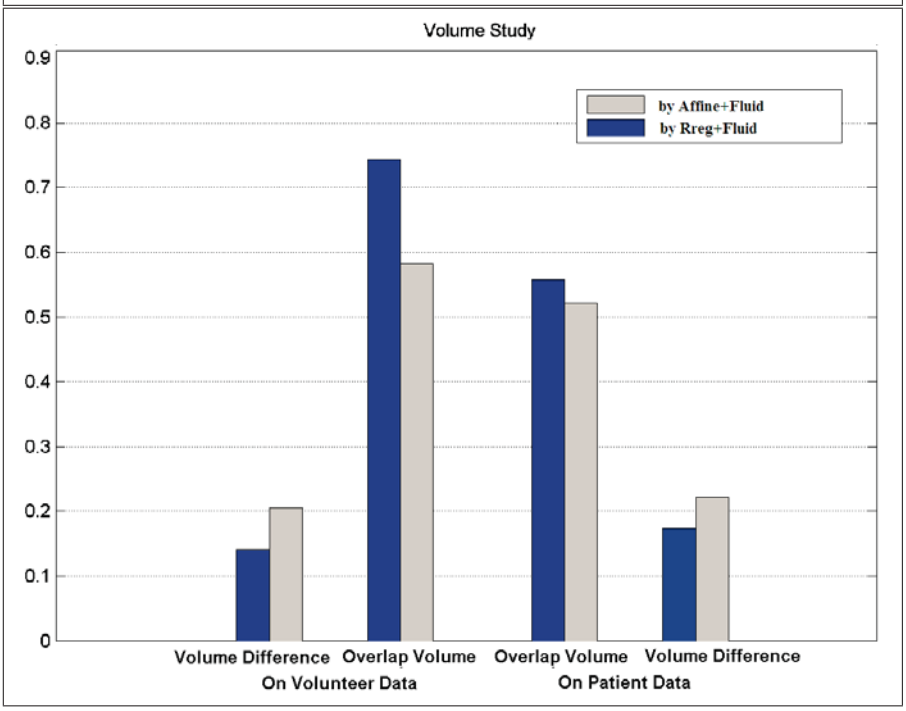

Figure 4.11: The mean surface distance distribution and standard deviation of the surface distance from healthy volunteer data and patient data (a); and the average volume difference and volume overlap of them (b). This figure shows the difference between the segmentation results by using Affine+Fluid and Rreg+Fluid.

than 5 mm. The mean and STD values of the surface distance of each local region are also presented in Table 4.2. The results indicated that the segmentation of patient data was more difficult than that of healthy volunteer data. Several facts contribute to this difficulty, including the lower image quality, the larger variations of the heart shape, and the larger inter-observer variations of the definition of the indistinct boundaries in the gold standard segmentation.

Notice that we group the errors using the thresholds of 2 and 5 mm mainly based on the following three observations: Firstly, the acquisition resolution of the MR data is $2 \times 2 \times 2$ *mm; secondly, most of the maximal point-to-surface distance errors between the manual segmentation and gold standard segmentation from cardiac MR slices are between 1 to 3 mm (Hautvast et al., 2006); finally, the mean point-to-surface distance in the connection areas is between 4 and 6 mm which is shown in Figure 6.7 in Section 6.4.4. The first two observations contribute to the selection of threshold 2 mm, whilst the last one contributes to the selection of 5 mm. This error grouping strategy will be used in other experiments throughout the remainder of the thesis.*

Conclusion

This experiment demonstrated the advantage of using a locally affine transformation model to further initialise the substructures of an object. The fluid registration benefitted from the initialisation of Rreg. Since it did not show a statistical significance of improvement, in the next experiment we will employ more data to compare the performance using different initialisation techniques.

4.5.3 Experiment-4: Initialisation in whole heart segmentation

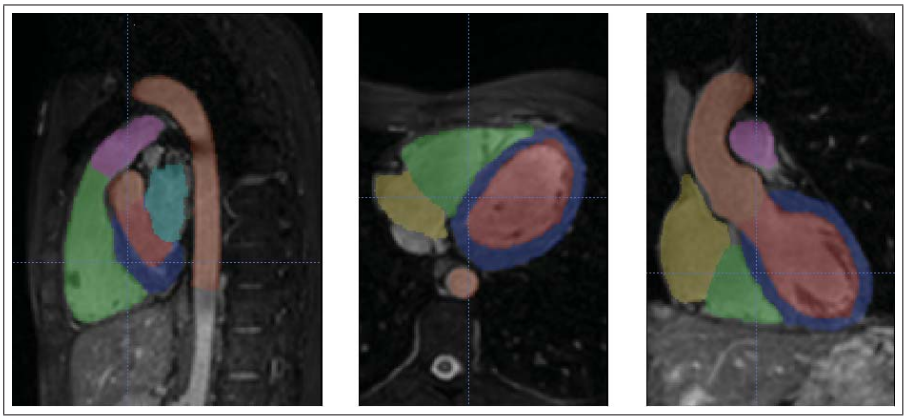

Figure 4.12: Atlas image and the segmentation labels of anatomical substructures superimposing onto it.

Data and experimental setup

The purpose of this experiment is to demonstrate the difference of performance of the three initialisation methods that can be used in a registration-based whole heart segmentation framework:

- A global affine registration (Affine).
- Rreg after an affine registration (Rreg).

- LARM after an affine registration (LARM).

The atlas image is the same as that used in Experiment-3, but using 7 substructures to define the local affine transformations: the left ventricle, right ventricle, left atrium, right atrium, pulmonary artery, ascending aorta, and descending aorta, as shown in Figure 4.12. Another 18 data are used as unseen images to register to the atlas image. These images have been manually delineated of the endocardium of the four chambers and the epicardium of the left ventricle. The accuracy of registration is assessed by the surface distance between each of them after the registration.

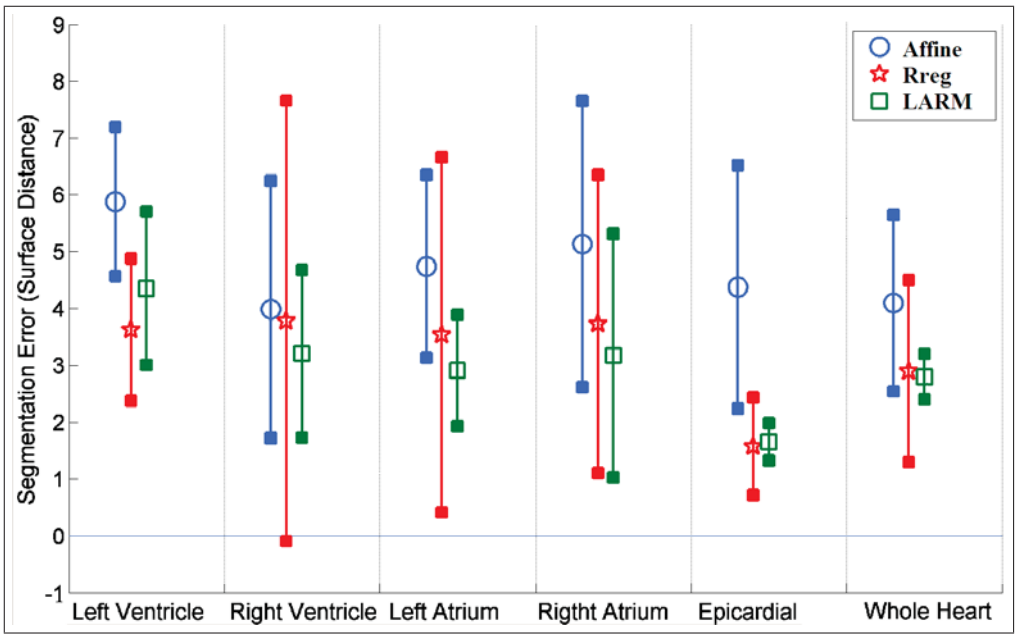

Figure 4.13: The registration accuracy of the three initialisation methods.

Result

Figure 4.13 plots the registration accuracy for each local region and all the surfaces as one measure, referred to as *Whole Heart*. The mean errors of Rreg and LARM were better than that of Affine in all structures. Also the improvement was significant, as the paired t-test p-values of the *Whole Heart* errors were both $P_{Affine,Rreg} < 0.001$ and $P_{Affine,LARM} < 0.001$. This was the courtesy of using the prior information of the local substructures for the initialisation. The mean accuracy of Rreg was shown to be no worse than that of LARM and the paired t-test p-value of the *Whole Heart* errors was $P_{LARM,Rreg} = 0.90$. In the case of the left ventricle, Rreg actually performed better. The reason is that the left ventricle region has a large volume and the contrast between the blood pool, myocardium, and background is good in this area. However, from the *standard error of the mean*, the standard deviation of the mean values of all cases, which indicates the variance of the mean and the robustness of the registration, LARM demonstrated the best result and Rreg did not always outperform Affine. For example, in the left atrium, Rreg had a large standard error of the mean due to some *failure* cases. One case is defined as a failure when the error of the registration result is worse than the error before the registration. The reason that Rreg performed less consistently in the left atrium was that the left atrium had relatively smaller volume size and could be poorly initialised solely using a global

affine registration. Without the global intensity information, Rreg was more likely to step into a local optimum.

Conclusion

This experiment demonstrated that locally affine registration can improve the initialisation of local regions, confirming the conclusion from Experiment-3. In addition, LARM is a better choice than Rreg because it provides better robustness. In the next experiment, we will demonstrate the advantage of a better initialisation in a whole heart segmentation framework.

4.5.4 Experiment-5: Whole heart segmentation using LARM

Data and experimental setup

The purpose of this experiment is to compare the whole heart segmentation result using the initialisation of LARM and the traditional initialisation of a global affine registration. The refinement is again the force-mask fluid registration (Zhuang et al., 2008b). The atlas image and unseen data are these used in Experiment-4. The two registration schemes to be compared are:

- An affine registration for initialisation and a force-mask fluid registration for refinement (Affine+Fluid).
- An affine registration for localisation, then LARM to further initialise the substructures, and finally a force-mask fluid registration for refinement (LARM+Fluid).

Result

Table 4.3: Segmentation accuracy after each registration step and the p-values of the paired t-test between the errors of the two registration schemes: Affine+Fluid and LARM+FLuid.

Unit (mm)	Affine	LARM	Affine+Fluid	LARM+Fluid	P-value
Left Ventricle	5.9 ± 1.3	4.4 ± 1.4	3.3 ± 2.0	2.4 ± 1.1	0.010
Right Ventricle	4.0 ± 2.3	3.2 ± 1.5	3.3 ± 3.7	2.6 ± 1.5	0.217
Left Atrium	4.7 ± 1.6	2.9 ± 1.0	3.0 ± 2.0	$1.9 \pm .78$	0.043
Right Atrium	5.1 ± 2.5	3.2 ± 2.1	4.3 ± 4.7	2.4 ± 2.7	0.111
Epicardium	4.4 ± 2.1	$1.7 \pm .32$	2.3 ± 1.7	$1.3 \pm .21$	0.023
Whole Heart	4.1 ± 1.6	$2.8 \pm .40$	2.7 ± 1.7	$1.8 \pm .42$	0.026

Table 4.3 presents the accuracy of each substructure after using the two initialisation methods and the two corresponding segmentation frameworks, and the p-values of the two tailed, paired t-test between the two groups of segmentation results. The fluid registration performed significantly differently after the initialisation of LARM: the mean *Whole Heart* segmentation error of LARM+Fluid (1.8 ± 0.42 mm) was more than twice the standard deviation smaller than that of Affine+Fluid (2.7 mm) and $P_{WholeHeart} = 0.026$. In particular the segmentation of the epicardium of the left ventricle, the mean error of Affine+Fluid (2.3 mm) was more than three times the standard deviation smaller from that of LARM+Fluid (1.3 ± 0.21 mm) and $P_{Epicardium} = 0.023$. However, the p-values of Right Ventricle (0.217) and Right Atrium (0.111) did not show evidence of significant difference between the two segmentation schemes, though the mean errors of LARM+Fluid were both smaller than those of Affine+Fluid.

It should be noted that the errors of each category are considered as normally distributed in the t-test. The assumption is based on the argument that this normal distribution is commonly accepted and the t-test is expected to be more accurate than using the Wilcoxon test which does not require the test groups to be normally distributed and may produce false negative. This assumption will be used through out the thesis when t-test is employed for the statistical difference test.

Conclusion

This experiment demonstrated the advantage of applying LARM to the whole heart segmentation framework. The initialisation of substructures contributed to a more accurate and robust performance from the following nonrigid registration and hence improved the segmentation performance. This confirms that the locally affine transformation model is a useful technique in the applications where a single global affine transformation cannot provide enough accuracy while a nonrigid registration would affect incorrectly the local topology.

4.6 Conclusion

In this chapter, we have investigated an alternative registration technique which globally deforms the image while locally still maintains the affinity/ rigidity of the substructures. The first method we studied is the region-based registration (Rreg), which does not maintain the global intensity class linkage, leading to reduced robustness of the registration. The locally affine registration method (LARM) is a new algorithm we contributed to this technique. It preserves the intensity class relationships between local regions and uses a regularisation procedure to maintain a global diffeomorphism.

At the same time, we introduced a new method to invert dense displacements using Dynamic Resampling And distance Weighted interpolation (DRAW). The dynamic resampling of DRAW can guarantee a sub-voxel maximal interpolation error and hence provide much more consistent performance against large displacement fields and scaling values.

Experiments have been designed to test the performance of the proposed algorithms. To validate the advantage of locally affine transformation model and LARM, we applied them to cardiac MR image segmentation and evaluated the accuracy using the distance between the segmented surfaces and manual delineated surfaces. We concluded from the results that the new techniques proposed in this chapter had significant positive impacts in the registration-based whole heart segmentation framework.

Chapter 5

Constrained Driving Forces in Nonrigid Registration

This chapter proposes a constrained nonrigid registration using free-form deformations (FFDs). Unlike many other methods employing penalty terms into the cost function, this new FFD registration constrains the driving forces using *a priori* knowledge from an atlas.

This chapter is organised as follows: Section 5.1 states the problems in the standard FFD registration. Section 5.2 then elaborates on a new algorithm which adaptively sets the status of control points in a FFD mesh. Section 5.3 employs two experiments, a phantom registration task and a cardiac MR image segmentation experiment, to compare the performance of the proposed method and the standard FFD registration. Finally, section 5.4 draws the conclusion.

5.1 FFD registration and problem statement

In the registration-based whole heart segmentation framework, nonrigid registration is used to refine the local details to achieve a high accuracy. This registration has two requirements:

- One is a diffeomorphic transformation to preserve the topology of the heart.
- The other is a robust algorithm to propagate the indistinct boundaries. For example, Figure 5.1 (d) shows an example of *epicardium leaking* where part of the epicardium is erroneously delineated to the adjacent liver tissue.

The nonrigid registration using FFDs, referred to as FFD registration, has been widely used in many applications since its introduction by Rueckert et al. (1999). This method employs one or a series of B-spline meshes to estimate the deformation field, mapping the reference image to the floating image (Rueckert et al., 1999). To achieve a diffeomorphic registration, Rueckert et al. (2006) extended the work of Choi and Lee (2000) by constraining the displacements of the control points in a FFD model within a fraction of the spacing of the FFD mesh. To model a large deformation field, a series of such constrained FFD transformation models are used and concatenated. The concatenation result of a set of diffeomorphic transformations is also diffeomorphic.

However, using the standard FFD registration in the registration-based segmentation framework (Rueckert et al., 2002) does not specially deal with problems in the indistinct regions. For example, Figure 5.1 shows a registration case between (a) and (c). In a standard FFD registration, all the control points including those located in the background and the indistinct

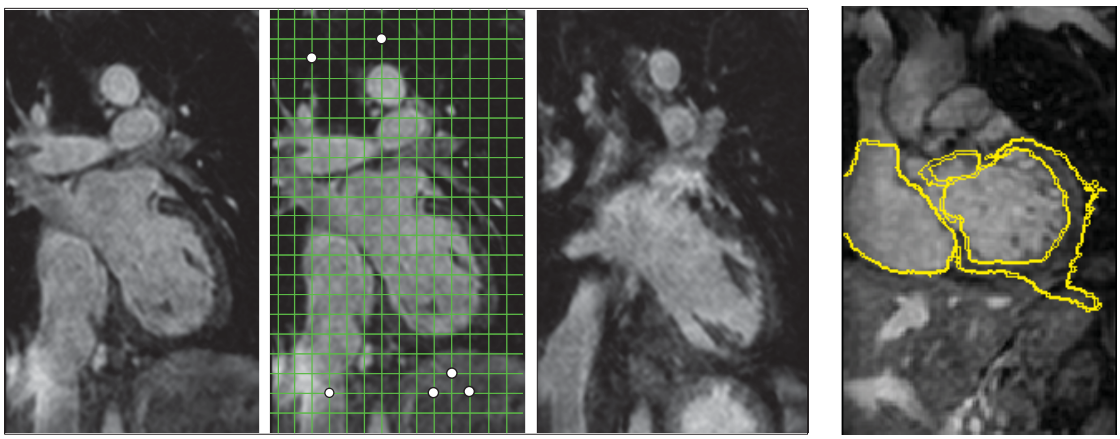

(a) (b) (c) (d)

Figure 5.1: (a): the reference MR image; (b): the FFD mesh on the reference space with unnecessary active control points (white dots); (c): the floating image. (d): an example showing the epicardium leaking in a segmentation using standard FFD registration for the segmentation refinement.

areas are optimised, shown in Figure 5.1 (c). As a result, the myocardium of the floating image could be registered to the liver of the reference image, because the intensity values of the myocardium and liver are similar in the reference image but not in the floating image. This is the main reason accounting for the epicardium leaking in the registration-based segmentation framework. Figure 5.1 (d) shows an example.

Schnabel et al. (2001) proposed a method to simulate Non-Uniform Rational B-splines (NURBS) by associating a status, *active* or *passive*, to each control point of the FFDs. Active control points were allowed to move, be optimised, during registration, while passive control points stayed fixed. The status of each control point was computed before the optimisation of each FFD level, using the *reference image measures* such as the local entropy or the *joint image pair measures* such as the gradient of the associated cost function (Schnabel et al., 2001). Furthermore, the status stayed constant during the optimisation process of each FFD level. This method, embedded into a multi-resolution registration scheme, improved the performance and significantly reduced the run-time compared to a standard FFD scheme (Schnabel et al., 2001). However, there are two potential challenges in terms of applying this framework to the refinement registration in the whole heart segmentation framework:

- In the context of cardiac MR segmentation, the adjacent tissues of the heart such as the lung and the liver, should be considered as background information. In other words, they should not affect the registration process. However, these areas will be taken into account by using the status setting proposed in (Schnabel et al., 2001), because they present relevant information for the status determination measures. For example, Figure 5.1 demonstrates a situation, where the control points located in the liver or papillary muscle (white dots) will also be considered as active. This not only increases the run-time but also induces misalignments in the areas with indistinct boundaries and generates erroneous outcomes such as the epicardium leaking in Figure 5.1 (d).

- If the status is pre-set and remains constant, some useful control points could be inac-

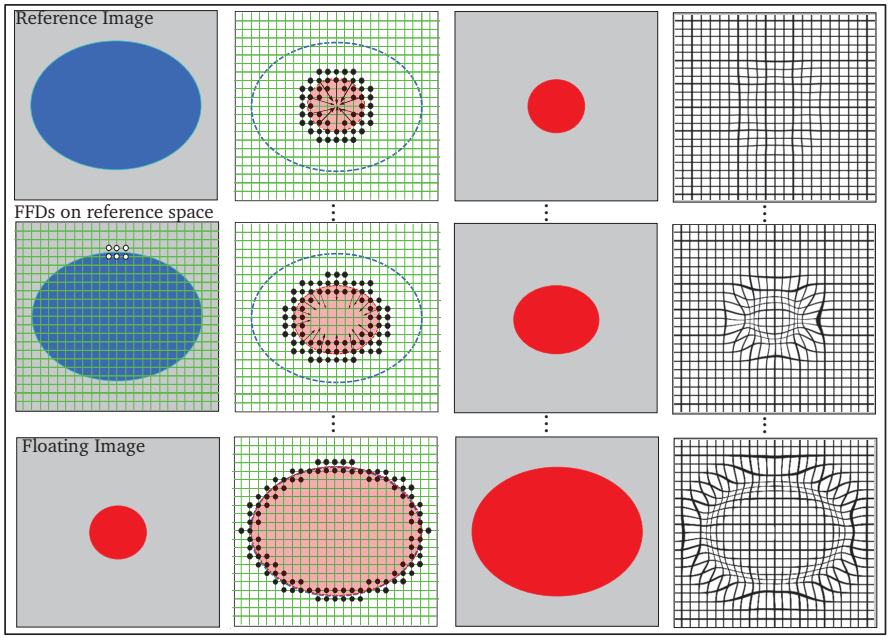

Figure 5.2: Registration of an ellipse, the reference image to a circle, the floating image using adaptive control point status FFDs. The white dots in (a) are special control points explained in the text. (b) shows the FFD meshes, the contour of the ellipse, and the contour of the inverse-transformed floating image. The black dots are activated control points and the arrows demonstrate the registration driving forces. (c) gives the floating image inversely transformed into the reference space at different registration steps. (d) demonstrates the deformed FFD meshes at different registration steps whose concatenation gives the resultant transformation.

tivated, leading to diminishing the modelling ability of the FFD mesh. For example, in the registration task in Figure 5.2, the control points around the contour of the ellipse, the white dots in middle row of figure 5.2 (a), will not be set as passive by using the measures proposed in (Schnabel et al., 2001). This is because the local supports of these control points are linked to the uniform regions with low intensity gradients in the floating image. The low gradient results in the low value of the local entropy of the uniform region or the derivative of the intensity-based cost functions, and thus inactivates the associated control points. In fact, only the control points mapped to the boundary of the circle in the floating image will be activated, as these black dots shown in the top row of Figure 5.2 (b). If the status is not adaptively updated but remains constant, the ellipse in the reference image will not be able to deform appropriately to match the circle in the floating image due to the diminished modelling ability.

5.2 FFDs with adaptive control point status

To account for the two challenges discussed in the last section, we propose to re-set the status of control points at the begging of each iteration step in the gradient ascent optimisation, i.e., an adaptive status for each control point, using the prior information from a pre-construct atlas. As shown in Figure 5.2 (c), for iteration step i, the floating image I_s is inversely transformed into I_s^i, in the coordinate of the reference image space (referred as reference space). Then, the

status of the control points should be updated based on the updated information from I_s^i given the shape of the floating image is *a priori* known from an atlas, as shown in Figure 5.2 (b).

The adaptive status of control points can be potentially extended from the two measures proposed in (Schnabel et al., 2001):

- For the *joint image pair measures* such as the gradient of the associated cost function, the status can be updated based on the updated derivative of the cost function with respect to displacements of control points at each iteration step. This method is however inefficient because the computation of the derivatives of all the passive control points is expensive and should be avoided.

- For the *reference image measures* such as the local entropy or local intensity variance, the status can be updated based on computing the measures using the updated information from the inversely transformed floating image I_s^i at each iteration. This scheme is however still not suitable for the registration task in the context of cardiac MR image segmentation where the control points linked to the liver are supposed to be passive, though it should work well for images with uniform background.

Therefore, in the context of atlas registration in the segmentation framework the status-setting is performed as:

$$\text{Status}(\varphi_j) = \begin{cases} active, & \text{if } T_i(\phi_j) \in \mathcal{M}_s \\ passive, & \text{if } T_i(\phi_j) \notin \mathcal{M}_s \end{cases} , \tag{5.1}$$

where ϕ_j is the coordinate of control point φ_j, $\mathcal{M}_s$ is a mask image generated using the prior knowledge from an atlas. Since the segmentation of the atlas is *a priori* known, this status-setting well suits the registration task required in the refinement of the segmentation framework. To avoid the effects caused from the background, $\mathcal{M}_s$ can be chosen to solely cover the region of interests such that the control points in the adjacent tissues with indistinct boundaries will not be activated, thus the registration robustness can be improved. Also, this status-setting can significantly reduce the run-time, because the optimisation does not involve computing the driving forces (derivatives of MI) for a large number of passive control points localised in the non-uniform background areas.

5.2.1 Directional optimisation

Since intensity non-uniformity (bias) and artefacts are commonly presented in cardiac MR images, directional adaptation perpendicular to the model surfaces is widely used in model-based segmentation (Lobregt and Viergever, 1995; Orderud et al., 2007). Hence, the active control points can be further constrained to solely move along the perpendicular direction to the inversely transformed atlas surface.

Let $\mathcal{C}_s$ be the boundary (surface) of the atlas, $\vec{v}_y^s$ be a vector perpendicular to surface $\mathcal{C}_s$ at coordinate y, T be the transformation and $y = T(x)$. $\vec{v}_y^s$ can be *a priori* computed from the normalised gradient of $\mathcal{C}_s$:

$$\vec{v}_y^s = \text{Normalise } \nabla \mathcal{C}(y) \ . \tag{5.2}$$

Therefore, the direction $\vec{v}_x^t$ for moving control point ϕ_j in the reference space where the FFD mesh is applied can be computed from the surface of the inverse-transformed atlas at coordinate

$x = \phi_j$. Since $T^{-1}(\mathcal{C}_s)(x) = \mathcal{C}_s(y)$ and $y = T(x)$, $\vec{v}_x^t$ can be computed as:

$$\begin{aligned} \vec{v}_x^t &= \text{Normalise } \nabla(T^{-1}(\mathcal{C}_s)(x)) \\ &= \text{Normalise } \nabla(\mathcal{C}_s(T(x)) \\ &= \text{Normalise } \big(\nabla\mathcal{C}_s(y) \cdot \nabla T(x)\big) \end{aligned} \quad . \tag{5.3}$$

5.3 Experiments and results

5.3.1 Experiment-1: Registration using phantom data

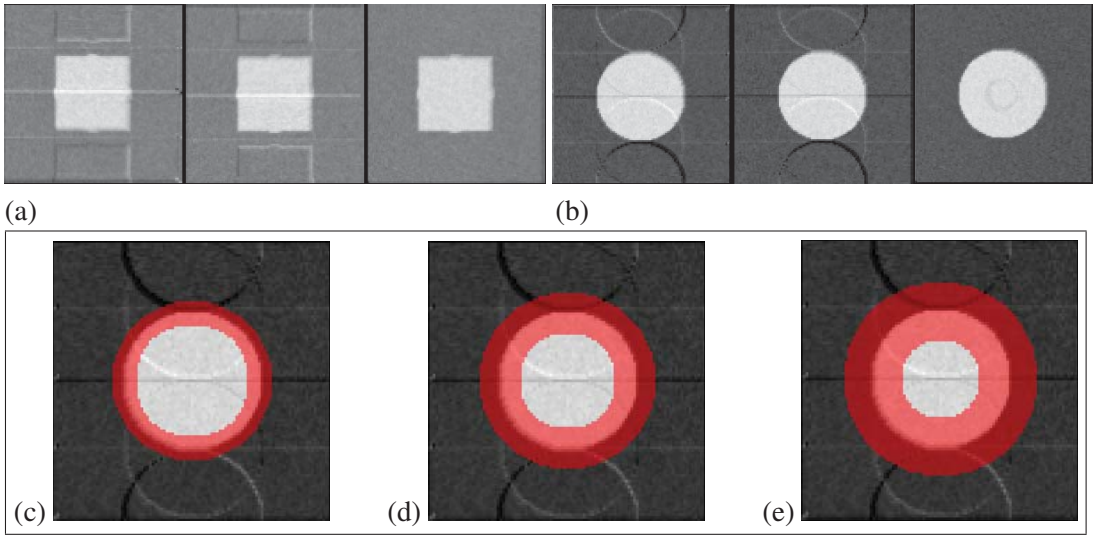

Figure 5.3: Images used in the experiment: (a): three views of the reference image; (b): the floating image; the images are with simulated noise and ghosting artefacts. (c)-(e): a single view of the three mask images (red) superimposing on the floating image, (c) 20 mm width, (d) 30 mm width, and (e) 40 mm width.

Data and experimental setup

The purpose of this experiment is to demonstrate the registration performance difference using the standard FFDs and adaptive status FFDs, and the performance difference of the adaptive status FFDs using different mask images $\mathcal{M}_s$ for the status setting. The reference and floating images used in this experiment are shown in Figure 5.3 (a) and (b). They were constructed from intensity uniform images with a square and a sphere. Rician noise with amplitudes of 3-5% of the intensity ranges was added and rotational and vertically translational motions were also simulated to the image construct to include some artefacts such as the ghosting in the images. The images are of resolution $100 \times 100 \times 100$ and of pixel size $2 \times 2 \times 2$ mm.

We employed 52 random affine transformations (without translation) to transform the floating image to generate 52 registration tasks. A nonrigid registration was used to register the transformed floating images to the reference image. The accuracy of a registration result was assessed using the surface-to-surface distance between the box in the reference image and the transformed sphere in resultant floating image. For each case, a root mean square (RMS) surface distance error measure and the computation time of registration were computed.

The nonrigid registration used two-level FFD meshes as the transformations models, a coarse level with isotropic spacing 20 mm and a fine level with isotropic spacing 10 mm. The

goal of the registration tasks was to align the surface of the box and the surface of the sphere, thus the active control points in the adaptive setting scheme should be associated with the region around the surface in the floating image. By changing the size of this region, we compared the results of four registration schemes:

(1) Adaptive control point status FFD registration with a mask image whose thickness is twice the FFD mesh spacing around the surface of the sphere. Figure 5.3 (c) shows the mask of 20 mm size, twice the 10 mm spacing FFD grid, while in the level of 20 mm spacing, the mask is 40 mm size, shown in (e). This scheme is referred to as ACPS-2.

(2) Adaptive control point status FFD registration with a mask image whose thickness is three times the FFD mesh spacing around the surface of the sphere. Figure 5.3 (d) shows the mask of 30 mm size, three times the 10 mm spacing FFD grid, while in the level of 20 mm spacing, the mask is 60 mm size. This scheme is referred to as ACPS-3.

(3) Adaptive control point status FFD registration with a mask image whose thickness is four times the FFD mesh spacing around the surface of the sphere. Figure 5.3 (e) shows the mask of 40 mm size, four times the 10 mm spacing FFD grid, while in the level of 20 mm spacing, the mask is 80 mm size. This scheme is referred to as ACPS-4.

(4) Standard FFD registration without status setting. This scheme is referred to as Full FFDs.

All the four registration schemes adopted the same gradient ascent optimisation scheme and the stopping criterion was the registration reaching an optimum of the normalised mutual information similarity measure. The concatenation scheme (Rueckert et al., 2006) was used to maintain diffeomorphism.

Result

Table 5.1 presents the results of the four registration schemes. In terms of registration accuracy, ACPS-2 performed significantly worse than the other three as their mean errors were all at least twice their standard deviations away from the mean error of ACPS-2. However, in terms of computation time ACPS-2 also had demonstrated a significant superiority over the other three: its average run-time was far (more than three times its standard deviations) away from the mean of the others. Full FFDs performed far slower as the mean run time of the other three schemes were all more than three times their standard deviations away from the mean of Full FFDs. Also the accuracy of Full FFDs was not significantly different from that of ACPS-3 ($P = 0.16$) and ACPS-4 ($P = 0.87$) using the paired t-test. It should be noted that the registration results, the RMS errors and run time in Table 5.1, were approximately considered as Gaussian distributed when doing the comparisons using mean and standard deviation, and the t-test, based on the same argument in Page 75, Section 4.5.4.

Conclusion

In conclusion, the performance of ACPS-3 and ACPS-4 was similar, and both were better than ACPS-2 in terms of the registration accuracy but worse in terms of the run time. No evidence showed that Full FFDs could achieve better registration accuracy than ACPS-3 or ACPS-4, but the computation time was significantly longer than that of the other schemes. Therefore, in

Table 5.1: The registration errors (RMS surface distance) and computation time of the four registration schemes. mm: millimeter, min: minute.

	ACPS-2	ACPS-3	ACPS-4	Full FFDs
Erorr (mm)	1.54 ± 0.14	1.26 ± 0.06	1.22 ± 0.06	1.23 ± 0.12
Run time (min)	8.2 ± 2.0	15.7 ± 5.1	18.2 ± 4.7	52.3 ± 12.9

cardiac MR registration, ACPS-2 and ACPS-3 are preferred because they have been shown to be able to achieve enough accuracy for the registration needs. Also, activating fewer control points can practically reduce the chance of registering the non-uniform background of the MR images and improve the registration within the heart region.

5.3.2 Experiment-2: Application to whole heart segmentation

Data and experimental setup

The purpose of this experiment is to compare the registration performance of the proposed ACPS FFDs and the standard FFDs when applied to the whole heart segmentation framework, leading to two registration schemes as follows:

- LARM_ACPS: A global affine registration for localisation, then the locally affine registration method (LARM) for substructure initialisation, finally the FFD registration with adaptive control point status for refinement of the local details.
- LARM_FFDs: A global affine registration for localisation, then LARM for substructure initialisation, finally the standard FFD registration for refinement of the local details.

The experiment employed 10 pathological MR cases, which displayed a variety of heart abnormalities due to either Tetralogy of Fallot or myocardial infarction. The acquisition of these images has been presented in Section 4.5.1. The manual segmentation, regarded as the gold standard segmentation, was done by a technician with cardiac anatomy knowledge, slice by slice using Analyze 8.1, Philips, The Netherlands. The segmentation error was computed from the RMS surface distance between the segmented surface and the gold standard.

Table 5.2: The segmentation error, RMS surface distance, and the percentage $(\%)$ of the error ranges: $<$2 mm, 2-5 mm, and $>$5 mm.

Method	Structure	RMS (mm)	$<$2 mm $(\%)$	2-5 mm $(\%)$	$>$5 mm $(\%)$
LARM_ACPS	Epicardium	2.3 ± 0.7	75.3 ± 6.2	19.9 ± 4.2	4.8 ± 3.7
	Left Ventricle	1.6 ± 0.3	83.8 ± 7.8	14.9 ± 7.3	1.3 ± 0.9
	Right Ventricle	1.9 ± 0.6	82.2 ± 5.7	14.5 ± 4.0	3.3 ± 3.2
	Left Atrium	2.3 ± 0.6	71.5 ± 10.4	24.0 ± 9.0	4.5 ± 5.3
	Right Atrium	1.8 ± 0.4	80.6 ± 6.7	16.9 ± 5.0	2.5 ± 2.7
	Whole Heart	1.8 ± 0.2	81.1 ± 4.0	16.7 ± 3.9	2.2 ± 1.2
LARM_FFDs	Epicardium	3.1 ± 1.1	72.5 ± 5.9	20.2 ± 4.2	7.4 ± 5.2
	Left Ventricle	1.8 ± 0.7	81.2 ± 8.4	16.7 ± 7.1	2.1 ± 2.7
	Right Ventricle	1.9 ± 0.6	80.0 ± 7.9	16.7 ± 5.8	3.2 ± 3.1
	Left Atrium	2.5 ± 1.0	68.2 ± 9.9	25.0 ± 6.3	6.8 ± 7.3
	Right Atrium	2.2 ± 0.7	74.2 ± 7.1	21.5 ± 5.7	4.3 ± 4.0
	Whole Heart	2.0 ± 0.3	77.0 ± 4.2	20.3 ± 4.0	2.7 ± 1.5

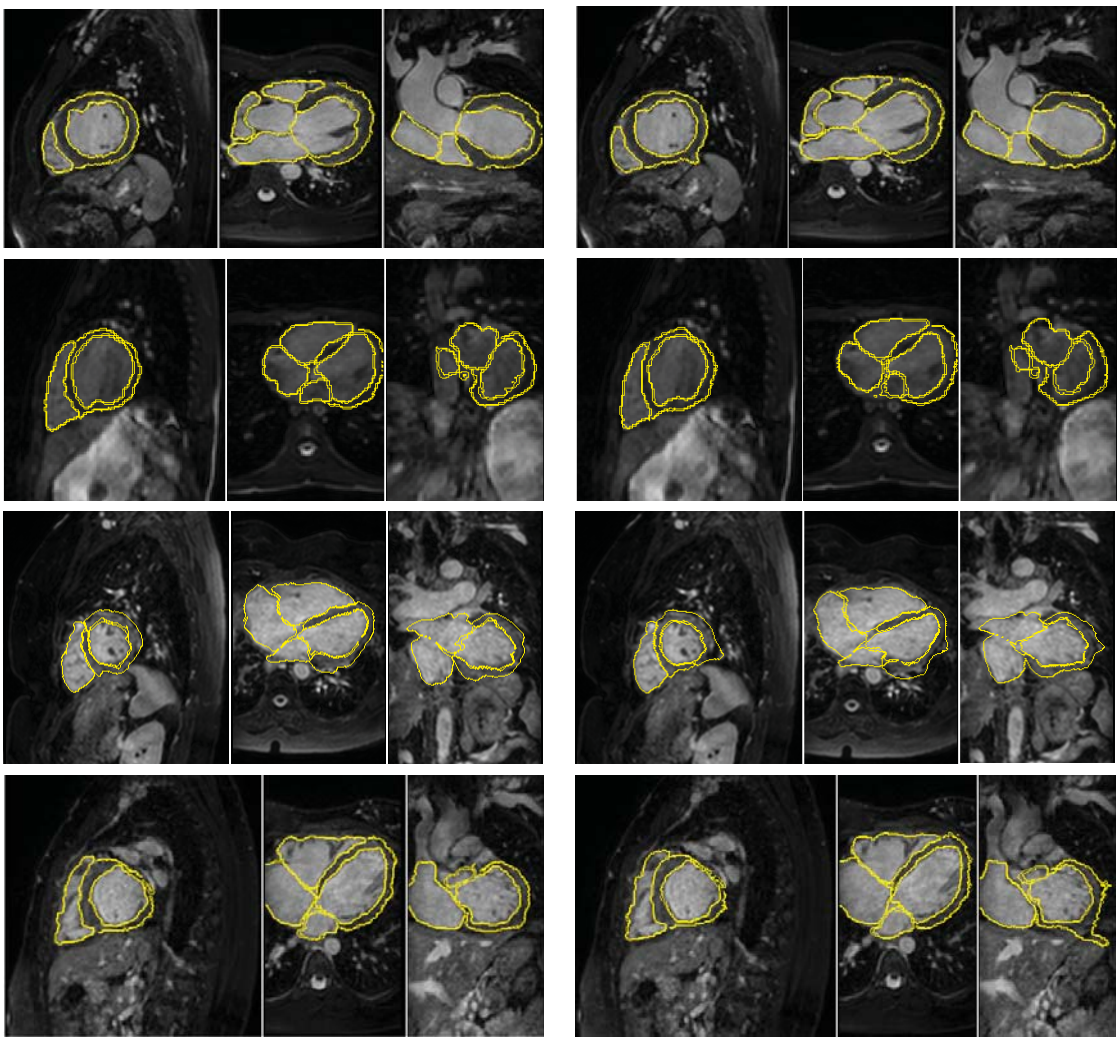

Figure 5.4: Three views, sagittal, transverse, coronal views of segmented contour superimposing on the MR images. These are four random examples of using the LARM_ACPS registration scheme (left) and the LARM_FFDs scheme (right).

Result

Table 5.2 presents the segmentation errors for each anatomical structures, including epicardial surface of the left ventricle (Epicardium), endocardial surface of the left and right ventricles (Left Ventricle and Right Ventricle), endocardial surface of the left and right atria (Left Atrium and Right Atrium) and all these surfaces as one measure (Whole Heart). LARM_ACPS almost outperformed LARM_FFDs in every categories, particularly, in Epicardium (P=0.04) and Whole Heart (P=0.03) categories the segmentation accuracy was significantly different, using 0.05 as the significance level in the paired t-test. The larger errors from the standard FFDs in the registration of epicardium was mainly due to adjacent tissues such as the liver and lung which could affect the registration of the indistinct boundaries. For this reason, the registration was more likely to step into local minima and produce unrealistic deformations, as the examples shown in Figure 5.4.

Table 5.2 also gives the error ranges of each structure category. Over 80% of the segmentation by LARM_ACPS was within 2 mm and more than 97% within 5mm. The segmen-

tation errors of different substructures could be quite different, for example the Left Ventricle (1.6 ± 0.3 mm) achieved much better, more than three times standard deviation, than that of the Left Atrium (2.3 ± 0.6) due to the limitation of the validation scheme.

Three Gaussian distribution assumption used in the t-test and the three groups of error distribution are based on the same arguments in Page 72 and Page 75, respectively. More detailed studies and discussion of the segmentation performance will be given in chapter 6.

Conclusion

This experiment showed that by taking the *a priori* knowledge into the status-setting of the FFD meshes, the proposed FFD registration improved the segmentation performance when applied to the registration-based segmentation propagation framework. This segmentation achieved a RMS surface-to-surface error of 1.8 ± 0.2 mm in the 10 pathological cases, considerably better than the segmentation by using the standard FFDs, particularly in the epicardium.

5.4 Conclusion

In this chapter, we have presented a new FFD registration with adaptive control point status. In this scheme, the control points activated for optimisation are related to the priorly selected regions and adaptively changeable according to the current deformation field. The phantom experiment demonstrated that the proposed method not only could achieve the high accuracy as the standard FFDs for the registration of the region of interests, but also significantly improved the computation time. The experiment of MR segmentation framework demonstrated a significantly different (better) accuracy using the proposed FFDs for the refinement, compared to the standard FFDs.

Chapter 6

Whole Heart Segmentation

This chapter describes a fully automatic whole heart segmentation framework using the two new registration algorithms introduced in the last two chapters: the locally affine registration method (LARM) and the free-form deformations with adaptive control point status (ACPS FFDs). Section 6.1 gives an introduction to this work. Section 6.2 presents the segmentation framework in detail, and Section 6.3 describes the procedure of constructing the atlas. Section 6.4 shows the validation results and Section 6.5 concludes this chapter.

6.1 Introduction

Magnetic resonance (MR) imaging has become a routine modality for the determination of patient cardiac morphology. The extraction of this information can be important for the development of new clinical applications as well as the planning and guidance of cardiac interventional procedures. To avoid inter- and intra-observer variability of manual delineation, it is highly desirable to develop an automatic technique for whole heart segmentation of cardiac MR images. However, automating this process is complicated by the limited quality of acquired images and the large shape variation of the heart between subjects.

We propose a registration framework able to preserve the topology and to deal with the large shape variability of the heart. The core process is based on the two new algorithms: the locally affine registration method (LARM) and the nonrigid registration algorithm using free-form deformations with adaptive control point status (ACPS FFDs). In this scheme, LARM is applied to obtain a robust initialisation of the different *substructures* of the heart such as the four chambers and the great vessels. The resultant transformation globally deforms the atlas but locally still maintains the shape of the substructures. This registration is able to avoid local optima during the optimisation of the global transformation. After the initialisation, ACPS FFD registration is used to refine the local details. The control point status-setting in ACPS FFD registration makes advantageous use of prior knowledge to avoid the *myocardial leaking* problem.

Furthermore, an inverse transformation is needed from LARM to propagate the segmentation. This is because LARM requires the local regions pre-defined in the reference image space, while the atlas which has the definition is the floating image in the segmentation framework. Hence, the Dynamic Resampling And distance Weighted interpolation (DRAW) method will be used to compute the inverse transformation for LARM registration.

6.2 Segmentation framework

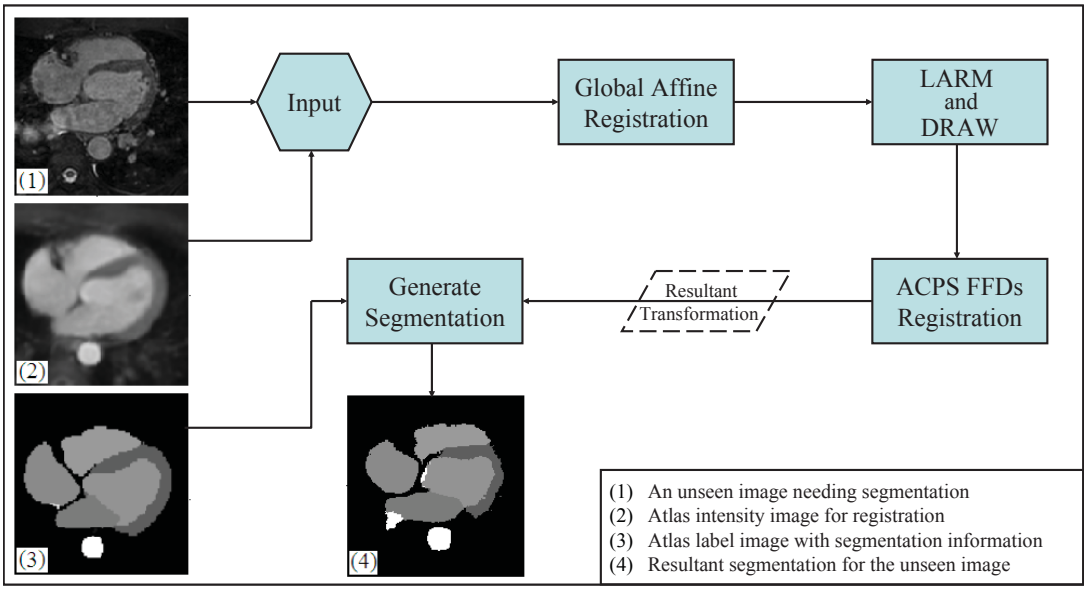

Figure 6.1: The framework of automatic whole heart segmentation based on atlas propagation.

The segmentation framework, registering the atlas to unseen images for segmentation propagation as illustrated in Figure 6.1, includes three registration steps:

(1) Firstly, a global affine registration is applied to localize the heart. In cardiac MR segmentation, localisation of the heart is an essential step for success and a challenging one to fully automate (Peters et al., 2009; Kurkure et al., 2009). In this framework, a global affine registration works well because of the following two reasons. Firstly, the field of view from different scans is similar. This MRI scan covers the background structures of the heart such as the back, chest, and the liver, which contribute to the localisation of the heart. Secondly, the atlas and unseen images have similar orientation. The MR data have been acquired from either short-axis or sagittal views and the rotation for compensating the orientation difference is smaller than 90 degrees. Figure 6.2 (left) shows an example image.

(2) LARM is then used to further initialise the substructures. Three stages of LARM registration are adopted in practice, where two, four, seven local affine transformations are used respectively.

In the first stage, only two local affine transformations are used. The corresponding local regions are defined as the *atrial region* including the two atria and the great vessels, and the *ventricular region* including the two ventricles. In the second stage, the right ventricle and the right atrium are separated from the regions defined in the first stage to add another two affine transformations. Finally, seven local regions, including the two ventricles, the two atria, the pulmonary artery, the ascending aorta, and the descending aorta, are used to define a seven-local-affine LARM.

In all the three stages, the atlas image is used as a reference image in LARM. Therefore,

DRAW is used to get the transformation field defined from the unseen MR image to the atlas.

(3) Finally, registration using ACPS FFDs is employed to refine the local details. In the status-setting, two mask images, $\mathcal{M}_s^1$ and $\mathcal{M}_s^2$, are used.

Firstly, the registration uses $\mathcal{M}_s^1$ to solely activate the control points which map onto the blood pool of the atlas. This registration mainly contributes to the alignment of the endocardial surfaces where the boundaries are normally distinct. Hence, $\mathcal{M}_s^1$ is only defined to cover these regions. The FFDs use isotropic B-spline meshes with a spacing of 20 mm.

Secondly, the registration employs $\mathcal{M}_s^2$ to activate the control points which map to a neighbouring region of the endocardial and epicardial surfaces. This step fine-tunes the registration of whole heart surfaces and uses finer B-spline meshes with a spacing of 10 mm.

For the implementation of registration, we use NMI (Studholme et al., 1999) as the similarity measure. The optimisation adopts the gradient ascent method and the multiresolution scheme (Thévenaz and Unser, 2000). The registration stops when the NMI measure has not improved in the last five steps.

6.3 Atlas construction

Atlas construction is a different topic outside the scope of this work, especially when involving the statistical shape modelling (Frangi et al., 2002). We propose to use a *simple atlas*, without statistical shape information, for the validation of the proposed method. This is because it is assumed that the existing statistical shape models could not perform better than a simple atlas when applied to new pathologies. Therefore, the atlas can be built from a selected reference space such as the mean of a group of images or a space defined by any cardiac MR case. Furthermore, it should be noted that the proposed segmentation method would benefit a lot more from using an atlas constructed from cardiac MR data exhibiting similar heart shapes and pathologies to the unseen data. However, to demonstrate the applicability of the proposed framework in the most challenging tasks, we propose to use an atlas constructed from healthy volunteer data, which is validated by evaluating the performance of this atlas in segmenting pathological cases.

Theoretically, one can use an MR image and its corresponding segmentation as the atlas for propagation. However, the noise and artefacts presented in a specific case can practically lead to segmentation bias in all the cases. To avoid this, we employ a number of MR images, such as five or ten in the experiments in Section 6.4, acquired using the same MRI sequence. They are then registered to a selected reference space. A mean intensity image, referred to as *atlas intensity image*, can be computed from this set of registered MR images. The labelling of each anatomical region of the reference space has the corresponding segmentation information of the atlas, referred to as *atlas label image*. Figure 6.2 shows an atlas case from Section 6.4, which is constructed from ten MR images.

To achieve the registration of this set of MR images, we manually label each anatomical

substructure of the images, including the blood pools of each chamber and great vessel and left ventricle myocardium. Figure 6.2 (right) shows a label image of an atlas. The label images are not only the corresponding segmentation of the MR images, but also with a uniform intensity value for each substructure. The deformation fields to register the MR images can be computed from the registration results of the corresponding label images by using the following steps:

- a global affine registration to localise the heart structure,
- LARM to further initialise the seven substructures,
- a fluid registration using the sum of the squared intensity difference as the similarity measure (Crum et al., 2005) to finally fine-tune the local detail. It should be noted that other methods such as the FFD registration should also work as well for this nonrigid registration task. Here, we used fluid registration simply because our FFD registration tool was only implemented using NMI similarity measure.

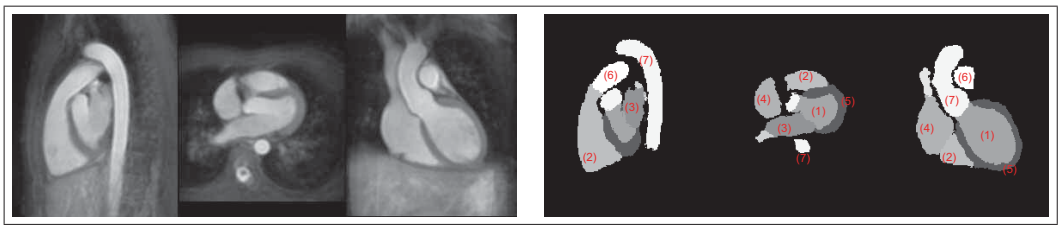

Figure 6.2: Left: an atlas intensity (MR) image using a reference space of the mean shape of 10 volunteer data. Right: corresponding segmentation, atlas label image of the atlas intensity image. Images are shown in sagittal, transverse, and coronal views. The numbers in the atlas label image indicate the names of local regions: left ventricle (1), right ventricle (2), left atrium (3), right atrium (4), myocardium (5), pulmonary artery (6), and aorta (7).

6.4 Experiments and results

Three steps have been done to demonstrate the performance of the proposed segmentation framework. Section 6.4.1 describes the data and the experimental set-up. Section 6.4.2 compares the segmentation results using three different atlases for propagation. Section 6.4.3 demonstrates the improvements by comparing the proposed algorithms with the alternative techniques. Section 6.4.4 analyses the segmentation performance of the proposed segmentation framework and performs the validation in detail.

6.4.1 Experimental set-up

Data

The cardiac MRI sequence used in the experiment was the balanced steady state free precession (b-SSFP) for whole heart imaging (see Section 4.5.1 for detail).

A *test dataset* of thirty-seven cardiac MR volumes on the end-diastolic phase was used as unseen images in our experiments, among which nineteen cases had confirmed pathologies including myocardium infarction, atrial fibrillation, tricuspid regurgitation, aortic valve stenosis, Alagille syndrome, Williams syndrome, dilated cardiomyopathy, aortic coarctation, and Tetralogy of Fallot, which induced a number of different forms of morphological abnormalities. It is

common to see that many of these patients had symptoms of a combination of more than one of these pathologies. The subjects, aged from 5 to 80, displayed a wide diversity of heart shapes. We further acquired a training dataset from another 10 healthy volunteers for the construction of atlases. The atlases were then used to segment the pathological data, instead of using an atlas with a similar heart shape to unseen images, to demonstrate the general performance of the proposed segmentation framework.

All these data have manual segmentation as the gold standard. They were either done using a mesh model with manual corrections (Peters et al., 2007) or using the manual editing tool in the commercial product Analyze 8.1 or 9.0, Philips, The Netherlands. The manual segmentation was completed by either a clinician or a research associate with detailed knowledge of heart anatomy. For the test dataset, the blood cavities of the four chambers and the myocardium of the left ventricle are separately segmented (examples of manual segmentation can be found in Figure 6.4 and Figure 6.5), while for the training dataset, in addition to these regions, the pulmonary artery, ascending aorta and aortic arch, and descending aorta are also separately delineated for the atlas construction registration. Figure 6.2 (right) shows an example of these substructure labels.

Evaluation protocols

Two different types of measures are used to evaluate the accuracy of a segmentation result: the surface distance measures and the volume measures.

The surface measures compute the surface-to-surface distance between the propagated segmentation and the gold standard segmentation. This surface distance is calculated using each surface point s_{seg} from the propagated segmentation to the triangle defined by the three closest surface points $\{s^1_{gd},\ s^2_{gd},\ s^3_{gd}\}$ of s_{seg} in the gold standard segmentation. The mean surface distance, ϵ_{mean}, standard deviation, ϵ_{std}, and the root mean square (RMS), ϵ_{rms} of a surface are computed. Six surfaces are considered:

(1) the endocardial surface of the left ventricle, referred to as *Left Ventricle*,

(2) the endocardial surface of the left atrium, referred to as *Left Atrium*,

(3) the endocardial surface of the right ventricle, referred to as *Right Ventricle*,

(4) the endocardial surface of the right atrium, referred to as *Right Atrium*,

(5) the epicardial surfaces of the left ventricles, referred to as *Epicardium*,

(6) the inclusion of all the five surfaces above as a whole heart segmentation accuracy, referred to as *Whole Heart*.

Volume measurement is of major interest in many clinical applications such as computing stroke volume, eject fraction and myocardium mass. Three widely used measures are employed in the validation, including:

- Dice Coefficient $= 2|V_{seg} \cap V_{gd}|/(|V_{seg}| + |V_{gd}|)$ (Dice, 1945),
- Volume Overlap $= |V_{seg} \cap V_{gd}|/|V_{seg} \cup V_{gd}|$ (Crum et al., 2006),

- Volume Difference $= 2 \times \mathrm{ABS}(|V_{seg}| - |V_{gd}|)/(|V_{gd}| + |V_{seg}|) \times 100\%$,

where, V_{seg} and V_{gd} denote the volumes from the propagated segmentation and gold standard respectively. Both Dice and volume overlap indicate how well the two volumes are overlapped, with maximum 1 meaning perfect overlap and minimum 0 indicating no overlap at all. Five substructures are measured, as follows:

(1) the blood cavity of left ventricle, referred to as *Left Ventricle*,

(2) the blood cavity of left atrium, referred to as *Left Atrium*,

(3) the blood cavity of right ventricle, referred to as *Right Ventricle*,

(4) the blood cavity of right atrium, referred to as *Right Atrium*,

(5) the myocardium of the left ventricle, including septum, referred to as *Myocardium*.

Three steps of evaluation

Step-one: This step uses the 19 pathological data as a test set to assess the sensitivity of the proposed approach to different atlases. Section 6.3 provides the detail of the atlas construction. Three atlases are tested, whose reference spaces are based on the following:

(1) A healthy volunteer MR image is randomly selected from the training dataset as the reference space, referred to as *One Shape*.

(2) The mean shape of five randomly selected training data is used as the reference space, referred to as *Five Shapes*. The mean of five shapes was computed based on the *iterative atlas construction* (Frangi et al., 2002). The registration in our construction employs the five corresponding *label images* and the three transformation models introduced in the atlas construction, described in Section 6.3.

(3) The mean shape of all the ten volunteer data is used as the reference space, referred to as *Ten Shapes*. Figure 6.2 shows the result of this atlas.

Step-two: This step assesses the improvement of the proposed two registration algorithms when applied to the segmentation framework. The atlas used is the *Ten Shapes*. Three registration frameworks, for the segmentation propagation, are used to segment the test set of thirty-seven cases, including:

- a single affine for global localisation and a traditional FFDs (Rueckert et al., 2006) for refinement, referred to as *Affine_FFDs*,

- a single affine for global localisation, then LARM for substructure initialisation, finally traditional FFDs for refinement, referred to as *LARM_FFDs*,

- the proposed framework, a single affine for global localisation, then LARM for substructure initialisation, finally a registration using ACPS FFDs for refinement, referred to as *LARM_ACPS*.

The FFD registration in all cases used multi-level, from isotropic 20 mm mesh spacing to 10 mm, FFD meshes (Schnabel et al., 2001) and the concatenation strategy (Rueckert et al., 2006) to maintain diffeomorphism.

Step-three: Finally, we focus on the segmentation results of the 37 test data using the proposed segmentation framework and the*Ten Shapes* atlas.

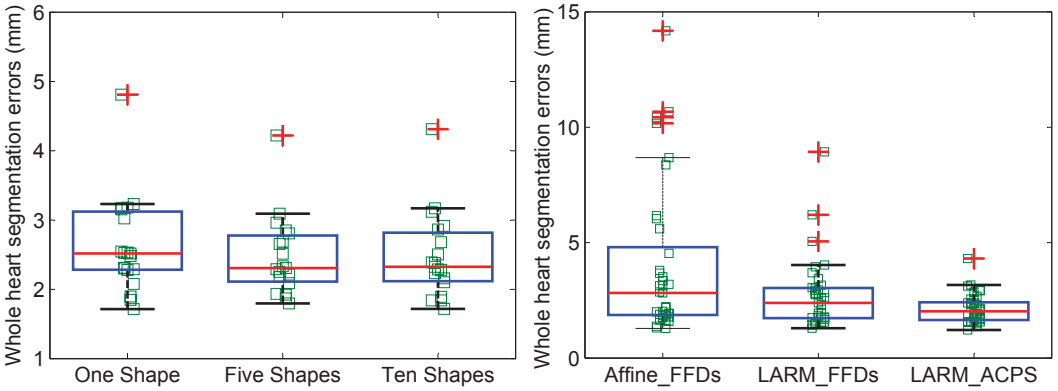

Figure 6.3: The individual plots and the Box-and-Whisker diagrams of the *Whole Heart* segmentation errors using the RMS surface-to-surface error measure, ϵ_{rms}. Left: the errors of the 19 pathological cases using the proposed segmentation approach combined with the three different atlases. Right: the errors of the 37 cases using the three different segmentation frameworks. Note that the red crosses are these considered as outliers in the box plots.

6.4.2 Sensitivity to different atlases

Figure 6.3 (left) plots the RMS surface distance errors of the 19 pathological cases. The mean and standard deviation of the errors are:

- using *One Shape* atlas: 2.63 ± 0.70 (mm),
- using *Five Shape* atlas: 2.47 ± 0.57 (mm),
- using *Ten Shape* atlas: 2.47 ± 0.61 (mm).

Both the Box-and-Whisker diagram and figures from mean and standard deviation show that the segmentation using the *Five Shapes* atlas had smaller error numbers while using the *One Shape* atlas had greater numbers. However, the differences between the mean and median numbers are all less than 0.2 mm. To assess the significance of the performance difference, the two tailed, paired t-test (Glantz, 2005) was used: $P_{1,5} = 0.068$ (between the *One Shape* and the *Five Shapes*), $P_{1,10} = 0.057$ (between the *One Shape* and the *Ten Shapes*), and $P_{5,10} = 0.95$ (between the *Five Shapes* and the *Ten Shapes*). There was no strong evidence showing significant difference between each population using a significance level of 0.05. However, both $P_{1,5}$ and $P_{1,10}$ were also close to the significance level. We then further computed the 0.95 confidence interval of them, which were $CI_{1,5} = [0.01, 0.32]$ mm and $CI_{1,10} = [0.01, 0.31]$ mm respectively. This showed there were small biases of the *One Shape* population with respect to the other two, but these biases were not practically important, as the mean errors of repeated manual segmentation to the gold standard segmentation, in ϵ_{rms}, are shown to be between 0.5 to

1.5 mm (Hautvast et al., 2006). In addition, the Pearson correlation coefficients are $r_{1,5} = 0.94$, $r_{1,10} = 0.93$, and $r_{5,10} = 0.98$ respectively.

In conclusion, the atlas based on the reference space of one subject could lead to a performance bias. However, no evidence showed that the segmentation of pathological data using the different atlases constructed from healthy subjects could lead to significant performance difference.

6.4.3 Performance using alternative techniques

Table 6.1 displays the RMS surface-to-surface segmentation errors of each substructure and all the surfaces as the *Whole Heart* measure of the three different registration frameworks. From the *Affine_FFDs* to the *LARM_FFDs*, the registration in all categories was improved, especially the maximal errors decreased. This segmentation was further improved by the usage of ACPS FFDs (see results in *LARM_ACPS*). The p-values of the *Whole Heart* RMS surface distance errors using the one tailed, paired t-test, assuming non improvement are:

- Test the *Affine_FFDs* against the *LARM_FFDs*: $P_{larm} = 0.002$.
- Test the *LARM_FFDs* against the *LARM_ACPS*: $P_{acps} = 0.002$.
- Test the *Affine_FFDs* against the *LARM_ACPS*: $P_{larm+acps} = 0.0002$.

These p-values suggest strong evidence to reject the null-hypothesis, thus the segmentation had been improved by the two proposed techniques with statistical significance. This conclusion is also supported by the results of the mean and standard deviation of the ϵ_{rms} in table 6.1, where the *Whole Heart* of *LARM_ACPS*, 2.14 ± 0.63 mm, had been improved about three times the standard deviations (0.63) from that of *Affine_FFDs*, 3.96 ± 3.23 mm.

Furthermore, Figure 6.3 (right) plots the errors of the *Whole Heart* measure. About two thirds of the segmentation results by the three methods had similar error figures, while the "bad" cases, based on ϵ_{rms}, differed significantly: By using LARM, the four outliers in the *Affine_FFDs* were improved to less than 9 mm in the *LARM_FFDs*, while by further using ACPS FFDs, the three outliers in the *LARM_FFDs* were improved to less than 4.5 mm.

Finally, Figure 6.4 displays the worst segmentation case for each of the three segmentation methods and their corresponding gold standard segmentations and the results by the three compared segmentation methods:

- Subject-1, with a *Whole Heart* error of 14.2 mm, is the worst case of the *Affine_FFDs*. This was from a patient with severe right ventricle and atrium hypertrophy. A global affine registration did not initialise well the substructures and this induced a misalignment of the two ventricles: a large part of the right ventricle was segmented as the left ventricle due to the misalignment of the septum (the red and green arrows in Figure 6.4). However, LARM well compensated this problem and corrected the segmentation of the two ventricles as the results of the *LARM_FFDs* and *LARM_ACPS* shown in Figure 6.4.
- Subject-116, with a *Whole Heart* error of 8.93 mm, is the worst case of the *LARM_FFDs*. This was from a healthy volunteer case, but the image quality was very low. The traditional FFDs without constraints from prior knowledge produced an unrealistic deformation

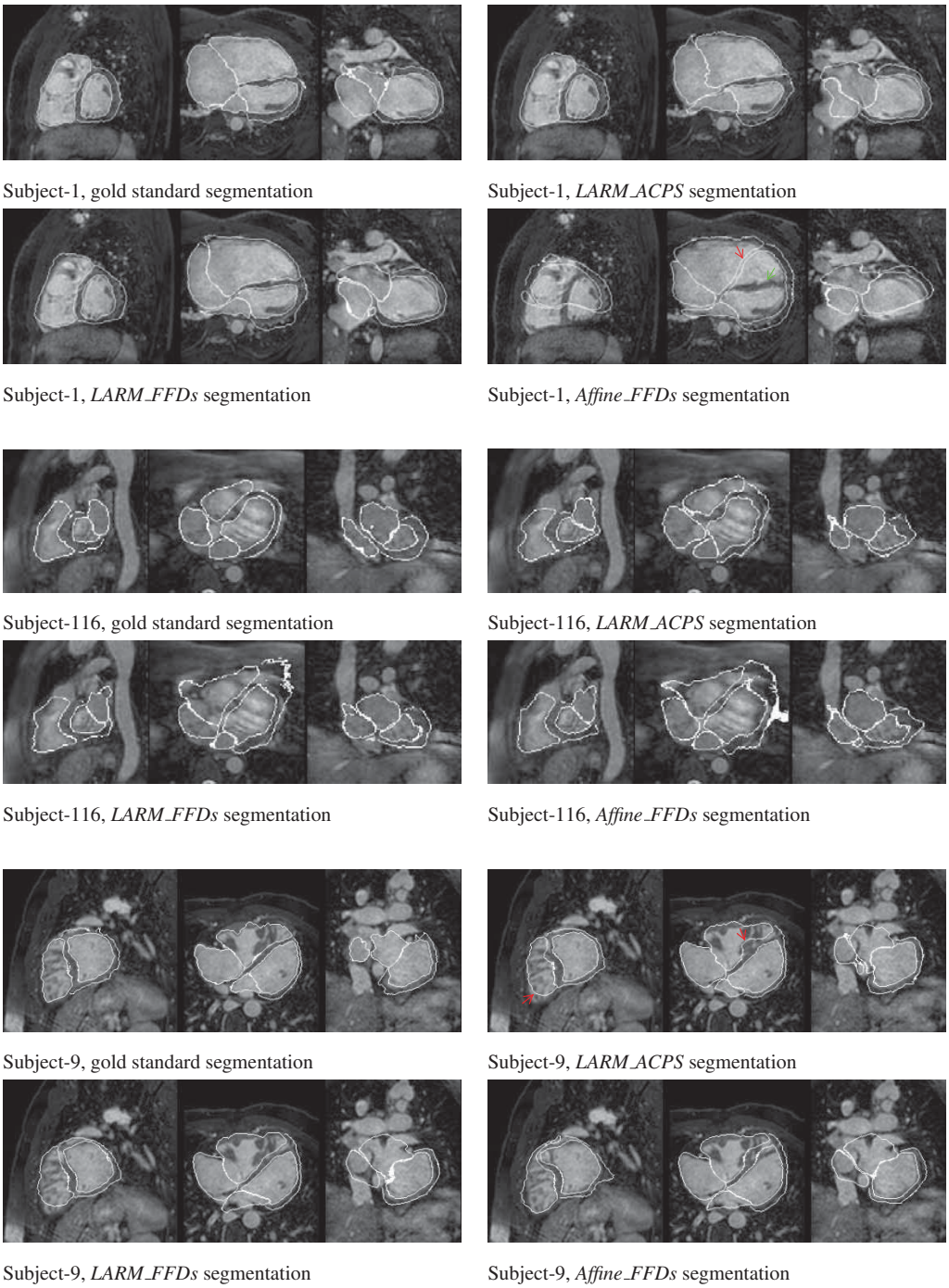

Subject-1, gold standard segmentation

Subject-1, *LARM_ACPS* segmentation

Subject-1, *LARM_FFDs* segmentation

Subject-1, *Affine_FFDs* segmentation

Subject-116, gold standard segmentation

Subject-116, *LARM_ACPS* segmentation

Subject-116, *LARM_FFDs* segmentation

Subject-116, *Affine_FFDs* segmentation

Subject-9, gold standard segmentation

Subject-9, *LARM_ACPS* segmentation

Subject-9, *LARM_FFDs* segmentation

Subject-9, *Affine_FFDs* segmentation

Figure 6.4: The worst cases by the three segmentation methods. Subject-1 is the worst case of the *Affine_FFDs*, subject-116 is the worst case of *LARM_FFDs*, and subject-9 is the worst case of *LARM_ACPS*. Images are displayed with delineated contour superimposed on the MR images, in sagittal, transverse, and coronal views. Subject-1 and subject-9 are pathological cases while subject-116 is a healthy case.

Table 6.1: Surface-to-surface segmentation errors in millimeters, ϵ_{rms} of the three methods and errors ϵ_{mean}, ϵ_{std}, and percentage with different ranges: < 2 mm, $2 - 5$ mm, and > 5 mm, of the 37 cases by the proposed approach.

(error in mm)	Affine_FFDs	LARM_FFDs	LARM_ACPS in different measures (ranges are of unit mm)					
Structures	ϵ_{rms}[max]	ϵ_{rms}[max]	ϵ_{rms}[max]	ϵ_{mean}	ϵ_{std}	$0-2$	$2-5$	>5
Left Ventricle	3.79 ± 4.38[**19.6**]	1.89 ± 1.10[**7.12**]	1.47 ± 0.32 [**2.38**]	1.06	1.02	82.9%	16.5%	0.6%
Left Atrium	3.26 ± 2.25[**11.5**]	2.81 ± 1.65[**9.28**]	2.38 ± 1.14 [**7.33**]	1.69	1.68	70.2%	23.5%	6.4%
Right Ventricle	3.23 ± 1.79[**7.50**]	2.75 ± 1.51[**8.57**]	2.13 ± 0.70 [**4.05**]	1.50	1.51	72.2%	24.1%	3.7%
Right Atrium	3.06 ± 1.74[**9.44**]	2.51 ± 1.20[**7.05**]	2.22 ± 0.75 [**5.74**]	1.51	1.62	73.0%	22.5%	4.5%
Epicardium	4.78 ± 4.88[**20.4**]	2.88 ± 2.12[**12.9**]	2.32 ± 0.82 [**5.43**]	1.69	1.60	68.6%	25.7%	5.6%
Whole Heart	3.96 ± 3.23[**14.2**]	2.71 ± 1.50[**8.93**]	2.14 ± 0.63 [**4.31**]	1.47	1.55	73.6%	22.5%	3.9%

field and resulted in an erroneous result, while ACPS FFD registration contributed to reduce this error.

- Subject-9, with a *Whole Heart* error of 4.31 mm, is the worst case of the *LARM_ACPS*. This case was also the worst result of the *LARM_ACPS* in terms of the error measure for the left atrium (7.33 mm), right ventricle (4.05 mm), and right atrium (5.74 mm). The large error for the right ventricle was mainly due to the inconsistent delineation of the cutting boundaries of chordae tendineae, papillary muscle, and trabeculae carnae (indicated by the red arrows in Figure 6.4) between the gold standard and propagated segmentations. The error for the atria was attributed to the fact that the propagated segmentation included parts of adjacent veins into the volume of atria, especially the left atrium; by contrast, the gold standard segmentation did not include them.

6.4.4 Performance of the proposed framework

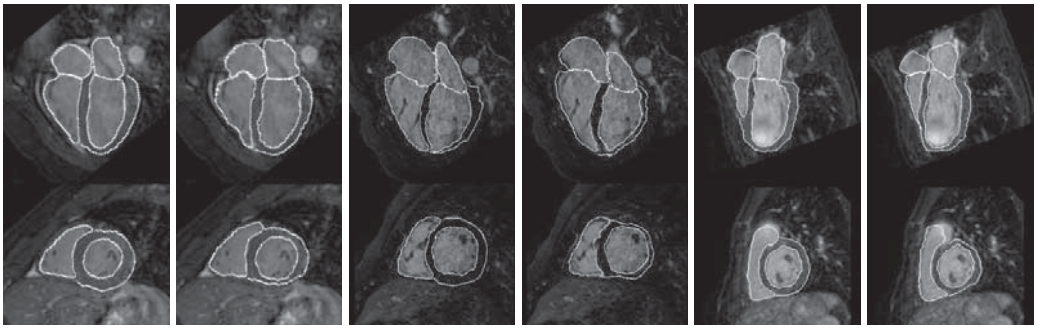

Subject-119, GD Subject-119, PS Subject-43, GD Subject-43, PS Subject-10, GD Subject-10, PS

Figure 6.5: Three segmentation cases. Images are displayed with delineated contour superimposing on the MR images, in four-chamber (top) and short-axis (bottom) views. Subject-119 is a healthy case while subject-10 and subject-43 are pathological cases. The *Whole Heart* segmentation errors of them in ϵ_{rms} measure are 2.39 mm, 3.17 mm, and 2.86 mm respectively. GD: gold standard segmentation; PS: propagated segmentation.

Table 6.1 lists the surface-to-surface errors of the proposed segmentation method for each surface category. The RMS error (and its maximum over the 37 cases), the mean error, the standard deviation, and the percentage of error ranges are presented. For an average whole heart segmentation, more than 95% surface-to-surface error is within 5 mm.

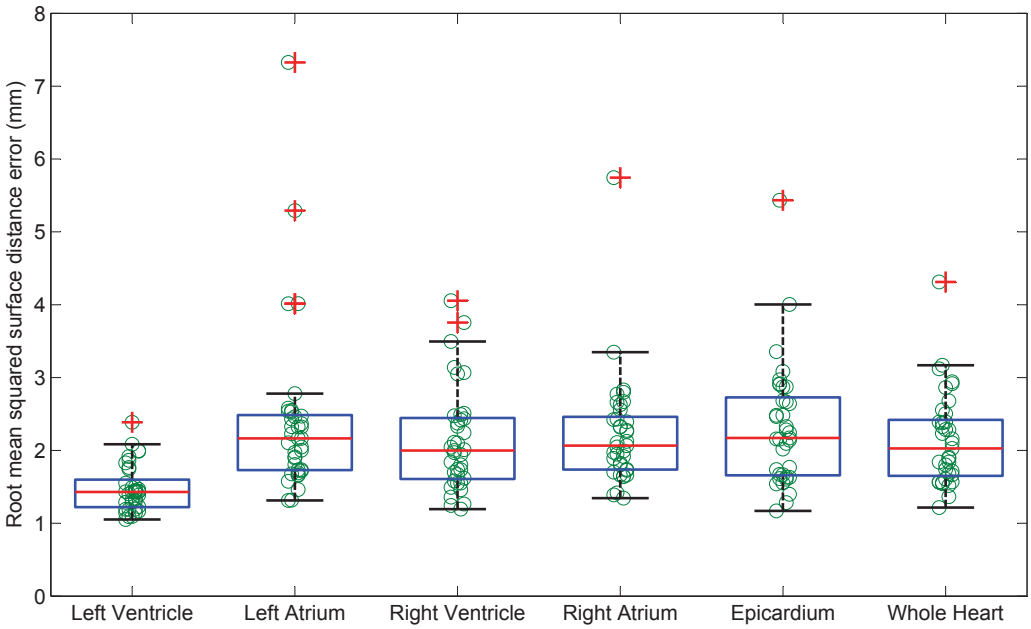

Figure 6.6: The individual plots and the Box-and-Whisker diagrams of the RMS surface distance measure, ϵ_{rms}, segmentation errors using the proposed segmentation method. This figure gives the errors of each substructures as well as the *Whole Heart* from the 37 cases.

Figure 6.6 plots all the errors and Box-and-Whisker diagrams of the 37 cases. It agrees with the results in table 6.1 that the segmentation of the *Left Ventricle* was better than other surface categories. The worst case for the *Left Ventricle* was subject-119, from a healthy volunteer, with a RMS surface error of 2.38 mm; the worst case of the *Epicardium* was subject-43, from a Tetralogy of Fallot patient, with a RMS surface error of 5.43 mm. The segmentation by the proposed method and the gold standard segmentation are shown in Figure 6.5. The worst segmentation of other surface categories was from subject-9, shown in Figure 6.4.

Finally, Figure 6.7 shows the colour map of surface-to-surface errors of the whole heart segmentation. One can realise from this map that the large errors were mainly distributed to the area of connections between substructures. For example, the area between the right ventricle and pulmonary artery was one of the worst regions. Similar situation was found in the areas between the left atrium and pulmonary veins and left auricula. The proposed method also had a moderate error range in a small part of the endocardium of the right ventricle. This was because there were many pathological cases which exhibited a thickened right ventricle myocardium, while the atlas image did not include such myocardium. The segmentation therefore could incorrectly segment part of the myocardium into the right ventricle blood cavity due to this ambiguity. Examples of this error can be found in cases of subject-1 and subject-9 in Figure 6.4.

Table 6.2 presents the mean segmentation errors and their worst cases in volume measures. This table also gives measures calculated based on all substructures in the column *All substructures*. The worst cases for each substructure using the Dice measure were subject-116 (*Left Ventricle*), subject-9 (*Left Atrium*), subject-10 (*Right Ventricle* and *Right Atrium*), and subject-43 (*Myocardium*). The segmentation of subject-116 and subject-9 are displayed in Figure 6.4 and that of subject-10 and subject-43 are shown in Figure 6.5.

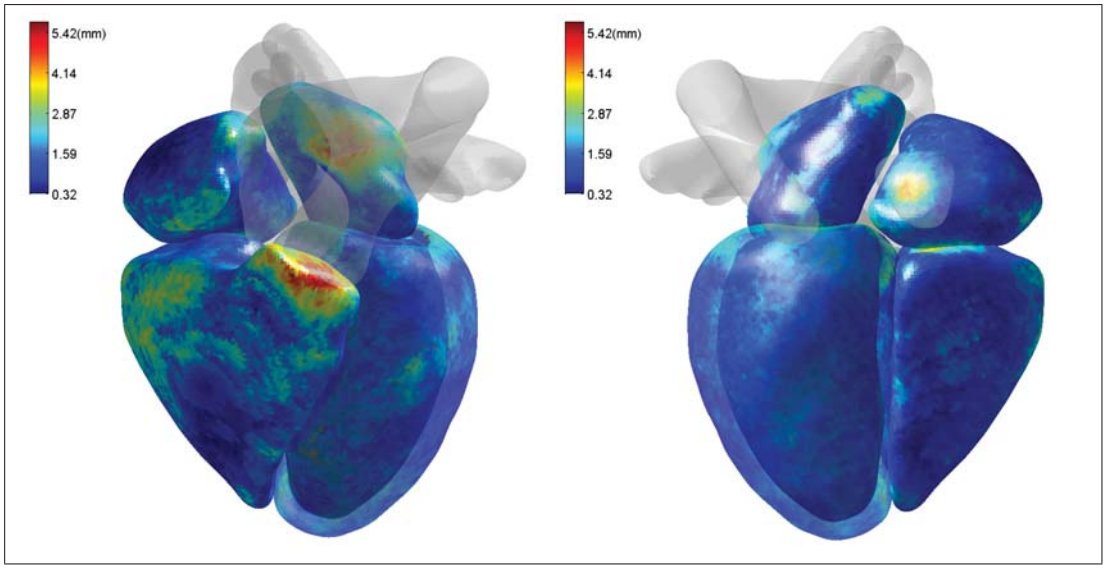

Figure 6.7: Two views showing the error map of surface-to-surface distance for the whole heart segmentation by the proposed method. (Please refer to the web version of this article for interpretation of the color map. A movie showing the color map from other angles can also be found at http://www.cs.ucl.ac.uk/staff/X.Zhuang/.)

Table 6.2: Segmentation errors by the proposed method using volume measures: Dice coefficient, volume overlap, percentage of volume difference (Diff), p-value and 0.95 confidence interval (CI) of the difference of the segmentation errors, unit mL, and Pearson correlation R.

Structures	Dice[min]	Overlap[min]	Diff(%)[max]	P-value (CI mL)	Pearson R
Left Ventricle	0.92 ± 0.02[**0.87**]	0.85 ± 0.04[**0.78**]	6.5 ± 4.9[**19.0**]	0.028 (0.5,7.5)	0.942
Left Atrium	0.81 ± 0.10[**0.47**]	0.69 ± 0.12[**0.30**]	14.1 ± 12.0[**48.4**]	0.667 (-2.7,4.2)	0.861
Right Ventricle	0.87 ± 0.04[**0.77**]	0.77 ± 0.06[**0.63**]	7.5 ± 4.9[**19.7**]	0.048 (0.1,12.3)	0.977
Right Atrium	0.84 ± 0.05[**0.71**]	0.73 ± 0.07[**0.55**]	9.0 ± 7.2[**28.7**]	0.217 (-6.8,1.6)	0.965
Myocardium	0.77 ± 0.06[**0.52**]	0.63 ± 0.07[**0.35**]	8.6 ± 6.9[**26.7**]	0.940 (-4.7,5.1)	0.892
All substructures	0.84 ± 0.08[**0.47**]	0.73 ± 0.10[**0.30**]	10.0 ± 9.6[**48.4**]	0.097 (-0.3,3.7)	0.974

From Table 6.2, we can see that there was no significant difference between the volumes of the gold standard and the propagated segmentation for the *Left Atrium* ($P = 0.667$), the *Right Atrium* ($P = 0.217$), the *Myocardium* ($P = 0.940$), and the *All substructures* volume ($P = 0.097$). However, the difference was found for the *Left Ventricle* ($P = 0.028$) and the *Right Ventricle* ($P = 0.048$). This was due to biases of the segmented volumes, shown in their confidence intervals. Figure 6.8 shows the Bland-Altman plots of the volumes, which confirms that both the *Left Ventricle* and the *Right Ventricle* had segmentation biases of 4.3 mL and 6.2 mL respectively. The larger bias of *Right Ventricle* were partly due to the inconsistent definition of the valves between the gold standard and the propagated segmentation, as the *Right Atrium* had -2.6 mL segmentation bias. Considering the ranges of their volumes were 67-204 mL and 65-488 mL, these biases should be practically unimportant. The bias for the segmentation of all substructures was 1.70 mL. Finally, their Pearson correlation coefficients are also given in table 6.2.

Figure 6.9 plots Bland-Altman and linear regression for the segmentation of all substructures. The proposed segmentation framework produced a mean bias of 1.7008 mL, which was

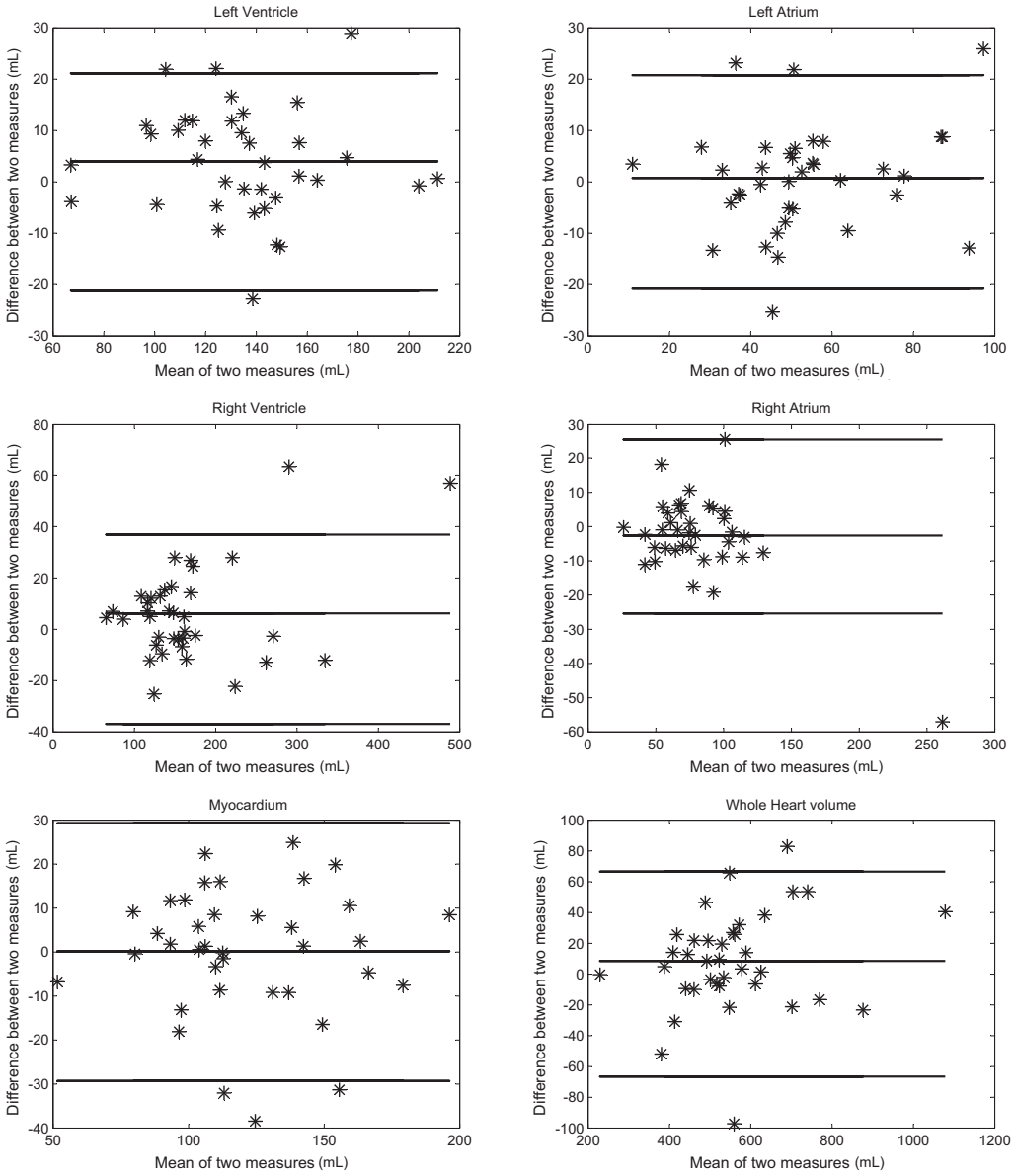

Figure 6.8: Bland-Altman plots of the segmented volumes using the proposed method and the gold standard segmentation volumes, for the blood cavities of the left ventricle, the left atrium, the right ventricle, and the right atrium, the volume of the left ventricle myocardium, and the whole heart volume including all these substrucutres. Middle line is the bias (mean), upper and lower lines are the 2 standard deviations.

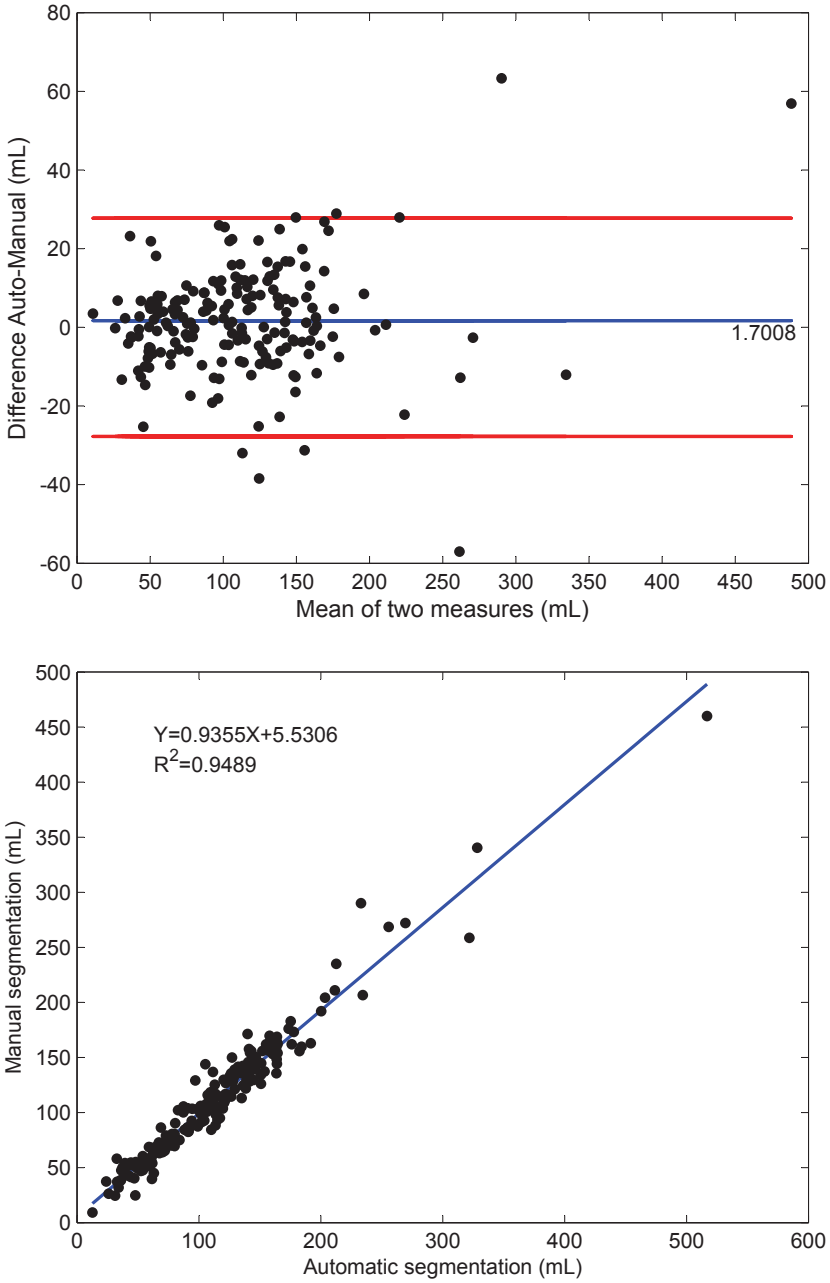

Figure 6.9: Bland-Altman plot (top) and linear regression plot (bottom) of all segmented volumes using the proposed method and the gold standard segmentation volumes.

relatively small compared to the mean value of these volumes 111.26 mL, and the regression value was 0.9489.

6.5 Conclusion

The majority of works in the literature reported mean surface distance (ϵ_{mean}) around 1.5 to 3.0 mm for ventricle segmentation. In recent works, Lynch et al. (2008) achieved 1.25 ± 1.34 mm for ventricle segmentation of cine MR data using level-set. Koikkalainen et al. (2008) investigated several artificial enlargement of the training set for statistical shape model and compared their performance in whole heart segmentation of MR data. A best result of 2.06 ± 0.58 mm (mean surface distance) was reported. Cocosco et al. (2008) validated their segmentation results using regression of segmented volumes and reported $R = 0.968$ (left ventricle) and $R = 0.969$ (right ventricle). Kurkure et al. (2009) reported a mean Dice number of 0.855 ± 0.123 for ventricle segmentation from cine cardiac MR images. van Assen et al. (2008) presented a semi-automatic method using a 3-D active shape model driven by fuzzy inference. They reported mean surface distance errors of 1.72 mm (encodardium) and 1.55 mm (epicardium) for ventricle segmentation of short-axis 3-D MR data from 15 healthy subjects. Finally, Peters et al. (2009) achieved 0.76 ± 0.30 means surface distance error for the whole heart segmentation, which is the best result reported to our knowledge. Their method was based on a deformable model trained with statistical shape information. However, the validation was not independent, as the meshes of gold standard segmentation came from the same mesh model of their segmentation tool with manual correction. Also, the testing data seemed to have the same or similar pathology. Therefore, an objective inter-work comparison is difficult due to the different testing datasets.

We have presented a registration-based segmentation propagation framework incorporating the new techniques we developed in the last two chapters. The segmentation method showed the potential of being able to segment the pathological data using an atlas constructed from healthy subjects. We showed that no significant difference was found by using the three atlases constructed from training sets of healthy subjects to segment the pathological cases. Additionally, we showed that the segmentation errors had been significantly reduced by the two proposed registration algorithms: the proposed locally affine registration method (LARM) for substructure initialisation and the proposed free-form deformations registration with adaptive control point status (ACPS FFDs) for refinement of local details. The proposed segmentation framework achieved a RMS surface-to-surface error of 2.14 ± 0.63 mm and a Dice measure of 0.84 ± 0.08 between the propagated segmentation and the gold standard segmentation.

It should be noted that we used an atlas constructed from healthy subjects for the segmentation of pathological data. In practice, one may construct an atlas from the training data with similar heart shapes and pathologies to the unseen data and achieve much better segmentation accuracy. For example, the RMS surface distance segmentation error for the test set only containing healthy subjects was 1.79 ± 0.44 mm, which was lower than the error of 2.14 ± 0.63 mm calculated for the test set including pathological subjects.

Chapter 7

Preliminary Results of Exploratory Extension Work

The segmentation framework in Chapter 6 is extendible to other applications. In this chapter, we will explore three applications: whole heart segmentation from multi-slice cardiac MRI in Section 7.1, whole heart segmentation from compounded 3D echocardiography in Section 7.2, and whole heart segmentation framework combined with the multi-atlas strategy in Section 7.3. The preliminary results are also presented.

7.1 Whole heart segmentation from multi-slice cardiac MRI

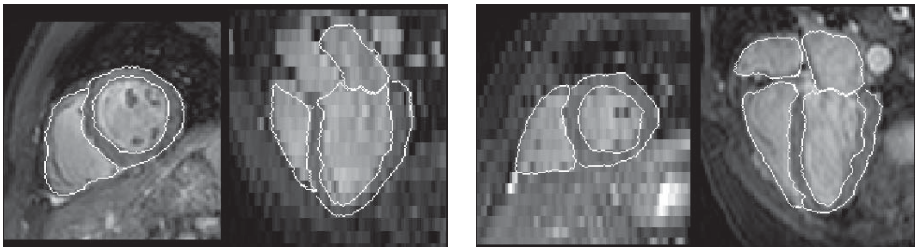

Figure 7.1: The short-axis and long-axis slices of the short-axis multi-slice (left) and long-axis multi-slice (right) segmentation examples.

A large number of cardiac MR segmentation works in the literature are on the multi-slice images which are currently more routinely used for cardiology studies (Kaus et al., 2004; Hautvast et al., 2006; van Assen et al., 2006; Lynch et al., 2008; Kurkure et al., 2009). In this section, we resample the 3D volumes to simulate multi-slice cardiac MRI and extend the segmentation framework for these data. For example, Figure 7.1 shows two segmentation examples of the short-axis and long-axis multi-slice images resampled from two 3D volumes.

7.1.1 Data and experimental setup

The test data are the thirty-seven 3D volumes used for the whole heart segmentation validation in Chapter 6. They are resampled into $1 \times 1 \times 8$ mm to simulate the multi-slice cardiac MR data. The original manual segmentation of the 3D volumes is regarded as the gold standard segmentation of the simulated multi-slice data. We employ the same atlas and segmentation framework used in Section 6.4.4 for the segmentation of the multi-slice MR data, and the surface-to-surface error measures and volume measures used in Section 6.4.1 for accuracy assessment.

It should be noted that the simulated images may not be representative of real clinical data. For example, clinical data are normally used for the assessment of the ventricle and ventricular function, and hence the coverage is limited to the ventricles only. Also, many clinical protocols use multi-chunk, breath-hold imaging where the surfaces between slices have poorer continuity than the simulated data. However, the image quality of multi-slice imaging provides better image quality within slices, in particular, higher signal to noise ratio and contrast to noise ratio. The initialisation of ventricle is also easier as all the images and template atlas can be truncated to the short-axis ventricle regions. Therefore, we could expect better results from the validation using an atlas constructed from real clinical data and the test set of real clinical data.

7.1.2 Results and discussion

Table 7.1: Surface-to-surface segmentation errors, ϵ_{rms}, ϵ_{mean}, ϵ_{std}, and the volume measures, Dice coefficient, volume overlap, percentage of volume difference (Diff), and Pearson correlation of the 37 cases,. *Whole Heart* in volume measures means *All Substructures*.

Structures	ϵ_{rms} (mm)	ϵ_{mean}	ϵ_{std}	Dice	Overlap	Diff (%)	Pearson
Left Ventricle	1.60 ± 0.31	1.15	1.11	0.91 ± 0.02	0.84 ± 0.04	7.2 ± 5.3	0.933
Left Atrium	2.68 ± 1.26	1.91	1.88	0.79 ± 0.12	0.67 ± 0.13	19.8 ± 20.3	0.831
Right Ventricle	2.22 ± 0.69	1.56	1.57	0.86 ± 0.04	0.76 ± 0.06	8.6 ± 6.6	0.974
Right Atrium	2.75 ± 1.27	1.89	1.99	0.81 ± 0.06	0.69 ± 0.08	11.5 ± 8.3	0.937
Epicardium	2.57 ± 0.87	1.86	1.77	0.75 ± 0.06	0.61 ± 0.07	10.4 ± 8.7	0.874
Whole Heart	2.39 ± 0.73	1.63	1.74	0.82 ± 0.05	0.71 ± 0.06	11.5 ± 6.7	0.967

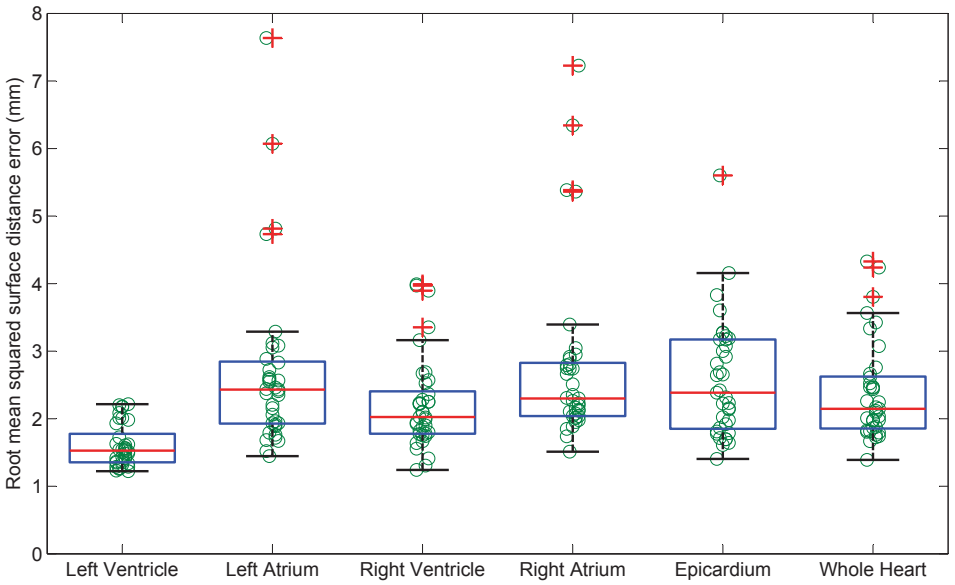

Figure 7.2: The individual plots and the Box-and-Whisker diagrams of the segmentation errors using the RMS surface distance measure, ϵ_{rms}. This figure gives the errors of each substructures as well as the *Whole Heart* from the 37 simulated multi-slice cases.

Table 7.1 provides the three surface-to-surface errors measures and the volume measures of the propagation results against the standard segmentations. The results are promising, particularly, the segmentation of ventricles which are the main interest of applications using multi-slice MRI. Figure 7.2 plots the errors (ϵ_{rms}) and Box-and-Whisker diagrams of the 37 cases in each substructures as well as the *Whole Heart*. Notice that the corresponding numbers and

figure of the segmentation of the original 3D volumes are presented in Table 6.1 and 6.2, and Figure 6.6. The segmentation of multi-slice images is not as good as that of the original 3D volumes. The *Whole Heart* errors, ϵ_{rms}, are significantly different ($P < 0.001$, and the 0.95 confidence interval is $[0.1519, 0.3454]$ mm). However, the robustness of the segmentation on the two data sets is similar as the maximal errors (4.31 versus 4.33 mm) and standard deviations (0.63 versus 0.73 mm) of their *Whole Heart* ϵ_{rms} errors are similar. The difference of segmentation accuracy is probably due to the poor resolution of the simulated multi-slice data between slices (8mm). Particularly, this poor resolution results in larger difference of the atria and myocardium segmentation where the volume sizes of the structures are relatively smaller.

7.2 Whole heart segmentation from compounded 3D echocardiography

7.2.1 Motivation

Ultrasound (US) imaging is a safe, low-cost, portable, and real-time interactive imaging technique, providing anatomical and diagnostic information for functional analysis. Three dimensional (3D) cardiac ultrasound, also known as echocardiography or echo by cardiologists, has the potential of providing more accurate quantitative analysis. However, most methods require some form of segmentation process, which can be difficult to automate due to the typically low signal-to-noise and small fields of view in US imaging.

Several papers have reported successful attempts at US segmentation in the literature (see survey from Noble and Boukerroui (2006)). Most of the reported segmentation algorithms use deformable models or contour models to search for optimal boundaries, with prior constraints to maintain an anatomically realistic shape of the segmented regions. These methods have either limited robustness or automation, similar to the problems which arise when they are applied to cardiac MRI as we discussed in Section 3.1. By contrast, no work has been published, to the best of our knowledge, on employing image registration techniques to perform atlas and segmentation propagation on US images. This is probably due to the difficulty of achieving a successful nonrigid registration using echo images. Furthermore, the current reported works mainly focused on the left ventricle or myocardium (Mitchell et al., 2002; Orderud et al., 2007; Zhu et al., 2007, 2009; Rajpoot et al., 2009a) due to the limited field of view of the acoustic window from US imaging. Whole heart segmentation, unlike the ventricle segmentation, can however provide more useful information for cardiology such as whole heart functional analysis, computational modelling, and guidance of interventional procedures. This whole heart anatomical information is mainly available from MRI or CT. It is anticipated if this information can also be extracted from US images, since it is the most commonly used modality for cardiac diagnosis. This segmentation also provides an important alternative choice for cardiologists when MRI and CT are not available or not appropriate for some patients.

Recently, compounding techniques have been shown to produce 3D echo images with a much wider field of view and better image quality than that from a single US scan (Grau and Noble, 2005; Grau et al., 2007; Yao et al., 2009; Rajpoot et al., 2009b). These compounded images are created by aligning and then combining the intensity information from multiple US image volumes. Figure 7.3 shows the example of two single-scan images and a compounded

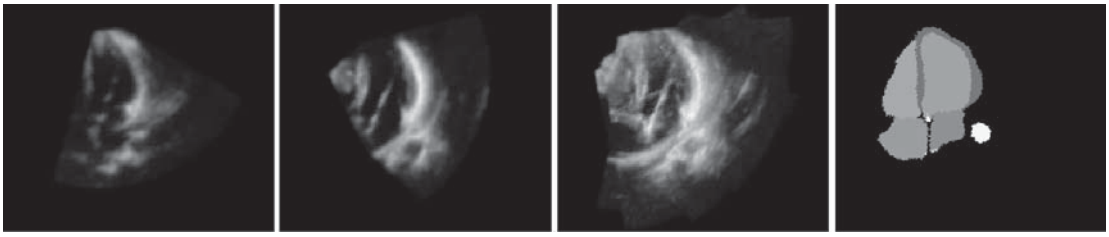

(a) (b) (c) (d)

Figure 7.3: Example images and outputs from algorithms used during segmentation process, (a) view from apical scan; (b) view from parasternal view; (c) compounded image from 12 scans; (d) corresponding segmentation labels of (c).

image. The extended field of view has the potential of having whole heart coverage to carry out the whole heart segmentation, and the combined intensity information can significantly reduce intensity variations of tissues and boundaries presented in single-scan US images. The resultant images hence have more consistent intensity distributions between the atlas and the US images to be segmented. This consistency of intensity distributions enables the registration algorithms to use intensity information for the atlas propagation-based segmentation framework.

Furthermore, the local phase analysis of US images provides a continuous scalar value to describe the feature presented in the image. Hence, intensity-based registration can also be applied to US images by considering the local phase value as *feature intensity* (Mellor and Brady, 2005; Zhang et al., 2007). Also, a similarity measure computed from local geometrical information such as normal vector of image intensity, also referred to as normalised gradient, was argued to be applicable to images with different intensity distributions (Zhuang et al., 2005; Haber and Modersitzki, 2006). This local geometrical information is based on observation of image structures and hence applicable to US images. Therefore, we propose to use more information from the compounded echo images for the computation of the similarity measure, including intensity information, local phase information, and local geometrical information.

Finally, it has been shown that the registration-based segmentation propagation framework can achieve a successful application in cardiac MR images in chapter 6. One main advantage of this segmentation framework is that it does not require a training phase from a large dataset for different pathologies, unlike the segmentation using statistical prior knowledge. Instead, it only needs the prior segmentation of the template image, the atlas, to perform the propagation. This framework is potentially applicable to a wide range of pathologies owing to the substructure initialisation provided by the locally affine registration method (LARM). This segmentation framework also has the potential of being applicable to other modalities including US imaging given a similarity measure for echo registration is achievable.

7.2.2 Method

7.2.2.1 Echo and echo compounding

The echo system includes a 2D matrix array transducer X3-1 on Philips iE33 system, Philips, the Netherlands. The acquisition has an opening angle of roughly 80 degrees and a maximal penetration depth between 15 and 18 cm.

Compounding US images can have three potential advantages:

- extension of the field of view,
- reduction of the speckle and artefacts and increase of the signal-to-noise ratio (Rohling et al., 1997),
- reduction of the intensity inconsistency due to the different incidence angles in the acquisitions.

The better image quality and better intensity consistency increase the confidence of using intensity-based similarity measures, while the wider field of view provides the potential to carry out whole heart functional analysis from cardiac US.

The following techniques are adopted to produce compounded images. Firstly, we acquire over ten US images for each subject using a variety of acoustic windows and probe positions. The aim is to achieve a maximal coverage of the heart from different angles. Triggered by electrocardiography (ECG) gating, wide sector acquisitions are taken with volunteers positioned in the left lateral decubitus position, breath-hold at end-exhale. At the same time, the echo transducer is attached with an array of light emitting diodes to enable its tracking during acquisitions. A probe calibration matrix is calculated as described by Ma et al. (2009). This matrix along with the probe tracking matrix is used to provide a starting estimate for image alignment. The alignment of all echo images is achieved by performing the semi-simultaneously (group-wise) registration scheme (Wachinger et al., 2007) and using the similarity measure of local phase and orientation information proposed by Grau et al. (2007). Figure 7.3 (c) shows the four-chamber view of a compounded image from 12 scans using the maximum method (Yao et al., 2009).

The echocardiography data were acquired and then compounded in St. Thomas' Hospital, London.

7.2.2.2 Registration for compounded echo and whole heart segmentation

The registration uses three different types of information extracted from the compounded 3D echo: image intensity I, local phase ϕ, and local geometric information $\vec{v}$.

The local phase ϕ, providing a quantitative, continuous and contrast invariant description of local features in images, can be derived using the monogenic signal (Mellor and Brady, 2005; Grau et al., 2007):

$$\phi(\mathrm{x}) = \mathrm{atan2}(\sqrt{\sum_{i=1}^{3}(g(\mathrm{x}) * h_i(\mathrm{x}) * I(\mathrm{x}))^2},\ g(\mathrm{x}) * I(\mathrm{x})), \tag{7.1}$$

where, g is the log-Gabor filter, convoluted with I to constitute the even component of the signal; $\{h_i\}$ are the odd anti-symmetric filters in the spatial domain, $i = 1, 2, 3$. More detail of the computation of local phase can be found in Section 3.2.3.

The local orientation, which denotes the perpendicular direction to the boundaries, can be computed from the normal vector of image intensity:

$$\vec{v}(\mathrm{x}) = \frac{\nabla I(\mathrm{x})}{||\nabla I(\mathrm{x})||}\ , \tag{7.2}$$

or the normal vector of local phase

$$\vec{v}(\mathrm{x}) = \frac{\nabla\phi(\mathrm{x})}{||\nabla\phi(\mathrm{x})||}\,, \tag{7.3}$$

since both intensity and local phase should present the same geometrical information of the image.

Combining intensity, local phase and local geometric information, we propose the following metric for the similarity measure of target image I_t and source image I_s:

$$\mathcal{C} = w_c\mathtt{NCC}(I_t, I_s) + w_f\mathtt{NCC}(\phi_t, \phi_s) + w_v\frac{1}{|\Omega|}\int_{\mathrm{x}\in\Omega}[\vec{v}_t(\mathrm{x})\cdot\vec{v}_s(\mathrm{x})]\,, \tag{7.4}$$

where Ω is the image volume, $\mathtt{NCC}(I_t, I_s)$ and $\mathtt{NCC}(\phi_t, \phi_s)$ are the normalised cross correlation (NCC) of the image intensity and phase; w_c, w_f, and w_v control the weight given to each terms.

For registration of cardiac images, we have proposed to use LARM registration to initialise the anatomical substructures between the atlas and the unseen image. LARM defines the local affine transformations based on the anatomical substructures of the heart, and it can preserve the local shape of substructures and provide a robust registration for the following nonrigid registration.

Therefore, we also adopt the locally affine transformation model for the substructure initialisation registration here. The segmentation propagation hence includes the following three steps:

- affine registration to localise the heart structure,
- LARM to further initialise the anatomical substructures, using four local affine transformations associated with the blood cavities of the four chambers,
- free-form deformation (FFD) registration (Rueckert et al., 2006) to refine the registration of the local details.

Gradient ascent optimisation is used for the three image registration processes. In LARM and FFD registrations, the local phase is not transformation invariant, and so updating local phase is computationally expensive. Therefore, we only re-estimate the local phase after every few iteration steps, typically 10 steps to ensure that errors do not accumulate.

7.2.3 Experiment

Data and experimental setup: To construct gold standard segmentation for validation, we acquired a 3D isotropic MR image at the end-diastolic cardiac phase (same phase as used for the compounded echo images) for each subject before acquiring the echo images. An automatic whole heart segmentation of the MR image was then achieved using the segmentation method we developed in Chapter 6 where a mean accuracy of 9.1% volume difference was reported for the segmentation of the four chambers. This segmentation of the MR image was then assumed to be the gold standard segmentation of the corresponding 3D echo with a rigid transformation from the MR image to the echo image. The rigid transformation was obtained using a feature-based registration algorithm (Ma et al., 2009). The registrations were also visually inspected,

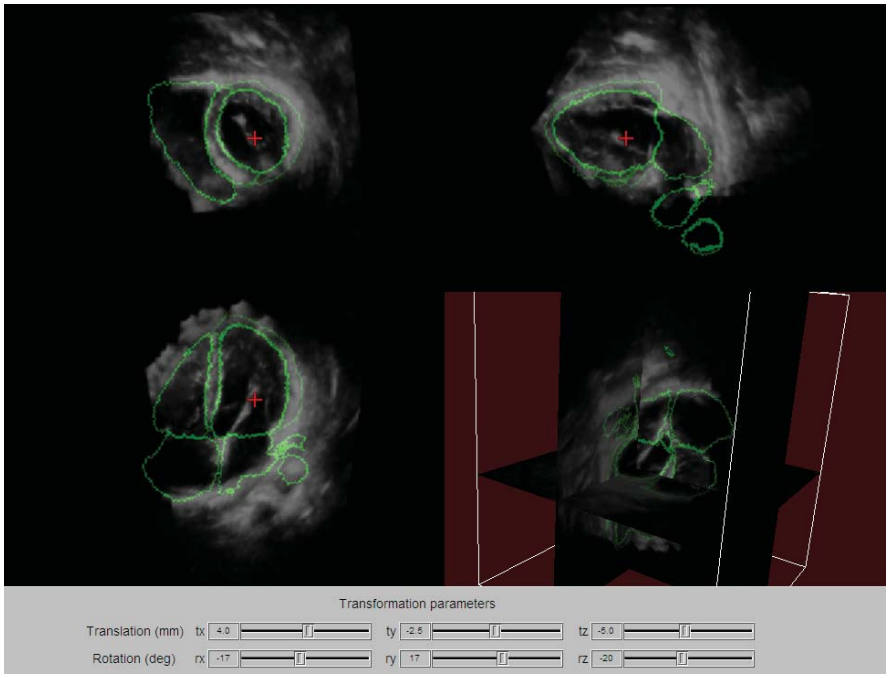

Figure 7.4: Manual correction to construct the gold standard of a compounded 3D echo. Top-left: short-axis view; top-right: two-chamber view; bottom-left: four-chamber view; bottom-right: orthogonal planes.

and small manual corrections were carried out if errors were observed. Figure 7.4 demonstrates an example of manual inspection. It should be noted that independent segmentations from MR and echo images may not perfectly match (Takuma et al., 2001). This is because the different acquisition positions from MRI (supine) and echo (left lateral decubitus) cause some deformation to the heart, in particular for the aorta. However, this difference in the four chambers, to be validated in this study, is practically negligible compared to the segmentation errors.

Twelve propagation cases were evaluated using four sets of echo and MR data and a validation strategy as follows: A dataset was chosen to represent the atlas, which was comprised of the compounded 3D echo and the label image produced by segmenting the MR volume, an example is shown in Figure 7.3 (c) and (d). This atlas was then propagated to segment the other three datasets. The above was repeated four times, taking a different dataset to represent the atlas each time. Segmentation results were assessed by comparison with the MR-derived gold standard using the volume difference measure,

$$\mathrm{VD} = \frac{2(|V_{seg} - V_{gd}|)}{V_{seg} + V_{gd}} \times 100\%, \tag{7.5}$$

where V_{seg} is the resultant segmentation, while V_{gd} is the gold standard. The volume measure was performed on the blood pools of the four chambers and the left ventricle myocardium. The average volume of the five regions was also computed, referred to as Whole Heart.

Result and discussion: Table 7.2 gives the mean segmentation accuracy of the twelve cases, while Figure 7.5 illustrates the visual results of four segmentation cases. The performance of the segmentation algorithm is promising; in particular, the algorithm achieved success in the four-

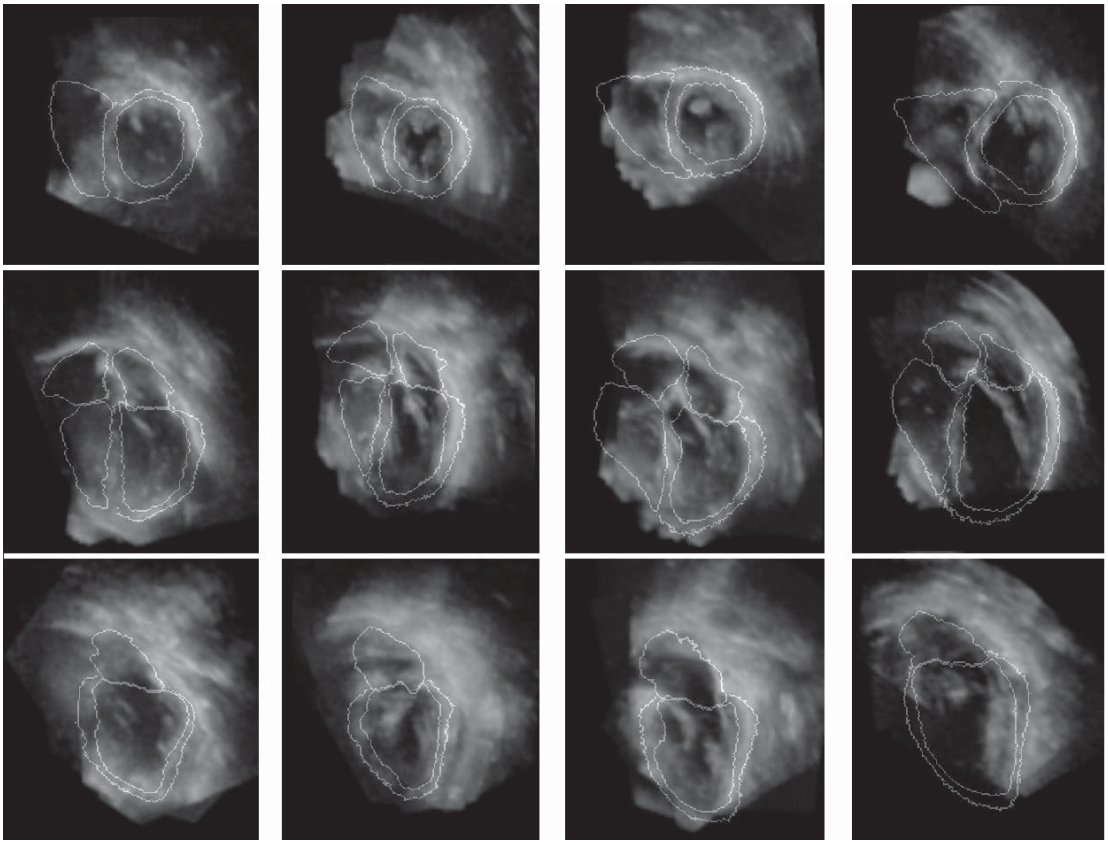

Figure 7.5: Illustration of the segmentation propagation results of four cases. The first row is short-axis view, the second row is the four-chamber view and the third row is the two-chamber view.

chamber regions which were not fully covered in the compounded image. This was probably owing to the good initialisation from LARM which registered the four chambers with locally affine transformations and maintained the local shapes of the four chambers between the atlas and the unseen image.

The segmentation achieved the best result in the left ventricle, the main interest of many echo segmentation works. This accuracy ($6.4 \pm 4.7\%$) is also comparable to the result ($6.5 \pm 4.9\%$) of the MR segmentation in Chapter 6. The segmentation of the two atria was worse. This may be due to the strong artefacts presented in the region of the left atrium and the incomplete coverage of the right atrium, as seen in the example images Figure 7.5.

Table 7.2: The segmentation accuracy presented in volume difference. Row *Before* means the segmentation before the nonrigid registration (but after a global affine registration), row *After* means after the nonrigid registration.

(%)	LeftVentricle	LeftAtrium	RightVentricle	RightAtrium	Myocardium	WholeHeart
Before	23 ± 14	29 ± 15	16 ± 9.0	22 ± 11	22 ± 12	22 ± 13
After	6.4 ± 4.7	16 ± 12	9.4 ± 9.5	16 ± 12	15 ± 13	14 ± 12

7.3 Whole heart segmentation using multi-atlas strategy

In atlas-based segmentation, multi-atlas or multi-template is a useful strategy (Rohlfing and Maurer, 2005; Aljabar et al., 2007, 2009; Lotjonen et al., 2010) to improve the segmentation. It has been shown that it is important to achieve successful nonrigid registration between the atlases and unseen images (Aljabar et al., 2007, 2009; Lotjonen et al., 2010). Therefore, the registration scheme including LARM and ACPS FFDs used in the segmentation framework will be needed in the multi-atlas methods. In this section, we employ two multi-atlas schemes to segment each of the five substructures of the heart and compare the results with that from the single atlas propagation.

7.3.1 Method

7.3.1.1 Atlas selection

In atlas segmentation framework, it is commonly assumed that the more similar the atlas to the unseen image, the better the segmentation using the atlas would be. This is applied to the multi-atlas schemes to use a limited number of atlases. In this study, we will use two methods to rank the atlases for the segmentation of each subject and fuse the segmentation results from the best ranked atlases.

- **Prior information using image similarity:** For a given unseen image, we first employ a *selection registration* to register each of the available atlases to the unseen image and then compute the image similarity values after the registration. The similarity values are then used as the rank of the atlases for the subject in the selection. The normalised mutual information (NMI) (Studholme et al., 1999) is as the similarity measure.

- **Posterior information using segmentation similarity:** For a given unseen image, we first employ the single-atlas segmentation propagation framework to achieve the segmentation using each of the available atlases. Then, the segmentation results are ranked according to their mean Dice coefficient values against the gold standard segmentation of the unseen image. This mean Dice value of the five substructures, the four chamber blood pools and myocardium of the left ventricle, is then used as the segmentation similarity for selection. It should be noted that this posterior information is practically unavailable information for atlas selection. It is used to show the possible best result using the multi-atlas segmentation scheme.

7.3.1.2 Registration

- **Propagation registration:** The propagation registration is the process of registering the selected atlas to the unseen image. This is the same as the framework described in the whole heart segmentation in Section 6.2, consisting of global affine registration, locally affine registration method (LARM), and free-form deformation registration with adaptive control point status (ACPS FFD).

- **Selection registration:** In the atlas selection using image similarity, the unseen image needs registering to each of the atlases to compute the NMI values. This registration is required to be fast compared to the segmentation propagation process, because the number of atlases is normally much greater than the number of atlases selected. Therefore,

we propose to employ a global affine registration followed by a LARM process, the first two steps used in the propagation registration, for the selection registration.

7.3.1.3 Fusion

Given n atlases have been selected for propagation, n segmentation labels are then generated for each substructure, U_i, i=1 . . . n. The fused segmentation of a substructure is then given by (Lotjonen et al., 2010):

$$U = \frac{1}{n} \sum_i U_i \tag{7.6}$$

To obtain a binary segmentation label, a threshold, typically 0.5, is used.

7.3.2 Data and experimental setup

The test data are the 21 cardiac MR images which have been manually segmented the four chambers and great vessels using the same tool, a mesh model with manual correction (Peters et al., 2007). Figure 4.12 shows an example of the image and manual segmentation. The manual segmentation is used as the atlas label image for propagation as well as the gold standard. It is also available from the manual segmentation to construct the label images of the substructures, used for LARM, and the mask images, used for ACPS FFD registration, required in the propagation registration.

The experiment adopts the *leave-one-out* validation strategy: For each MR image, considered as an unseen subject, the other 20 MR data and the corresponding atlas label images are used as available atlas pool. In this experiment, three segmentation schemes are used for comparisons:

- **Mean atlas**: In this segmentation, the available atlas images are used to construct a mean shape atlas as the process described in Chapter 6. The propagation is then based on the mean intensity MR image and the mean atlas label image. The segmentation of each subject only needs one propagation registration and no fusion is required.

- **NMI similarity**: In this segmentation, each of the available atlases is propagated to the unseen subject using the propagation registration. Then, n best ranked results are selected for fusion of each substructure. The similarity measure in this ranking is based on the *prior information using image similarity*.

- **Post information**: In this segmentation, each of the available atlases is propagated to the unseen subject using the propagation registration. Then, n best ranked results are selected for fusion of each substructure. The similarity measure in this ranking is based on the *posterior information using segmentation similarity*.

7.3.3 Results and discussion

Figure 7.6 shows the mean Dice coefficient values of the propagation segmentation against the gold standard for each substructure and the mean of the 5 substructures. The multi-atlas schemes are seen to improve the segmentation accuracy compared to using single-atlas propagation. The diagrams of *Post information* shows that the best accuracy is achieved using the number of 5 to 10 “best” atlases. The accuracy tends to decrease after more than 10 segmentation are fused. For the segmentation of *NMI similarity*, the accuracy is evidently improved using

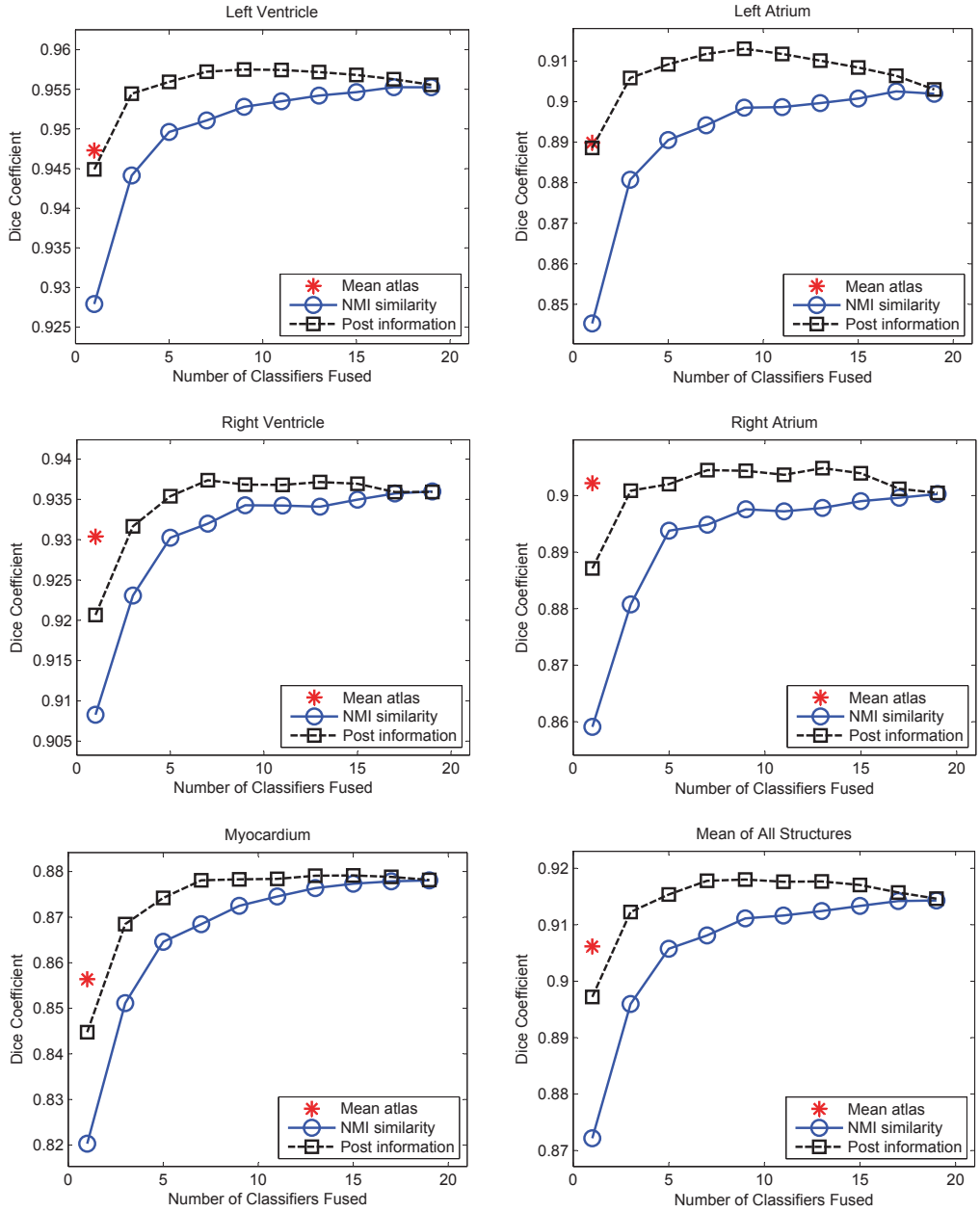

Figure 7.6: The segmentation accuracy, assessed by Dice coefficient, of each substructure and the mean of the five structures. The results of three segmentation framework are presented: the segmentation propagation by using single *Mean atlas*, using multi-atlas ranked by the prior information of *NMI similarity*, and multi-atlas ranked the posterior information of Dice segmentation errors, referred to as *Post information*.

less than 10 atlases for fusion. The accuracy is improved less significantly using more than 10 atlases. The difference indicates that the atlas selection is important not only for the accuracy of segmentation, but also for providing a feasible framework within an affordable computation expense.

Furthermore, the segmentation of *Mean atlas* out performs the best segmentation in *Post information* when using the *one best atlas* propagation. In particular, the segmentation of right atrium by *Mean atlas* is better than the multi-atlas scheme using *NMI similarity*. This is probably due to the fact that the atlas intensity image of the mean atlas has much better image quality such as low noise and few artefacts. In atlas propagation, there are two main factors that affect the segmentation performance: the atlas image quality and the shape difference between the atlas and unseen image. Since LARM is employed to cope with the challenge due to the shape difference, it is concluded that it is more important to use an atlas whose atlas intensity image has better image quality such as with high contrast to noise ratio.

Finally, the whole heart segmentation result includes five labels, the four chambers and myocardium. It is still problematic to employ the traditional fusion method to maintain a diffeomorphic segmentation in the resultant fusion, i.e. the fused whole heart segmentation should not have local regions overlap each other (overlap segmentation) or unrealistic empty regions between two connected tissues (empty segmentation). Figure 7.7 shows the two examples. In the future, alternative techniques should be considered to provide a more realistic and reasonable fusion, such as the shape-based averaging method (Rohlfing and Maurer, 2007) and the simultaneous truth and performance level estimation (STAPLE) algorithm (Warfield et al., 2004).

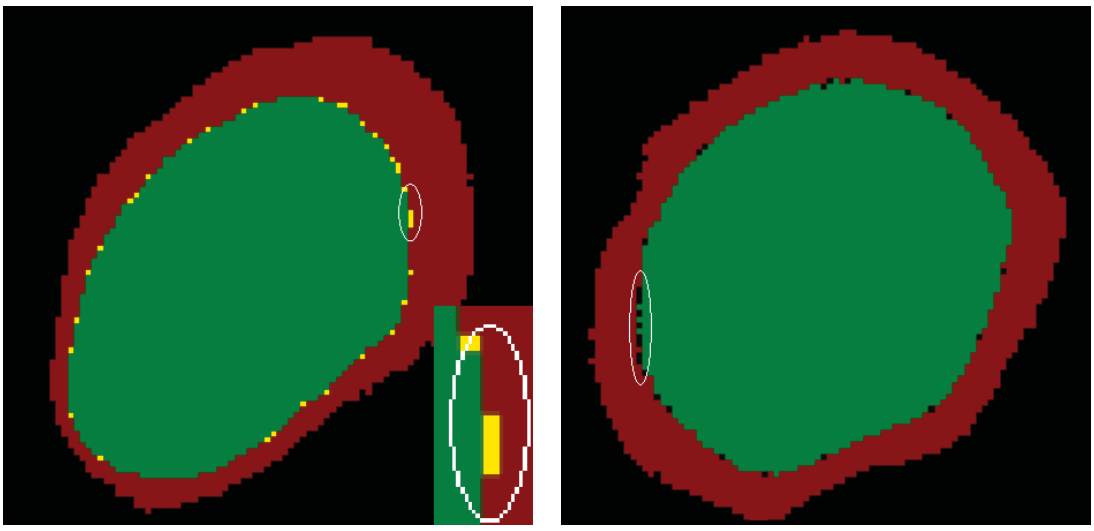

Figure 7.7: The over segmentation (left) and empty segmentation (right) of the left ventricle after fusion.

Chapter 8

Spatial Information Encoded Mutual Information

Mutual Information (MI), an information (entropy) based theory, assumes an *intensity class correspondence* instead of an intensity correspondence between the images in image registration (Viola and Wells, III, 1995; Wells III et al., 1996; Collignon et al., 1995; Maes et al., 1997; Viola and Wells, III, 1997). It has been widely used in many applications and shown to be robust against noise and artefacts, and applicable to images with different intensity distributions, such as those from different imaging modalities (Studholme et al., 1999; Rueckert et al., 1999; Pluim et al., 2003). Recently, some studies showed that this method might not be appropriate in situations when the assumption of intensity class correspondence could not be perfectly met (Studholme et al., 2006; Loeckx et al., 2007, 2010). This chapter will provide an insight into these problems and propose a method of spatial information encoded mutual information (SIEMI) to tackle them.

Section 8.1 gives an insightful interpretation of the problems in MI-based nonrigid registration. Section 8.2 reviews existing works related to the encoding of spatial information. Section 8.3 proposes a unified framework for spatial information encoding and for the SIEMI registration. Section 8.4 presents experiments to study the performance of the SIEMI registration with alternative techniques. Section 8.5 focuses on the applications of the SIEMI registration. Comparisons with the normalised mutual information (NMI) registration are also given. Finally, Section 8.6 draws conclusions.

8.1 Interpretation of the problem

8.1.1 Definition of terms and notations

Intensity distribution: Intensity distribution describes the appearance and contrast of organs presented in a medical image.

Intensity class: It is commonly assumed that imaged intensity values should be related to tissue types in intensity-based registration, for the images such as CT or MRI. Therefore, it is assumed that n_{tis} intensity values are presented in an image scanned from n_{tis} types of tissue. However, the intensity of one tissue type normally has an intensity range in *in vivo* scans due to the non-uniformity of tissue property and noise. Also, a number of different tissue types, referred to as a class of tissue, may have their intensity ranges overlapped. Hence, the intensity distribution of a medical image is presented as n_C classes of intensity ranges, referred to as

intensity classes. It should be noted that the intensity distribution of other imaging modalities, such as ultrasound, where intensity values do not correspond to tissue types, is not within the scope of this study.

Correspondence and mapping of intensity classes: Let I_r and I_f be two images to be registered and T be the transformation to map I_r to the transformed floating image I_f^T. The registration of the two images can be formulated as the maximum of log-likelihood of them, as follows (Roche et al., 2000):

$$\underset{T}{\operatorname{argmax}} \log P(I_r|I_f^T) = \underset{T}{\operatorname{argmax}} \sum_{x\in\Omega} \log p\big(I_r(x)|I_f^T(x)\big).$$

This is a one-direction registration similarity formulation for the registration from image I_r to I_f. Similar similarity can be formulated when we need a symmetric metric for the similarity by considering the registration as two-direction to optimise the two transformations T and T^I:

$$\underset{T,T^I}{\operatorname{argmax}} \log P(I_r|I_f^T)P(I_f|I_r^{T^I})$$

Here, for simplicity of explanation without losing generality, we only use the one-direction asymmetric similarity for following explanation.

It is assumed that one type of tissue in one image should be mapped to the corresponding type in the other. Hence, it is reasonable to define for intensity class C_i, of image I_r, and C_j, of the transformed image I_f^T, that:

$$\begin{gathered}\forall x \in \Omega, \exists C_i, C_j \text{ that } \; I_r(x) \in C_i \text{ and } I_f^T(x) \in C_j \\ \text{then } p\big(I_r(x)|I_f^T(x)\big) = p(C_i|C_j).\end{gathered}$$

The formulation of registration can be related to mutual information in the following form:

$$\begin{aligned}&\underset{T}{\operatorname{argmax}} N\Big(\sum_{C_i,C_j} p(C_i,C_j)\log\frac{p(C_i,C_j)}{p(C_i)p(C_j)} + \sum_{C_i} p(C_i)\log p(C_i)\Big)\\ &= \underset{T}{\operatorname{argmax}} N(MI(I_r, I_f^T, T) - H(H_r))\end{aligned}$$

where $N = |\Omega|$. Therefore, the correspondence of intensity classes is assumed in the MI-based registration (Roche et al., 2000).

Bijective intensity class mapping: In registered images, the intensity classes of them, $\{C_i\}$ and $\{D_j\}$, are mapped: $f_{\text{map}} : C_i \mapsto D_j$. If this mapping is of one-to-one correspondence, it is called a bijective intensity class mapping.

Global intensity class linkage: The intensity class correspondence is found when two images are correctly mapped. However, this global correspondence is normally unknown before the registration due to the erroneous mappings in local regions. The *global intensity class linkage* refers to the intensity class correspondence estimated from the global scale of the two images. This information provides reference of intensity class correspondence for the nonrigid registration of local regions.

Spatial variable s and local region Ω_s: The spatial variable s is an index of a set of

spatial positions, $s = 1 \ldots n_s$. The positions are defined according to the nonrigid transformation parameters. For example, in fluid registration each pixel (or voxel) can be assigned as a value of the spatial variable s, while in free-form deformation (FFD) registration each control point can be assigned as a value of s. It is also common to define a local region Ω_s for s such as the user-defined cubic regions (Studholme et al., 2006) or the local support volume of the FFD control point (Loeckx et al., 2007, 2010).

SIEMI: The vector similarity measure of the spatial information encoded mutual information and its registration implementation using the local ascent optimisation scheme are both referred to as SIEMI.

8.1.2 Insight into the problem

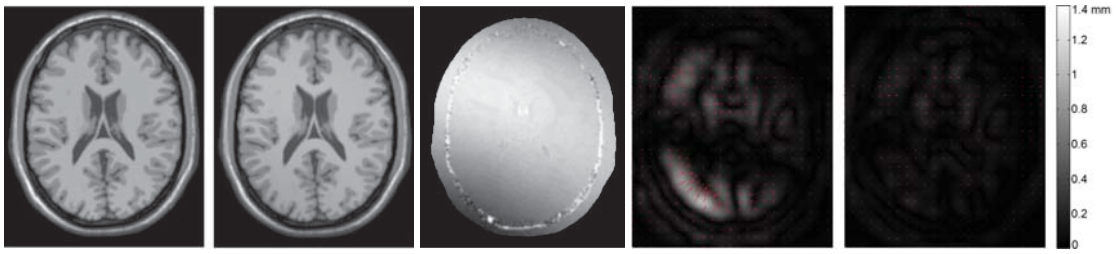

(a) (b) (c) (d) (e)

Figure 8.1: (a) T1-weighted brain image without an intensity non-uniformity field; (b) T1 image with an intensity non-uniformity field; (c) the non-uniformity field map; (d) the deformation field of registering (a) to (b) using normalised mutual information measure; (e) the deformation field of registering the two images using the proposed registration method. The error bar is the indicator for (d) and (e). A larger erroneous deformation is presented in (d) compared to (e). The error of (d) also follows the pattern of the bias field map in (e), while the registration error in (e) is evidently reduced. Brain MR data downloaded from BrainWeb.

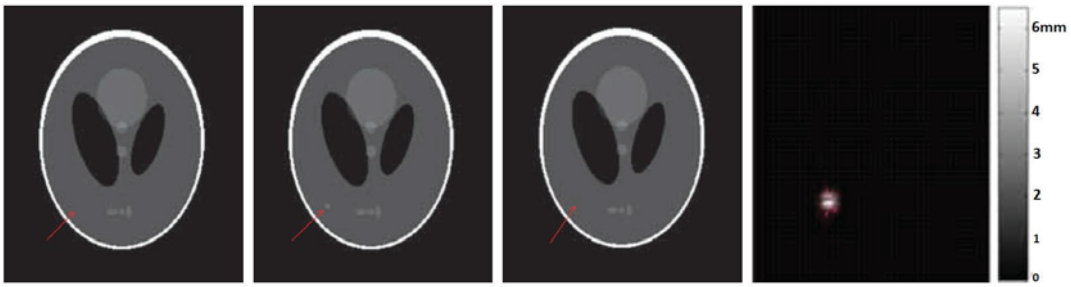

(a) (b) (c) (d)

Figure 8.2: (a) A Shepp-Logan phantom (Jain, 1989, page 438); (b) The same phantom with an extra intensity class, indicated by the arrow, to simulate a tumour or an intensity non-uniformity block; (c) the resultant image of registering floating image (b) to reference image (a), using normalised mutual information: the region was contracted as pointed out by the arrow; (d) the displacement field of the registration described in (c), where red arrows indicate the displacement vector direction. The displacement field of using the proposed registration method is very close to identity and the resultant image is almost identical to (b) by human eyes. Therefore, they are not displayed in the figure.

In the interpretation of the MI function, three forms are widely used:

$$\begin{aligned} MI(I_r, I_f^T) &= \sum_{r,f} p(r,f) \log \frac{p(r,f)}{p(r)p(f)} \\ &= H(I_r) + H(I_f^T) - H(I_r, I_f^T) \\ &= H(I_f^T) - H(I_f^T | I_r) \ , \end{aligned} \tag{8.1}$$

where $p(r)$, $p(f)$, and $p(r,f)$ are the marginal and joint probability distribution functions (PDFs), and H is the entropy measure.

One popular interpretation of the MI function (Pluim et al., 2003) is based on dispersion of the joint histogram table, meaning that the less dispersed the joint histogram is, the better two images are assumed to be registered. Under this interpretation, the maximisation of MI is related to the minimisation of dispersion of the joint histogram table, given the two images are initially well overlapped. Therefore, a correspondence of intensity classes is assumed in the MI-based registration. The advantage of this assumption is the applicability of MI to images with a nonlinear relationship of intensity distributions, including images from different imaging modalities where image intensity classes reflect tissue classes.

However, there are situations where MI registration may be inappropriate due to the violation of the assumption of intensity class and tissue class correspondence. The most common situation, to our knowledge, happens in registering *in vivo* medical images with intensity *non-uniformity*, also referred to as intensity *distortion* or intensity *bias*. Intensity non-uniformity results in the same tissue type having different intensity values in different positions, and thus some regions of the tissue having different intensity classes. Since patterns of non-uniformity fields tend to vary in different images, the extra intensity classes of one tissue type contribute to a many-to-many mapping of intensity classes within this tissue and lead to errors in nonrigid registration.

Figure 8.1 shows an example of registering two initially aligned brain MR images, downloaded from BrainWeb[1]. One of them contains an intensity non-uniformity field while the other does not. The nonrigid registration using NMI measure (Studholme et al., 1999) generates a large erroneous deformation field. This deformation field also corresponds to the pattern of the non-uniformity field map, meaning the error is not solely caused by the interpolation. Figure 8.1 (e) shows a more promising result using the proposed method which will be described later. The proposed method performs much better and demonstrates a good robustness against the intensity non-uniformity.

The second common situation occurs in registration of contrast enhanced images such as dynamic contrast enhanced MRI (Melbourne et al., 2007) or perfusion MRI (Li and Sun, 2009), where the intensity values of images change with respect to the biological uptake of contrast agents.

Thirdly, in multi-modality image registration the intensity of several tissues with a number of intensity classes in one imaging modality may correspond to only one class in an other modality. Loeckx et al. (2007, 2010) showed an example of a CT-MR registration application, though nonrigid multi-modality registration is not as common as mono-modality registration

[1] www.bic.mni.mcgill.ca/brainweb/

described in the above two situations.

We summarise that the problem in these situations is attributed to the *non-bijective* mapping of the intensity class correspondence, meaning the mapping of tissue type related intensity classes is not one-to-one between two images. The non-bijective mapping can consequently bring ambiguity or noise into the tissue correspondence. This effect may not be so profound in rigid or affine registration, where the transformation parameters globally change the contribution of all pixel pairs to the joint histogram table. In this case, the local effects from noisy correspondence can be either balanced out or reduced owing to the basis of statistical estimation of the MI computation. However, the transformation parameters in nonrigid registration have more profound effects on local volumes, such as within the local support volumes. As a result, this correspondence will generate false forces to misalign the local details. For example, the tissue pointed by the arrow in Figure 8.2 (a) has one intensity class, which however should map to two classes of the corresponding tissue in Figure 8.2 (b). Consequently, the registration using NMI measure will squeeze the small region with the extra intensity class, as the results show in Figure 8.2 (c) and (d).

Finally, it is inappropriate to use MI-based registration when at least one of the registration images come from an imaging technique where the imaged pixel intensity values do not represent tissue types. One example is ultrasound imaging, where the intensity values are related to tissue boundaries and incident angles of the ultrasound beams more than to the types of homogeneous tissues. In this situation, the intensity class correspondence can not be assumed to be the same correspondence of tissue types between the two images, and hence registration based on features is more commonly used such as the phase registration (Mellor and Brady, 2005). This situation is not included in this work.

8.2 Related work

The problem of the non-bijective correspondence of intensity classes can be improved if the computation of information (entropy) in MI considers the spatial difference of each message element. For example, the message *aabbaa* has the same information as that of *aabbbb* or *aaaabb*. However, in image registration the message *112233* may be considered as more similar to *aabbaa* than to *aabbbb* or *aaaabb*. To include this spatial information, one can use the *local mutual information* (LMI) computed from a joint histogram table estimated from *local regions* of the images such as computing the LMI between *aabb* of *aabbaa* and *1122* of *112233*.

Studholme et al. (2006) proposed regional mutual information (RMI) which considered the spatial information as an extra channel and computes the mutual information of the three channels:

$$\mathrm{RMI}(I_r, I_f, S, T) = \sum_{r,f,s} p(r,f,s) \log \frac{p(r,f,s)}{p(r)p(f)p(s)} \ . \tag{8.2}$$

A new metric was derived from RMI, denoted as RMI′:

$$\begin{aligned} \mathrm{RMI}'(I_r, I_f, T) &= \sum_{s} p(s) \sum_{r,f} p_s(r,f) \log \left(\frac{p_s(r,f)}{p_s(r)p_s(f)} \right) \\ &= \sum_{s} p(s) \mathrm{MI}_s(I_r, I_f, T) \ , \end{aligned} \tag{8.3}$$

which is a linearly weighted sum of a set of LMIs $\{\mathrm{MI}_s\}$, where $\{s\}$ are local regions. The LMIs are computed using the local joint probability distribution $p_s(r, f)$, based on the local joint histogram table:

$$p_s(r, f) = \mathcal{H}_s(r, f)/N_s \ , \tag{8.4}$$

where $N_s = \sum_{r.f} \mathcal{H}_s(r, f)$ is the normalisation factor.

Loeckx et al. (2007, 2010) considered the spatial coordinates of pixels in the reference image as known conditions and proposed to compute the conditional mutual information (cMI) of the two images:

$$\mathrm{cMI}(I_r, I_f, T|X) = \sum_s p(s) \sum_{r,f} p(r, f|s) \log \left(\frac{p(r, f|s)}{p(r|s)p(f|s)} \right) . \tag{8.5}$$

Similarly to the theory of RMI′, the conditional probability distribution was computed based on the joint PDFs $p(r, f, s)$ by extending the spatial dimension as an extra channel to construct a 3D joint histogram table. However, the spatial binning in cMI used a multi-dimensional cubic B-spline kernel function as the smoothing function in the Parzen window estimation (Parzen window function), while the RMI′ used a *boxcar* function, the 0-order B-spline function. As a result, the local joint probability was non-linearly weighted in the local cMI computation by considering the distance of each pixel to the centre of the spatial bin. If one uses a 0-order B-spline kernel function as the Parzen window function, as the case for RMI′ (Studholme et al., 2006), the joint histogram becomes:

$$\begin{aligned} \mathcal{H}(r, f, s) &= \sum_{x \in \Omega} \omega_r(I_r(x))\omega_f(I_f(x))\omega_s(x) \\ &= \sum_{x \in \Omega_s} \omega_r(I_r(x))\omega_f(I_f(x)) \cdot 1 = \mathcal{H}_s(r, f) \ , \end{aligned} \tag{8.6}$$

where, ω_r, ω_f, and ω_s are the Parzen window functions. Due to $p(s) = N_s/N$, where $N_s = \sum_{r,f} \mathcal{H}(r, f, s)$ and $N = \sum_{r,f,s} \mathcal{H}(r, f, s)$ are the normalisation factors, then,

$$\begin{aligned} p(r, f|s) &= p(r, f, s)/p(s) \\ &= \frac{\mathcal{H}_s(r, f)/N}{N_s/N} = p_s(r, f) \ . \end{aligned} \tag{8.7}$$

Therefore, the conditional MI is equivalent to RMI′. Loeckx et al. (2010) further showed that the cMI registration performed better than the registration using the original RMI similarity form in Eq. (8.2).

Encoding spatial information using a set of LMI has two potential drawbacks: reduced statistical power of the similarity measures (Likar and Pernus, 2001; Pluim et al., 2000) and loss of the global intensity class linkage (Zhuang et al., 2008c), both leading to reduced registration robustness. Likar and Pernus (2001) proposed to use the joint probability distribution from the histogram of the complementary volume of the local region, and considered it as *a priori* information to estimate the joint PDFs, using a mixture model:

$$p(r, f) = w\, p_{_L}(r, f) + (1 - w)\, p_{_G}(r, f) \ . \tag{8.8}$$

where $p_L = \frac{1}{N_L}\sum_{x\in\Omega_s}\omega_r(I_r(x))\omega(I_f^T(x))$ is estimated from the local region Ω_s and $p_G = \frac{1}{N_G}\sum_{x\in\overline{\Omega}_s}\omega_r(I_r(x))\omega(I_f^T(x))$ is estimated from the complementary volume $\overline{\Omega}_s$, N_L and N_G are normalisation factors. The implementation in the work used the portion between the volume of the local region and the whole volume, $|\Omega_s|/|\Omega|$, to set the weighting w for a local affine registration. This is equivalent to the implementation of LARM in Section 4.2 by using the standard MI and assuming that the associated local volume of the local affine transformation should be the local region.

8.3 SIEMI: Spatial Information Encoded Mutual Information

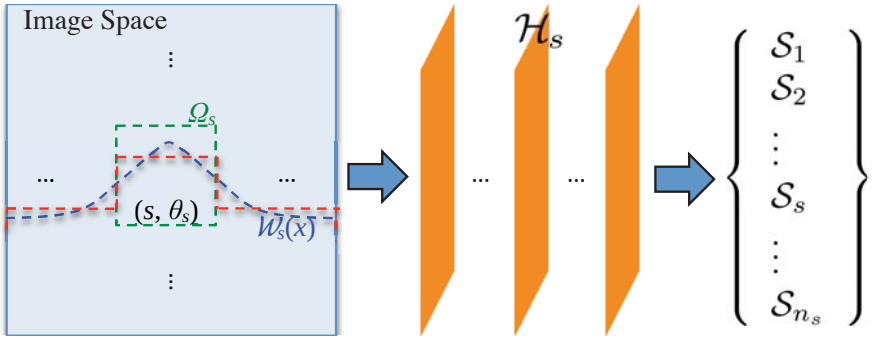

Figure 8.3: The spatial variable s, associated local region Ω_s, transformation parameter θ_s, weighting function $\mathcal{W}_s(x)$, and associated joint histogram table $\mathcal{H}_s$ and entropy measure $\mathcal{S}_s$. The spatial information encoded similarity measure is the vector representation of $\{\mathcal{S}_s\}$.

In this work, spatial information encoding is achieved by constructing a set of spatial variable associated joint histogram $\{\mathcal{H}_s\}$, from which a set of spatial variable associated entropy measures, $\{\mathcal{S}_s\}$, are computed, as illustrated in Figure 8.3. For the computation of $\mathcal{H}_s$, two points are summarised from the discussions in the above two sections. One is that the local estimation, encoding spatial information, potentially provides important information for correcting local misalignments in the nonrigid registration. The other is that the estimation should combine the local and global information within a weighting system to maintain both the global intensity class linkage and the spatial information. Therefore, we propose to encode the spatial information by weighting the contribution of pixel pairs to the joint histogram table according to their spatial coordinates.

This section is organised as follows: Section 8.3.1 describes the framework of spatial encoding. Section 8.3.2 presents the similarity measure of SIEMI. Section 8.3.3 provides the computation of driving forces and proposes an efficient optimisation scheme for SIEMI registration. Section 8.3.4 discusses the choice of weighting function and unifies the existing works.

8.3.1 Encoding spatial information

8.3.1.1 A mixture model for weighting local and global information

Let I_r be the reference image, I_f^T the transformed floating image by nonrigid transformation T, θ_s the parameter of T, and Ω_s the user-defined local region. The definition of s, θ_s and Ω_s are related to each other. The information within Ω_s is referred to as the *local information* of s and that within the complementary volume $\overline{\Omega}_s$ is referred to as the *global information*.

Let $p_s(r, f)$ be the spatial variable associated joint PDF. The estimation using the traditional computation of information theoretic measures is given by:

$$\begin{aligned} p_s(r,f) &= \frac{1}{N}\sum_{x\in\Omega}\omega_r(I_r(x))\omega_f(I_f^T(x)) \\ &= \frac{N_{_L}}{N}\frac{1}{N_{_L}}\sum_{x\in\Omega_s}\omega_r(I_r(x))\omega_f(I_f^T(x)) + (1-\frac{N_{_L}}{N})\frac{1}{N_{_G}}\sum_{x\in\overline{\Omega}_s}\omega_r(I_r(x))\omega_f(I_f^T(x)) \\ &= w\, p_{_L}(r,f) + (1-w)\, p_{_G}(r,f)\ , \end{aligned} \tag{8.9}$$

which is equivalent to Eq. (8.8). The estimation of $p_s(r, f)$ is separated into two parts: one from the local information and the other from the global information.

To assess the weight of each pixel $x \in \Omega$, Eq. (8.9) is rewritten as follows:

$$p_s(r,f) = \frac{1}{N}\sum_{x\in\Omega_s}\omega(\circ)\frac{wN}{N_{_L}} + \frac{1}{N}\sum_{x\in\overline{\Omega}_s}\omega(\circ)\frac{(1-w)N}{N_{_G}}\ , \tag{8.10}$$

where $\omega(\circ) = \omega_r(I_r(x))\omega_f(I_f^T(x))$. By valuing $w = N_{_L}/N$, the weights of all pixels $x \in \Omega$ in Eq. (8.9), $\frac{wN}{N_{_L}} = \frac{(1-w)N}{N_{_G}} = 1$, are the same. This weighting scheme results in the same value for all computed local measures, $\mathcal{S}_1 = \mathcal{S}_2 = \cdots = \mathcal{S}_{n_s}$, and hence no spatial information is encoded.

To tackle the problem, we propose to consider the pixel pairs from the local information with higher weights to differentiate them from the others in the estimation of the spatial variable associated PDF $p_s(r, f)$. For example, by setting $w = 2N_{_L}/N$ the weights of the pixel pairs are given by:

$$\begin{array}{ll} \frac{2N_{_L}/N}{N_{_L}} = \frac{2}{N}, & x \in \Omega_s \\ \frac{1-2N_{_L}/N}{N_{_G}} = \frac{1-N_{_L}/N_{_G}}{N}, & x \in \overline{\Omega}_s \end{array}\ . \tag{8.11}$$

The spatial information of the pixels within Ω_s is then encoded in the computation of the spatial variable associated measures. Based on this idea, we introduce a new parameter $\lambda \in [0, 1]$, indicating the trade-off between the local information and global information, to generalise this weighting scheme between the local and global information such that $w = w(\lambda)$. To interpolate $w(\lambda)$, three conditions are introduced:

- $\lambda = 1$. It occurs when the pixels from global information have the highest weights, the same as pixels from the local information. This corresponds to the traditional estimation: $w(\lambda) = w(1) = N_{_L}/N$.

- $\lambda = 0$. When the pixel from global information is unavailable or assigned with zero weight, only LMIs are applied: $w(\lambda) = w(0) = 1$.

- $\lambda = 0.5$. The estimation from the global information or the local information contributes equally to the local joint PDF estimation in Eq. (8.9). This also means the sum of the weights from the global information is equal to the sum from the local information: $w(\lambda) = w(0.5) = 0.5$.

A quadratic polynomial function can then be interpolated:

$$w(\lambda) = \frac{2N_L}{N}\lambda^2 - (1 + \frac{N_L}{N})\lambda + 1,\ \lambda \in [0, 1]\ . \tag{8.12}$$

It should be noted that the quadratic polynomial is only one of the possible solutions for this interpolation.

8.3.1.2 Fine encoding of spatial information

Although $w(\lambda)$ provides a mechanism to differentiate the confidence of a pixel at different local regions, it does not provide the function to encode the finer detail within the local region in the joint PDF estimation. This encoding means the pixel pairs from the same local region have the same weight regardless of their difference in spatial coordinates:

$$\mathcal{W}_s(x) = \begin{cases} \frac{wN}{N_L}, & x \in \Omega_s \\ \frac{(1-w)N}{N_G}, & x \in \overline{\Omega}_s \end{cases}\ . \tag{8.13}$$

The weighting function is illustrated as the red dash-line in Figure 8.3 (left).

Therefore, we further propose to generalise the weighting scheme such that the value of $\mathcal{W}_s(x)$ is monotonically decreasing with respect to the distance between x and the coordinate of s. The weighting function is illustrated as the blue dash-line in Figure 8.3 (left). In this scheme, the spatial variable associated joint histogram table is computed as follows:

$$\mathcal{H}_s(r, f) = \sum_{x \in \Omega} \omega_r(I_r(x))\omega_f(I_f^T(x))\mathcal{W}_s(x)\ . \tag{8.14}$$

Then, the joint PDF is $p_s(r, f) = \frac{1}{N_s}\mathcal{H}_s(r, f)$, where $N_s = \sum_{r,f} \mathcal{H}_s(r, f)$ is the normalisation factor. Theoretically, the spatial variable associated measure $\mathcal{S}_s$ is then computed using the whole information within the images, *not* solely within the local support volume of the transformation parameter.

The derivative of $\mathcal{H}_s(r, f)$ with respect to a transformation parameter θ_t is given by:

$$\frac{\partial \mathcal{H}_s(r, f)}{\partial \theta_t} = \sum_{x \in \Omega_t} \frac{\partial \omega_f(I_f^T(x))}{\partial \theta_t}\omega_r(I_r(x))\mathcal{W}_s(x)\ , \tag{8.15}$$

where Ω_t *is the local support volume* of the transformation parameter. The computation of $\partial\omega_f(I_f^T(x))/\partial\theta_t$ is the same as that in the traditional MI registration (Viola and Wells, III, 1997; Maes et al., 1997; Wells III et al., 1996). The computation complexity of Eq. (8.15) is $O(|\Omega_t|)$, because the update for the joint histogram table is only within the local support volume of the transformation parameter. The computation for the marginal histogram and PDFs is similar, based on which MI or the normalised measures and their derivatives are computed.

8.3.2 Similarity measure

The spatial variable associated entropy measures $\{\mathcal{S}_s\}$ are computed from their associated PDFs. The computation results in a vector measure composed of $\{\mathcal{S}_s\}$ between two registration images, as shown in Figure 8.3 (right). This measure is referred to as the *spatial information*

encoded mutual information (SIEMI):

$$\text{SIEMI} = \{\mathcal{S}_1, \mathcal{S}_2, \cdots, \mathcal{S}_s, \cdots, \mathcal{S}_{n_s}\}^{\mathrm{T}} \ , \tag{8.16}$$

To present a scalar value of SIEMI, one of the most widely used schemes is to compute the weighted sum of $\{\mathcal{S}_s\}$:

$$\text{SIEMI}_{\text{sum}} = \sum_s p(s)\mathcal{S}_s \ , \tag{8.17}$$

where $p(s) = \frac{N_s}{\sum_t (N_t)}$.

Alternatively, since SIEMI is a vector, the squared magnitude of the vector can be computed as a scalar similarity measure:

$$\text{SIEMI}_{\text{mag}} = \sum_s \left(\mathcal{S}_s\right)^2 . \tag{8.18}$$

Both SIEMI$_{sum}$ and SIEMI$_{mag}$ are then scalar-value function and can be optimised using these traditional methods such as the gradient ascent optimisation scheme. The entropy measure $\mathcal{S}_s$ can be the joint entropy, MI, or the normalised forms such as NMI (Studholme et al., 1999) and entropy correlation coefficient (Maes et al., 1997). However, the un-normalised measures may not have finite bound of values. Theoretically, both of SIEMI$_{sum}$ and SIEMI$_{mag}$ could fail to work in some cases when some of $\{\mathcal{S}_s\}$ have very large values and derivatives, such as using MI or negative joint entropy, and hence dominate the optimisation of the global scalar measure. Also, Studholme et al. (Studholme et al., 1999) showed that NMI was robust to the changes in overlap. Therefore, we use NMI for the implementation of $\mathcal{S}_s$ in this work. Notice that the results using other MI forms may not be significantly different in practice.

8.3.3 Driving forces and optimisation

Given the transformation parameter θ_s, the steepest ascent direction of registration using the scalar SIEMI is given by the derivative of SIEMI in Eq. (8.17) or Eq. (8.18) as follows:

$$\begin{aligned} \vec{F}_{SA}(\theta_s) &\equiv \frac{\partial \text{SIEMI}}{\partial \theta_s} \\ &= \sum_t \frac{\partial C(\mathcal{S}_t)}{\partial \theta_s}, \text{where } C(\mathcal{S}_t) \text{ is } (\mathcal{S}_t)^2 \text{ or } p(t)\mathcal{S}_t \ . \end{aligned} \tag{8.19}$$

The computation complexity of Eq. (8.19) is $O(n_s|\Omega_s|)$, where n_s is the number of spatial variable values whose associated joint histogram tables need updating. However, this computation may be practically too expensive when n_s is large, compared to only $O(|\Omega_s|)$ in standard MI.

Since SIEMI is a vector of $\{\mathcal{S}_s\}$, we propose to optimise each $\mathcal{S}_s$ with respect to the related transformation parameter θ_s using a direction of local ascent, resembling a greedy strategy:

$$\vec{F}_{LA}(\theta_s) \equiv \partial \mathcal{S}_s / \partial \theta_s \ . \tag{8.20}$$

The computation complexity of Eq. (8.20) is now *significantly reduced* to $O(|\Omega_s|)$, which compares with $O(n_s|\Omega_{\theta_s}|)$ of Eq. (8.19). This *local ascent optimisation* assumes that the optimisation of each $\mathcal{S}_s$ would not deteriorate that of others, and thus would globally converge.

The convergence of local ascent optimisation, along with the comparisons with the registration using global ascent optimisation for $\text{SIEMI}_{\text{sum}}$, $\text{SIEMI}_{\text{mag}}$, and NMI, will be validated in Section 8.4.1.

The implementation of gradient ascent optimisation uses decreasing step length, without line-search, to advance in each iteration (Klein et al., 2007). The optimisation is stopped when the similarity measure(s) can not be further improved within the last five steps or reach the user-defined maximal iteration number.

8.3.4 Choice of $\mathcal{W}_s(x)$ and unifying exiting work

The amount of information used in the computation of $\mathcal{H}_s$ in Eq. (8.14) is related to the none-zero-value domain of the weighting function $\mathcal{W}_s(x)$. The more information used in the computation of $\mathcal{H}_s$, the better statistical power and maintenance of the global intensity class linkage, and hence the better registration robustness. A strategy to improve the robustness is to start the registration using $\mathcal{W}_s(x)$ with a large none-zero-value domain and then hierarchically change to $\mathcal{W}_s(x)$ functions with smaller non-zero-value domains.

By using the cubic B-spline function β^3 in FFD registration such that:

$$\mathcal{W}_s(x) = \beta^3_{\Delta_1}(x_1 - \phi_{s1})\beta^3_{\Delta_2}(x_2 - \phi_{s2})\beta^3_{\Delta_3}(x_3 - \phi_{s3}) \,, \tag{8.21}$$

where $x = [x_1, x_2, x_3]^{\text{T}}$ is the coordinate of the pixel x, $[\phi_{s1}, \phi_{s2}, \phi_{s3}]^{\text{T}}$ is the coordinate of the s corresponded control point, and $[\Delta_1, \Delta_2, \Delta_3]$ are the FFD spacing values in the three dimensions. Then, the spatial variable associated $\mathcal{H}_s$ turns to be the 3D joint histogram table $\mathcal{H}(r, f, s)$ in (Loeckx et al., 2007) and $p_s(r, f)$ becomes the conditional PDF $p(r, f|s)$. The corresponding $\text{SIEMI}_{\text{sum}}$ is then given by:

$$\text{SIEMI}_{\text{sum}}|_{\mathcal{S}_s=\text{MI}} = \sum_s p(s) \sum_{r,f} p(r, f|s) \log \frac{p(r, f|s)}{p(r|s)p(f|s)} \,, \tag{8.22}$$

which is the cMI in (Loeckx et al., 2007, 2010). By using the *boxcar* function for $\mathcal{W}_s(x)$, Eq. (8.22) becomes the RMI' measure, Eq. (8.3), derived in (Studholme et al., 2006).

In the weighting scheme using Eq. (8.21), SIEMI adopts to set the none-zero-value domain of $\mathcal{W}_s(x)$ to the local support region of the transformation parameters. The problem, due to the small number of sample points used to construct $\mathcal{H}_s$, remains in the FFD registration using fine B-spline meshes, particularly in 2D applications.

In this study, we propose to use the Gaussian kernel function for $\mathcal{W}_s(x)$:

$$\mathcal{W}_s(x) = Ae^{-\left(\frac{(x_1-\phi_{s1})^2}{2\sigma_1^2} + \frac{(x_2-\phi_{s2})^2}{2\sigma_2^2} + \frac{(x_3-\phi_{s3})^2}{2\sigma_3^2}\right)} \,, \tag{8.23}$$

where $A = 1$ and $[\sigma_1, \sigma_2, \sigma_3]$ are the standard deviations. In practice, the locality of the Gaussian function is set to the volume within three times the standard deviation. Therefore, $\mathcal{W}_s(x)$ using Eq. (8.23) is equivalent to the cubic B-spline function in Eq. (8.21), given $\sigma_i = \frac{2}{3}\Delta_i$, $i = 1, 2, 3$, where Δ_i is the FFD spacing in each dimension.

The standard deviation values in Eq. (8.23) decide the extent of image region used in the computation of $\mathcal{H}_s$. Hence, it regulates the locality of the computed $\mathcal{S}_s$. In FFD registration,

we incorporate the hierarchy scheme into the multi-resolution FFD scheme (Schnabel et al., 2001) by setting $\sigma_i = l\Delta_i$, $i = 1, 2, 3$, $l \in [1, 2]$. The information used in the computation of $\mathcal{H}_s$ is not limited within the local support volume of the FFD transformation parameter in this scheme. By setting $l = 2$, the locality of the Gaussian function can be extended to up to 3^d times of the local support volume in this scheme, where d is the dimension. It should be noted that the computation complexity of the optimisation using Eq. (8.20) is not significantly increased along with the increased value of l. This is because it is determined by the size of local support volume of the transformation parameter as shown in Eq. (8.15).

Finally, we also derive the SIEMI registration using solely the mixture model encoding method in Eq. (8.10) for comparisons. This weighting scheme is given by Eq. (8.13). We use a set of different λ values in $\{0, 0.25, 0.5, 0.75, 1\}$ to derive five SIEMI registration methods, denoted as $\mathcal{C}_0$, $\mathcal{C}_{.25}$, $\mathcal{C}_{.5}$, $\mathcal{C}_{.75}$, and $\mathcal{C}_1$ respectively, where the $\{\mathcal{S}_s\}$ in $\mathcal{C}_0$ are the local NMI and in $\mathcal{C}_1$ are the standard NMI.

8.4 Experiments: SIEMI and different spatial encoding schemes

8.4.1 Experiment-1: Local ascent VS global steepest ascent optimisation

Data and experimental setup

This experiment used 2D brain MR T1 images, downloaded from BrainWeb, to demonstrate the difference of SIEMI registration using the steepest ascent optimisation, Eq. (8.19), and local ascent optimisation, Eq. (8.20). Only 2D images from the central slice of the axial view are selected for registration. One of the registration images has an intensity non-uniformity field (20%) while the other does not.

Twenty-four initial deformation fields, regarded as the ground truth, were generated using the combinations of isotropic scaling, between [0.95, 1.05], and FFD transformations with 45×54 mm mesh spacing, moving the central control points either 15 mm or -15 mm at each direction. The warping index, root mean square residual displacement error, of the initial transformation fields ranged between $[3.47,\ 4.63]$ (3.90 ± 0.49) mm for the brain tissue.

Four registration methods using FFDs were applied to register the 24 tasks, generated from the initial deformation fields:

- use NMI similarity measure and steepest ascent optimisation scheme, referred to as NMI;
- use the sum of $\{\mathcal{S}_s\}$, Eq. (8.17), as the similarity measure and steepest ascent optimisation, referred to as $\text{SIEMI}_{\text{sum}}$;
- use the magnitude of $\{\mathcal{S}_s\}$, Eq. (8.18), as the similarity measure and steepest ascent optimisation, referred to as $\text{SIEMI}_{\text{mag}}$;
- use the vector representation of SIEMI as the similarity measure and local ascent optimisation scheme, referred to as SIEMI.

The weighting function $\mathcal{W}_s(x)$ in $\text{SIEMI}_{\text{sum}}$, $\text{SIEMI}_{\text{mag}}$, and SIEMI was the same Gaussian function in Eq. (8.23) with $l = 2$.

The registration used a series of concatenated isotropic FFDs with two levels (spacing 20mm and 10mm) (Rueckert et al., 2006) and the multi-resolution optimisation scheme

(Thévenaz and Unser, 2000). The optimisation employed 100 iteration steps for the 20 mm spacing FFDs and 40 steps for 10 mm spacing FFDs. The warping index was calculated every 10 steps to assess the registration accuracy.

Results and discussion

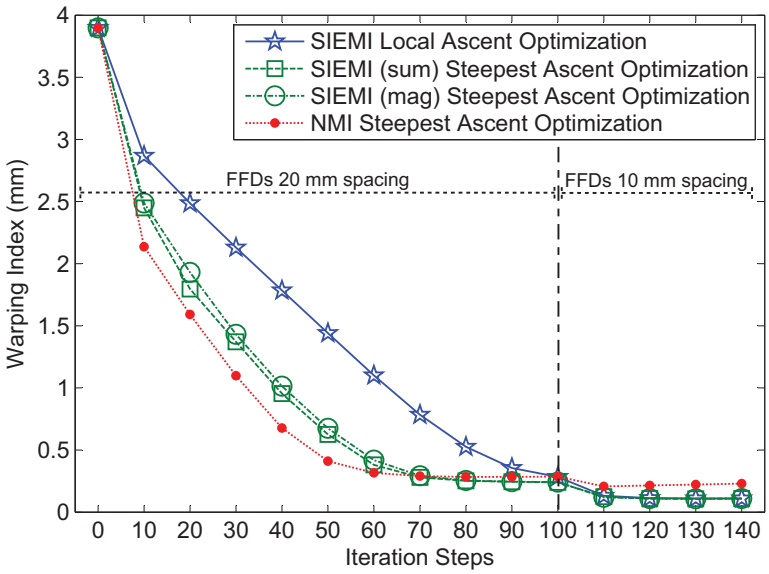

Figure 8.4: The mean warping index every10 iteration steps. The first 100 steps are the 20 mm spacing FFD registration while the last 40 steps are the 10 mm spacing FFD registration.

Table 8.1: The registration accuracy, given by the warping index, of the four registration schemes. The table also gives the ratios of computation time of the other three methods compared to that of SIEMI, and the p-values of the two tailed, paired t-test between the other three groups and SIEMI.

	NMI	$\text{SIEMI}_{\text{sum}}$	$\text{SIEMI}_{\text{mag}}$	SIEMI
Warping index (0.01 mm)	23 ± 0.9	11 ± 0.6	11 ± 0.5	11 ± 0.7
Ratio of computation time	0.60	160	144	1
P-value against SIEMI	<0.0001	0.462	0.662	—

Figure 8.4 shows the mean registration errors (warping index) of the 24 cases by the four methods. All registration schemes converged within the number of iteration steps. The final registration accuracy is given in Table 8.1 where the evidently small standard deviation values, all less than 0.01 mm, indicates their consistent performance in the test cases.

No statistically significant difference was found in terms of accuracy between the registration using local ascent optimisation and the registration using global steepest ascent optimisation, as the p-values of the paired t-test between the results of SIEMI and the results of $\text{SIEMI}_{\text{sum}}$ and $\text{SIEMI}_{\text{mag}}$ were 0.462 and 0.662, respectively.

The computation time for the four methods was different from Table 8.1. NMI was the most efficient registration and only needed 60% the computation time as that of SIEMI, while $\text{SIEMI}_{\text{sum}}$ and $\text{SIEMI}_{\text{mag}}$ were both more than 100 times slower.

However, the speeds of convergence were different, which is seen in Figure 8.4. NMI was the most efficient, $\text{SIEMI}_{\text{sum}}$ and $\text{SIEMI}_{\text{mag}}$ were marginally slower, while SIEMI converged

the slowest. Therefore, NMI was the most computationally efficient. SIEMI was slower than NMI, but still much more efficient than $\mathrm{SIEMI}_{\mathrm{sum}}$ and $\mathrm{SIEMI}_{\mathrm{mag}}$ due to over one hundred times difference for each iteration.

8.4.2 Experiment-2: Weighting function using cubic B-spline

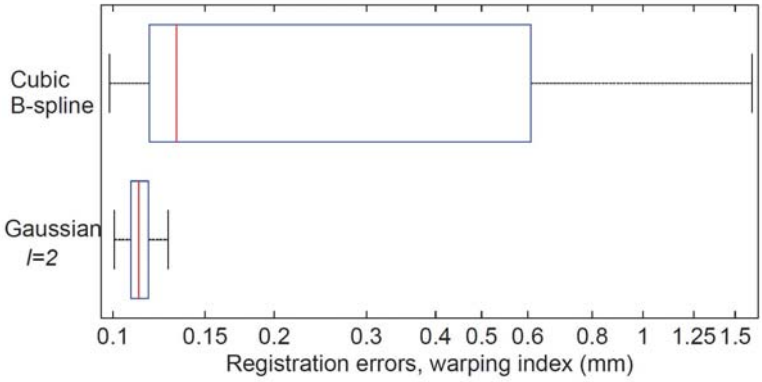

Figure 8.5: The Box-and-Whisker diagrams of the SIEMI registration results using the cubic B-spline in Eq. (8.21) and the Gaussian with $l = 2$ in Eq. (8.23) for spatial information encoding.

In this experiment, we employed 60 registration tasks to study the difference of using Eq. (8.21) and Eq. (8.23) with $l = 2$ for the SIEMI registration. The test data were the same as those used in Section 8.4.1. We generated 60 deformation fields using the combinations of isotropic scaling, between (0.90, 1.1), and FFD transformations with 45×54 mm mesh spacing, moving the central control points either 15 mm or -15 mm at each direction. The warping index of the initial transformation fields ranged between $[3.54,\ 6.68]$ (4.80 ± 0.91) mm for the brain tissue. To maximise the robustness of the registration scheme, the hierarchy scheme employed three levels of FFD meshes, isotropic 40 mm, isotropic 20 mm, and isotropic 10 mm. Correspondingly, the local support regions of the control points started from 160×160 mm^2 and down to 80×80 mm^2, and to 40×40 mm^2.

Figure 8.5 plots the Box-and-Whisker diagrams of the SIEMI registration results using the two difference weighting schemes. Even though the registration started with a coarse FFD level of isotropic 40 mm, where the locality of $\mathcal{W}_s(x)$ in Eq. (8.21) was a region of 160×160 mm^2, to hierarchically maintain the global intensity class linkage, it was still problematic to use the small number of sample points in the construction of $\mathcal{H}_s$ in the weighting scheme of Eq. (8.21). However, this was not the case for the registration using Eq. (8.23) where evidently better robustness was reported.

8.4.3 Experiment-3: Spatial information encoding using mixture model

Data and experimental setup

This experiment used brain MR T1 weighted images, downloaded from BrainWeb, to demonstrate spatial information encoding using the mixture model and the corresponding registration methods $\{\mathcal{C}\}$. Three levels of intensity non-uniformity were tested: 0% (non-bias), 20%, and 40%. Again, only 2D images from the central slice of the axial view were used due to the large number of registration tasks.

Forty initial transformations, regarded as the ground truth, were generated using the same

method in Section 8.4.2. These initialisations were applied to the T1 images of three different bias fields, and the deformed images were then used as reference images to register to the T1 image without intensity non-uniformity. The warping index of the initial transformation fields ranged between $[4.43,\ 7.20]$ (4.64 ± 1.36) mm. The warping index after registration was calculated as the registration accuracy.

We employed the five mixture-model-encoding methods, $\mathcal{C}_0, \mathcal{C}_{.25}, \mathcal{C}_{.5}, \mathcal{C}_{.75}, \mathcal{C}_1$ which is the standard NMI registration, and the SIEMI using Gaussian weighting function and $l = 2$ in the FFD registration, referred to as SIEMI. The transformation model was a series of concatenated isotropic FFDs with three levels (spacing 16mm, 8mm, 4mm in each dimension) (Rueckert et al., 2006) and the optimisation was the multi-resolution scheme (Thévenaz and Unser, 2000) using gradient ascent.

Table 8.2: The warping index (0.01 mm) of the FFD registration results using different cost functions on the T1-T1 with 0%, 20%, 40% bias fields. Row T1-T1 gives the mean accuracy of the three different bias levels.

(0.01 mm)	$\mathcal{C}_0$	$\mathcal{C}_{.25}$	$\mathcal{C}_{.5}$	$\mathcal{C}_{.75}$	$\mathcal{C}_1$(NMI)	SIEMI
T1-T1(0%)	29 ± 28	21 ± 12	18 ± 8.3	18 ± 9.9	20 ± 16	22 ± 15
T1-T1(20%)	32 ± 30	26 ± 21	24 ± 1.6	27 ± 1.8	42 ± 41	21 ± 11
T1-T1(40%)	37 ± 34	28 ± 9.9	34 ± 11	44 ± 9.5	62 ± 29	23 ± 8.7
T1-T1	33 ± 31	25 ± 15	25 ± 10	30 ± 13	41 ± 35	22 ± 12

Results and discussion

Table 8.2 shows the results of the 6 registration methods. The registration using the mixture model, with λ from 0 to 1, performs the best when λ was set to a value between 0.25 to 0.75. However, the ideal value for λ was not consistent in the different levels of intensity non-uniformity fields, Smaller values of λ, corresponding to less weight of the global information, tended to favour the registration tasks with stronger non-uniformity fields, while the methods using larger values of λ performed better in the tasks with less strong non-uniformity.

The $\mathcal{C}_1$ (NMI) registration was shown to be the worst choice for registering images with strong non-uniformity fields: the registration errors of $\mathcal{C}_{.5}$ and SIEMI were both three times the standard deviation smaller than that of $\mathcal{C}_1$ (NMI). In the tasks without non-uniformity, $\mathcal{C}_1$(NMI) performed no worse than any other methods. The t-test between NMI and the best results from $\{\mathcal{C}\}$ and SIEMI were P=0.432 (between $\mathcal{C}_{.5}$ and $\mathcal{C}_1$ (NMI)) and P=0.514 (between SIEMI and $\mathcal{C}_1$ (NMI)), respectively.

The results from SIEMI registration indicated that the spatial information encoding using the Gaussian function was more useful, especially in strong non-uniformity fields. This was probably because the encoding scheme was pixel-wise, while the mixture model scheme did not provide the encoding within local support regions.

8.4.4 Experiment-4: LARM and SIEMI registration

Data and experimental setup

This experiment applied SIEMI to the locally affine registration method (LARM). For the locally affine transformation, four local regions were defined on the four chambers, as the boundary lines shown in Figure 8.6 (left). The values of the spatial variable values were set to the cen-

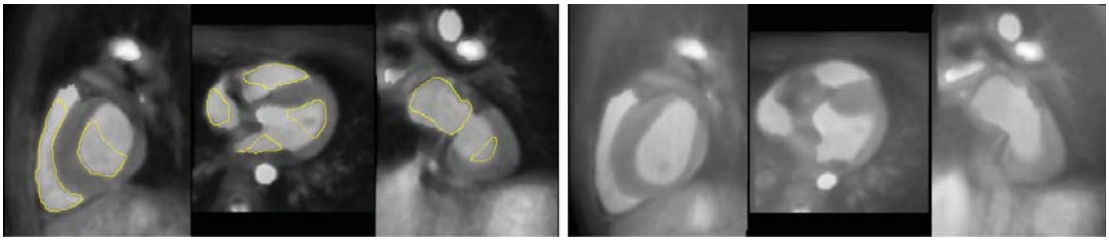

Figure 8.6: The cardiac MR images for registration. Left: The MR image superimposed on by the contour of four pre-defined local regions. Right: The MR image with a 100% bias field and deformed by an initial transformation with warping index of 7.54 mm.

Table 8.3: The warping index (mm) of the locally affine registration results using different cost functions on cardiac MR images with 0%, 50%, 100% bias fields.

(mm)	$\mathcal{C}_0$	$\mathcal{C}_{.25}$	$\mathcal{C}_{.5}$	$\mathcal{C}_{.75}$	$\mathcal{C}_1$(NMI)	SIEMI
$\mathcal{B}$_0%	1.0 ± 1.2	0.27 ± 0.15	0.20 ± 0.02	0.22 ± 0.02	1.9 ± 2.7	0.20 ± 0.02
$\mathcal{B}$_50%	1.2 ± 1.1	$1.1 \pm .66$	0.99 ± 0.29	$1.0 \pm .28$	2.1 ± 2.4	0.89 ± 0.24
$\mathcal{B}$_100%	2.3 ± 1.3	2.3 ± 1.3	2.6 ± 1.6	3.2 ± 2.2	5.1 ± 3.3	2.2 ± 1.1
Total	1.5 ± 1.3	1.2 ± 1.2	1.3 ± 1.4	1.5 ± 1.8	3.0 ± 3.2	1.1 ± 1.1

tre of the four local regions. The local support volume of each local affine was defined to 10 mm dilation of the corresponding local region. The local support volume was also set to the spatial variable s associated local region Ω_s in the mixture model based encoding scheme, the registration methods $\{\mathcal{C}\}$. The Gaussian function encoding in LARM registration,

$$\mathcal{W}_s(x) = Ae^{-\left(\frac{(x_1-\phi_{s1})^2}{2\sigma_1^2}+\frac{(x_2-\phi_{s2})^2}{2\sigma_2^2}+\frac{(x_3-\phi_{s3})^2}{2\sigma_3^2}\right)},$$

is set as follows: $A = 1$ and the standard deviation $\sigma_1 = \sigma_2 = \sigma_3 = 30$ mm, about the mean distance from the boundary of the local support volume to the centre of the volume.

The cardiac MR image, in Figure 8.6 (left), was an intensity mean image of ten volunteer images which had been registered into a selected common space. Twenty initial local affine transformations were generated by randomly translating and rotating the four local regions to provide a local displacement within 10 mm. The four local regions were guaranteed to be non-overlapping each other in the simulation. The warping indexes of the 20 transformations ranged between 4.23 and 14.8 (8.23 ± 3.1) mm. Figure 8.6 (right) shows a deformed MR image using an initial transformation whose warping index is 7.54 mm.

Twenty intensity non-uniformity fields were also simulated using $\mathcal{B} = a_1x_1^2 + a_2x_2^2 + a_3x_3^2 + a_4x_1x_2 + a_5x_1x_3 + a_6x_2x_3 + a_7x_1 + a_8x_2 + a_9x_3$, where $x = [x_1, x_2, x_2]$ is the pixel coordinate, and $\{a_i\}$ are random values within $[-1, 1]$. The magnitudes of non-uniformity fields were normalised to 0% (non-bias), 50%, and 100% of the intensity range of the original image. Figure 8.6 (right) is an MR image with a 100% field.

Results and discussion

The registration results are presented in Table 8.3. The registration with spatial information encoding, SIEMI and one of $\{\mathcal{C}\}$, performed better than NMI in the tasks with intensity non-uniformity. In the experiment, $\mathcal{C}_0$ performed better and seemed more competitive compared

to other methods. This was particularly evident in the strongest field (100%) cases, where no significant difference was found (P=0.704) between the results of $\mathcal{C}_0$ and that of SIEMI. SIEMI was the one which achieved the best accuracy from Table 8.3. Furthermore, $\mathcal{C}_1$ (NMI) did not perform well in the tasks without intensity non-uniformity, compared to $\mathcal{C}_{.5}$ and SIEMI, whose warping indexes were both more than three times standard deviation away from that of $\mathcal{C}_1$ (NMI).

In the experiment, $\mathcal{C}_0$ performed well, while $\mathcal{C}_1$ (NMI) did much worse, even in the non-bias (0%) cases. This was probably attributed to the usage of the intensity information from the background including the abdomen, lung, and liver. These background structures were not of interest to the registration, but they presented information which might have biased the PDF estimation. As a result, the registration without global information worked much better, such as the case of $\mathcal{C}_0$.

8.5 Experiments: Applications

8.5.1 Experiment-5: Application to cardiac MRI and whole heart segmentation

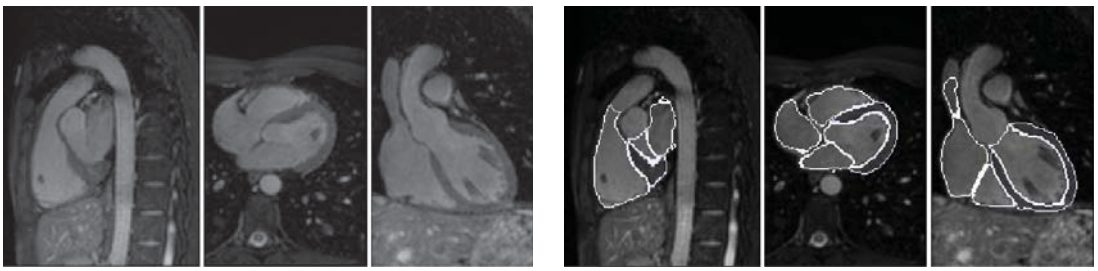

(a) (b)

Figure 8.7: Example of an MR image (a) and its manually delineated surfaces (b). Images shown in sagittal, axial, and coronal views.

Data and experimental setup

This experiment had two steps. Firstly, we employed a set of cardiac MR data to assess the applicability of SIEMI and also compared its performance to that of NMI registration. The data were acquired from 20 different subjects using the MR sequence in Section 4.5.1. For each MR image, the surfaces of the substructures have been manually delineated, including the endocardium of the four chambers and the epicardium of the left ventricle using the same tool and protocol, a mesh model with manual correction (Peters et al., 2007). Figure 8.7 shows one example of an MR image and its manually delineated surfaces.

Every image from this data pool was considered as a reference image and registered to one floating image which was "randomly" selected from the rest of the data pool. The "randomly" is quoted because the selection of floating images was designed to deliberately prevent a repeated registration combination by swapping the reference and floating images. This selection hence presented 20 different registration tasks as the test set. The two nonrigid registration schemes, NMI and SIEMI, combined with an initialisation of LARM, were used to register this test set. LARM, using the standard NMI and including a global affine registration, was applied prior to the nonrigid registration because of the large shape variation of the heart between different subjects. The nonrigid transformation model used was the free-form deformation (Rueckert

Table 8.4: The errors of NMI and SIEMI registration are assessed using the root mean square (RMS) surface distance between the surfaces of the two images. The table also gives the p-value and 95% confidence interval (CI) of the two tailed, paired t-test between the two groups of registration results.

NMI error (mm)	SIEMI error (mm)	P-value [CI (mm)]
1.56 ± 0.55	1.19 ± 0.21	0.0005 [0.192, 0.563]

et al., 1999). The optimisation of all registration employed the multi-resolution scheme with the finest level of $2 \times 2 \times 2$ mm and the gradient ascent optimisation scheme. The registration error was assessed by computing the RMS surface distance between the surfaces of the reference image and the propagated surfaces of the floating image after the registration.

In the second step of this experiment, we replaced the third step in the whole heart segmentation framework in Section 6.2, Chapter 6 as follows:

(1) Firstly, a global affine registration is applied to localise the heart.

(2) LARM is then used to further initialise the substructures.

(3) Finally, registration using ACPS FFDs is employed to refine the local details. In this step, the similarity measure is changed to SIMIE and the opitmisation is the local ascent scheme.

We then redid the whole heart segmentation using the propagation scheme described above for all the 37 volumes. The atlas was the same *Ten Shape* atlas used in Section 6.4.4.

These MR images contained noise and artefacts and their intensity distributions were not exactly the same due to the variation of the scanning environment, the parameters of the MRI sequence and the varying conditions of the scanned subjects. This presented a challenge for the NMI registration to achieve a high accuracy without considering the spatial difference. Hence, the proposed SIEMI registration was expected to perform better.

Results and discussion

Table 8.4 presents the RMS surface distance error of the two registration schemes in the first step. The difference of mean registration errors between SIEMI registration and NMI registration was 0.37 mm (P=0.0005, 95% confidence interval [0.192, 0.563] mm). This difference of the two registration methods also indicated that the intensity distributions of the MR images were not always perfectly matched.

Table 8.5: Surface-to-surface segmentation errors, ϵ_{rms} (mm), of the whole heart segmentation framework using NMI and SIEMI in the refinement registration and their two tailed, paired t-test P-value of each substructure as well as the Whole Heart.

	Left Ventricle	Left Atrium	Right Ventricle	Right Atrium	Epicardium	Whole Heart
SIEMI	1.45 ± 0.35	2.30 ± 1.11	2.03 ± 0.66	2.19 ± 0.75	2.27 ± 0.89	2.08 ± 0.64
NMI	1.47 ± 0.32	2.38 ± 1.14	2.13 ± 0.70	2.22 ± 0.75	2.32 ± 0.82	2.14 ± 0.63
P-value	0.3131	0.0475	0.0090	0.4480	0.2502	0.0093

Figure 8.8 and Table 8.5 give the segmentation errors using the whole heart segmentation framework described in the experiment. Table 8.5 also presents the segmentation errors from

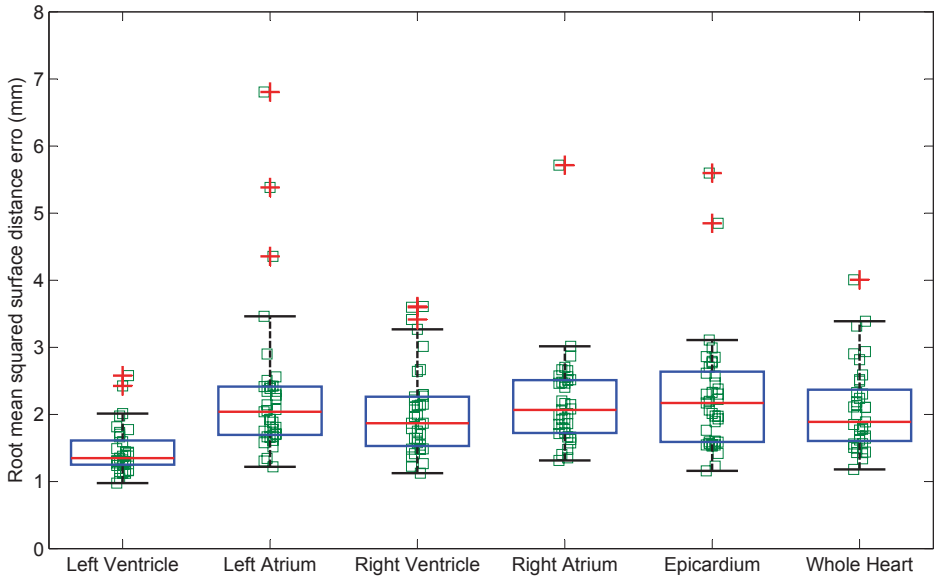

Figure 8.8: The individual plots and the Box-and-Whisker diagrams of the segmentation errors using the RMS surface distance measure, ϵ_{rms}. This figure gives the errors of each substructures as well as the *Whole Heart* from the 37 subjects.

Section 6.4.4 for comparisons. The mean errors of the segmentation using SIEMI registration for refinement were better than those of the original segmentation. Statistical significant difference was also found in the segmentation of Left Atrium, Right Ventricle, and Whole Heart. However, the difference was not practically important, as they were smaller than 0.1 mm in all categories.

The improvement of using SIEMI registration was not so significant compared to the result in the first step. This was probably due to the difference of both error ranges and error assessment. Firstly, the data in the first step were acquired from healthy volunteers and the heart shape had a small variation across the subjects. The challenge for the refinement registration, NMI and SIEMI, was mainly on dealing with the noise and intensity non-uniformity presented in the images. While in the second step, the data were acquired from patients with a variety of pathologies as well as healthy subjects. Hence, the large shape variation induced segmentation errors, which might make the improvement of SIEMI due to the intensity non-uniformity less significant.

Secondly, the manual segmentation in the first step was done using the same tool and protocol, while in the second step we used a variety of tools and protocols. Therefore, the error of the segmentation error assessment in the second step might have such a large variation that the improvement by using SIEMI became less detectable.

8.5.2 Experiment-6: Application to dynamic contrast enhanced MRI

Data and experimental setup

Dynamic contrast enhancement MRI (DCE MRI) causes time-varying intensity and consequently changes the intensity class correspondence between images from different time points (Melbourne et al., 2007, 2008), as one simulated example in figure 8.9 shows. In this

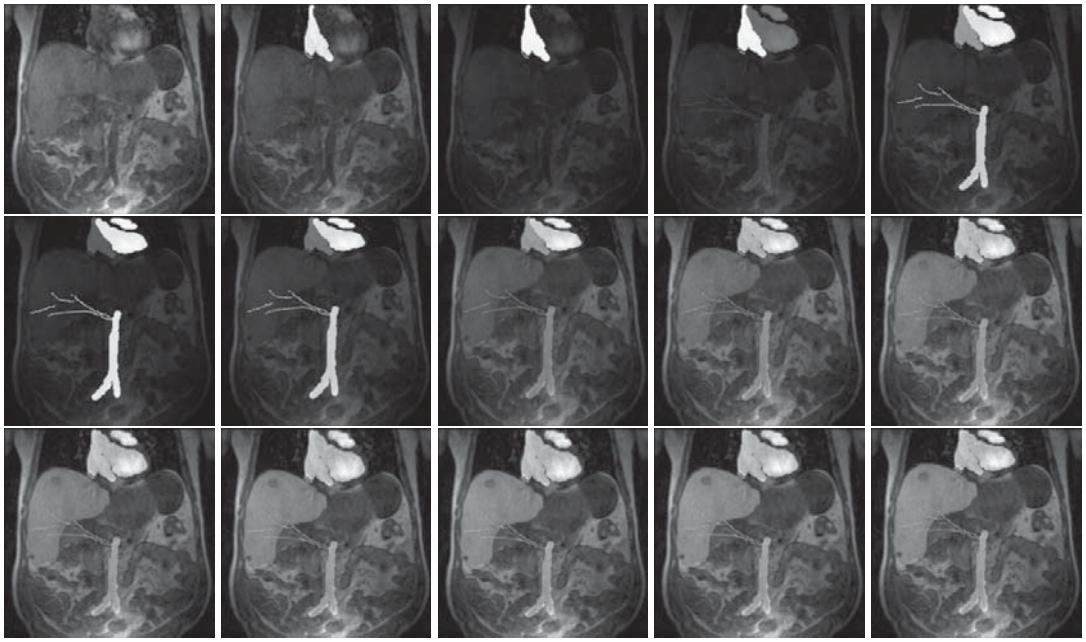

Figure 8.9: One example of the simulated dynamic contrast enhanced MR data in 15 time points. The first row shows the time point 1 to 5 (from left to right), and the second and third rows show from time point 6 to 10 and time point 11 to 15, respectively. Images courtesy of Andrew Melbourne.

experiment, we employed the simulated DCE MR images to demonstrate the problems of the intensity changes to NMI registration, exploring the new application of SIEMI registration. The intensity classes in the simulated DCE MR data are not bijectively matched to that of the MR image without enhancement. For example, the intensity values of the blood pools in the DCE MR data vary as a function of time and positions, and correspond to several intensity classes. However, the blood pool intensity in the non-enhancement image is quite constant and corresponds to one class.

The simulated DCE MRI included free-breathing motions which deformed the images. Nonrigid registration using the FFD transformation model (Rueckert et al., 1999) was applied to recover the respiratory motion, using NMI and SIEMI registration. Four sets of DCE MR images were simulated with different magnitudes of motions. The images from different time points were all registered to the reference image, the MR image without enhancement, to correct the motion. The warping index, RMS residual displacement, was calculated on the liver region which was of interest to the registration:

$$\text{Warping Index} = \sqrt{\sum_{x \in V_{liver}} \frac{||D(x) - G(x)||^2}{|V_{liver}|}}, \tag{8.24}$$

where D and G are the registration resultant deformation field and the ground truth deformation field from the simulation respectively.

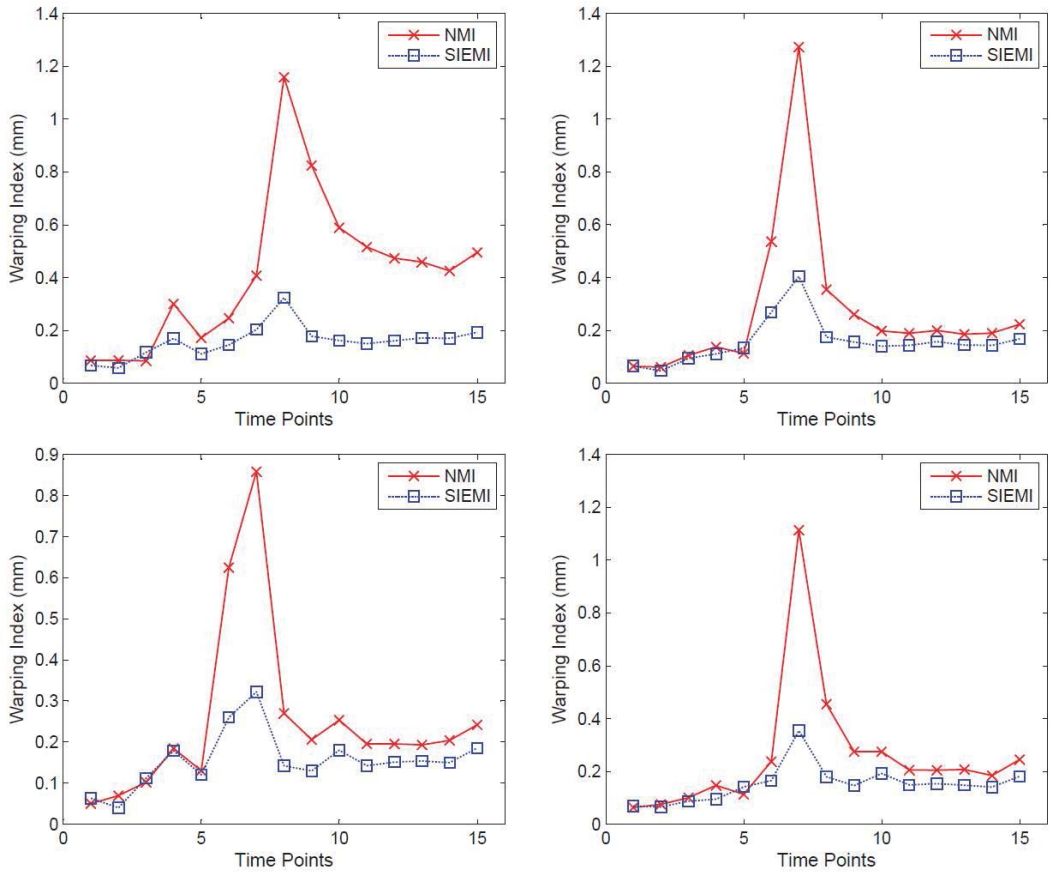

Figure 8.10: Registration accuracy of the liver by the two methods in the four simulated cases.

Results and discussion

Figure 8.10 plots the registration accuracy of all cases using the four different methods. The SIEMI registration performed better than the NMI, particularly in the time points between 5 to 10 when the contrast agents started to enter the liver region and change the intensity values. The results also show that during the time points between 1 to 5, the NMI performed no worse than SIEMI did. This was because during these time points, the intensity values of the liver region had not been changed as the contrast agent had not yet arrived. However, after the contrast agent entering the liver, the intensity distribution changed for the contrast enhanced images. From time point 10 to 15, the contrast agent in the liver was in late enhancement and the intensity distribution was more constant. The standard NMI hence achieved a relatively good accuracy, but not as good as SIEMI registration did, because there was still intensity non-uniformity remained in the images due to the enhancement procedure.

8.6 Conclusion

In this chapter, we have investigated the registration of mutual information (MI), including the normalised mutual information (NMI), and the problem when applied to images without a bijective intensity class correspondence. To tackle the problem, we presented a generalised framework for spatial information encoding and proposed to use the spatial information encoded mutual information (SIEMI). The encoding framework uses a weighting scheme to differen-

tiate the contribution of pixel pairs to the spatial variable associated measures, from which a set of spatial variable associated entropy measures are computed and thus the spatial information is encoded in this set of measures. We also showed that the conditional mutual information (cMI) (Loeckx et al., 2007, 2010) and the equivalent RMI′ (Studholme et al., 2006) are the scalar representation of SIEMI using sum of the spatial variable associated measures and B-spline kernel function for the weighting.

Section 8.4 employs four experiments to study the different performance of the SIEMI using alternative techniques, such as the optimisation schemes and the different weighting schemes. The application of SIEMI in LARM registration has been also illustrated. We conclude from the results that SIEMI registration using local ascent is efficient and no accuracy is sacrificed compared to the usage of global steepest ascent optimisation scheme. The weighting scheme using the Gaussian kernel function has shown the best results compared to either the cubic B-spline function or the mixture model encoding scheme.

Section 8.5 illustrates the application of SIEMI registration to cardiac MR data and the whole heart segmentation, and the simulated dynamic contrast enhancement MRI. The comparisons to NMI registration have also been presented. The results show that SIEMI registration performed significantly better than the NMI registration.

Chapter 9

Conclusion and Future Work

9.1 Conclusion

Providing morphological and pathological information from cardiac MRI is one of the most popular research topics in medical image computing field. In particular, the ability to accurately extract and precisely interpret this information can enable the development of many novel clinical applications. Whole heart segmentation, providing important morphological information of the whole heart as well as the anatomical substructures, has a great value for these applications such as the computational modelling of the heart, and the planning and guidance of cardiac interventional procedures. The work in this thesis has been focused on developing a fully automatic whole heart segmentation scheme, using image registration and atlas propagation techniques.

The main challenge of achieving robust whole heart segmentation is the initialisation of substructures and inclusion of constraints using prior knowledge in the segmentation framework. We have proposed to use locally affine transformation for the initialisation and developed a new locally affine registration method (LARM). LARM globally deforms the images, but locally maintains the shape of substructures, providing an extra initialisation to the global affine registration. Compared to existing techniques, the proposed LARM has the advantage of preserving the global intensity class linkage of the registration images and maintaining diffeomorphism of the resultant transformation. The intensity class linkage improves the registration robustness in images with different intensity distributions, and the diffeomorphism is an important property which can preserve the topology and anatomical consistency of the images. The experiments have shown that the substructure initialisation using LARM can significantly improve the performance of the following nonrigid registration.

To provide a nonrigid registration for the refinement of the whole heart segmentation, we have proposed the registration using the free-form deformations with adaptive control point status (ACPS FFDs). The control point status in this method is used to constrain the driving forces in the registration, and the adaptive status is a result of incorporating prior information of the heart shape and image quality. Compared to the traditional FFD registration without using the prior knowledge, ACPS FFD registration has been shown to achieve a significantly better accuracy in the whole heart segmentation. In particular, it efficiently avoids the myocardium leaking problem commonly presented in cardiac MR segmentation. Finally, the experiments have also showed that ACPS FFD registration is more computationally efficient than the traditional FFD

registration.

In the segmentation framework, it is needed to compute the inverse deformation field of the resultant transformation from the LARM registration. This is actually a common requirement in many image registration applications. Therefore, we propose a generic method to invert dense displacements, using Dynamic Resampling And distance Weighted interpolation (DRAW). Unlike other techniques reported in the literature, DRAW interpolates the inverse field using the close scatter points which are selectively transformed from the forward space. The dynamic resampling avoids unnecessary computation and also improves the interpolation accuracy. We have showed that DRAW has the capability of providing sub-voxel maximal errors, which has not been reported before to the best of our knowledge.

We apply these three new techniques to provide a whole heart segmentation framework for cardiac MR data. In the segmentation framework, we use the multi-stage LARM scheme to hierarchically increase the number of user-defined local affine transformations. This scheme further improves the preservation of the local shape of the substructures while still maintains the flexibility of the transformation model. The hierarchy scheme is also applied to the ACPS FFD registration by using a set of mask images to hierarchically increase the number of activated FFD control points. In the segmentation experiment, the three test atlases were all constructed from healthy control subjects. No statistically significant difference was found using the different atlases when applied to pathological cases. For the new registration algorithms, both LARM and ACPS FFD registration significantly improved the segmentation performance, compared to the traditional framework of global affine plus FFD registration. The segmentation framework has been shown to be robust and applicable to a wide range of pathologies in the experiment. We have also showed that this segmentation framework is extensible to other applications, such as the multi-slice cardiac MR segmentation, the cardiac ultrasound segmentation, and the multi-atlas segmentation scheme.

Finally, we have presented a generalised spatial information encoding method and the application in the entropy measure based registration, the spatial information encoded mutual information (SIEMI). The spatial encoding is achieved by introducing a weighting scheme to evaluate the contribution of pixels according to their coordinates. This weighting scheme spatially differentiates the contribution of pixels to the spatial variable associated joint histogram tables and the computed entropy measures, by which the spatial information is then encoded. We have applied the SIEMI registration to the whole heart segmentation framework, replacing the nonrigid registration using NMI measure. The results showed that the SIMIE registration achieved better accuracy compared with the NMI nonrigid registration. However, the improvement was not practically significant. We concluded that this was due to the large variations of the gold standard segmentation. The two registration methods were also applied to the whole heart cardiac MR registration, where the gold standard segmentation was more consistent and a significant improvement was reported by the SIEMI registration. Furthermore, SIEMI registration should be widely applicable, since it is a general approach proposed to tackle the problems in the nonrigid MI registration due to the non-bijective intensity class correspondence. We have demonstrated the applicability as well as the superior performance to NMI registration using the brain MR data with intensity non-uniformity and the dynamic contrast enhancement MRI

of the liver.

9.2 Limitation and future work

The thesis focuses on image registration techniques and the registration-based whole heart segmentation. This induces three limitations of the proposed segmentation framework. First of all, it is difficult to consider the thin regions, which can be critical in separating substructures, using the intensity-based registration. For example, the thin membrane separates the epicardium and the liver, and the thin atrial wall separates the two atria. These tissues are usually displayed as thin regions whose intensity values differ from their neighbouring regions. However, the intensity-based registration may fail to incorporate this important information due to the relatively small size of these regions. Secondly, the propagation may have a large variation in the delineation of the valves. It is highly desired to have consistent definitions for these valves in all segmentation results. Finally, this approach is computationally inefficient. It may take more than one hour to segment one volume, which is much slower compared to the segmentation using deformable models and boundary-searching techniques.

Compensative techniques should be considered to deal with these problems in a product-orientated implementation. For example, the boundary-searching techniques can be incorporated to tackle the first limitation. It is relatively easy to detect the septum and membrane using an edge detection algorithm within an initialised local region. Alternatively, feature-based registration may work well for the images with thin structures (Mellor and Brady, 2005; Grau et al., 2007; Karacali, 2007; Haber and Modersitzki, 2007). Furthermore, a flat plane positioned by some landmarks may be used to achieve a consistent definition of a valve. For example, the plane defined by the basal myocardium of the left ventricle is usually used to define the mitral valve in the computational modelling of the heart. Finally, parallel computation such as using graphic processing units can be used to decrease the computation time of the registration and segmentation.

The whole heart segmentation is extensible to other frameworks such as the whole heart segmentation of multi-atlas cardiac MR, cardiac ultrasound, and the multi-atlas methods demonstrated in Chapter 7 where preliminary results have also been provided. Furthermore, the registration techniques, particularly LARM and SIEMI registration, are applicable and extensible to other tasks.

LARM provides an efficient and effective way to register multiple organs and objects in inter-subject cases. For example, the registration of prostate from cardiac MRI is a challenging task because the large variation of the relative positions of the objects presented in the image. Some applications include the registration of connected rigid objective such as the joint region of limbs and the registration of objects, such as the liver, due to respiratory motions. LARM registration should be able to provide enough accuracy for the former application while can only provide an initialisation for the latter application.

Both LARM and ACPS FFD methods improve the registration performance because of the incorporation of prior knowledge to constrain the flexibility of the transformation model. A potential technical extension of the two methods is to provide the mechanism of maintaining local affinity and local deformation within the same framework. For example, in the application

of the prostate registration, LARM provides a good initialisation for both prostate region and femur region. The accuracy of the femur registration is good enough as it is not the interest of the application, while the accuracy is not enough for the prostate region. Therefore, it is interesting to have a framework which can increase the degree of freedom for the registration of the prostate region while still maintain the affinity of the femur region.

Finally, SIEMI registration is another generally applicable registration algorithm. We have showed its application and good performance in the dynamic contrast enhancement MRI of the liver and brain MRI. Similar performance should be achievable in *in vivo* data. Other applications include the registration of myocardial perfusion MRI (Li and Sun, 2009), the CT-MR registration tasks described in (Loeckx et al., 2007, 2010), and the registration of brain MRI where one of the image has small tumour tissues while the other does not.

Bibliography

Aljabar, P., Heckemann, R., Hammers, A., Hajnal, J., Rueckert, D., 2009. Multi-atlas based segmentation of brain images: Atlas selection and its effect on accuracy. NeuroImage 46 (3), 726 – 738.

Aljabar, P., Heckemann, R., Hammers, A., Hajnal, J. V., Rueckert, D., 2007. Classifier selection strategies for label fusion using large atlas databases. In: Medical Image Computing and Computer Assisted Intervention (MICCAI), Part I. Vol. 4791 of Lecture Notes in Computer Science. pp. 523–531.

Andreopoulos, A., Tsotsos, J. K., 2008. Efficient and generalizable statistical models of shape and appearance for analysis of cardiac MRI. Medical Image Analysis 12 (3), 335 – 357.

Arsigny, V., 2006. Processing data in lie groups: An algebraic approach. application to non-linear registration and diffusion tensor MRI. Ph.D. thesis, INRIA Sophia-Antipolis.

Arsigny, V., Pennec, X., Ayache, N., 2005. Polyrigid and polyaffine transformations: A novel geometrical tool to deal with non-rigid deformations - application to the registration of histological slices. Medical Image Analysis 9, 507–523.

Ashburner, J., 2007. A fast diffeomorphic image registration algorithm. NeuroImage 38, 95–113.

Azhari, H., Sideman, S., Weiss, J. L., Shapiro, E. P., Weisfeldt, M. L., Graves, W. L., Rogers, W. J., Beyar, R., 1990. Three-dimensional mapping of acute ischemic regions using MRI: Wall thickening versus motion analysis. Am J Physiol Heart Circ Physiol 259, H1492–H1503.

Barkhausen, J., Ruehm, S. G., Goyen, M., et al, 2001. MR evaluation of ventricular function: true fast imaging with steady-state precession versus fast low-angle shot cine MR imaging: feasibility study. Radiology 219, 264–269.

Berr, S., Roy, R., French, B., Yang, Z., Gilson, W., Kramer, C., Epstein, F., 2005. Black blood gradient echo cine magnetic resonance imaging of the mouse heart. Magnetic Resonance in Medicine 53 (5), 1074–1079.

Biesdorf, A., Wörz, S., Kaiser, H.-J., Stippich, C., Rohr, K., 2009. Hybrid spline-based multimodal registration using local measures for joint entropy mutual information. In: Medical Image Computing and Computer Assisted Intervention (MICCAI'09). Springer, pp. 607–615.

Bolson, E. L., Sheehan, F. H., September 1993. Centersurface model for 3D analysis of regional left biventricular function. IEEE Computers in Cardiology, London, U.K., 735–738.

Bolson, E. L., Sheehan, F. H., Legget, M. E., Jin, H., McDonald, J. A., Sampson, P. D., Martin, R. W., Bashein, G., Otto, C. M., September 1995. Applying the centersurface model to 3-d reconstructions of the left ventricle for regional functional analysis. IEEE Computers in Cardiology, Vienna, Austria, 63–67.

Canny, J., 1987. A computational approach to edge detection. In: RCV87. pp. 184–203.

Cerqueira, M. D., Weissman, N. J., Dilsizian, V., Jacobs, A. K., Kaul, S., Laskey, W. K., Pennell, D. J., Rumberger, J. A., Ryan, T., Veran, M. S., 2002. Standardized myocardial segmentation and nomenclature for tomographic imaging of the heart. Circulation 105, 539–542.

Chandrashekara, R., Rao, A., Sanchez-Ortiz, G. I., Mohiaddin, R., Rueckert, D., 2003. Construction of a statistical model for cardiac motion analysis using nonrigid image registration. In: Taylor, C. J., Noble, J. A. (Eds.), Information Processing in Medical Imaging, 18th International Conference, IPMI 2003, Ambleside, UK, July 20-25, 2003, Proceedings. Vol. 2732 of Lecture Notes in Computer Science. Springer, pp. 599–610.

Choi, Y., Lee, S., 2000. Injectivity conditions of 2D and 3D uniform cubic b-spline functions. Graphical Models 62, 411–427.

Christensen, G. E., Rabbitt, R. D., Miller, M. I., 1994. 3D brain mapping using a deformable neuroanatomy. Physics in Medicine and Biology 39 (3), 609–618.

Cigarroa, C. G., de Filippi, C. R., Brickner, M. E., Alvarez, L. G., Wait, M. A., Grayburn, P. A., 1993. Dobutamine stress echocardiography identifies hibernating myocardium and predicts recovery of left ventricular function after coronary revascularization. Circulation, American Heart Association 88, 430–436.

Cocosco, C. A., Niessen, W. J., Netsch, T., Vonken, E.-j. P., Lund, G., Stork, A., Viergever, M. A., 2008. Automatic image-driven segmentation of the ventricles in cardiac cine MRI. Journal of Magnetic Resonance Imaging 28, 366–374.

Collignon, A., Maes, F., Delaere, D., Vandermeulen, D., Suetens, P., Marchal, G., 1995. Automated multimodality medical image registration using information theory. In: Bizais, Y., Barillot, C., Paola, R. D. (Eds.), 14th Int. Conf. Information Processing in Medical Imaging; Computational Imaging and Vision 3. pp. 263–274.

Commowick, O., Arsigny, V., Costa, M. J., Ayache, N., Malandain, G., 2006. An efficient locally affine framework for the registration of anatomical structures. In: IEEE International Symposium on Biomedical Imaging (ISBI). IEEE, pp. 478–481.

Commowick, O., Arsigny, V., Isambert, A., Costa, J., Dhermain, F., Bidault, F., Bondiau, P. Y., Ayache, N., Malandain, G., 2008. An efficient locally affine framework for the smooth registration of anatomical structures. Medical Image Analysis 12 (4), 427–441.

Cootes, T. F., Beeston, C., Edwards, G. J., Taylor, C. J., 1999. A unified framework for atlas matching using active appearance models. Lecture Notes in Computer Science 1613, 322–333.

Cootes, T. F., Taylor, C. J., Cooper, D. H., Graham, J., Jan 1995. Active shape models: Their training and application. Computer Vision and Image Understanding 61 (1), 38–59.

Crum, W. R., Camara, O., Hawkes, D. J., 2007. Methods for inverting dense displacement fields: Evaluation in brain image registration. In: Ayache, N., Ourselin, S., Maeder, A. J. (Eds.), Medical Image Computing and Computer-Assisted Intervention - MICCAI 2007, 10th International Conference, Brisbane, Australia, October 29 - November 2, 2007, Proceedings, Part I. Vol. 4791 of Lecture Notes in Computer Science. Springer, pp. 900–907.

Crum, W. R., Camara, O., Hill, D. L. G., Nov. 2006. Generalized overlap measures for evaluation and validation in medical image analysis. IEEE Transactions on Medical Imaging 25 (11), 1451–1461.

Crum, W. R., Hill, D. L. G., Hawkes, D. J., 2003. Information theoretic similarity measures in non-rigid registration. In: Taylor, C. J., Noble, J. A. (Eds.), Information Processing in Medical Imaging, 18th International Conference, IPMI 2003, Ambleside, UK, July 20-25, 2003, Proceedings. Vol. 2732 of Lecture Notes in Computer Science. Springer, pp. 378–387.

Crum, W. R., Tanner, C., Hawkes, D. J., 2005. Anisotropic multi-scale fluid registration: Evaluation in magnetic resonance breast imaging. Physics in Medicine and Biology 50 (21), 5153–5174.

Cullen, J. H. S., Horsfield, M. A., Reek, C. R., Cherryman, G. R., Barnett, D. B., Samani, N. J., 1999. A myocardial perfusion reserve index in humans using first-pass contrast-enhanced magnetic resonance imaging. Journal of the American College of Cardiology 33 (5), 1386–1394.

Dawant, B. M., Hartmann, S. L., Thirion, J. P., Maes, F., Vandermeulen, D., Demaerel, P., 1999. Automatic 3-d segmentation of internal structures of the head in MR images using a combination of similarity and free-form transformations: Part I, methodology and validation on normal subjects. IEEE Transactions on Medical Imaging 18 (10), 909–916.

Dice, L. R., 1945. Measures of the amount of ecologic association between species. Ecology 26 (3), 297–302.

Earls, J. P., Ho, V. B., Foo, T. K., Castillo, E., Flamm, S. D., 2002. Cardiac MRI: Recent progress and continued challenges. Journal of Magnetic Resonance Imaging 16, 111–127.

Ecabert, O., Peters, J., Schramm, H., Lorenz, C., von Berg, J., Walker, M. J., Vembar, M., Olszewski, M. E., Subramanyan, K., Lavi, G., Weese, J., Sept. 2008. Automatic model-based segmentation of the heart in CT images. IEEE Transactions on Medical Imaging 27 (9), 1189–1201.

Edelman, R. R., Chien, D., Kim, D., 1991. Fast selective back-blood MR imaging. Radiology 181, 655–660.

Fact Sheet No. 317, World Health Organization, February 2007. Cardiovascular diseases. URL `http://www.who.int/mediacentre/factsheets/fs317/en/`

Frangi, A. F., Niessen, W. J., Viergever, M. A., 2001. Three-dimensional modeling for functional analysis of cardiac images: A review. IEEE Transactions on Medical Imaging 20, 2–25.

Frangi, A. F., Rueckert, D., Schnabel, J. A., Niessen, W. J., Sep. 2002. Automatic construction of multiple-object three-dimensional statistical shape models: Application to cardiac modeling. IEEE Transactions on Medical Imaging 21 (9), 1151–1166.

Glantz, S. A., 2005. Primer of Biostatistics, sixth Edition. McGraw-Hill.

Gotte, M. J. W., van Rossum, A. C., Twisk, J. W. R., Kuijer, J. P. A., Marcus, J. T., Visser, C. A., 2001. Quantification of regional contractile function after infarction: Strain analysis superior to wall thickening analysis in discriminating infarct from remote myocardium. Journal of the American College of Cardiology 37 (3), 808–817.

Grau, V., Becher, H., Noble, J. A., Sep. 2007. Registration of multiview real-time 3-D echocardiographic sequences. IEEE Transactions on Medical Imaging 26 (9), 1154–1165.

Grau, V., Noble, J. A., 2005. Adaptive multiscale ultrasound compounding using phase information. In: Duncan, J. S., Gerig, G. (Eds.), Medical Image Computing and Computer-Assisted Intervention - MICCAI 2005, 8th International Conference, Palm Springs, CA, USA, October 26-29, 2005, Proceedings, Part I. Vol. 3749 of Lecture Notes in Computer Science. Springer, pp. 589–596.

Griffin, L. D., 2001. Histograms of infinitesimal neighbourhoods. Lecture Notes in Computer Science 2106, 326–334.

Haber, E., Modersitzki, J., 2006. Intensity gradient based registration and fusion of multi-modal images. In: Larsen, R., Nielsen, M., Sporring, J. (Eds.), Medical Image Computing and Computer-Assisted Intervention - MICCAI 2006, 9th International Conference, Copenhagen, Denmark, October 1-6, 2006, Proceedings, Part II. Vol. 4191 of Lecture Notes in Computer Science. Springer, pp. 726–733.

Haber, E., Modersitzki, J., 2007. Intensity Gradient Based Registration and Fusion of Multi-modal Images. Methods of information in medicine 46 (3), 292–299.

Hajnal, J. V., Hill, D. L. G., Hawkes, D. J., June 2001. Medical Image Registration. CRC Press.

Hartmann, S. L., Parks, M. H., Martin, P. R., Dawant, B. M., 1999. Automatic 3-d segmentation of internal structures of the head in MR images using a combination of similarity and free-form transformations: Part II, validation on severely atrophied brains. IEEE Transactions on Medical Imaging 18 (10), 917–926.

Hautvast, G., Lobregt, S., Breeuwer, M., Gerritsen, F., 2006. Automatic contour propagation in cine cardiac magnetic resonance images. IEEE Transactions on Medical Imaging 25 (11), 1472–1482.

Heath, M. D., Sarkar, S., Sanocki, T. A., Bowyer, K. W., 1997. Robust visual method for assessing the relative performance of edge-detection algorithms. IEEE Transactions on Pattern Analysis and Machine Intelligence 19 (12), 1338–1359.

Jain, A. K., 1989. Fundamentals of Digital Image Processing. Englewood Cliffs, NJ, Prentice Hall.

Jaume, C.-R., Osvaldo, P.-V., Santiago, A.-B., Joan, C.-C., Guillermo, O.-M., Marc, S., Marina, S.-P., Antoni, R., Jordi, S.-S., 2004. Regional wall motion and wall thickening visual scores from gated spect in anterior and infero-lateral myocardial infarctions. Nuclear medicine communications 25 (2), 201–206.

Karacali, B., 2007. Information theoretic deformable registration using local image information. International Journal of Computer Vision 72 (3), 219–237.

Kass, M., Witkin, A., Terzopoulos, D., 1988. Snakes: Active contour models. International Journal of Computer Vision 1 (4), 321–331.

Kaus, M., von Berg, J., Niessen, W. J., Pekar, V., 2003. Automated segmentation of the left ventricle in cardiac MRI. In: Ellis, R. E., Peters, T. M. (Eds.), Medical Image Computing and Computer-Assisted Intervention - MICCAI 2003, 6th International Conference, Montréal, Canada, November 15-18, 2003, Proceedings, Part I. Vol. 2878 of Lecture Notes in Computer Science. Springer, pp. 432–439.

Kaus, M. R., von Berg, J., Weese, J., Niessen, W., Pekar, V., 2004. Automated segmentation of the left ventricle in cardiac MRI. Medical Image Analysis 8 (3), 245 – 254.

Klein, S., Staring, M., Pluim, J. P. W., Dec. 2007. Evaluation of optimization methods for nonrigid medical image registration using mutual information and B-splines. IEEE Trans. Image Processing 16 (12), 2879–2890.

Koikkalainen, J., Tolli, T., Lauerma, K., Antila, K., Mattila, E., Lilja, M., Lotjonen, J., Nov. 2008. Methods of artificial enlargement of the training set for statistical shape models. IEEE Transaction on Medical Imaging 27 (11), 1643–1654.

Kurkure, U., Pednekar, A., Muthupillai, R., Flamm, S. D., Kakadiaris, I. A., May 2009. Localization and segmentation of left ventricle in cardiac cine-MR images. IEEE transactions on bio-medical engineering 56, 1360–70.

Lapp, R. M., Lorenzo-Valdes, M., Rueckert, D., 2004. 3D/4D cardiac segmentation using active appearance models, non-rigid registration and the insight toolkit. In: Medical Image Computing and Computer-Assisted Intervention - MICCAI 2004, Proceedings. Lecture Notes in Computer Science. Springer, pp. 419–426.

Leemput, K. V., Maes, F., Vandermeulen, D., Suetens, P., 1999. Automated model-based tissue classification of MR images of the brain. IEEE Transactions on Medical Imaging 18 (10), 897–908.

Li, C., Sun, Y., 2009. Nonrigid registration of myocardial perfusion MRI using pseudo ground truth. In: Medical Image Computing and Computer-Assisted Intervention – MICCAI 2009. Vol. 5761 of LNCS. Springer, pp. 165–172.

Lieberman, A. N., Weiss, J. L., Jugdutt, B. I., Becker, L. C., Bulkley, B. H., Garrison, J. G., Hutchins, G. M., Kallman, C. A., Weisfeldt, M. L., 1981. Two-dimensional echocardiography and infarct size: Relationship of regional wall motion and thickening to the extent of myocardial infarction in the dog. Circulation 63, 739–746.

Likar, B., Pernus, F., 2001. A hierarchical approach to elastic registration based on mutual information. Image and Vision Computing 19, 33–44.

Little, J. A., Hill, D. L. G., Hawkes, D. J., 1997. Deformation incorporating rigid structures. Computer Vision and Image Understanding 66 (2), 223–232.

Lobregt, S., Viergever, M., 1995. A discrete dynamic contour model. IEEE Transactions on Medical Imaging 14 (1), 12–24.

Loeckx, D., Maes, F., Vandermeulen, D., Suetens, P., 2006. Comparison between parzen window interpolation and generalised partial volume estimation for nonrigid image registration using mutual information. In: International Workshop on Biomedical Image Registration (WBIR). pp. 206–213.

Loeckx, D., Slagmolen, P., Maes, F., Vandermeulen, D., Suetens, P., 2007. Nonrigid image registration using conditional mutual information. In: Karssemeijer, N., Lelieveldt, B. P. F. (Eds.), Information Processing in Medical Imaging, 20th International Conference, IPMI 2007, Kerkrade, The Netherlands, July 2-6, 2007, Proceedings. Vol. 4584 of Lecture Notes in Computer Science. Springer, pp. 725–737.

Loeckx, D., Slagmolen, P., Maes, F., Vandermeulen, D., Suetens, P., 2010. Nonrigid Image Registration Using Conditional Mutual Information. IEEE Transactions on Medical Imaging 29 (1), 19–29.

Lorenzo-Valdes, M., Sanchez-Ortiz, G. I., Elkington, A. G., Mohiaddin, R., Rueckert, D., 2004. Segmentation of 4D cardiac MR images using a probabilistic atlas and the EM algorithm. Medical Image Analysis 8, 255–265.

Lorenzo-Valdes, M., Sanchez-Ortiz, G. I., Mohiaddin, R., Rueckert, D., 2002. Atlas-based segmentation and tracking of 3D cardiac MR images using non-rigid registration. In: Dohi, T., Kikinis, R. (Eds.), Medical Image Computing and Computer-Assisted Intervention - MICCAI 2002, Proceedings. Lecture Notes in Computer Science 2488. Springer, pp. 642–650.

Lorenzo-Valdes, M., Sanchez-Ortiz, G. I., Mohiaddin, R., Rueckert, D., 2003. Segmentation of 4D cardiac MR images using a probabilistic atlas and the EM algorithm. In: Ellis, R. E., Peters, T. M. (Eds.), Medical Image Computing and Computer-Assisted Intervention - MICCAI 2003, 6th International Conference, Montréal, Canada, November 15-18, 2003, Proceedings, Part I. Vol. 2878 of Lecture Notes in Computer Science. Springer, pp. 440–450.

Lotjonen, J., Kivisto, S., Koikkalainen, J., Smutek, D., Lauerma, K., 2004. Statistical shape model of atria, ventricles and epicardium from short- and long-axis mr images. Medical Image Analysis 8, 371–386.

Lotjonen, J., Wolz, R., Koikkalainen, J., Thurfjell, L., Waldemar, G., Soininen, H., Rueckert, D., 2010. Fast and robust multi-atlas segmentation of brain magnetic resonance images. Neuroimage 49, 2352–65.

Lynch, M., Ghita, O., Whelan, P. F., 2008. Segmentation of the left ventricle of the heart in 3-D+t MRI data using an optimized nonrigid temporal model. IEEE Transactions on Medical Imaging 27 (2), 195–203.

Ma, Y. L., Penney, G. P., Rinaldi, C. A., Cooklin, M., Razavi, R., Rhode, K. S., 2009. Echocardiography to magnetic resonance image registration for use in image-guided cardiac catheterization procedures. Physics in Medicine and Biology 54 (16), 5039–5055.

Maes, F., Collignon, A., Vandermeulen, D., Marchal, G., Suetens, P., Apr. 1997. Multimodality image registration by maximization of mutual information. IEEE Transactions of Medical Imaging 16 (2), 187–198.

Melbourne, A., Atkinson, D., Hawkes, D. J., 2008. Influence of organ motion and contrast enhancement on image registration. In: Metaxas, D. N., Axel, L., Fichtinger, G., Székely, G. (Eds.), Medical Image Computing and Computer-Assisted Intervention - MICCAI 2008, 11th International Conference, New York, NY, USA, September 6-10, 2008, Proceedings, Part II. Vol. 5242 of Lecture Notes in Computer Science. Springer, pp. 948–955.

Melbourne, A., Atkinson, D., White, M. J., Collins, D., Leach, M., Hawkes, D., 2007. Registration of dynamic contrast-enhanced MRI using a progressive principal component registration (ppcr). Physics in Medicine and Biology 52, 5147–5156.

Mellor, M., Brady, M., 2005. Phase mutual information as a similarity measure for registration. Medical Image Analysis 9, 330–343.

Mitchell, S. C., Bosch, J. G., Lelieveldt, B. P. F., van der Geest, R. J., Reiber, J. H. C., Sonka, M., 2002. Active appearance models: Segmentation of cardiac MR and ultra sound images. IEEE Transactions on Medical Imaging 21 (9), 1167–1178.

Montagnat, J., Delingette, H., 2005. 4D deformable models with temporal constraints: Application to 4D cardiac image segmentation. Medical Image Analysis 9, 87–100.

Narayanan, R., Fessler, J. A., Park, H., Meyer, C. R., 2005. Diffeomorphic nonlinear transformations: A local parametric approach for image registration. In: Christensen, G. E., Sonka, M. (Eds.), Information Processing in Medical Imaging, 19th International Conference, IPMI 2005, Glenwood Springs, CO, USA, July 10-15, 2005, Proceedings. Vol. 3565 of Lecture Notes in Computer Science. Springer, pp. 174–185.

National Institutes of Health [online], March 2008.
URL http://www.nhlbi.nih.gov/health/dci/Diseases/HeartAttack/HeartAttack_WhatIs.html

National Institutes of Health [online], August 2009.
URL http://www.nhlbi.nih.gov/health/dci/Diseases/tof/tof_what.html

Noble, J. A., Boukerroui, D., Aug. 2006. Ultrasound image segmentation: A survey. IEEE Transaction on Medical Imaging 25 (8), 987–1010.

Oosterhof, T., Mulder, B., Vliegen, H., de Roos, A., 2006. Cardiovascular magnetic resonance in the follow-up of patients with corrected tetralogy of fallot: A review. American Heart Journal 151, 265–272.

Ordas, S., Frangi, A. F., 2005. Automatic quantitative analysis of myocardial wall motion and thickening from long-and short-axis cine MRI studies. In: IEEE Engineering in Medicine and Biology Society. pp. 7028–7031.

Orderud, F., Hansegård, J., Rabben, S. I., 2007. Real-time tracking of the left ventricle in 3D echocardiography using a state estimation approach. In: Ayache, N., Ourselin, S., Maeder, A. J. (Eds.), Medical Image Computing and Computer-Assisted Intervention - MICCAI 2007, 10th International Conference, Brisbane, Australia, October 29 - November 2, 2007, Proceedings, Part I. Vol. 4791 of Lecture Notes in Computer Science. Springer, pp. 858–865.

Ourselin, S., Roche, A., Subsol, G., Pennec, X., Ayache, N., 2001. Reconstructing a 3d structure from serial histological sections. Image Vision Comput. 19 (1-2), 25–31.

Penney, G. P., Weese, J., Little, J. A., Desmedt, P., Hill, D. L. G., Hawkes, D. J., 1998. A comparison of similarity measures for use in 2D-3D medical image registration. IEEE Transaction on Medical Imaging 17 (4), 586–595.

Pereles, F. S., Kapoor, V., Carr, J. C., Simonetti, O. P., Krupinski, E. A., Baskaran, V., Finn, J. P., 2001. Usefulness of segmented truefisp cardiac pulse sequence in evaluation of congenital and acquired adult cardiac abnormalities. American journal of roentgenology 177 (5), 1155–1160.

Perperidis, D., Mohiaddin, R., Rueckert, D., 2005. Construction of a 4D statistical atlas of the cardiac anatomy and its use in classification. In: Duncan, J. S., Gerig, G. (Eds.), Medical Image Computing and Computer-Assisted Intervention - MICCAI 2005, 8th International Conference, Palm Springs, CA, USA, October 26-29, 2005, Proceedings, Part II. Vol. 3750 of Lecture Notes in Computer Science. Springer, pp. 402–410.

Peters, J., Ecabert, O., Meyer, C., Kneser, R., Weese, J., 2009. Optimizing boundary detection via simulated search with applications to multi-modal heart segmentation. Medical Image Analysis 14, 70–84.

Peters, J., Ecabert, O., Meyer, C., Schramm, H., Kneser, R., Groth, A., Weese, J., 2007. Automatic whole heart segmentation in static magnetic resonance image volumes. In: Medical

Image Computing and Computer-Assisted Intervention. Vol. 4792 of Lecture Notes in Computer Science. Springer, pp. 402–410.

Pham, D. L., Xu, C., Prince, J. L., 2000. Current methods in medical image segmentation. Annual Review of Biomedical Engineering 02, 315–337.

Philips Healthcare [online], 2009a.
URL `http://www.medical.philips.com/main/products/mri/systems/index.wpd`

Philips Healthcare [online], 2009b.
URL `http://www.medical.philips.com/main/products/mri/options_upgrades/coils/intera/coils_cardiac.wpd`

Philips Healthcare [online], 2009c.
URL `http://www.healthcare.philips.com/au/products/ultrasound/systems/ie33/index.wpd`

Pilgram, R., Schubert, R., Fritscher, K. D., Zwick, R. H., Schocke, M. F., Trieb, T., Pachinger, O., 2006. Shape discrimination of healthy and diseased cardiac ventricles using medial representation. Journal International Journal of Computer Assisted Radiology and Surgery 1 (1), 33–38.

Pitiot, A., Malandain, G., Bardinet, E., Thompson, P. M., 2003. Piecewise affine registration of biological images. In: Gee, J. C., Maintz, J. B. A., Vannier, M. W. (Eds.), Biomedical Image Registration, Second International Workshop, WBIR 2003, Philadelphia, PA, USA, June 23-24, 2003, Revised Papers. Vol. 2717 of Lecture Notes in Computer Science. Springer, pp. 91–101.

Pizer, S. M., Fletcher, P. T., Joshi, S. C., Thall, A., Chen, J. Z., Fridman, Y., Fritsch, D. S., Lu, A. C. L., Muller, K. E., Tracton, G., Yushkevich, P. A., Chaney, E. L., Nov. 2003. Deformable M-reps for 3D medical image segmentation. International Journal of Computer Vision 55 (2-3), 85–106.

Pluempitiwiriyawej, C., Moura, J. M. F., Wu, Y.-J. L., Ho, C., 2005. STACS: New active contour scheme for cardiac MR image segmentation. IEEE Transactions on Medical Imaging 24, 593–603.

Pluim, J. P. W., Maintz, J. B. A., Viergever, M. A., 2000. Interpolation artefacts in mutual information-based image registration. Computer Vision and Image Understanding 77 (2), 211–232.

Pluim, J. P. W., Maintz, J. B. A., Viergever, M. A., 2003. Mutual information based registration of medical images: A survey. IEEE Transaction on Medical Imaging 22 (8), 986–1004.

Powell, M. J. D., 1964. An efficient method for finding the minimum of a function of several variables without calculating derivatives. Computer Journal 7, 155–162.

Rajpoot, K., Noble, J. A., Grau, V., Szmigielski, C., Becher, H., 2009a. Image-driven cardiac left ventricle segmentation for the evaluation of multiview fused real-time dimensional echocardiography images. In: Medical Image Computing and Computer-Assisted Intervention – MICCAI 2009. Vol. 5762 of LNCS. Springer, pp. 893–900.

Rajpoot, K., Noble, J. A., Grau, V., Szmigielski, C., Becher, H., 2009b. Multiview rt3d echocardiography image fusion. In: Ayache, N., Delingette, H., Sermesant, M. (Eds.), Functional Imaging and Modeling of the Heart, 5th International Conference, FIMH 2009. Vol. 5528 of Lecture Notes in Computer Science. Springer, pp. 134–143.

Roche, A., Malandain, G., Ayache, N. J., 2000. Unifying maximum likelihood approaches in medical image registration. International Journal of Imaging Systems and Technology 11 (1), 71–80.

Rohlfing, T., Maurer, C. R., 2007. Shape-based averaging. IEEE Trans. Image Processing 16 (1), 153–161.

Rohlfing, T., Maurer, J. C. R., 2005. Multi-classifier framework for atlas-based image segmentation. Pattern Recognition Letters 26, 2070–2079.

Rohling, R., Gee, A. H., Berman, L. H., 1997. Spatial compounding of 3-D ultrasound images. In: Information Processing in Medical Imaging. Vol. 1230 of Lecture Notes in Computer Science. pp. 519–524.
URL http://dx.doi.org/10.1007/3-540-63046-5_53

Rouchdy, Y., Pousin, J., Schaerer, J., Clarysse, P., 2007. A nonlinear elastic deformable template for soft structure segmentation: Application to the heart segmentation in MRI. Inverse Problems 23 (3), 1017–1035.

Rueckert, D., Aljabar, P., Heckemann, R. A., Hajnal, J. V., Hammers, A., 2006. Diffeomorphic registration using b-splines. In: Medical Image Computing and Computer-Assisted Intervention - MICCAI 2006, Proceedings. Lecture Notes in Computer Science 4191. Springer, pp. 702–709.

Rueckert, D., Frangi, A. F., Schnabel, J. A., Aut 2003. Automatic construction of 3-D statistical deformation models of the brain using nonrigid registration. IEEE Transactions on Medical Imaging 22 (8), 1014–1025.

Rueckert, D., Lorenzo-Valdeés, M., Chandrashekara, R., Sanchez-Ortiz, G. I., Mohiaddin, R., 2002. Non-rigid registration of cardiac MR: Application to motion modelling and atlas-based segmentation. In: IEEE International Symposium on Biomedical Imaging (ISBI). IEEE, pp. 481–484.

Rueckert, D., Sonoda, L. I., Hayes, C., Hill, D. L. G., Leach, M. O., Hawkes, D. J., 1999. Nonrigid registration using free-form deformations: Application to breast MR images. IEEE Transactions on Medical Imaging 18, 712–721.

Schnabel, J. A., Rueckert, D., Quist, M., Blackall, J. M., Castellano-Smith, A. D., Hartkens, T., Penney, G. P., Hall, W. A., Liu, H., Truwit, C. L., Gerritsen, F. A., Hill, D. L. G., Hawkes, D. J., 2001. A generic framework for non-rigid registration based on non-uniform multi-level free-form deformations. In: Medical Image Computing and Computer-Assisted Intervention - MICCAI 2001, Proceedings. Vol. 2208 of Lecture Notes in Computer Science. Springer, pp. 573–581.

Sermesant, M., Forest, C., Pennec, X., Delingette, H., Ayache, N., 2003. Deformable biomechanical models: Application to 4D cardiac image analysis. Medical Image Analysis 7, 475–488.

Sermesant, M., Moireau, P., Camara, O., Sainte-Marie, J., Andriantsimiavona, R., Cimrman, R., Hill, D. L. G., Chapelle, D., Razavi, R., 2006. Cardiac function estimation from mri using a heart model and data assimilation: Advances and difficulties. Medical Image Analysis 10, 642–656.

Setser, R. M., Fischer, S. E., Lorenz, C. H., 2000. Quantification of left ventricular function with magnetic resonance images acquired in real time. Journal of Magnetic Resonance Imaging 12, 430–438.

Sheehan, F. H., Bolson, E. L., Dodge, H. T., Mathey, D. G., Schofer, J., Woo, H. K., 1986. Advantages and applications of the centerline method for characterizing regional ventricular function. Circulation 74 (2), 293–305.

Shepard, D., 1968. A two-dimensional interpolation function for irregularly-spaced data. In: 23rd national Conference of the ACM. ACM Press, pp. 517–527.

Siddiqi, K., Pizer, S., 2008. Medial Representations: Mathematics, Algorithms and Applications. Springer Verlag.

Simonetti, O., Finn, J., White, R., Laub, G., Henry, D., 1996. Black blood T2-weighted inversion-recovery MR imaging of the heart. Radiology 199 (1), 49–57.

Studholme, C., Drapaca, C. S., Iordanova, B., Cardenas, V., May 2006. Deformation-based mapping of volume change from serial brain MRI in the presence of local tissue contrast change. IEEE Transactions on Medical Imaging 25 (5), 626–639.

Studholme, C., Hill, D. L. G., Hawkes, D. J., Jan 1999. An overlap invariant entropy measure of 3D medical image alignment. Pattern Recognition 32 (1), 71–86.

Suinesiaputra, A., Frangi, A. F., Lamb, H. J., Reiber, J. H. C., Lelieveldt, B. P. F., 2005. Automatic prediction of myocardial contractility improvement in stress MRI using shape morphometrics with independent component analysis. In: Christensen, G. E., Sonka, M. (Eds.), Information Processing in Medical Imaging, 19th International Conference, IPMI 2005, Glenwood Springs, CO, USA, July 10-15, 2005, Proceedings. Vol. 3565 of Lecture Notes in Computer Science. Springer, pp. 321–332.

Suinesiaputra, A., Üzümcü, M., Frangi, A. F., Kaandorp, T. A. M., Reiber, J. H. C., Lelieveldt, B. P. F., 2004. Detecting regional abnormal cardiac contraction in short-axis MR images using independent component analysis. In: Barillot, C., Haynor, D. R., Hellier, P. (Eds.), Medical Image Computing and Computer-Assisted Intervention–MICCAI 2004, 7th International Conference Saint-Malo, France, September 26-29, 2004, Proceedings, Part I. Vol. 3216 of Lecture Notes in Computer Science. Springer, pp. 737–744.

Suri, J. S., 2000. Computer vision, pattern recognition and image processing in left ventricle segmentation: The last 50 years. Pattern Analysis and Applications 3 (3), 209–242.

Takuma, S., Ota, T., Muro, T., Hozumi, T., Sciacca, R., Di Tullio, M. R., Blood, D. K., Yoshikawa, J., Homma, S., 2001. Assessment of left ventricular function by real-time 3-dimensional echocardiography compared with conventional noninvasive methods. Journal of the American Society of Echocardiography 14, 275–284.

Thévenaz, P., Unser, M., Dec. 2000. Optimization of mutual information for multiresolution image registration. IEEE Transactions on Image Processing 9 (12), 2083–2099.

Thibodeau, G., Patton, K., 2004. STRUCTURE & FUNCTION OF THE BODY, 12th Edition. Mosby.

Uribe, S., Muthurangu, V., Boubertakh, R., Schaeffter, T., Razavi, R., Hill, D. L., Hansen, M. S., 2007. Whole-heart cine MRI using real-time respiratory self-gating. Magnetic Resonance in Medicine 57 (3), 606–613.

Uribe, S., Tangchaoren, T., Parish, V., Wolf, I., Razavi, R., Greil, G., Schaeffter, T., 2008. Volumetric cardiac quantification by using 3D dual-phase whole-heart MR imaging. Radiology 248, 606–614.

van Assen, H. C., Danilouchkine, M. G., Dirksen, M. S., Reiber, J. H. C., Lelieveldt, B. P. F., 2008. A 3-D active shape model driven by fuzzy inference: Application to cardiac CT and MR. IEEE Transactions on Information Technology in Biomedicine 12 (5), 595–605.

van Assen, H. C., Danilouchkine, M. G., Frangi, A. F., Ords, S., Westenberg, J. J. M., Reiber, J. H. C., Lelieveldt, B. P. F., 2006. SPASM: A 3D-ASM for segmentation of sparse and arbitrarily oriented cardiac MRI data. Medical Image Analysis 10, 286–303.

van der Geest, R. J., de Roos, A., van der Wall, E. E., Reiber, J. H. C., June 1997. Quantitative analysis of cardiovascular MR images. International journal of cardiac imaging 13 (3), 247–258.

Vercauteren, T., Pennec, X., Perchant, A., Ayache, N., 2007. Non-parametric diffeomorphic image registration with the demons algorithm. In: Ayache, N., Ourselin, S., Maeder, A. J. (Eds.), Medical Image Computing and Computer-Assisted Intervention - MICCAI 2007, 10th International Conference, Brisbane, Australia, October 29 - November 2, 2007, Proceedings, Part II. Vol. 4792 of Lecture Notes in Computer Science. pp. 319–326.

Viola, P., Wells, III, V. M., 1997. Alignment by maximization of mutual information. International Journal of Computer Vision 24 (2), 137–154.

Viola, P. A., Wells, III, W. M., 1995. Alignment by maximization of mutual information. In: ICCV. pp. 16–23.

Wachinger, C., Wein, W., Navab, N., 2007. Three-dimensional ultrasound mosaicing. In: Ayache, N., Ourselin, S., Maeder, A. J. (Eds.), Medical Image Computing and Computer-Assisted Intervention - MICCAI 2007, Part II. Vol. 4792 of Lecture Notes in Computer Science. Springer, pp. 327–335.

Warfield, S. K., Zou, K. H., Wells III, W. M., 2004. Simultaneous truth and performance level estimation (STAPLE): An algorithm for the validation of image segmentation. IEEE Transaction on Medical Imaging 23 (7), 903–921.

Weese, J., Kaus, M., Lorenz, C., Lobregt, S., Truyen, R., Pekar, V., 2001. Shape constrained deformable models for 3D medical image segmentation. In: Insana, M. F., Leahy, R. M. (Eds.), Information Processing in Medical Imaging, 17th International Conference, IPMI 2001, Davis, CA, USA, June 18-22, 2001, Proceedings. Vol. 2082 of Lecture Notes in Computer Science. Springer, pp. 380–387.

Wells III, W. M., Viola, P., Atsumi, H., Nakajima, S., Kikinis, R., 1996. Multi-modal volume registration by maximisation of mutual information. Medical Image Analysis 1 (1), 35–51.

Westbrook, C., Roth, C. K., Talbot, J., 2004. MRI in Practice. Blackwell Publishing.

Yao, C., Simpson, J., Jansen, C., King, A., Penney, G., 2009. Spatial compounding of large sets of 3D echocardiography images. In: SPIE, Medical Imaging 09.

Zhang, W., Noble, J. A., Brady, J. M., 2007. Adaptive non-rigid registration of real time 3D ultrasound to cardiovascular MR images. In: Karssemeijer, N., Lelieveldt, B. P. F. (Eds.), Information Processing in Medical Imaging, IPMI 2007. Vol. 4584 of Lecture Notes in Computer Science. Springer, pp. 50–61.

Zhang, Y., Brady, M., Smith, S., 2001. Segmentation of brain MR images through a hidden markov random field model and the expectation maximization algorithm. IEEE Transactions of Medical Imaging 20 (1), 45–57.

Zhu, Y., Papademetris, X., Sinusas, A. J., Duncan, J. S., 2007. Segmentation of myocardial volumes from real-time 3D echocardiography using an incompressibility constraint. In: Ayache, N., Ourselin, S., Maeder, A. J. (Eds.), Medical Image Computing and Computer-Assisted Intervention - MICCAI 2007, 10th International Conference, Brisbane, Australia, October 29 - November 2, 2007, Proceedings, Part I. Vol. 4791 of Lecture Notes in Computer Science. Springer, pp. 44–51.

Zhu, Y., Papademetris, X., Sinusas, A. J., Duncan, J. S., 2009. A dynamical shape prior for lv segmentation from rt3d echocardiography. In: Medical Image Computing and Computer-Assisted Intervention - MICCAI 2007. Vol. 5761 of Lecture Notes in Computer Science. Springer, pp. 206–213.

Zhuang, X., December 2006. Medical image registration based on normal vector information. Master's thesis, Shanghai Jiao Tong University.

Zhuang, X., Arridge, S., Hawkes, D. J., Ourselin, S., 2011. A nonrigid registration framework using spatially encoded mutual information and free-form deformations. IEEE Transactions on Medical Imaging 30 (10), 1819–1828.

Zhuang, X., Gu, L., 2006. Normal vector information registration and comparisons with mutual information. In: IEEE Engineering in Medicine and Biology Society. Vol. 38. pp. 27–30.

Zhuang, X., Gu, L., Xu, J., 2005. Medical image alignment by normal vector information. In: International Conference Computational Intelligence and Security. Vol. 3801 of Lecture Notes in Computer Science. pp. 890–895.

Zhuang, X., Hawkes, D. J., Crum, W. R., Boubertakh, R., Uribe, S., Atkinson, D., Batchelor, P., Schaeffter, T., Razavi, R., Hill, D., 2008a. Robust registration between cardiac MRI images and atlas for segmentation propagation. In: Medical Imaging 2008. Vol. 6914 of Proceedings of SPIE. p. 07.

Zhuang, X., Hawkes, D. J., Ourselin, S., 2009a. Unifying encoding of spatial information in mutual information for nonrigid registration. In: Information Processing in Medical Imaging. Vol. 5636 of Lecture Notes in Computer Science. pp. 491–502.

Zhuang, X., Hawkes, D. J., Ourselin, S., 2010a. Spatial information encoded mutual information for nonrigid registration. In: International Workshop on Biomedical Image Registration (WBIR). Vol. 6204 of Lecture Notes in Computer Science. pp. 246–257.

Zhuang, X., Leung, K., Rhode, K., Razavi, R., Hawkes, D. J., Ourselin, S., 2010b. Whole heart segmentation of cardiac MRI using multiple path propagation strategy. In: Medical Image Computing and Computer Assisted Intervention (MICCAI'10). Vol. 6361 of Lecture Notes in Computer Science. pp. 435–443.

Zhuang, X., Ourselin, S., Razavi, R., Hill, D., Hawkes, D. J., 2008b. Automatic whole heart segmentation based on atlas propagation with a priori anatomical information. In: Medical Image Understanding and Analysis - MIUA 2008, University of Dundee, Dundee, Scotland, 2nd-3rd July, 2008, Proceedings. pp. 29–33.

Zhuang, X., Rhode, K., Arridge, S., Razavi, R., Hill, D., Hawkes, D., Ourselin, S., 2008c. An atlas-based segmentation propagation framework using locally affine registration – application to automatic whole heart segmentation. In: Medical Image Computing and Computer-Assisted Intervention. Vol. 5242 of Lecture Notes in Computer Science. pp. 425–433.

Zhuang, X., Rhode, K., Razavi, R., Hawkes, D. J., Ourselin, S., 2010c. A registration-based propagation framework for automatic whole heart segmentation of cardiac MRI. IEEE Transactions on Medical Imaging 29 (9), 1612–1625.

Zhuang, X., Rhode, K. S., Razavi, R., Hawkes, D. J., Ourselin, S., 2009b. Free-form deformations using adaptive control point status for whole heart MR segmentation. In: Functional Imaging and Modeling of the Heart. Vol. 5528 of Lecture Notes in Computer Science. pp. 303–311.

Zhuang, X., Yao, C., Ma, Y. L., Hawkes, D. J., Penney, G., Ourselin, S., 2010d. Registration-based propagation for whole heart segmentation from compounded 3d echocardiography. In: IEEE International Symposium on Biomedical Imaging (ISBI). pp. 1093–1096.

Automatic Whole Heart Segmentation Based on Image Registration ZHUANG, Xiahai PhD Thesis 2010 UCL